University of Colorado Boulder

Department of Aerospace Engineering Sciences

NanoSAM II - Project Final Report

ASEN 4028 - Senior Design

May 3, 2021

Project Customers

Jim Baer Email: jim134@comcast.net	Jaykob Velasquez Email: jvelasq1@ball.com

Project Advisor

Dr. Allison Anderson Email: allison.p.anderson@colorado.edu

Team Members

Jaret Anderson Email: jaret.anderson@colorado.edu	Jackson Kistler Email: jackson.kistler@colorado.edu
Daniel Barth Email: daba8552@colorado.edu	David Perkins Email: david.perkins@colorado.edu
Matthew Bridges Email: matthew.bridges@colorado.edu	Donavon Schroeder Email: donavon.schroeder@colorado.edu
Jashan Chopra Email: jashan.chopra@colorado.edu	Ryan Smithers Email: ryan.smithers@colorado.edu
Axel Haugland Email: amha7057@colorado.edu	Emma Tomlinson Email: emma.tomlinson@colorado.edu
Abigail Hause Email: abigail.hause@colorado.edu	Daniel Wagner Email: dawa1596@colorado.edu

Contents

List of Figures

List of Tables

Acronyms

ADC	=	Analog to Digital Converter
ADCS	=	Attitude Determination and Control System
BOM	=	Bill of Materials
CAM	=	Computer Aided Manufacturing
CTE	=	Coefficient of Thermal Expansion
EDAC	=	Error Detection and Correction
ESD	=	Electrostatic Discharge
FBD	=	Functional Block Diagram
FOV	=	Field of View
GUI	=	Graphical User Interface
ICD	=	Interface Control Document
LEO	=	Low-Earth Orbit
LSB	=	Least Significant Bit
MTF	=	Modular Transfer Function
NanoSAM	=	Nano-Stratospheric Aerosol Measurement
NASA	=	National Aeronautics and Space Administration
NS1	=	NanoSAM I
NS2	=	NanoSAM II
SEC-DED	=	Single Error Correction, Double Error Detection
SEE	=	Single Event Error
SNR	=	Signal to Noise Ratio
SAGE	=	Stratospheric Aerosol and Gas Experiment
SAM	=	Stratospheric Aerosol Measurement
SPI	=	Serial Peripheral Interface
TVS	=	Transient Voltage Suppression
V&V	=	Verification and Validation

Nomenclature

R_λ	=	Responsivity at given wavelength
λ	=	Wavelength
I_p	=	Photodiode Current [A]
V	=	Voltage [V]
P_i	=	Incident Power [W]
$\mathcal{R}$	=	Responsivity [A/W]
V_{cc}	=	Supply Voltage [V]
f	=	Frequency [Hz]
C_f	=	Feedback Capacitance [F]
R_f	=	Feedback Resistance [Ohms]
V_{DS}	=	MOSFET Drain-Source Voltage [V]
T	=	Temperature [K]
B	=	Thermistor Sensivity Constant [K]
q	=	Elementary Charge [C]
k_B	=	Boltzmann Constant [m^2 kg s^{-2} K^{-1}]

I. Project Purpose

Authors: Jaret Anderson

The goal of the Nano-Stratospheric Aerosol Measurement (NanoSAM) mission is to produce a compact method of profiling aerosol concentrations in the stratosphere. Aerosol concentration affects visibility in the atmosphere, an important aspect to consider for crewed aircraft. Additionally, according to an article by NASA Langley, atmospheric aerosol concentration affects the radiative balance of the Earth by changing how sunlight reflects off of clouds in the atmosphere, which has implications on Earth's climate and environmental change [1]. This same article states that "current observations of the buildup [of aerosols in the atmosphere] are available only for a few locations around the globe and these observations are fragmentary" [1]. Therefore, NanoSAM aims to fill the need of increasing the availability of these measurements by providing a low-cost, low-mass instrument that can be deployed into Low-Earth Orbit (LEO) as a constellation.

NanoSAM seeks to use solar occultation to measure the aerosol concentrations, similar to Stratospheric Aerosol Measurement II (SAM-II) experiment from 1978 [3]. Solar occultation is "a technique in which the transmission of sunlight through the Earth's atmosphere is measured and ratioed to solar measurements recorded with no atmospheric attenuation" [2]. The NanoSAM CubeSat is designed to meet or exceed the optical specifications of SAM-II so that it produces data that will have the same degree of scientific usefulness as this legacy system. This saves the need to perform exhaustive research into the rationale behind the optics performance metrics, something that Ball Aerospace, the customer of this project, wishes to avoid. The NanoSAM CubeSat as a whole is designed to have a mass of approximately 1.33 kg, which is the the standard mass of a 1U CubeSat according to the NASA CubeSat 101 guide [5]. This is only around 2% of the 76 kg mass of the Stratospheric Aerosols and Gases Experiment III (SAGE-III) system [6], the latest instrument in the SAM and SAGE series of aerosol profiling satellites. Packaging the NanoSAM aerosol measurement sensor in such a small enclosure greatly reduces launch costs associated with the instrument, greatly reducing the barrier to entry of deploying a constellation of NanoSAM CubeSats. Deploying these instruments as a constellation would lead to a much higher measurement frequency than SAM-II, which is what makes this project of interest to the customer. For solar occultation measurements, the total number of measurement windows is a direct function of orbital parameters. This means that a constellation of four NanoSAM CubeSats would be able to gather four times as much data as a single CubeSat. This solves the issues outlined by NASA surrounding the fragmentary availability of stratospheric aerosol measurements [1].

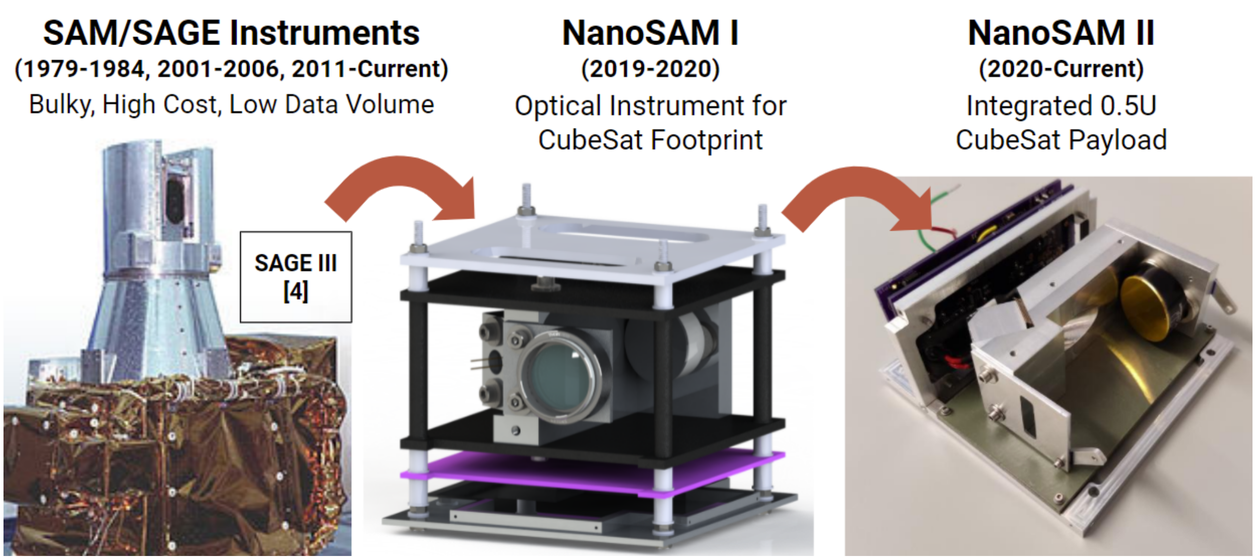

Fig. 1 Design Heritage [4]

Shown above in Fig. 1 is the evolution of the NanoSAM mission. The NanoSAM I project focused on creating an optic which matched the performance metrics of the SAM-II instrument but fit within a CubeSat footprint. This optic from last year's project was being integrated into a 0.5U CubeSat payload this year by the NanoSAM II team. The size of 0.5U was chosen such that this payload could be integrated into a 1U or 1.5U CubeSat by future teams. The

NanoSAM II payload has four key subsystems:

1) Optics, focusing on aligning and improving the optic designed by NanoSAM I
2) Structures, focused on creating a 0.5U structure that can meet thermal and vibrational requirements while accommodating each of the other subsystems' hardware
3) Electronics, focused on creating a low-noise board to condition and digitize the optics signals
4) Software, focused on processing, storing, and downlinking data accurately and on time

Along with designing and manufacturing the payload, the NanoSAM II team has run component-level, subsystem-level, and system-level testing to ensure that the payload meets each of the project requirements. To guide your reading of the upcoming sections, here is a brief overview of the results from this year's efforts: The optics were not fully aligned due to COVID-19 restrictions preventing the team from spending ample time with an interferometer. The structure met size requirements and vibrational requirements and is largely considered a success. The electronics required one redesign in the middle of the year and the final board has one white-wire fix, but this subsystem also met requirements and is considered a success. The software is a fully-functional set of flight software and an accompanying ground software GUI for sending commands and displaying results, and overall this subteam exceeds expectations for the project. Whole system testing could not be completed due to the optic not being properly aligned, and photodiode measurements from the integrated payload were critical to the usefulness of these system-level tests. More detailed results for each subteam are presented over the course of this report.

II. Project Objectives and Functional Requirements

Authors: Jaret Anderson, Axel Haugland

A. Specific Objectives

Specific objectives of the project are the tasks and specifications that the NanoSAM II project seeks to meet for a successful mission. These objectives are broken into three levels of success to support the NanoSAM II project requirements in Tab. 1. While the project is incorporating lessons learned and some legacy hardware provided by the NanoSAM I team, this year's specific objectives have their own unique set of design challenges that set them apart from simply iterating on the goals of NanoSAM I. Testing will be carried out on the existing hardware to learn all possible lessons from last year's progress, and the known issues from the NanoSAM I Project Final Report will be kept in mind. However, NanoSAM II places an increased emphasis on the design required for successful optics performance in the spaceflight environment.

All level one objectives represent new capabilities beyond what was accomplished by NanoSAM I in the 2019-2020 academic year. Achieving the Level 1 objectives would allow NanoSAM II to carry out a solar attenuation test with the optics and electronics in a 0.5U enclosure, three times smaller than the test structure designed for last year. Level 2 objectives are those that lead to an improved ground performance, coming from iterations in optics and electronics design along with implementing existing industry standards for CubeSat payload housings. Lastly, level 3 objectives relate to testing to verify that the payload is flight capable and meets the objectives set forth by the customer. Level 3 will require the team to prepare the enclosure such that it can be successfully mated with a typical industry bus and also passes environmental testing. Due to the current social and economic environment, it is unknown if the payload will be able to be flown this year. By designing to a payload with flexible software and structural constraints, this project aims to minimize future teams' work required to make payload systems compatible with a bus.

These three levels of objectives support the uncertainty in the availability of testing equipment and facilities that this year's team will face. Early testing will be done using the previous team's components while the design team focuses on the new design required to meet Level 1 objectives. This early testing will help inform and improve testing procedures for the upgraded system in order to validate the level 2 objectives. Level 3 environmental tests will then be carried out in the case that COVID-19 restrictions can be relaxed in the Spring of 2021, allowing the team to access the facilities necessary to verify the environmental objectives. The values for the thermal and vibrational requirements were referenced from the QB50 System Requirements guidelines for CubeSats [10].

By creating a payload which satisfies these objectives, the NanoSAM II team will provide a deliverable to the customer which can be integrated with a CubeSat Bus by a future team. This integrated CubeSat can then be tested and certified for flight, at which point a NanoSAM CubeSat would be ready to be launched into orbit. If proven successful, more NanoSAM CubeSats could be manufactured and launched into a constellation. To support these multi-year goals, the NanoSAM II team will be providing more deliverables than just the payload hardware itself. Detailed documentation will be kept during all phases of design, manufacturing, integration, and testing to ensure future teams are aware of what successes and failures the NanoSAM II team faced. This documentation is crucial to ensure that future teams understand how the NanoSAM II payload functions, saving on future design and debugging work. This documentation is being kept both on Google Drive and on GitHub to ensure easy collaboration.

	Level 1 (Solar Tracking Test)	**Level 2** (Improved Ground Performance)	**Level 3** (Flight Capability Testing)
Payload Housing	The payload housing contains the integrated electronics board and optics bench inside a 0.5U enclosure.	The payload housing structural interface is compatible with an industry standard bus.	The payload housing functions within the operating temperature range of -20°C to 50°C and its lowest vibrational natural frequency is greater than 100Hz [10].
Data Capture	Software and electronics acquires, digitizes, packetizes, and downloads raw data from a photodetector to a computer at a rate of at least 50Hz within the mission-specific measurement schedule detailed in the CONOPS.	Error checking measures are implemented in the ground software to detect data corruption occurring during transmission.	Data is transferred from the payload to a computer emulating an industry standard CubeSat bus communications system [11].
Electronics & Control	The redesigned electronics board successfully controls and powers all on-board operations and has a footprint compatible with the 0.5U payload enclosure.	The redesigned electronics board supports all optical design improvements.	The redesigned electronics board remains within the operating temperature range of -20°C to 50°C and its lowest vibrational natural frequency is greater than 100Hz [10].

Table 1 Specific Objectives

Crucial context for the above objectives is that NanoSAM II is one project in a line of many to ultimately create a NanoSAM CubeSat. Fig. 2 emphasize how the design carried out for the NanoSAM II project fits into the context of the entire NanoSAM mission.

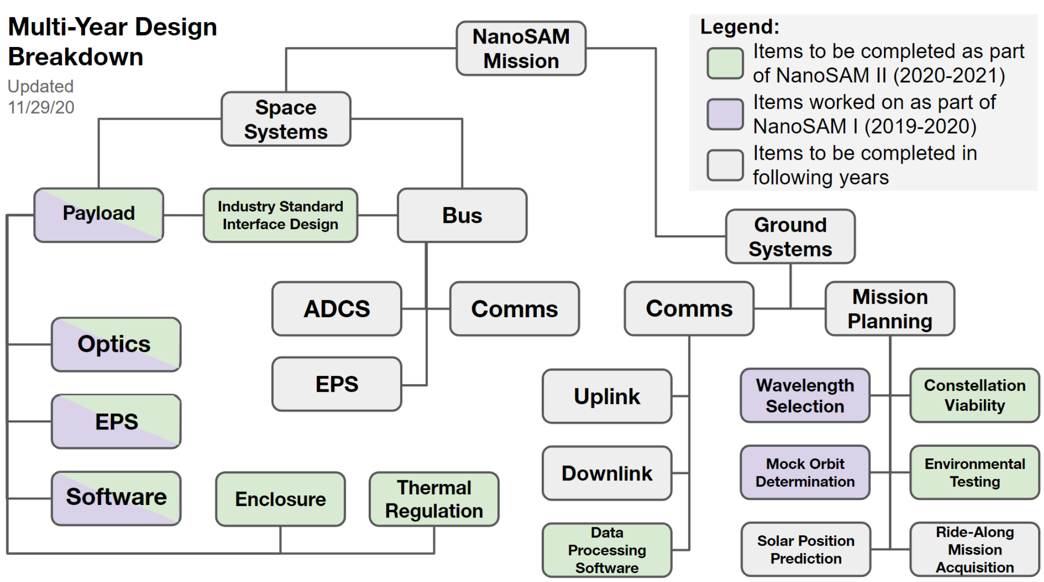

Fig. 2 NanoSAM Mission Multi-Year Design Breakdown

B. Concept of Operations

The Concept of Operations (CONOPS) in Fig. 3 shows the expected operation of the NanoSAM CubeSat on orbit. This year's tests are designed to emulate many of the challenges faced while executing this CONOPS so that the payload can be determined to satisfy the functionality required to carry out the mission shown below. The team also animated this CONOPS, which can be found at this link: https://youtu.be/6p307_xWcEk

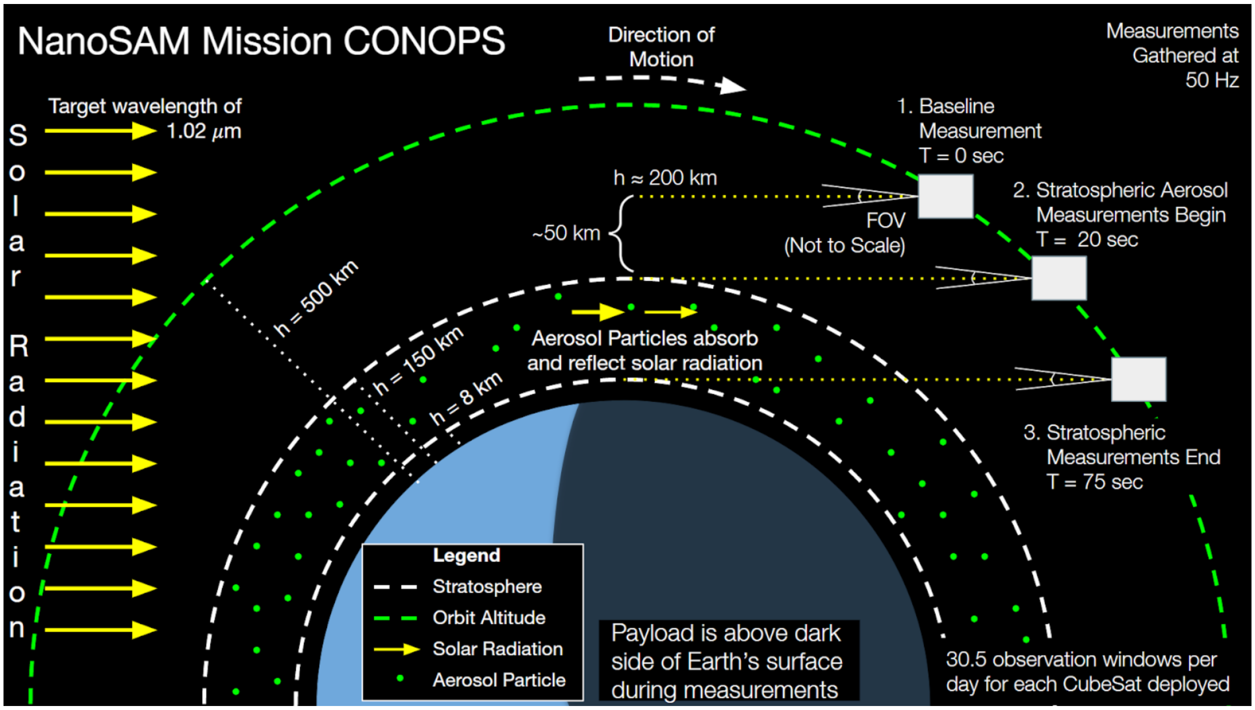

Fig. 3 NanoSAM Mission CONOPS

By choosing a circular orbit at an altitude of 500km, the payload will pass through an average of 30.5 measurement windows every 24 hours. A measurement window is the region in the orbit where the instrument is seeing sunlight that has passed through the stratosphere (and therefore interacted with stratospheric aerosols). Each of these windows were calculated to last approximately 75 seconds from the point of calibration to when the payload passes into the Earth's shadow when the orbital plane is parallel to the line connecting the Earth and the Sun. However, as the mission continues this orbit will precess around the Earth, leading to this data window being elongated, with a maximum value of 200 seconds for the length of the data window. Therefore, the team that launches a NanoSAM CubeSat will have to configure the timing software to account for this procession and dynamically adjust the length of data capture as a function of time along the orbit. The spacecraft is over parts of the Earth's surface that are not illuminated by the Sun during the time that the payload is gathering data. This means that this instrument would be a strong candidate for integration with another mission that is carrying out remote sensing on illuminated parts of the Earth's surface. This would free up additional power for NanoSAM during the parts of the orbit where it would be active. It would also increase the robustness of the mission proposal for the remote sensing payload, as it would eliminate the window of spacecraft inactivity on the dark side of the planet.

C. Functional Block Diagram

The top of the Functional Block Diagram (FBD) in Fig. 4 shows where light enters the system. After being filtered by both a longwave-pass and bandpass filter, the light is focused on a precision pinhole before being measured by a photodiode. This photodiode serves as the data interface between the optics and electronics subsystems, turning the photons into an analog signal. This signal is then conditioned and digitized. The microcontroller serves as the interface between electronics and software, receiving this digitized light signal before storing and ultimately downlinking it to the bus. The software subsystem takes care of many other functions as well, such as system state monitoring, timing, command handling, and error detection and correction. To facilitate these other functions, signals are also collected from temperature sensors on the electronics boards as well as on the optics bench. These temperature measurements are used to determine the heating feedback input, which drives whether or not the optics heater is turned on or off.

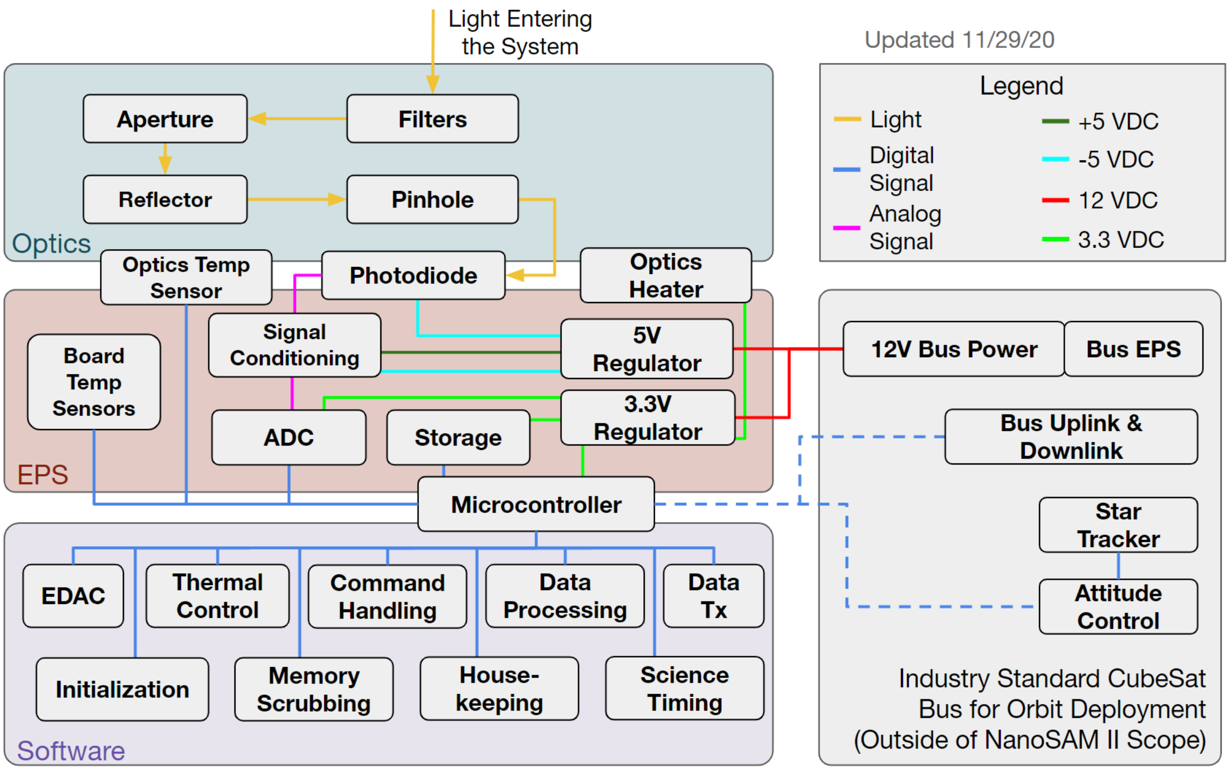

Fig. 4 Functional Block Diagram

Since designing a bus is outside of this year's scope, the team will be using a 12V power supply and a laptop to emulate the bus for testing. Additionally, the software will be operating under the assumption that there is an attitude determination and control subsystem included with the bus that is capable of pointing the payload at the sun during the sunset and sunrise portions of each orbit. However, designing this functionality is a hefty undertaking, so it will have to be a strong focus if a future NanoSAM project decides to take on bus design.

D. Functional Requirements

The following high level functional requirements are derived from the specific objectives laid out above. The goal of these functional requirements is to leave no specific objective uncovered.

Number	Name	Requirement Description
1.0	Data Capture	The supporting electronics and software shall digitize, packetize, and store housekeeping data and information collected from the photodiode.
2.0	Communications	The supporting electronics and software shall communicate digitzed data to a ground computer during testing, and to a standard bus system for downlink during on-orbit operations.
3.0	SAM-II Equivalent Optics	NanoSAM II shall have optical performance capabilities that are equivalent to or surpass that of SAM-II.
4.0	Payload Dimensions	The payload shall have dimensions to allow for integration with an industry standard CubeSat bus in future years
5.0	Flight Testing	All payload components shall maintain their design requirements through space environment testing
6.0	Cost	The project shall limit all spending to a budget of $5,000.

Table 2 High Level Functional Requirements

There is a clear rationale for each functional requirement in Tab. 2. For Req. 1.0, the direct relationship between capturing optical data and measuring stratospheric aerosol concentration dictates that accurate data capture must be a focus of this year's efforts. The rationale behind Req. 2.0 is that communicating the data captured by the payload to scientists is crucial so that these scientists can make useful conclusions from this data. Req. 3.0 was given to the team directly from the customer, because deriving the optical parameters required for the data to be scientifically valid is a challenge well outside of the scope of the project. Choosing to match the optical performance of the SAM-II system means that the team knows the data it is gathering is scientifically relevant. For Req. 4.0, it was essential that the team keep the payload volume and mass small enough such that the payload can viably be integrated with a CubeSat bus in future years. Req. 5.0 came about because the team would like to hand off a payload to future teams that has passed environmental testing and demonstrated rigor against the harsh conditions of space. Finally, Req. 6.0 is derived simply from the maximum allowable spending allocated to the team. If this is exceeded, there will not be the money to provide all of the resources required to complete the project.

III. Final Design

Authors: Axel Haugland, Jashan Chopra, Jackson Kistler, David Perkins, Daniel Wagner, Daniel Barth, Emma Tomlinson, Donavon Schroeder, Ryan Smithers, Abby Hause

This section presents the overall project requirements and the final design that was produced to satisfy them. This information is provided for the four subsystems being developed for NanoSAM II: structures, electronics, software, and optics.

A. Requirements Development

The requirements flow-down from functional requirements are depicted in Tab. 3 through 8. The first high level functional requirement, data capture, covers a wide range of necessities for the system's collected data. The Level 1 flow down of this splits up all the data the system captures into different categories. Optics data is the first flow-down requirement. It delegates how the scientific irradiance data of the system will be gathered and stored through the optics system. The second flow down, calibration, specifies a dataset that is necessary for the science data to be interpreted. Error checking is also needed as a flow down to be confident that the data captured is correct. Outside of the science data, housekeeping data is tracked to ensure the system is running as intended and to mitigate any temperature or storage problems. Power consumption data is also tracked as CubeSats provide a limited amount of power to the system.

L0	L1	L2	L3	Name	Requirement Description
1.0				Data Capture	The supporting electronics and software shall digitize, packetize, and store housekeeping data and information collected from the photodiode.
	1.1			Optics Data	Optical and electronic subsystems shall communicate data through their photodiode connection to collect mission data.
		1.1.1		Sampling Rate	The system shall gather samples at a rate of at least 50 Hz for the duration of the mission.[3]
			1.1.1.1	Processing	The system shall process and store data at a rate higher than the data collection rate of 50 Hz.
		1.1.2		Data Collection Bit Size	Data shall be collected to 10 bit resolution.[3]
		1.1.3		Storage Size	The system shall include enough storage space for one orbital period.
		1.1.4		Data Collection Timing	Data shall be stored for the entire stratospheric measurement window during both sunrise and sunset.
	1.2			Calibration	System shall store solar irradiance data for calibration prior to the sunset stratospheric data window and following the sunrise stratospheric data window.
	1.3			Error Checking	Software shall correct single bit errors and trigger a rollback if data that cannot be corrected.
	1.4			Housekeeping	Software shall collect and monitor system state data.
		1.4.1		Temperature data	Temperature data shall be tracked for the EPS board and optical sensor.
		1.4.2		Power data	Power usage data shall be tracked for the EPS board.
		1.4.3		Storage capacity	Storage capacity shall be tracked.
	1.5			Power Consumption	The system power draw shall not exceed 7.3W. [66]

Table 3 Functional Requirements Flow Down: Requirement 1

The Level 2 requirements under 1.1 (Optics data) give information about the necessary attributes for the optics data.

Sampling rate and bit size will collect a certain amount of data, which must be stored. This means a requirement is necessary for available storage space. Since the system is constantly collecting data, the data stored needs to be limited to only the necessary data to ensure storage does not run out. This is covered in the timing requirement. The required processing rate is a function of the sample rate, so this requirement is a Level 3 requirement under sample rate. The Level 2 requirements of 1.4 (Housekeeping) declare what specific housekeeping data is needed. Temperature data is needed to control our heating system, storage is needed to determine data clearing, and power data is needed to ensure the system can run on the supplied power.

The second high level functional requirement ensures that the system can communicate the necessary data to a ground system. The flow-down requirements are all different qualities needed to properly communicate data. A low signal to noise ratio is necessary for the signal to be accurately interpreted. Data transfer over a set amount of time is important as the system needs to transfer all the necessary data during a downlink, or the data will be incomplete. Fault mitigation should be communicated so an error in housekeeping can be taken into account when analyzing the received data. These all ensure proper communication with the ground system.

L0	L1	L2	Name	Requirement Description
2.0			Communications	The supporting electronics and software shall communicate digitized data to a ground computer during testing, and to a standard bus system for downlink during on-orbit operations.
	2.1		SNR	The optical instrument shall have a signal-to-noise ratio of 3500 or greater.[8]
	2.2		Fault Mitigation	Warning messages shall be down-linked if software system detects anomalies in housekeeping data.
	2.3		Downlink Data Transfer	Data needs to complete data transfer during downlink period with a maximum transfer rate of 9.6 kbps over a minimum window of 5 minutes.[67] [68]

Table 4 Functional Requirements Flow Down: Requirement 2

The third high level functional requirement details the optics qualities needed to match SAM-II functionality and obtain accurate data. The aerosol specific wavelength and vertical resolution are directly inherited from SAM-II. The tracking accuracy is necessary for consistent baseline irradiance values throughout a data set. If the baseline values are inconsistent throughout collection, the data will give an inaccurate aerosol reading. The Level 2 flow down requirements, field of view and modular transfer function, are two other optical necessities that are derived from the vertical resolution.

L0	L1	L2	Name	Requirement Description
3.0			SAM-II Equivalent Optics	NanoSAM II will have optical performance capabilities that are equivalent to or surpass that of SAM-II
	3.1		Wavelength	The optics system shall capture light at a center wavelength of 1.03 µm.
	3.2		Vertical Resolution	The optical design shall have a vertical resolution of 1 km [69].
		3.2.1	FOV	The FOV shall be 1.3 arcminutes to achieve a resolution of 1km.
		3.2.2	MTF	The imager shall have a 0.74 MTF in order to meet the resolution and contrast of the SAM-II system.[8]
	3.3		Tracking Accuracy	The system shall demonstrate solar tracking accuracy of 1 arc-min/mRad or finer during ground testing.[70]

Table 5 Functional Requirements Flow Down: Requirement 3

The fourth high level functional requirement determines what the system must consider when integrating into a CubeSat. The flow-down requirements split this into three considerations. Both mass and volume are important as smaller sizes will be easier to incorporate. The output of the system also needs to interface with the CubeSat.

L0	L1	L2	Name	Requirement Description
4.0			Payload Dimensions	The payload shall have dimensions to allow for integration with an industry standard CubeSat bus in future years
	4.1		Payload Size	The payload shall fit into a 0.5U volume.
	4.2		Payload Mass	The payload shall have a total mass less than or equal to 0.615 kg. [5]
	4.3		Payload Interface	The payload enclosure shall have a defined interface for integrating with a CubeSat bus.

Table 6 Functional Requirements Flow Down: Requirement 4

The fifth functional requirement determines system survivability in both a launch and space environment. The Level 1 requirements are the main environmental parameters accounted for in design, proximity to a vacuum, temperature variations, and vibrations. The Level 2 vibration requirements specify two different considerations for vibration design to ensure a secure system. The Level 2 thermal requirements detail the necessary temperature for electronics survival and the need for temperature control, which are both influenced by the exterior temperature.

L0	L1	L2	Name	Requirement Description
5.0			Flight Testing	All payload components shall maintain optimal performance through space environment testing.
	5.1		Vibration	The system shall maintain optics performance following exposure to vibration.
		5.1.1	Mirror Alignment	Launch vibration stresses shall not deform the optical alignment such that optical performance measures drop below SAM-II the baseline.
		5.1.2	Natural Frequency	The lowest vibrational natural frequency of the system must be greater than 90 Hz. [10]
	5.2		Thermal	The payload shall remain at optimal performance over an environmental temperature range of -120 to 120 degrees Celsius. [71]
		5.2.1	Thermal Control	Software shall be able to detect when the system exits outside of the lower bound of the acceptable temperature range and activate thermal heating control.
		5.2.2	Payload Temperature	The payload contents shall operate across a temperature range of -20°C to 60°C. [10]
	5.3		Vacuum	Electronic and optical components shall maintain their optimal performance in vacuum conditions

Table 7 Functional Requirements Flow Down: Requirement 5

The high level functional requirement for cost has no flow-down requirements and is given by the class parameters.

L0	L1	L2	Name	Requirement Description
6.0			Cost	The project shall limit all spending to budget of $5,000

Table 8 Functional Requirements Flow Down: Requirement 6

The subsequent sections will bridge the gap between specific subsystem requirements and the impacts that these decisions made on the final design outlined above.

B. Structures Final Design

The driving functional requirements for the structures subsystem can be seen in Tab. 6 and Tab. 7. The functional requirements from 4.0 bound the design space by putting limits on the structure's size, mass, and interface methods. NanoSAM II includes external walls to protect the payload and mount the optics lens, and the structure supports the electronics and optics internally, which drives the shape of the main internal ribs (highlighted in blue), seen in Fig. 5 below.

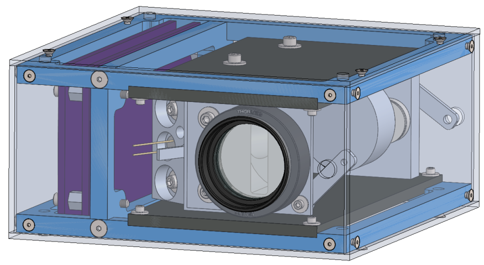

Fig. 5 Structures Overall Design - Rib Highlights

With the inclusion of the walls, the dimensions of the structure are $9.97cm \times 9.92cm \times 4.92cm$. The longest dimension, $9.97cm$, is due to the lens mount on the wall. These dimensions meet functional requirement 4.1. Additionally, the mass of the constructed payload was approximately 0.51kg, which meets functional requirement 4.2. Three ribs interlock to seat the optics system between two thermal isolation boards (structural fiberglass) to reduce temperature changes on the photodiode (see Fig. 74 and the corresponding section for motivation). The structure meets functional requirement 4.3 by having four internal holes through the payload meeting PC104 specifications [18]. These specifications allow for future integration with commercially available CubeSat structures, such as the ISIS 3U [22].

Functional requirements from 5.0 necessitate models to predict the effects of vibration and thermal changes. Before testing, the models constructed for the structure suggested that the structure will meet these requirements. The design requirements derived from requirements 5.1 and 5.2 influenced the decisions to separate the optical system with the thermal boards, as these boards would allow the payload to manipulate the temperature of the optics mostly independently of the external environment. Additionally, these fiberglass boards were predicted to reduce some of the vibrations experienced by the optics.

C. Electronics Final Design

Although the core components of the electronics design remain relatively unchanged from NanoSAM I, the design as a whole went through a large change in the transition to a split board design. This section will cover the analog and digital board designs individually as well as the routing to ensure board to board compatibility.

Analog Board

The analog board consists of a signal conditioning block, a bipolar voltage regulator, a board connector for routing between the analog and digital boards, and a thermistor circuit for temperature monitoring. We connected a M22-2030305 90 degree header connector to the through holes for the photodiode, which was also used as the connector for the resistor heater and optics temperature sensor. These connections were made with shielded cable because of signal integrity concerns between the photodiode attached to the optical bench and the analog board. The anode of the photodiode is connected to the -5V terminal of the analog voltage regulator in a reverse biased photoconductive setup. This photoconductive setup is utilized to widen the depletion region and reduce the seen capacitance of the photodiode. This results in a faster response and improves the response linearity, resulting in a better matching of the fundamental equations used to resolve incident power from the ADC's voltage measurement. The photoconductive mode does result in increased thermal Johnson noise as well as increased dark current noise, however these two contributions to noise were assumed to be below the noise floor. [23]. The cathode of the photodiode is connected to an AD8671 operational amplifier, designed for low noise and low input bias current precision measurements [40]. The AD8671 is powered by the plus and minus terminals of the 5V analog voltage regulator. The input and output of the AD8671 are connected in parallel with a feedback resistor and feedback capacitor which dictate the outputs of this transimpedance amplifier setup according to the equations presented below. To avoid oversaturation of the analog to digital converter, the feedback resistor is sized such that it corresponds to 95% of the maximum desired output voltage, which is 3.3V when provided with the maximum expected output current from the photodiode. This maximum expected current is derived from the maximum expected incident power, and the maximum responsivity which occurs at 30°C. These calculations are an input from the optics subsystem, and the relevant equations are given below in Eqs. 1-3. We thus use a resistor of 1174 ohms and a capacitor of 1 microfarad.

$$I_p = P_i \mathcal{R} \tag{1}$$

$$R_f = \frac{0.95 * V_{cc}}{I_s} \tag{2}$$

$$C_f = \frac{1}{2\pi R_f f} \tag{3}$$

The feedback capacitor value is chosen such that the cutoff frequency of the transimpedance amplifier is set between 100-200 Hz. The ADC samples at 208 samples per second, which makes the Nyquist frequency 104 Hz. We can be sure that as long as we cut off any signals with frequencies larger than 104 Hz we will avoid signal aliasing in our digitized data. The minimum cutoff frequency is 50 Hz due to design requirement 1.1.1.1. The actual expected frequency of the data depends on the satellite scan rate, which is low enough that the current is essentially a DC signal [6]. The scientific reason for a scanning procedure rather than a consistent angle towards the sun is to get a better average of the light attenuation and to avoid anything that could corrupt the data.

The output of the amplifier is a voltage linearly proportional to the photodiode's output current. This voltage is read by the LT2470 analog to digital converter. This ADC is a 16-bit sigma-delta converter with a 203Hz sampling rate and a 10ppm / °C precision reference. There is a 3.3V zener diode before the input to the ADC to prevent an overvoltaging of its input pin [41]. There is also a secondary trace that goes directly to the microcontroller's 12 bit on-board ADC in the event that the primary ADC ceases function. The ADC is supplied with 3.3V that comes from a LT6654-3.3V voltage reference. This voltage reference ensures a stable and extremely low noise voltage input over a range of temperatures and other noise factors [42]. The analog ground plane provides the zero volt reference for the ADC. The ADC communicates with the microcontroller via a serial programmable interface (SPI) connection. The +5V and -5V voltages mentioned come from a LTC3260 Low Noise Dual Supply Inverting Charge Pump, which is configured for a 12V bus supply [43].

The last major component of the analog board is the board connector, the FTSH-116-01-L-D from SamTec. They are reliable, cheap, and low profile, with a total of 32 sockets for connections. SamTec recommends that subsequent pins be grounded to reduce any possible noise in the system [44]. Thus, there are essentially 16 pins available for cross-board connections. We found that the height offered by the FTSH connector was required for the Teensy 4.0 to fit between the two boards. We show the final schematic of the analog board in Fig. 6-7 below. Larger versions of all schematics and board layouts can be accessed with the hyperlinks in the figure captions.

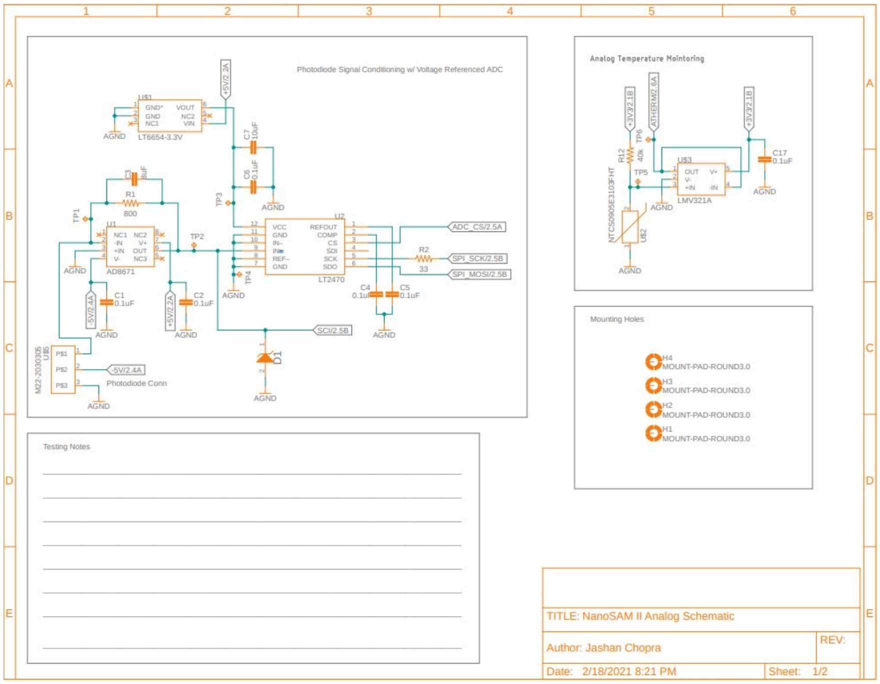

Fig. 6 Analog Board Schematic [1/2] - Link to View Full-Resolution Copy

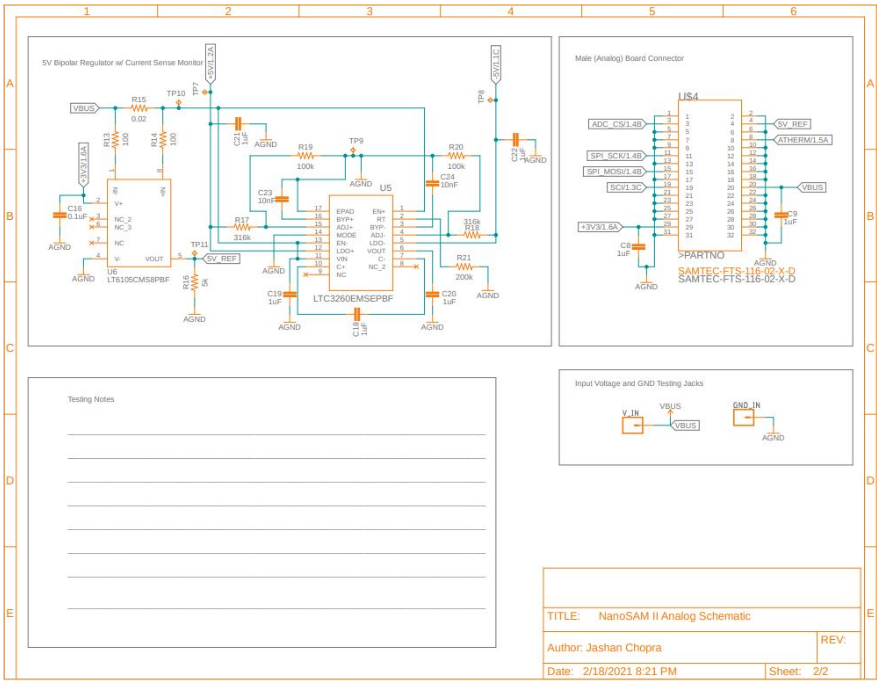

Fig. 7 Analog Board Schematic [2/2] - Link to View Full-Resolution Copy

Digital Board

The heart of the digital board is the Teensy 4.0 microcontroller. This microcontroller was largely chosen because of heritage from NanoSAM I. It has a number of analog I/O pins that connect to a 12-bit on board ADC and digital I/O pins with SPI communication, and it runs Arduino software [45]. In a worse case scenario, a single event upset can cause a latch up in the microcontroller which may prevent the primary code loop from running. Although there exist backups in software to protect against these latch ups, it's important to have a hardware solution as well [46]. Thus the digital board contains a MIC1832 watch dog monitor. The design of this watchdog monitor involves biasing the TD pin with the 3.3V input to make the total watching timer 1.2 seconds. The microcontroller will send a 50-100 nanosecond pulse at least every 0.1 seconds to the /ST pin on the watchdog, which resets the watchdog timer. If a latch up causes the primary software loop to fail, and this reset signal is not sent, then the RST pin on the MIC1832 will assert high for 250 milliseconds. This pin pulling high will activate a P-Channel MOSFET in series with the microcontrollers supply voltage, thus shorting it. Shorting the voltage input acts to reset the Teensy 4.0, upon which it will resend the watchdog signal. The RST pin is normally pulled low with a typical 10 kohm resistor. We additionally use a hardware switch on the voltage input to the MIC1832 that allows for a manual shutdown of this watchdog. If the boards are powered before the Teensy can start to send the watchdog reset signal, then the watchdog will short the Teensy, and we are stuck without Teensy power unless externally powered by the USB connection. Moving the hardware switch to the off position shuts down the MIC1832 and thus makes sure voltage will always go through the P-Channel MOSFET to power the Teensy.

The digital board also contains two MT25QL128ABA flash modules for data storage before downlink occurs. These flash modules provide 128 Megabytes of data storage, with the second flash module being used for backup storage. The ADC collects data at 203 samples per second at 16 bits. With a higher end estimate of the science collection period as 240 seconds, giving us 2.93 Megabytes per orbit. We calculate an upper limit of 88 Megabytes assuming 30 collection periods before downlink, in a worse case scenario. Housekeeping data only needs to be sampled at 10 samples per second, with the microcontrollers 12 bit ADC. Assuming we constantly collect housekeeping data for the entire orbital period, this puts as at about 3.6 Megabytes per full orbit. This puts our estimated upper limit at around 6.53 Megabytes, using roughly 2.5% of our total possible data storage. We can thus collect multiple days of data without downlink if conditions require. The flash modules communicate with the microcontroller via an SPI connection, and contain a pullup resistor and decoupling capacitor on the voltage input, per datasheet specifications [47]. The digital board uses a LT8610A high efficiency voltage regulator to down convert the bus voltage to 3.3V to power the digital components. The inductor is sized at 8.76 microhenry, with a current rating larger than the 100 mA maximum expected output, as utilized by the microcontroller. We use two 1210 footprint X5R rated decoupling capacitors in parallel on the voltage output to reduce the output ripple voltage. The FB pin capacitor is sized by the typical voltage divider equation as given by the datasheet [48]. The expected output voltage results in a maximum switching frequency of 20 megahertz, although we size the primary feedback resistor as 110 kohm to set the switching frequency at a lower 0.4 megahertz. The datasheet suggests a 90% efficiency for a 3.3V 100mA output, which supports our later claim that overheating on the board will not be an issue.

Thermal models dictate that a heating element on the photodiode block is required. The heating resistor is activated by an N-channel MOSFET that can be activated with a high assertion from the microcontroller, normally pulled down by a standard 10 kohm resistor. To prevent larger current output from our voltage regulators, the resistor heater is directly supplied with the bus voltage, assumed to be 12V. There is a transient voltage suppression diode on the input to prevent any voltage spikes above 12V, since we cannot guarantee any regulation of the bus voltage input. We size the resistor using the typical power expression, accounting for the voltage lost by the N-channel enhancement MOSFET and the voltage dropped across the TVS diode, as shown in Eq. 4 below.

$$R_H = \frac{(V_{cc} - V_{DS} - V_{TVS})^2}{P_{req}} \tag{4}$$

The last two elements of the digital board are an LMT86LP optical temperature sensor and the male side of the primary board connector. Similar to the board thermistor setup, the output is buffered with a LMV321A operational amplifier. This sensor outputs an analog voltage which will be read by the 12 bit ADC onboard the microcontroller giving a 0.043°C resolution. The sensor itself boards a maximum 0.4°C accuracy, although measurements will take a difference so we are not concerned with absolute accuracy.

It will be supplied with the digital 3.3V power source, and can operate from -50°C to 150°C, operating with only 5.4 microamps of current. The -10.9 mV/°C slope allows us to backconvert to temperature if necessary; although corrections to the science data will be in terms of voltage difference between LMT86LP measurements at the data collection period and the calibration period. Additionally, we place a passive resistor-capacitor (RC) filter on the output of the LMT86LP for noise concerns. Wall outlets in the aerospace lab testing environment can result in 60Hz noise sources present, so we set the cutoff frequency of the low pass filter to 50Hz. Because temperature changes so slowly, this low frequency is fine. Using the standard RC low pass filter equation, given below in Eqs. 5-6, we choose a feedback resistance of 9.76 kohms, and a capacitor value of 47 nanofarads. We want the voltage attenuation to be as low as possible, and we are using a standard capacitor value, which we then size to a common resistor that is easily purchased. This results in a voltage attenuation of 0.99. In reality, because we are comparing the voltage output of the LMT86LP to a calibration measurement, this voltage attenuation doesn't matter, because it will be constant between the two measurements. The digital board houses the SAM1153-16-ND male board connector, which functions exactly the same as the description in the analog board section. A schematic of the digital board is given below in Figs. 8-9.

$$X_c = \frac{1}{2\pi f C_f} \tag{5}$$

$$\frac{V_{out}}{V_{in}} = \frac{X_c}{\sqrt{R_c^2 + X_c^2}} \tag{6}$$

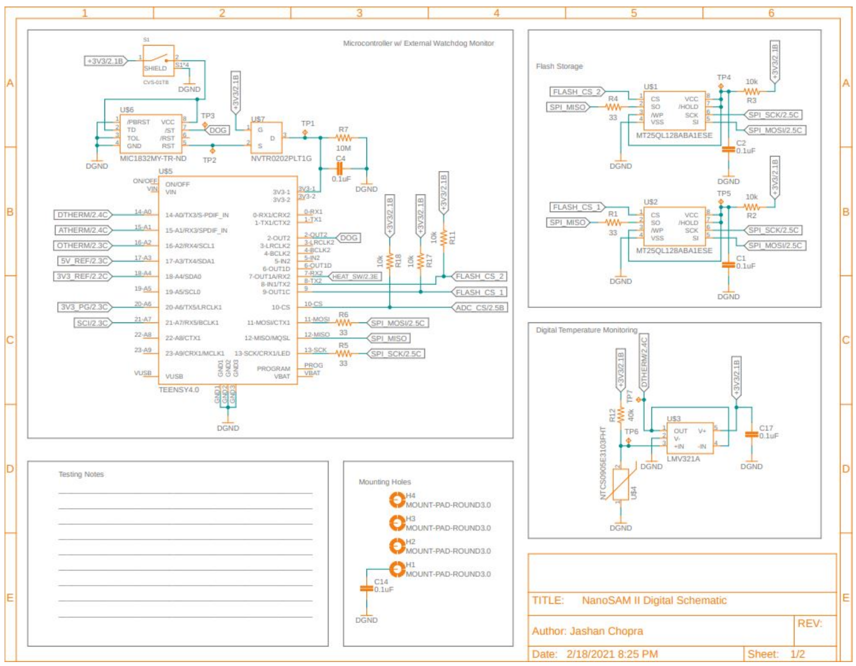

Fig. 8 Digital Board Schematic [1/2] - Link to View Full-Resolution Copy

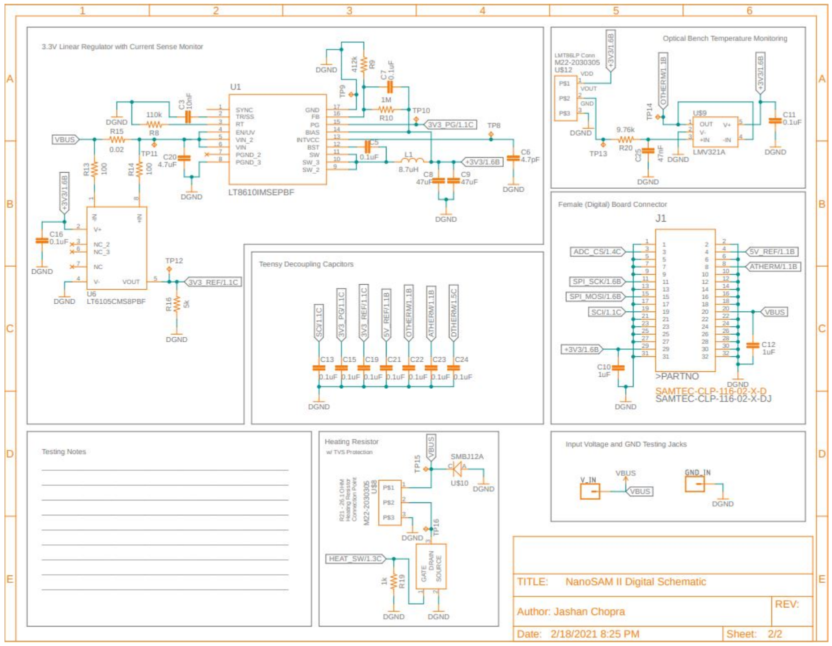

Fig. 9 Digital Board Schematic [2/2] - Link to View Full-Resolution Copy

Both of the boards utilize a LT6105 precision, extended input range current sense amplifier on the voltage input line for their respective voltage regulators. The current sense monitor outputs a voltage that is linearly proportional to the current on the primary sense resistor, which is then fed to the microcontroller and converted back to voltage by software. Both of the boards have an identical Vishay NTCS0805E3 thermistor setup for monitoring temperature. The output voltage from the voltage divider is then buffered with a LMV321A operational amplifier. The driving equations for converting the voltage to temperature are given below in Eqs. 7-8. The thermistor used has a B value of 3940, and a standard resistance of 10 kohms. The output voltage at $-30°C$ will be 2.747V, and the output at $30°C$ will be 0.55V, fitting within our microcontrollers ADC range. These temperature ranges were chosen for calculation due to the standard thermal range expected for the payload. The size of the series resistor in feedback is determined as the square root of the multiple of the minimum and maximum resistances corresponding to the temperature bounds, giving roughly 40 kohms [51].

$$R_T = R_{25} \exp B\left(\frac{1}{T} - \frac{1}{298.15}\right) \tag{7}$$

$$V_{out} = V_{cc}\left(\frac{R_T}{R_T + R_s}\right) \tag{8}$$

Each board has four mounting holes that provide locations to mount the boards to the structure, and to provide additional structural support for the board connector. The bottom left mounting hole on the digital board also connects to the CubeSat chassis for a chassis-ground connection. Due to the necessity of ground connections on the subsequent pins of the board connector, the analog and digital ground planes are only connected through this board connector. The purpose for the single ground connections is to create as close to a star ground as possible, which serves to avoid noise by avoiding the creation of ground loops [52]. The team decided to opt for a two layer board as additional layers were not necessary and increase routing complexity. The bottom layer of each board is filled with a ground plane for signal integrity and ease of routing. Test points were placed close to the outside of the board when possible for ease in testing. A small cutout on the right side of the board is used for the physical wires leaving the photodiode, optics heater, and optics temperature sensor through holes. The locations for ground and voltage input to the system for testing are located by the bottom left ground hole near the board connector. Each board thermistor is placed near the center of the board to get as close to an accurate reading of the entire board. Proper design rules were implemented to the board traces, using the standard 6 mil traces, and 10 mil traces for voltage lines. The CAM jobs from OSHPark, a board manufacturing company, for the boards are shown below, in Figs. 10-11.

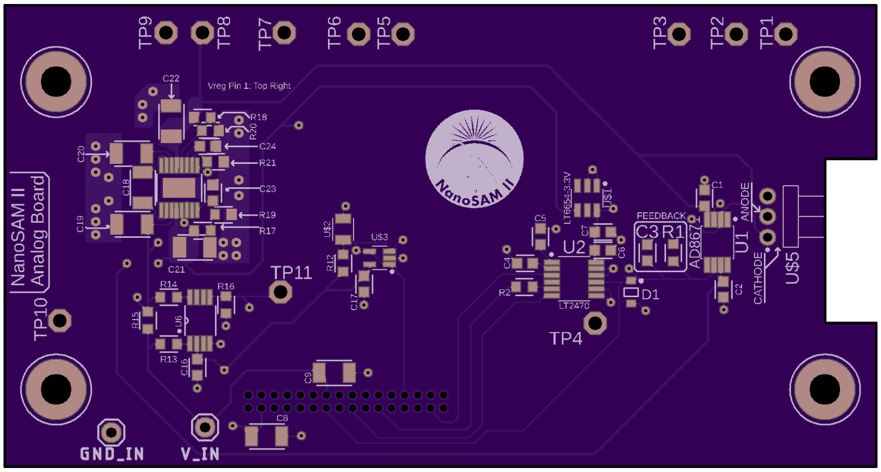

Fig. 10 Analog Board Top Layout Gerber

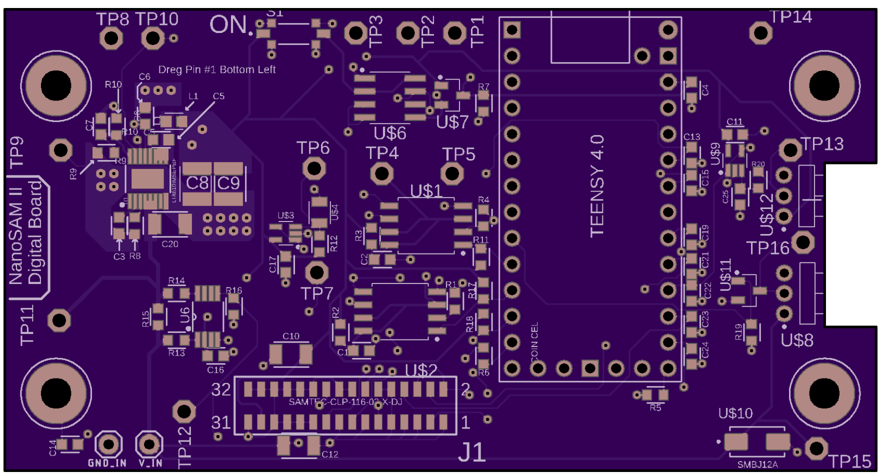

Fig. 11 Digital Board Top Layout Gerber

The signal to noise ratio drives one of the central requirements that the electronics board should meet. The 3500 SNR requirement derives from the assumption that the Sage II mission had its only source of noise as the quantization error of its 10 bit ADC. Quantization error is given below, but this calculation proceeds as $12 * 2^{10} = 3547.24$. The manufacturer datasheet estimates the dark current as $2pA$ at a $10mV$ bias voltage, at room temperature. The dark current is directly proportional to the bias voltage, and to the temperature of the photodiode, which gives our team a dark current of $1nA$ [53]. The Johnson noise and shot noise are intrinsic properties of the photodiode, and were calculated with the equations provided below. Each of these noise components is multiplied by the feedback resistor in our op-amp circuit to convert the current into a voltage via Ohm's law. We assume the temperature will be 30°C at a maximum. The shunt resistance is given from the photodiode datasheet, and q is the elementary charge [28].

$$V_{shot} = R_f * \sqrt{2q(I_s + I_d)f} \tag{9}$$

$$V_{johnson} = R_f * \sqrt{\frac{4k_B T f}{R_{shunt}}} \tag{10}$$

$$V_{dark} = R_f * I_{dark} \tag{11}$$

For circuitry noise, we considered the inherent noise of the low pass filter op-amp, the effect of a noisy voltage regulator signal on the amplifier, and the quantization noise of the ADC. The quantization error is an inherent property of ADCs [54]. The error from the low pass filter and the error from the regulator are specified in the datasheets for our specific components. Our ADC is a 16 bit ADC, being run at 3.3V, which makes the LSB equivalent to $3.3V/2^{16}$.

$$V_{low pass} = \frac{28nV}{\sqrt{f}} \tag{12}$$

$$V_{regulator} = 0.1mV \tag{13}$$

$$V_{quantization} = \frac{LSB}{\sqrt{12}} \tag{14}$$

The overall signal to noise ratio is the voltage of our expected signal divided by the quadrature sum of the noise sources discussed. This means that the signal to noise ratio depends on the incoming signal. If we assume that the average signal will be around 80% of our expected maximum voltage output, then we get a signal to noise ratio of 17000. The noise sources discussed here are quite small which leads to a theoretically high signal to noise ratio. The reality is that a SNR of 3500 means the error can be no greater than 0.008V, which is too small to guarantee, as inherent system noise, signal losses, and manufacturing losses are not factored into our signal to noise ratio. Future teams should seek to derive a SNR requirement based on the actual minimum resolution required to resolve particles in the stratosphere, instead of the current basis for SNR of an ideal heritage system.

$$SNR = \frac{0.8 * I_s R_f}{\sqrt{V_{quantization}^2 + 2V_{regulator}^2 + V_{low pass}^2 + V_{dark}^2 + V_{johnson}^2 + V_{shot}^2}} \tag{15}$$

Functional requirement 1.5 states that the EPS system shall draw no more than 7.3W of power. To meet this, a worse case analysis of power draw was performed. Without the optics bench heater, we consume only around 1.66W of power. A worse case scenario of heater usage will result in a total power usage of 7.17W, putting us below our requirement. Tthe average power usage during testing was much lower because the digital components are not constantly using their full power draw. The voltage regulators are also efficient, and do not drop all the lost power directly to heat.

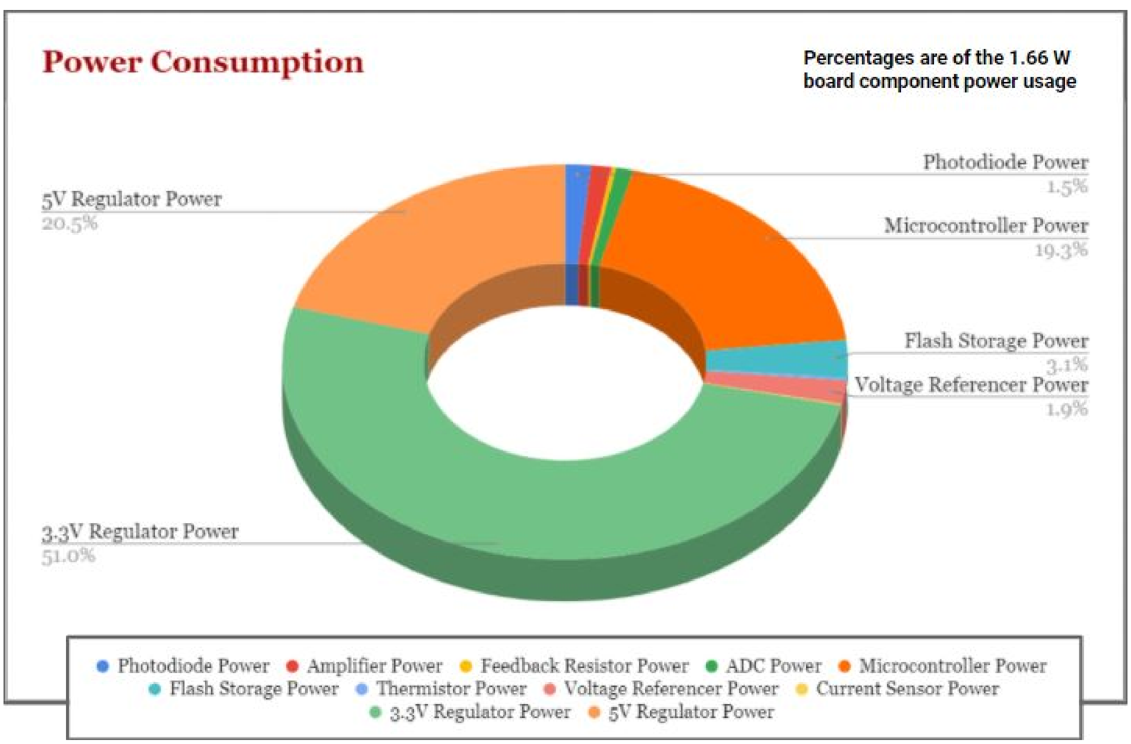

Fig. 12 Theoretical Power Draw by Component

This concludes the electronics detailed design. More details can be found in the Electronics Master Summary in the */Electronics/* folder of the NSII Project Archive. The BOM spreadsheet provides an extensive bill of materials separated by each board, containing the price and Digikey part number for each component. The master electronics calculations spreadsheet is used for important equations that size components, as discussed throughout this section. Additional documents are specified in the folder read me file.

D. Optics Final Design

The driving critical project element of the optical system is to match SAM-II instrument legacy performance. Specifically, this includes the requirements surrounding data capture, center wavelength, vertical resolution and field of view, and MTF. Additionally, the optical system needs be small enough to fit within .5U size requirement that is part of the structural critical project element.

The overall design concept of the optical system is shown below in Fig. 105, and the individual components will be discussed in the following sections.

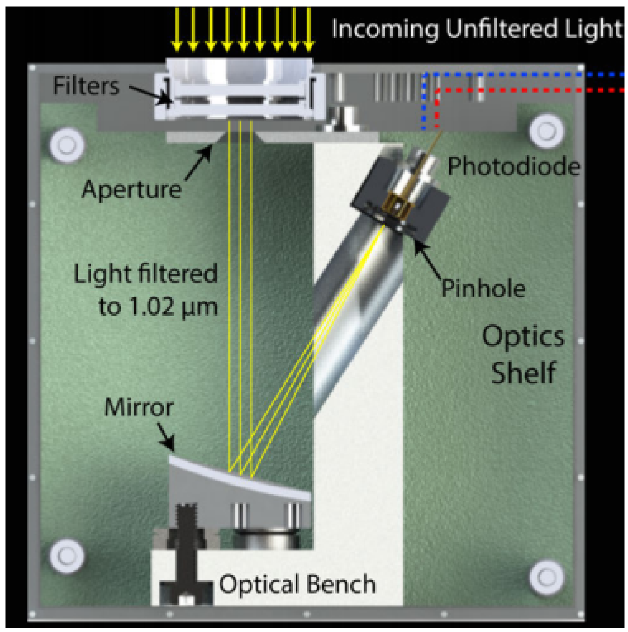

Fig. 13 Overview of Optical System [8]

1. Filters

The filter system selected by NanoSAM I consisted of a bandpass filter, the FLH1030 from ThorLabs, which has a center wavelength (CWL) of 1.03 μm and a longwavepass filter, the FELH1000, which has a cutoff wavelength of 1.00 μm. The longwavepass filter is used to ensure that there is no leakage from light with a wavelength smaller than 1.00 μm through the bandpass filter, as this would cause the system to report more attenuation due to sources which are not stratospheric aerosols. The longwavepass filter also will be used to protect the system as it will be mounted with the uncoated side out. This will help keep the passband from drastically shifting due to thermal expansion. The bandpass filter was selected by last years team as it was the COTS filter that had a CWL closest to that of 1.02 μm. The NanoSAM II filter design is similar to that of the NanoSAM I design, with the only change being that the new design utilizes a bandpass filter with a center wavelength of 1.02 μm.

One of the major parameters that affects system performance is how the CWL of the bandpass filter changes with temperature, as the layers of silica expand and contract. The calculation of the effect that temperature change has on CWL is rather involved, so it is included in the optics section of Appendix A.

These calculations led to the conclusion that the CWL will change by non-negligible amount due to thermal change, and therefore the bandpass filter should be included within the bounds of the thermal isolation of the optical bench.

However, due to the difficulty of manufacturing parts to do this, this task was deemed to be out of scope and left for a future team.

2. Aperture

The aperture dimensions selected by NanoSAM I are 20 mm by 5 mm. In order to meet the field of view/vertical resolution requirements the size of the vertical dimension must remain 20 mm. The horizontal width could be changed to optimize the MTF, but this would require the NanoSAM II system to be aligned so that the interferometer could be used. Because NanoSAM II never achieved full alignment (this will be discussed later), therefore aperture optimization is being left to a future team. NanoSAM I used a Zemax model to predict an aligned MTF of .8597 with the current 20x5mm aperture, so this aperture is deemed sufficient for now.

3. Off-Axis Parabolic Mirror

The Off-Axis Parabolic Mirror (OAP) was chosen by NanoSAM I. It is an aluminum 25.4mm diameter mirror, with a 54.45mm focal length, and a 30° offset angle. These dimensions were chosen for two reasons; to meet the MTF requirement and to meet the payload size requirement. There is a balance to be struck between these two requirements, a larger OAP will provide a higher MTF (which is desirable), but the OAP also needs to be small enough to fit within the size requirement. As is detailed in the structures section, the size of the OAP, its focal length, and its offset angle allow the optical system to fit within the .5U size requirement. Additionally, interferometer measurements taken by NanoSAM I calculated a MTF of approximately .85, which meets the MTF requirement. This same measurement was taken on the NanoSAM II system, and the results are detailed in the Verification and Validation section.

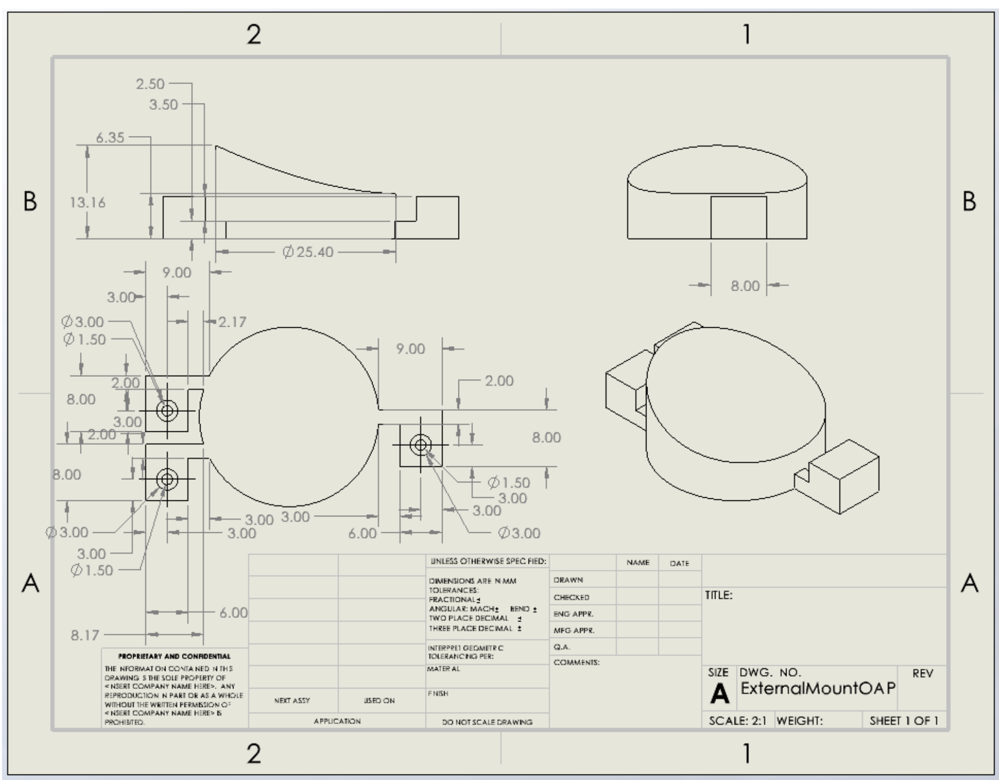

Fig. 14 CAD Drawing of External OAP Design

External Mount OAP Design

The use of a custom OAP is likely required to meet the SAM II equivalent optics requirement based on the results of the results of the optical alignment process discussed later in the Verification and Validation section. A design for an OAP was formulated with the main goal being to minimize surface deformation during mounting. One way to do this is to use an external mounting method. The mounting pads would be on the outside of the OAP instead of on the back of the surface as is the case with the current OAP. This design was created toward the end of the second semester, with guidance from Jim Baer, when it was found that the current OAP did not meet the MTF requirement as described in the subsystem testing section. A drawing of the preliminary design can be found in Fig. 14.

The surface is described by the parabola $y = .0106x^2$ (x and y in mm) revolved 2π radians to create a paraboloid. From that paraboloid, the smaller mirror is then cut such that the OAP has a diameter of 25.4 mm with the minimum height being at 6.35 mm and the maximum height being at 13.16 mm. This ensures that the mirror will have an off-axis angle of 30◦ and that the surface is identical to that of the current OAP. The mounts were then added to the outside with the L-shaped tabs coming out of the back of the OAP by 9 mm, so that the surface is not deformed very much. The tabs have spots for 1.5mm radius bolts to be used with a 3 mm radius countersink. The bolt holes are in the center of the tabs. This design is preliminary and should be reviewed and by a future team along with Jim Baer to improve on the design and ensure that the best design is used for the payload. Note that this design is just a preliminary design left for a future team to use and not the OAP that was used this year. Early in the design process, NanoSAM II briefly considered purchasing a custom OAP. Edmund Optics provided a rough estimate of $1200 for an arbitrary custom OAP.

4. Pinhole

All of the light reflected off the OAP converges at the focal point, which is where the pinhole is placed. As mentioned above, the OAP has a focal length of 54.45 mm, which means that the pinhole is placed 54.45 mm from the OAP. Fig. 105 shows the location of the pinhole relative to the OAP.

The pinhole field stop is 15µm in diameter. The size of the pinhole determines the field of view (FOV), and therefore the vertical resolution of the optical system. Both of these are SAM-II legacy requirements that fulfill the optics critical project element. An approximation of the FOV is calculated using the equation

$$FOV = \frac{d}{f} * 57.3 \tag{16}$$

In this equation, d is the diameter of the field stop, and f is the focal length of the OAP. Using Eq. 16 the FOV is calclulated to be

$$FOV = \frac{15 * 10^{-6} m}{.05445 m} * 57.3 = .0158^\circ = .948 arcminutes \tag{17}$$

The inherited SAM-II requirement for FOV is 1.3 arcminutes. However, NanoSAM customer and Optical Engineer Jim Baer has informed the optics team that Eq. 16 provides an approximation that is actually slightly smaller than the actual FOV. The next smallest commercially available pinhole is 20µm, which would result in an approximate FOV of 1.26 arcminutes. While this is much closer to the required FOV, Mr. Baer has informed the team that this will result in an actual FOV that is too large to meet the vertical resolution requirement. Therefore, due to customer preference NanoSAM II will use a 15 µm pinhole.

The vertical resolution is then calculated based off of the FOV, using the Eq. 18.

$$VR = 2.86 * 10^6 * tan(FOV) \tag{18}$$

where FOV is input in radians, and VR is calculated in meters.

Using Eq. 16, the Vertical Resolution is calculated to be

$$VR = 2.86 * 10^6 * tan(.948 * \frac{\pi}{60 * 180}) = 789m. \tag{19}$$

This is slightly better vertical resolution than the required 1km, so this fulfills the SAM-II legacy requirement. Additionally, the improved vertical resolution justifies the use of a pinhole that gives a FOV slightly smaller than 1.3 arcminutes.

To be sure that the purchased pinhole would be sufficient for the FOV and Vertical Resolution requirements, the tolerance of the pinhole was looked into. The purchased pinhole has a manufacturing tolerance of $\pm 5\mu m$. This means that the minimum pinhole diameter is $10\mu m$, and the maximum diameter is $20\mu m$. Using Equation 16, these values provide a minimum possible FOV of .6314 arcminutes, and a maximum possible FOV of 1.262 arcminutes. Both are underneath the 1.3 arcminute requirement. Using Equation 18, these produce corresponding vertical resolutions of 525.2912m and 1050.50m, respectively. The minimum vertical resolution handily meets the vertical resolution requirement of ≤ 1km, but the maximum value is slightly over. However, because this is a worst case scenario and the maximum vertical resolution is only slightly over the desired 1km, it is deemed to be an acceptable risk.

5. Photodiode

The photodiode was discussed in depth in the electronics subsection of the detailed design, thus this section will briefly go over the use of a photodiode from an optics standpoint. The photodiode is the component that allows the optics system to pass data to the electronics and software systems so that it can be stored and processed. This works towards fullfilling the SAM-II data capture requirements. Namely, that data from the optical system is captured. All of the components up to this point, (filters, aperture, OAP, and pinhole) ensure that the light that reaches the photodiode is at the correct wavelength (1020nm) and is sufficiently focused at this point so that the photodiode receives the desired data.

One other factor that would lead to issues in data capture is that of photodiode saturation. In order to ensure that this does not occur, a feedback resistor was sized using knowledge of an estimate of maximum incident power and responsivity values. These calculations are fairly lengthy, so they are included in the optics section of Appendix A.

The maximum current was found to be 0.0027 A. This value was then used to size the feedback resistor to prevent photodiode saturation as described in the electronics section.

6. Optical Bench

The purpose of the optical bench is to hold the OAP and photodiode block in the desired configuration. Because the adjustments needed for alignment will be done with shims and alignment tooling, the optical bench does not directly meet any SAM-II requirements. However, the size of the optical bench is largely determined by the .5U size restriction that is a structural critical project element. As is discussed in the structures subsection, the final dimensions of the payload are 9.96x9.62x4.92, meeting the .5U size restriction. The manufacturing and integration part of the project proved that the optical bench is a sufficient size to hold the optical components in the required position, while being small enough to fit within the overall size requirement.

E. Software Final Design

The NanoSAM II software system consists of five conceptual modules, further divided into several submodules. This modular design maximizes the potential for redesign and reuse of NanoSAM's software and streamlines the development process. Figure 15 shows a functional block diagram indicating each conceptual module and the flow of information to and from each module

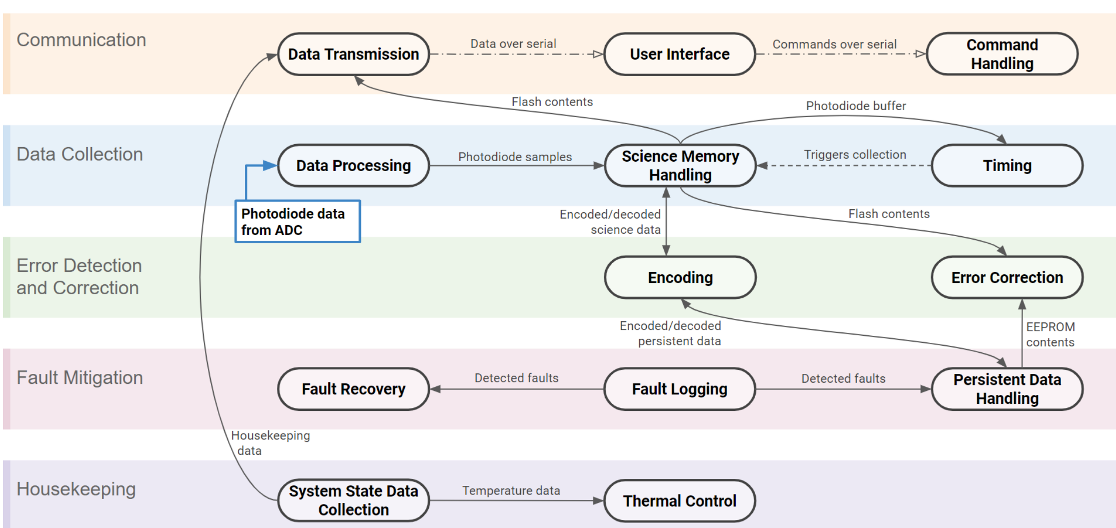

Fig. 15 Software conceptual block diagram

1. Software Architecture

The flight software's responsibility is compartmentalized within several files. Module functionality is further divided into several driver functions which are called sequentially in a continuous loop. An event system was implemented that allows communication between files without direct function calls and enables timed and recurring events to interrupt the main loop without pausing execution. Included in each file is a single global configuration file that defines all constant and global variables such as data rates, timing intervals, and temperature thresholds for heater control. The configuration file allows for quick and easy changes to these parameters in a single location. The header tree in figure 16 provides a high level illustration of the relationships between files. Note that the implementation file for each header is not shown.

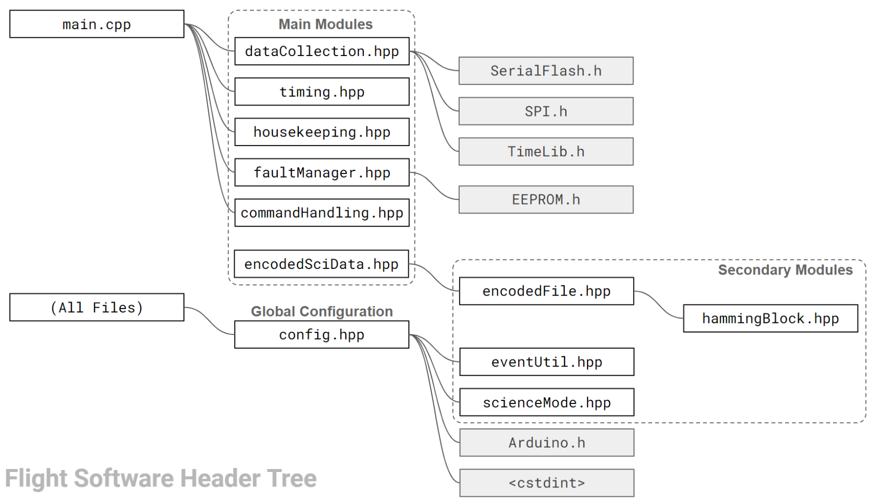

Fig. 16 Header tree

2. Data Processing and Handling

Each photodiode sample is converted to a digital signal using both the primary 16 bit ADC and the backup 12 bit ADC on board the Teensy microcontroller. The data processing module records irradiance samples at a rate of 50 Hz, storing each sample in a temporary data buffer. Before the contents of the buffer are saved to long term memory, a timestamp is appended indicating the end of the collection window. Since the sampling rate is a known constant, the time of each sample can be extrapolated from this single timestamp. The irradiance data buffer and timestamp are then encoded with a Hamming code EDAC scheme and written to a file on one of the external flash modules. Alternatively, a command allows unencoded irradiance samples to be streamed over the Teensy's serial connection in real time for testing. Since an ADCS system is out of the project scope for this year, pointing data is not included with each sample, instead, a place in the code is reserved for appending pointing data when the format is known. Key data parameters are shown in table 9.

Parameter	Value	Units
Photodiode Sampling Rate	50	Hz
Primary ADC Resolution	16	Bits
Backup ADC Resolution	12	Bits
Maximum Window Duration	240	Seconds
Maximum data per Window (encoded)	27009	Bytes
Minimum Time to Fill Flash	>38	Days

Table 9 Science data parameters

Each data file contains the contents of a single collection window. Commands allow every saved file on the flash to be "downlinked" via serial connection or scrubbed for errors. Memory scrubbing and dowlinking can be time intensive when many files exists on the flash memory, so when a scrub or downlink is initiated, file processing is staggered over several iterations of the main loop to avoid imposing on the 50 Hz irradiance sampling rate. A unique event system was designed and implemented to allow for these kind of staggered processes.

3. Timing

The timing of the data collection window is determined by the sunrise and sunset as viewed by NanoSAM's optical instrument. In the case of a sunset, the timing module will detects the moment the irradiance value drops below a threshold, which occurs when the sun passes below the horizon, marking the end of the collection window. Inversely, in the case of a sunrise, the timing module detects the moment the sun rises above the horizon, marking the beginning of the collection window. To ensure that all relevant irradiance data is captured in both cases, NanoSAM captures irradiance data continuously, which is stored in a short term data buffer. The size of the data buffer is sufficient to store all relevant data for a sunset and sunrise event, with an additional margin to record several seconds of full sunlight to be used for calibration. To prevent a single erroneous sample from triggering a state change, the moving average of the last several irradiance samples is compared to the threshold irradiance for detecting sunset and sunrise.

At any given time the software system is in one of five finite timing states: Standby, sunset mode, pre-sunrise mode, sunrise mode, or safe mode. The system state at any given time is determined by the timing module. The FSW executes different processes depending on the current timing state.

- **All states:** Incoming commands are executed. Faults are logged. Housekeeping data is recorded.
- **Safe Mode:** Photodiode data is not collected. Safe mode can only be exited via a command.
- **Standby:** Photodiode data is collected but not monitored. Memory scrubbing and science data downlinking are allowed. Standby mode can only be exited via a command.
- **Sunset:** Photodiode data is collected and monitored for a sunset event. When sunset is detected the data buffer is saved and the software enters pre-sunrise mode.
- **Pre-Sunrise:** Photodiode data is collected and monitored for a sunrise event. When sunrise is detected the sunrise collection timer is started and the software enters sunrise mode.
- **Sunrise:** Photodiode data is collected. when the sunrise collection timer expires the data buffer is saved and the software enters standby mode.

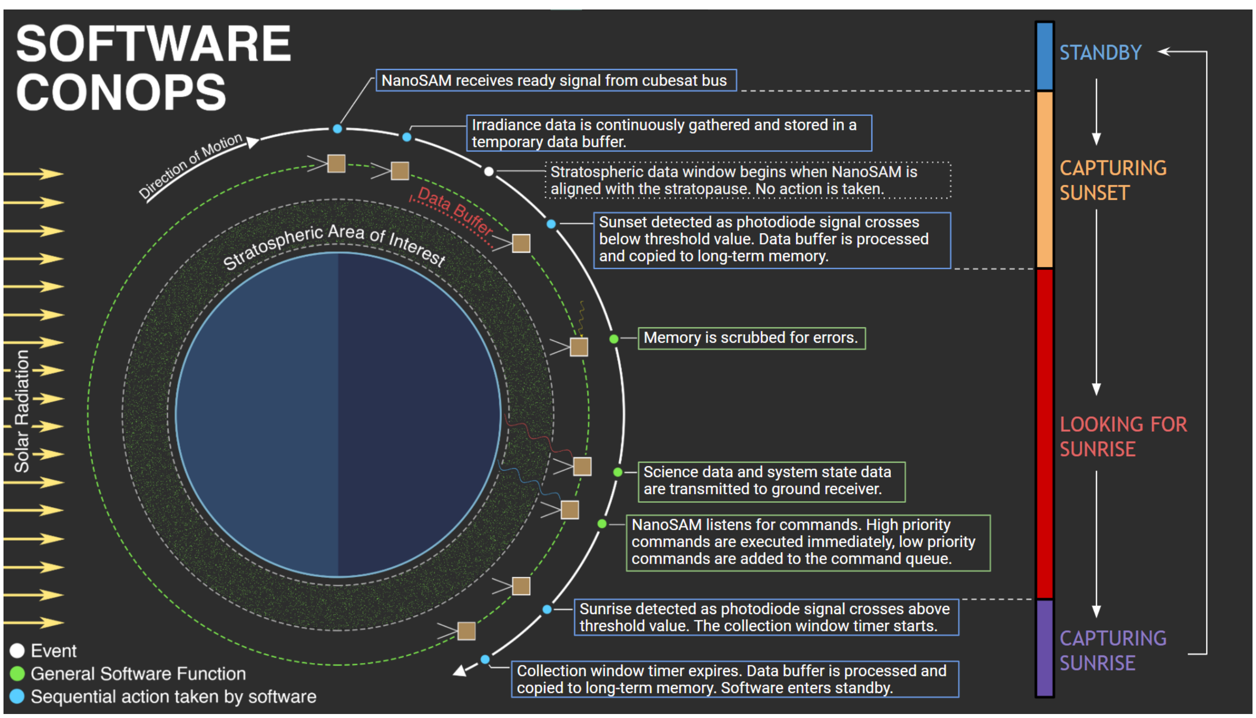

Fig. 17 Software concept of operations indicating the relative sequence of events and timing states

Fig. 17 illustrates the sequence of software events and timing states. Before a sunset event, NanoSAM listens for a go-ahead signal from the bus indicating that the satellite is aligned with the sun and ready for data collection. When the go-ahead signal is received, the software enters sunset mode, and the timing module begins monitoring incoming irradiance samples for a sunset event. The software takes no action at the moment that the sun enters the upper stratosphere as viewed by NanoSAM's optic, nor is it aware that this moment has occurred; the timing module is only concerned with the moment of sunset, at which point the data buffer containing all relevant data is saved to long term memory, the system then enters pre-sunrise mode and begins watching for a sunrise event in the incoming irradiance samples. When a sunrise is detected, the sunrise collection timer is started, and the software enters the sunrise mode. When the collection window timer expires, the data buffer is saved to long term memory and the software enters standby mode until it receives another ready signal from the bus.

4. Command Handling

During normal operations the NanoSAM flight software listens for commands sent by the ground system, which are transmitted to the payload as 32 bit command codes. In its default configuration the command handling module parses incoming commands as they are received. Command execution can also be paused via a special command. When command execution is paused, new commands are placed in a queue instead of being executed. Another command triggers the execution of every command in the queue in the order they were received. This allows a sequence of commands to be preprogrammed and executed in order. In the event of user error when queueing commands, the command queue can be cleared. In its current state the FSW can parse 38 unique commands. To protect the hardware, several potentially dangerous commands capable of causing data loss are locked behind a safeguard. Attempting to send a dangerous command without first disabling the safeguard yields a warning — the safeguard must first be disabled via a separate command before these commands can be executed.

5. Error Detection and Correction

Since NanoSAM II forgoes radiation hardened components in favor of inexpensive COTS electronics, data is vulnerable to radiation induced single event errors (SEE's). When a charged particle impacts a memory module it may flip a single bit or several adjacent bits, this is known as a single event error (SEE). An SEE can occur in any memory location including the external flash, RAM, and Teensy program flash, as well as inside the CPU registers. Errors in the RAM and CPU registries are of secondary concern, since their contents are cleared after a system reset, however, flash memory is highly susceptible to errors, since corrupted data stays corrupted even through power cycling. Thus an error in the program memory could cause the software malfunction or stop functioning permanently. Similarly, an error in the external flash modules where science data is stored will compromise the quality of that data.

To mitigate the effects of SEEs, all science data and persistent system data is encoded with a (72,64) Hamming code, which stores eight redundant bits for every 64 bits of data, yielding a 72 bit encoded block. This configuration is capable of single error correction and double error detection (SEC-DED) meaning that memory blocks with a single corrupted bit can be corrected, while memory blocks with exactly two corrupted bits can be detected. For memory blocks with errors in more than two bits the error detection algorithm yields erroneous results. Even though multiple-bit errors account for less than 3% of SEE's, they pose a significant threat to data integrity [64]. To protect against multiple bit errors, the bits of each encoded block are interleaved so that burst errors affecting several consecutive bits cause single bit errors in several blocks — which can be corrected — instead of large and potentially undetectable errors in one or two blocks. No such EDAC scheme was implemented for the program memory, however, the microcontroller can be reprogrammed via its connection to the CubeSat bus or ground computer if a hangup persists after power cycling.

Once memory is encoded and written to the flash or EEPROM it can be scrubbed periodically to prevent a buildup of errors. The scrubbing algorithm scans each encoded block for errors, correcting single bit errors and clearing blocks with double bit errors. When a scrub is complete the number of detected errors and the size of each error is reported so that the frequency of errors can be tracked throughout the mission.

The exact rate of SEE's is highly variable and depends on many factors including memory architecture and orbital inclination, thus the vulnerability of memory hardware to radiation is usually determined experimentally. In the absence of reliable data pertaining to the rate of SEEs, the team has justified the use of a software based SEC-DED EDAC scheme by conducting research on other, similarly low-cost CubeSat missions. A good example of a similar EDAC strategy is the CanX-1(Canadian Advanced Nanospace eXperiments) 1U CubeSat. This mission designed and built its own on-board computer without any radiation hardened elements. Instead, Hamming codes and Reed-Solomon encoding techniques were used to correct errors in memory in two independent scrubbing routines which periodically washed the static random-access memory. These design choices as well as the success of this mission has provided good reference for our team's design choices. [58].

6. Housekeeping

The housekeeping module is responsible for the collection of system state data, including heater status, power draw, and temperature of the electronics boards and optical bench. System state data is recorded at a frequency of 1Hz and stored temporarily in a buffer containing the last 5000 samples — enough to account for a single orbit. The temperature of the optical bench is interpolated from the optics thermistor voltage using a preprogrammed lookup table. Once the optics temperature is determined it is passed to the thermal control sub-module, which toggles the resistive heater on the optical bench to maintain a safe operating temperature.

7. Fault Mitigation

The fault mitigation module monitors temperature data and software functionality and logs a fault when an abnormality is detected. When a fault is detected the software automatically takes action to correct the fault when possible, such as re-enabling automatic heater control when a temperature reading is out of the acceptable range. The fault mitigation module is also responsible for handling persistent payload data, which is written to EEPROM and loaded on startup. Persistent payload data includes:

- **Fault Log:** A log of all detected faults including the number of occurrences and the timestamp and startup number of the last occurrence of each fault type.
- **EEPROM Write Count:** Total number of writes to the EEPROM since programming.
- **Restart Flag:** Whether the last restart was expected. The flight software enters safe mode on startup if the last restart was unexpected.
- **Startup Count:** How many times the microcontroller has been reset since programming.
- **Consecutive Bad Restart Count:** The number of startups since the last expected restart.
- **Recovered Timing Mode:** The last known timing state.

Each of the 1080 bytes of EEPROM is guaranteed 100,000 write cycles before it becomes unreliable. To extend to lifetime of the EEPROM, the address of persistent data is shifted each time new data is written. On startup, the EEPROM is scanned to find the most recent entry before persistent data is loaded.

Finally, the fault mitigation module is responsible for feeding the watchdog. If the software hangs up and the watchdog is not fed it will trigger a power cycle. The purpose of power cycling is two fold: To correct any occurrences of latchup caused by high energy particles shorting an integrated circuit, and to force the software to reinitialize, which clears potentially-corrupted variables in the RAM and CPU registers. When starting from an unexpected reset, the software automatically enters safe mode, which reduces usage of program memory and therefore minimizes the chance of encountering a corrupted instruction or variable.

8. User Interface

When configured for spaceflight, NanoSAM will be connected to a CubeSat bus, which will handle all downlink and uplink operations, including science data and commands, via dedicated communication hardware onboard the CubeSat bus. In lieu of a CubeSat bus and wireless communication hardware the NanoSAM II prototype is connected via USB to a laptop or desktop computer which acts as a placeholder for both the bus and ground systems. A graphical user interface was created that allows a user to send commands and receive data from the payload.

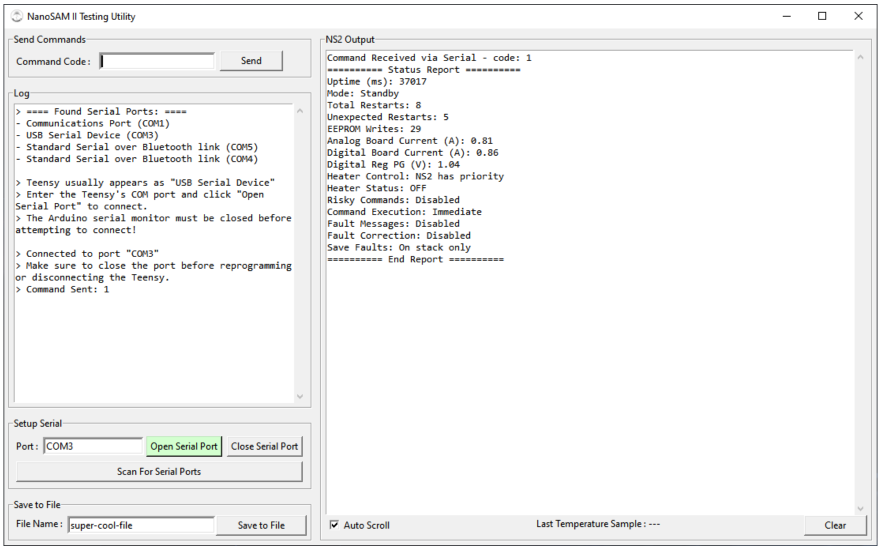

Fig. 18 NanoSAM II Graphical User Interface

The final build of the GUI is shown in figure 18. All payload output is displayed on the right hand side, and can be saved to a file during system tests for later processing. Output is saved automatically to a backup file in the case of hardware or software failure during a test. Warnings, faults, and status updates from the FSW are displayed in real time to keep test operators maximally informed and to enable efficient debugging. The user interface was implemented in python and tested extensively on several machines to account for a wide range of potential user errors and hardware differences. It is compiled into a single stand-alone executable capable of running on most Windows systems.

IV. Manufacturing

Authors: Emma Tomlinson, David Perkins, Jashan Chopra, Abigail Hause, Dan Wagner

A. Structures Manufacturing

This year the manufacturing process for senior projects was slightly different than past years due to COVID-19 restrictions. The biggest impact that the pandemic had on manufacturing was that the team was not able to be trained on the machine shop machinery, so any part that required milling had to be manufactured by AES machine shop staff. While this cut down on the amount of time the team had to spend making the parts, it was imperative that CAD files for the parts were sent to the machine shop with enough time to allow the machinists to finish making them before the deadlines set. Additionally, the job shop model made it somewhat more difficult to troubleshoot issues quickly, as these issues otherwise would have been easily solved if the design team was in the shop manufacturing the parts. Overall, the structures design (three interlocking ribs with two thermal isolation boards) was easy to manufacture and assemble. The table below is a full list of all parts machined and purchased to build the structure. This does not include the parts needed for the optic unless there is overlap between parts.

All hardware and raw materials were purchased from McMaster Carr. Generally we were able to receive orders from McMaster Carr within a week or so after placing the order, but on some occasions it took between 2-5 weeks. Longer lead times seemed to be more likely for less common shapes and materials such as the hex stock that was ordered to make the board-board and board-rib spacers (S08 and S09). If possible, future teams should order materials before winter break. This way materials have about three weeks to arrive before the next semester begins and the team can immediately start construction upon returning in the spring.

Part Number	Description	Purchased/Manufactured?
S01	Top Horizontal Structural Rib	Manufactured
S02	Bottom Horizontal Structural Rib	Manufactured
S03	EPS Structural Rib	Manufactured
S04	Front Housing Panel, Back Housing Panel	Manufactured
S05	Left Housing Panel, Right Housing Panel	Manufactured
S06	Top Housing Panel, Bottom Housing Panel	Manufactured
S07	Structural Rib to Board Rib Screws	Purchased
S08	Electronics Board-Board Spacer	Manufactured
S09	Electronics Board-Rib Spacer	Manufactured
S10	Electronics Screws	Purchased
S11	PCB Washers, Optics Bench Washers	Purchased
S12	External Screws	Purchased
S13	FRP Fiberglass Isolator	Manufactured
S14	Thermal Isolator to Structural Rib Screws	Purchased
S15	Thermal Isolator to Structural Rib Washers	Purchased

Table 10 Structural Parts List

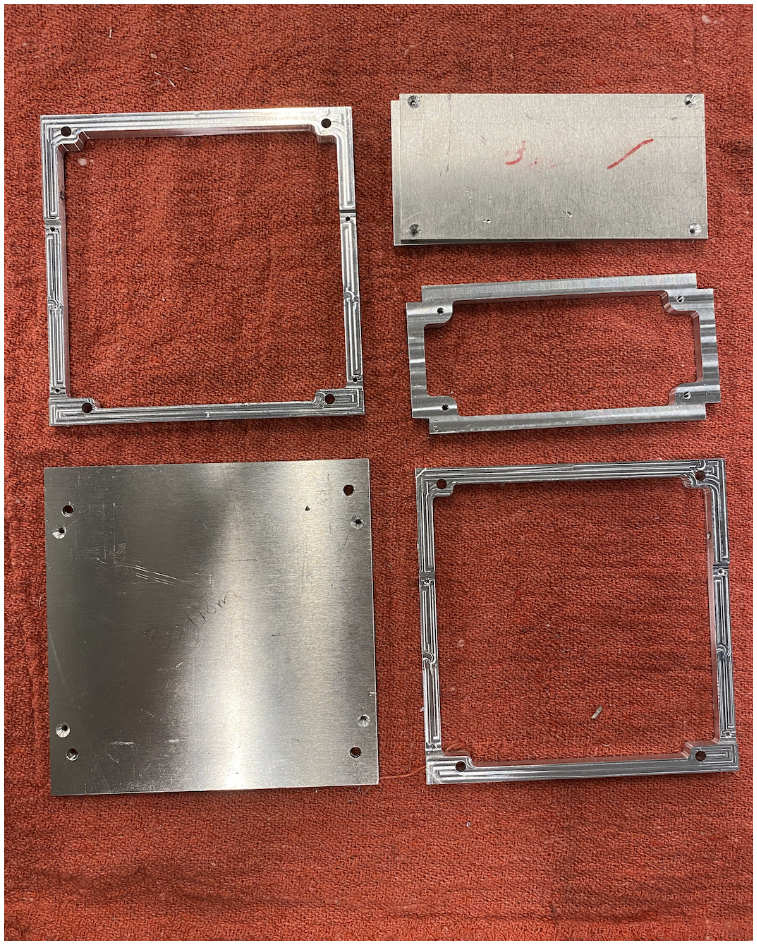

Fig. 19 Structural Ribs and Housing Panels

1. Horizontal and EPS Structural Ribs

Two horizontal structural ribs and one EPS structural rib were constructed. Both were made out of 1/4 inch thick 6061 Aluminum and were milled. This milling operation was time-consuming as it was necessary to reduce the thickness of the piece from 1/4 inch to 0.5cm (0.19685 inch), and future designs might want to reconsider the thicknesses of these parts.

2. Housing Panels

All of the housing panels were made out of 0.063 inch thick 6061 aluminum. The housing panels were straightforward to mill because they are rectangular pieces of metal with drilled through-holes. The front panel required a special tap done for the optical filter to screw into. A thread mill was ordered from McMaster Carr for this tap because the machine shop did not have one in the needed size. The thread mill we ordered was a #6 minimum thread with 32-64 threads per inch. The NanoSAM I team had ordered a tap for this, but it was not well catalogued; NanoSAM II ensures that this tap is clearly labeled for future teams.

3. Challenges Faced

One of the challenges faced was overall fit of the assembled system together. This is largely due to difficulties in assigning appropriate tolerances between parts of different materials. For instance, the fiberglass isolating boards had a tolerance of ±0.025", which is quite large on the scale of this project. To fully integrate these parts with the rest of the structure, the corresponding slots on the structural ribs had to be sanded down by hand to accommodate an increase in thickness. The tolerance issues encountered at the thermal isolation boards also affected the overall fit of the walls of the structure, as the small displacement slightly misaligned the ribs when fully assembled, and so the hole positions on the walls did not align as perfectly as they should have. Nonetheless, all of the walls were installed properly.

Another major challenge faced that was not apparent during the design phase was the difficulty in routing the electronics wiring. Small spaces and the EPS rib made it difficult to position the heater, the photodiode, and the temperature sensor simultaneously during assembly. Additionally, powering and communicating with the Teensy required wires and a Micro-USB connection through the external wall, which required a quick drill press fix.

B. Electronics Manufacturing

The electronics PCBs were printed by OSHPark, and they cost $30 for three copies of each board. We ordered all electronics components from Digikey, and parts shipped in roughly three-five business days. The final boards were manufactured solely in AERO150 which is the electronics lab in the aerospace building. We applied solder paste to the board manually using the solder extruder in the lab, and it was not necessary to purchase a solder stencil. We then placed the components using the manual pick and place machine, and then melted the solder using the standard profile (leaded solder and medium board size) in the lab's reflow oven. The Teensy 4.0 and the board to board connector were hand soldered. After being trained by the lab TA, Camilla, we were able to manufacture the boards in around four sessions, so roughly 8 hours. Pictures of the final manufactured boards are show below in Fig. 20 and 21 respectively.

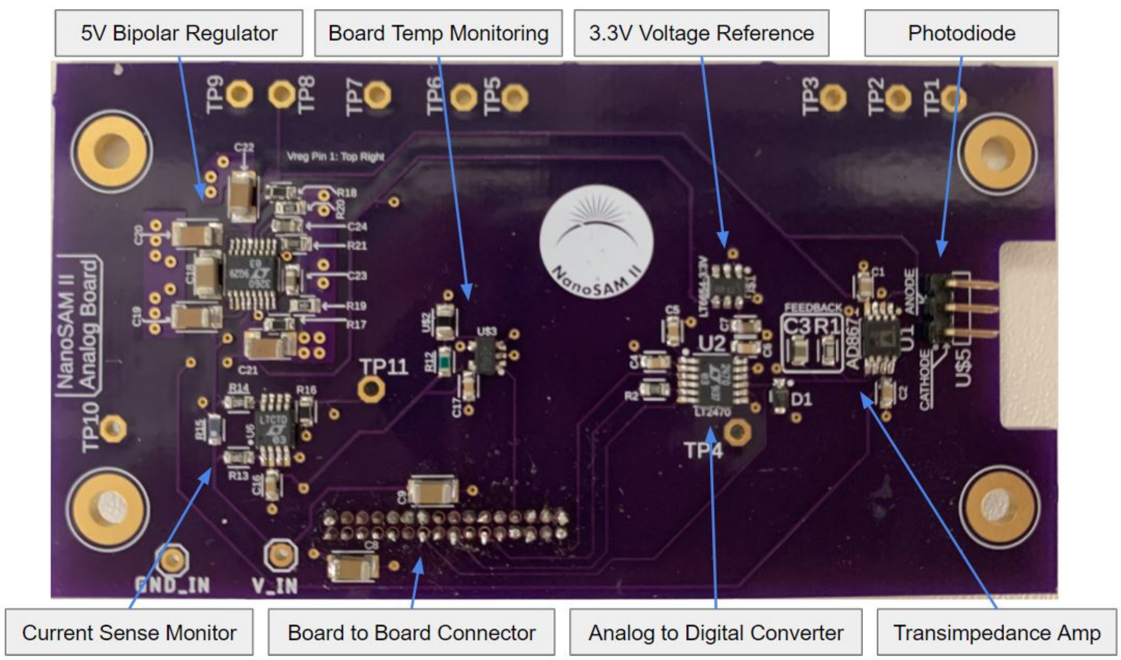

Fig. 20 Manufactured Analog Board

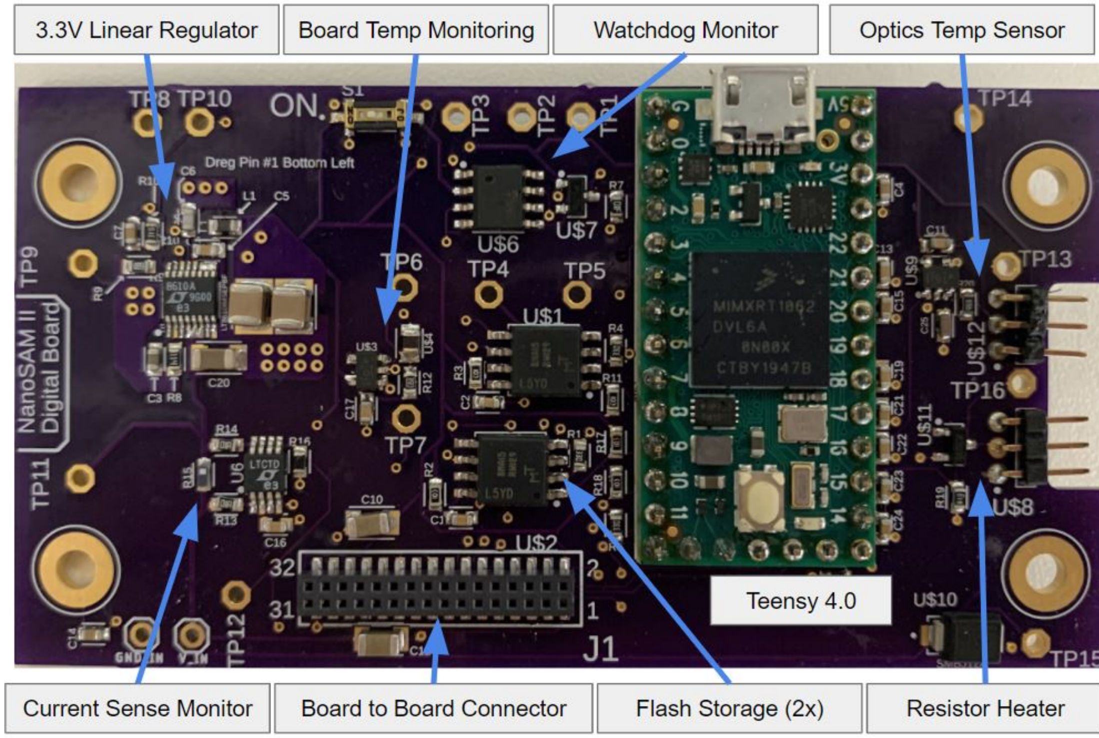

Fig. 21 Manufactured Digital Board

The last electronics manufacturing task was creating the shielded wire connectors for the optics temperature sensor, the optics bench resistor heater, and the photodiode. We used twisted shielded pair wires that were provided from the electronics lab. We first cut the outer plastic with a xacto knife, separated the shielding from the actual wires so that it could be twisted into a wire for GND connections, stripped about a 1/4 inch of the end of the other two wires, and then connected them to the tabs of the female receptacle connectors. We used heat shrink tubing on the individual solder joints where the wires were attached to external device pins to prevent them from touching each other or any metal on the CubeSat chassis. Heat shrink tubing was then put over all the pins together so that it would cover all the way from the external device pins to where the outer plastic was cut off. We then performed the same task on the other side of the wire, connecting it to the external devices. We then marked the female receptacle connectors with a dot for the top side, and an X for the bottom side. A picture of these manufactured connectors is shown below, in Fig. 22.

Fig. 22 Manufactured External Connectors

There are a number of improvements that can be made with these external connectors. Due to the location of these external connectors on the board and the location of the devices as attached to the optics bench, the wires were forced into a high degree turn. Since the payload is also so small, the wires are short and thus have increased stiffness. It should be noted that the heat shrink tubing makes the connectors significantly less flexible so reducing the amount of heat shrink tubing used is recommended. Additionally, it was later learned that heat shrink tubing could potentially experience outgassing in a vacuum environment, which is another reason heat shrink use should be limited in the future. The main point of failure was the tabs on the M22 female receptacle, so we chose to apply hot glue to the solder joints. Hot glue is also prone to outgassing in a vacuum environment, so a more sturdy connector should likely be chosen. We would recommend a clipped or locked connector to make a more secure connection that can then be removed more easily for testing. To attach these components to the optics bench, we used a basic epoxy, JB Weld ClearWeld. The shielded wires are also quite thick, even though we went for a rather small guage. The three wires next to each other just barely fit across the length of the electronics board. We would thus recommend either increasing the size of the cutout in the side of the electronics boards, or placing the optics temperature sensor and resistor heater connection points on the opposite side of the photodiode. Fig. 23 shows the electronics boards with soldered wires and external connections, before it was integrated into the full structure.

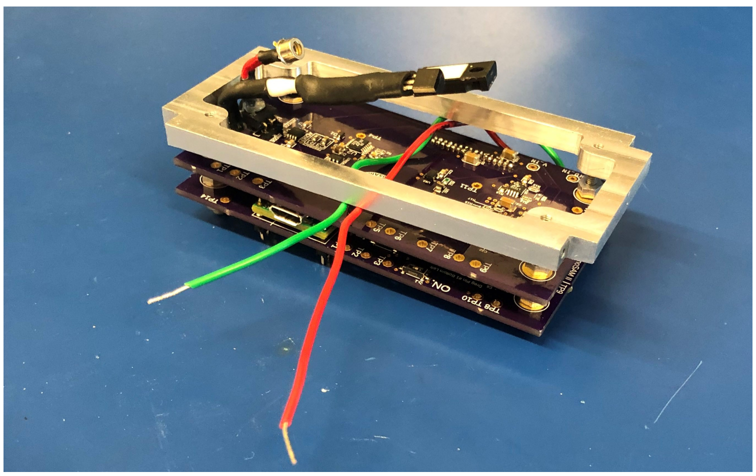

Fig. 23 Electronics Final Assembly before Integration

C. Optics Manufacturing

Overall, the optics bench and the photodiode block proved tricky to manufacture, especially considering the required tolerances on these parts. These difficulties are discussed further in this section, but are generally due to extremely fine tolerances required to make the optics system align properly. Tab. 11 below is a full list of all major parts machined and purchased to build the optics, followed by Tab. 12, which contains hardware used for alignment. This does not include purchased screws or washers, which are not considered to be significant to the design.

Part Number	Description	Purchased/Manufactured?
Op01	Optical bench base plate mirror mount	Manufactured
Op02	Optical bench base plate diode mount	Manufactured
Op03	Diode block	Manufactured
Op06	Photodiode	Purchased
Op07	OAP Mirror	Purchased
Op08	Spherical washers for OAP mirror	Purchased
Op09	Standard washers for OAP mirror mounting hardware	NS1 Hardware
Op10	OAP mirror mounting screws	NS1 Hardware
Op11	Front aperture plate	Manufactured
Op13F, Op13R	Front crosshair, rear crosshair	Manufactured
Op17	Dowel pins	Purchased
Op18	Pinhole	Purchased
Op19	Pinhole	Purchased

Table 11 Critical Optics Parts

Part Number	Description	Purchased/Manufactured?
A01	Kinematic base interface plate	Manufactured
A02	Tension screw holder	Manufactured
A03	Kinematic base	Purchased
A04	Focus shim, 0.1mm thickness and 0.0005" thickness	Manufactured
A05	In plane shim, 0.1mm thickness and 0.0005" thickness	Manufactured
A06	Out of plane shim, 0.1mm thickness and 0.0005" thickness	Manufactured

Table 12 Critical Alignment Parts

1. Purchased Parts

All hardware and raw materials were also purchased from McMaster Carr. Specialty components, such as the OAP or the pinhole, were purchased from Edmund Optics.

2. Optics Bench

One simulator optics bench and one optics bench for alignment were manufactured. This allowed for vibration testing with the simulator and alignment with a more finely manufactured bench. The bench used for alignment featured dowel pins at the interface between the diode mount plate and the mirror mount plate, which aligned these two parts (and therefore the mirror relative to the aperture) to a finer tolerance than could be done with just screws.

3. Photodiode Block

The photodiode block was the most difficult part to manufacture. This part was extremely finely toleranced, and required nearly exact concentricity between the pinhole mount slot and the photodiode mount slot in order to capture the oncoming light. Originally, this part was had a small mistake in design such that it had 0.5mm of adjustability in both the in plane and out of plane directions, as opposed to the required 1mm of adjustability in these directions. To correct this, the mounting holes were widened on the photodiode block. The photodiode block was also threaded such that it could attached to a 3-axis stage to measure its position relative to the bench for shimming.

4. Shims

The shims were thin pieces of stainless 18-8 steel designed to fit around the photodiode block and fix its position relative to the optics bench in order to align the pinhole. The NanoSAM II team manufactured a total of 90 shims, with 3 sets of 30 shims for each direction. Each of these sets contained 20 0.1mm thickness shims and 10 0.0005" thickness shims. The complex focus shims were manufactured by electrical discharge manufacturing (EDM) by the Cooperative Institute for Research in Environmental Sciences (CIRES) at CU, and the remaining shims were cut by hand. Future teams should consider cutting fewer shims of varying thicknesses all by EDM for best results.

5. Alignment Hardware

The alignment hardware given to the optics team streamlined the sessions at Meadowlark. These parts could be improved by shifting hole placements to ensure ease of assembly and disassembly once shims are in place. Another improvement would be a guide to quickly line up the interferometer with the mirror's main axis.

6. Challenges Faced

Manufacturing the optical components for NanoSAM II proved to be difficult. These parts are highly toleranced and sensitive to deformations. One difficult manufacturing step was the installation of the pinhole to the photodiode block. The pinhole itself is sensitive to dust and is also extremely small. To make it slightly easier, a pinhole mount disk was manufactured. The pinhole was first epoxied to the mount disk after carefully aligning it with a small fridge magnet. After this epoxy dried, the seat for the pinhole mount disk inside the photodiode block was epoxied, and the mount disk with the pinhole was positioned into this seat with a rod with a small fridge magnet.

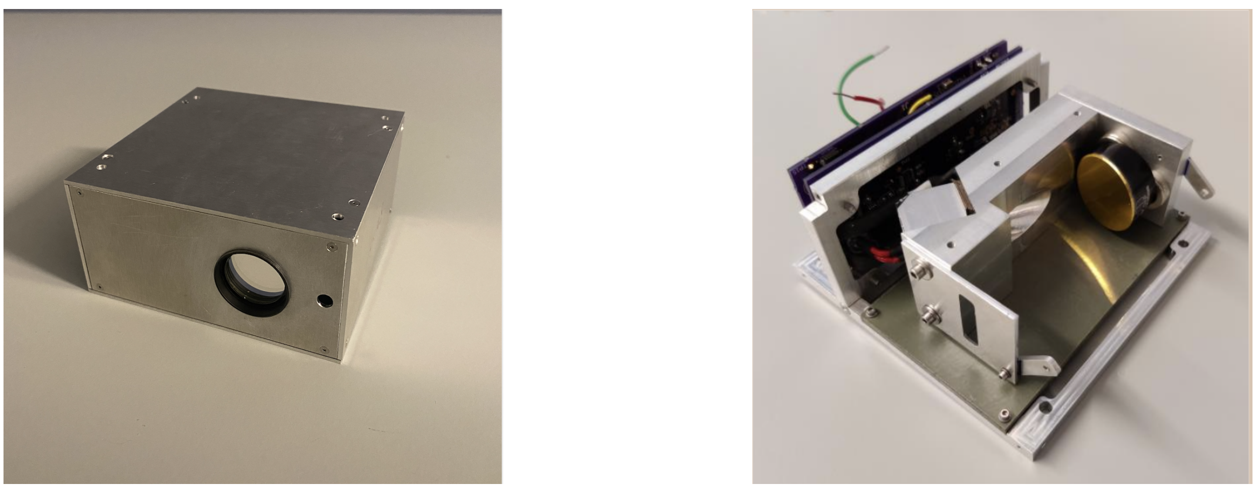

Fig. 24 Manufactured system with and without housing panels

D. Software Manufacturing

To streamline development, the NanoSAM II software focuses on using open-source libraries and standardized frameworks wherever possible. Writing lines of code has no material cost, however, with less than one year to design, implement, and test a complete software system, efficient use of time was a necessity. Using free third-party tools for code development, compilation, and version control has enabled us focus solely on writing code while maintaining an architecture that is thoroughly tested and evaluated to a degree not possible had every software component been custom made.

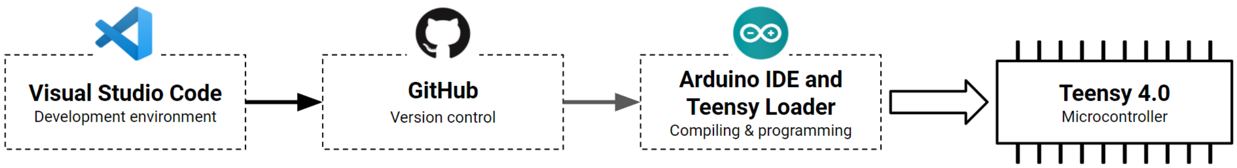

Fig. 25 Software development pipeline

The Arduino Integrated Development Environment (IDE) provides a simple and standardized method of compiling and uploading programs to Arduino-compatible microcontrollers. With the addition of the Teensy Loader, a free and open source add on for the Arduino IDE, new code can be compiled, uploaded to the microcontroller, and executed in seconds. Small development boards like the Teensy 4.0 are designed with ease of use in mind, and can interface with any computer via USB [45]. In addition, serial data are sent and received via the Arduino IDE's built in serial monitor. This shifted the workload away from developing hardware and software systems for communicating with the microcontroller, and towards implementing the logic needed to collect scientific data. Additionally, multiple microcontrollers were used across the development team to enable rapid testing of new software components at any point during development. Testing new code on secondary-hardware protected the primary hardware components from damage and inspired confidence in NanoSAM's code base as it grew in complexity.

To ensure that the codebase remained manageable and easily accessible as multiple developers made contributions, GitHub was used for version control and collaboration. Using GitHub allowed the entire team to review and discuss changes to the code asynchronously. This review process ensured that new code was free of most logic and syntax errors before proposed changes were merged to the codebase, and kept everyone up to date on the latest development progress. As a result, software development ran into relatively few roadblocks.

V. Verification & Validation

Authors: Matt Bridges, Axel Haugland, Daniel Barth, Abby Hause, Dan Wagner, Ryan Smithers

NanoSAM II has a test plan that is organized along a component, subsystem, then system level testing breakdown. Each component in a subsystem must pass its individual tests before the team will integrate these components into the subsystem. Similarly, each subsystem has to pass its own tests before the entire payload is integrated. This means that if a test run on the integrated system does not succeed, the troubleshooting can focus on the interfaces between components and subsystems rather than on the components themselves.

A. Component Tests

1. Electronics

The isolated electronics testing consisted of verifying that each component of the boards worked as expected. The main purpose of this testing was to make sure that integration level tests did not have to concern themselves with failure analysis involving the electronics boards themselves, and to verify that the overall design worked as expected. This was done by testing the voltage at a series of test points on both the analog and digital board. We first tested the analog and digital board isolated from each other. This configuration does result in some test points not showing the expected design voltages, because the boards need to be connected for all features to work. This testing was mainly to verify that the voltage regulators worked as expected. We then combined the boards and performed an integration test of all the voltages, and tested the external devices. For each test I will discuss what went wrong initially, describe how we debugged and fixed it, and then show the final voltage measurement results for verification. To see the full testing notes as they were written on the day of the test, see the "Electronics System Test" PDF in the *NSII/Electronics/Design folder*.

2. Electronics Analog Test

The first thing we did was perform a connectivity test using a digital multimeter from the AERO150 lab. We did not comprehensively test connectivity on every single line, but we generally made sure there were no voltage to ground shorts anywhere on the board. It also helped us check that our manufacturing process was good and that devices were appropriately soldered onto the board. In the individual analog test all of the ground points floated at around 2-4mV, which is a good indicator that the ground plane was low noise. We originally found that test points 7 and 8 were showing +/- 12V, and test point 3 was showing 5V. What happened is that we ordered the wrong LT6654 voltage reference, accidentally ordering the 5V model instead of the expected 3.3V model. Additionally, we were sent the wrong size resistor by Digikey (10k instead of 100k), which resulted in the voltage divider circuit on the analog voltage regulator output performing an unnoticeable downconversion. Switching to the right parts for the voltage divider and the voltage reference fixed both of these issues. For brevity, test point values for the individual analog and digital tests are not given, as they are similar to the test result values for the integrated electronics board test. Full electronics testing results are provided in the Electronics Master Summary in the *NSII / Electronics /* folder.

3. Electronics Digital Test

The digital ground test points showed a similar noise floor to the analog board, which again showed a lack of overall noise on the boards that we were happy with. Test point 1 is the voltage into the Teensy which varied over the course of multiple tests. We first saw a low voltage here, and then in later tests we saw 3.3V making it through the MOSFET. We did expect a floating value when the watchdog is triggered, but it appeared that turning off the watchdog with the hardware switch had no effect on the output of test point 1. Either the MOSFET or the design of the watchdog hardware circuit itself was not functioning properly. More detailed discussion about the failure of this watchdog circuit and recommendations are described in the Electronics Master Summary document. We did not fix this issue, as we powered the Teensy with its USB connection. In initial tests the digital regulator was only outputting 0.4V, as indicated by test points 4, 5, and 10. Test point 8 was showing 4.4V as opposed to the roughly 2.8-3.6V it should when the internal electronics of the voltage regulator are working as expected. First, we realized that the inductor L1 had been placed on the board upside down. Fixing this issue fixed the digital voltage regulator, which we could tell because test point 8 then regulated to 3V, and the voltage on the primary decoupling capacitors of the digital power regulator showed 3.3V. We also recognized that by placing a 10k ohm resistor on the voltage input to the flash modules, read by test points 4 and 5, that we were unnecessarily dividing the voltage input. Upon checking the previous design, these resistors were meant to be sense resistors for cutting off the voltage input if required. We replaced them with 1 ohm resistors and test points 4 and 5 then regulated back to 3.3V, as expected. Test point 10, the digital regulators "power good" pin never showed 3.3V as it should have, so we expect that either this pin was broken on our digital regulator, or we misunderstood the purpose of this pin. Either way, the regulator was outputting 3.3V so we knew it was working correctly despite the erroneous reading from test point 10. Additionally, the digital thermistor was not working at first. It turns out the thermistor was soldered on the board poorly, and was not making a concrete electrical connection and thus not dividing the voltage properly, which led to test points 6 and 7 showing the full undivided 3.3V. We did not fix the digital thermistor for this test, but we did fix it for the integration test.

Test Point	Actual Value	Expected Value
Analog 1	3-4mV floating	0V
Analog 2	2-3mV floating	0V
Analog 3	3.3V	3.3V
Analog 4	3.7mV	0V
Analog 5	0.65V floating	0.6V [Room Temp]
Analog 6	0.61V floating	0.6V [Room Temp]
Analog 7	5.0V	5V
Analog 8	-4.97V	-5V
Analog 9	3.8mV	0V
Analog 10	12.01V	12V
Analog 11	3.8mV floating	0V
Digital 1	2.02V, 0.8V	3.3V [Teensy on]
Digital 2	N/A [Not Tested]	0V
Digital 3	N/A [Not Tested]	0V
Digital 4	3.3V	3.3V
Digital 5	3.3V	3.3V
Digital 6	0.367V	0.6V
Digital 7	0.367V	0.6V
Digital 8	3.3V	3.3V
Digital 9	4.6mV	0V
Digital 10	0.35mV floating	3.3V
Digital 11	12V	12V
Digital 12	5.6mV	Input Current, Variable
Digital 13	N/A [Not Tested]	0V
Digital 14	N/A [Not Tested]	0V
Digital 15	12V	12V
Digital 16	10mV	0V

Table 13 Board Integration Test Results

4. Electronics Integration Test

For the integration test we plugged in the Teensy and ran software tests. We did not connect the photodiode, optics temperature sensor, and resistor heater here. During the integration test we found a few issues with the soldering on the board to board connector, which just required us to apply more solder. After that we saw all the voltages successfully going through the board to board connector. We also found the ADC issue here which we patched with a white wire, as discussed in the lessons learned section. The digital thermistor also worked once we fixed the solder and the electrical connection. We did not wait long enough after heating this element up, so the results of the digital thermistor test showed the temperature as roughly 100 degrees Fahrenheit. The analog temperature sensor showed that the result was room temperature, and the design is identical, so we trust the thermistors. We saw later during the thermal test that the board thermistors track the temperature of the boards quite well. Due to the watchdog issues we saw with the individual digital board test, we chose not to test the watchdog software. We did see in a later test that the Teensy was able to drive a pin high logically to turn on the resistor heater, so we are confident that the Teensy could output the watchdog logical high signal to reset the watchdog's timer. We see some loss in the analog thermistor value as it travels through the board to board connector and to the Teensy. We see the power usage for the analog board was about 40.8mW using the current sense measurement and the input voltage, and the power usage for the digital board was about 67.2mW.

5. Electronics External Connector Test

There were initially some issues with our connectors as well as the software. We had labeled the logic pin that activates the resistor heater wrong, and when we fixed that label the logic was successfully running high and the resistor heater path was closed, allowing current to flow, and heat the resistor. We remade our connectors and made sure to correctly label them, which resulted in the optics temperature sensor working correctly and the photodiode recording some data. After the white wire fix, we saw that the ADC SPI connection was able to read the photodiode, as well as the SCI backup pin. We also verified that the flight software was able to write files to the on-board flash modules. The low pass filter on the optics temperature sensor should have slightly reduced the voltage, but we saw an exact 1-1 ratio here. We saw that only around 2mV difference was detected between the SCI pin and the board connector pin on the digital board side, so we can be fairly certain that what the Teensy 4.0 read is the actual reported photodiode value. One issue we noticed here is that there is no way to measure the current draw of the resistor heater itself, since we supply the voltage directly from the bus input without a current sense monitor in the loop. We should have added a step in the test plan to read the current draw from the lab station power supply. Since the resistance and voltage are constant going through the resistor heater, we can be fairly certain of the power it draws in design, but it would still be good to test this.

Test Point	Actual Value	Expected Value
Analog 2	50-70mV [iPhone Flashlight]	[Depends on Light]
Board Connector Pin 19	2mV less than Analog 2	N/A
Digital 13	1.85V	1.77V at 30 deg C
Digital 14	1.85V	1.77V at 30 deg C
T14/T13 Low Pass Ratio	1	0.989775
Digital 15	12V	12V
Digital 16	6mV	0V

Table 14   External Connector Test Results

6. Verified Electronics Requirements

The electronics testing proved crucial to the mission success. We identified a series of problems and took straightforward steps to debug and fix these issues. Overall the electronics testing took around 2 weeks after we completed the manufacturing. We would have liked to repeat some of these tests, especially looking more into the watchdog hardware circuit, however we simply did not have time due to the lost margin that was used for redesigning the board. All electronics components worked as expected except the watchdog hardware circuit. However, the watchdog was not involved in any of the requirements, and the Teensy was still able to be powered by the USB. Thus, these electronics test proved that the design performed as expected and met the requirements. Table 15 shows the requirements that were verified by these electronics system tests, along with a brief explanation of how the tests verified the requirements.

L0	L1	L2	L3	Name	Requirement Verification
1.0				Data Capture	Electronics collects analog board, digital board, optics board temperature, and photodiode data. It is successfully digitized by the on-board ADC as well as the Teensy ADC, and successfully packetized and stored on the on-board flash modules by FSW.
	1.1			Optics Data	The photodiode collects data and the external connector from the photodiode to the board works as expected.
		1.1.1		Sampling Rate	Both the on-board ADC and the Teensy ADC work and collect data at a rate greater than 50 Hz.
			1.1.1.1	Processing	The Teensy and associated FSW operate at a much higher rate than 50Hz and are able to process and store data faster than this rate.
		1.1.2		Data Collection Bit Size	The on-board ADC works at 16 bits, and the Teensy works at 12 bits, both are operational.
		1.1.3		Storage Size	The flash modules contain enough storage for many days of data collection, and read/write operations to the flash modules were successful.
	1.4			Housekeeping	Software was able to collect and monitor all system state data.
		1.4.1		Temperature data	All three temperature monitors worked as expected.
		1.4.2		Power data	The current sense monitors worked as expected and matched the current draw from the power supply used for testing.
	1.5			Power Consumption	We limited the power supply at 0.5A (6W at 12V) and it did not current limit. The boards drew minimal power throughout all tests. We did not measure the resistor heater current draw, however we can be confident the system power draw did not exceed 7.3W.
2.0				Communications	The electronics and software worked together and successfully communicated with the computer in AERO150, and Axel's laptop.

Table 15 Functional Requirements Verification

7. Optics Solar Tracking Test

The first optical component level test to be discussed is the solar tracking test. The purpose of this test is to confirm that the purchased solar tracker meets the required 1 arc-minute tracking accuracy. It is noted here that in the final spaceflight iteration of NanoSAM, this is not the solar tracker that will be used, because it is assumed that NanoSAM will be aboard a satellite that has its own bus and attitude control. However, a solar tracker with the required accuracy is needed in order to complete accurate ground tests of NanoSAM II.

The test was be run using the Orion Solar StarSeeker Tracking Altazimuth Mount purchased by the NanoSAM I team. This is the solar tracker that will be used to run full integration tests of NanoSAM II. No test facility is needed because this test needs to be run outside on a sunny day.

To run the test, the solar tracker (powered by the 8 AA batteries) was be set up according to the instruction manual. Once the solar tracker was assembled, attached to the mount, and powered on, the tracker will automatically align itself to the sun. A cell phone was then attached to the Solar tracker, and a timelapse video of the sun was taken over the course of an hour. A picture of the setup can be seen in Fig. 26

Fig. 26 Solar Tracker Test

To ensure the tracking accuracy requirement is met, the video was processed using a webplot digitizer to determine how much the the center of the sun moved in relation to the original position. The angular diameter of the sun as viewed from the earth is 30 arcminutes, and this was used to scale the movement of the center of the sun. The resulting recorded movement is shown in Fig. 27 below.

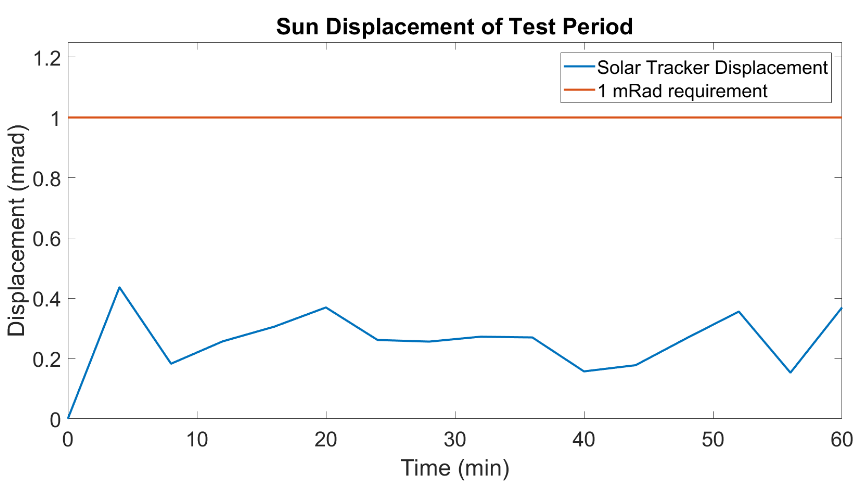

Fig. 27 Solar Tracker Results

Fig. 27 clearly shows that the solar tracker meets the 1 mrad SAM-II legacy requirement.

8. Optics Field of View Test

The other measurement to be taken from the optical system was the field of view. However, due to conversations with project customer Jim Baer, it was decided not to run this test. The 1.3 arcminute field of view requirement is based off a desired vertical resolution of 1km, assuming that NanoSAM is in a 500km orbit. However, our customer pointed out that since this year's NanoSAM II design will not be put into orbit, and that future teams will be responsible for finding a satellite to integrate NanoSAM into that may have a different orbital radius, testing the field of view was best left for a future team. Theoretical calculations of the field of view and vertical resolution were detailed in the design section, and the design theoretically would meet the field of view and vertical resolution requirements.

B. Subsystem Level Tests

1. Optics

Alignment The primary subsystem level test for the optical system is the alignment test. The purpose of the alignment procedure is to achieve a MTF that meets the SAM-II legacy requirement of 0.74. There is not an individual test run to calculate the MTF of the optical system; the MTF is a measurement taken during the alignment process.

The optics alignment procedure is an iterative process, that should end when the optics team considers the system to be sufficiently aligned. The threshold for what is considered sufficiently aligned is determined by meeting the required .74 MTF. Unfortunately, due to lack of time and facility access, the optics team was not able to complete this procedure.

The MTF of the optical system can be degraded by several factors, including defocus, tilting, in-plane and out-of plane radial displacement, mirror irregularity, central obstructions, comatic aberrations, and ripple noise [8]. NanoSAM I used Zemax to model system MTF at the pinhole by combining effects of radial in-plane and out-of-plane displacement. Using this model, NanoSAM I calculated the maximum displacements possible to achieve the required MTF, and they are shown below in Fig. 28.

	NanoSAM (feasible alignment)	
Target MTF Best possible MTF of SAM-II at critical angular frequency with 50 mm aperture & 75% obstruction	0.74	
Predicted Mirror MTF with WFE Obtained using Zemax for angular frequency of 2.57 [cycles/mrad]	0.86	
MTF Degradation Factor		
Focus (Z') Displacement	0.94	45 μm error **
Out-of-plane (X') Displacement	0.97	30 μm error **
Filter TWFE	0.98	0.03 λ WFE
Filter TWFE	0.98	0.03 λ WFE
Analysis		
Combined Degradations = $\prod$ MTF Degradation Factors	0.88	
System MTF = Combined Degradations * Actual Mirror MTF	0.75	
$\text{Margin} = \dfrac{\text{System MTF}}{\text{Target MTF}} - 1$	0.01%	
		** feasible displacement

Fig. 28 MTF displacement chart [8]

Because NanoSAM II is using the same optical design with the all of the same size components as NanoSAM I, these measurements hold true. The measurements in Fig. 28 show the alignment team the margins they need to meet to achieve the desired MTF. If the required MTF is met, then optical system will meet the SAM-II legacy requirement that makes up a critical project element.

Alignment Sessions The optics team had five two-hour sessions at Meadowlark Optics, who generously allowed NanoSAM to use their interferometer. The first three sessions were practice sessions, to gain familiarity with the interferometer and associated optical equipment, and develop an alignment procedure. The general procedure involves aligning the mirror to the interferometer beam using micrometers until it is in focus, and then measuring the Zernike coefficients at that point. There is a linear relationship between Zernike coefficients and alignment error, so as the Zernike coefficients are driven to zero (by moving the micrometers based on the linear relationship), the mirror is moved into an aligned position.

The last two sessions were spent working with the manufactured hardware to align and measure the MTF of the mirror, place the pinhole so that light could pass through it, and align the crosshairs to the interferometer beam.

Using a concave lens to reflect the beam from the OAP, the OAP was aligned and the surface was measured. The measured characterization can be seen below, in Fig. 29.

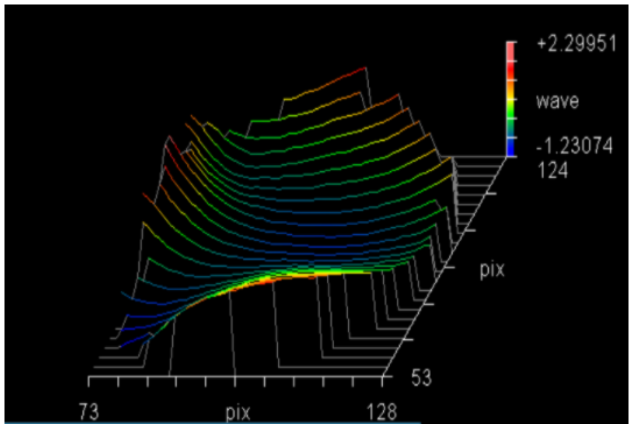

Fig. 29 OAP Wavefront Error

The key thing to notice in this figure is the three red areas around the edge of the OAP. These are directly over the locations of the three bolts that are used to fasten the OAP to the optical bench. The torque from the bolts is deforming the surface of the OAP, causing wavefront error. In order to compensate for this, the aperture is used to focus the incoming light on the center of the OAP. In Fig. 29, this is the blue center area that has a much lower wavefront error than the edges.

A mask was used on the interferometer to model the 20x5mm aperture used by NanoSAM I, and the resulting wavefront error of this part of the OAP is shown in Fig. 30.

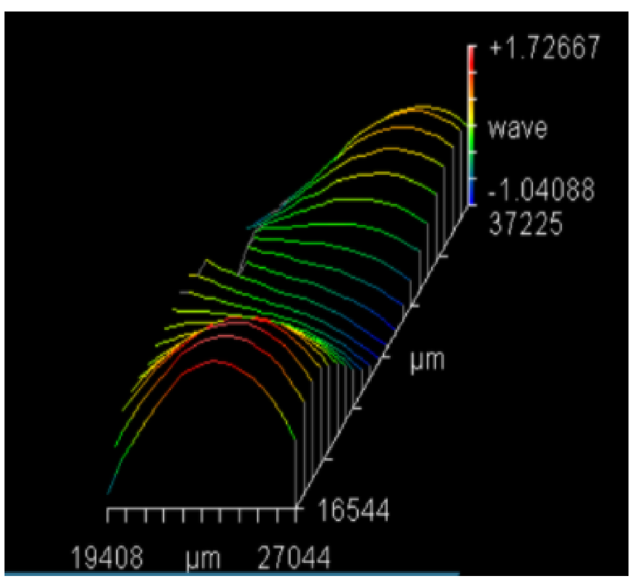

Fig. 30 OAP Wavefront Error with Aperture [8]

In Fig. 30, the wavefront error is reduced, but not enough. Using data from the interferometer, the mirror's MTF was calculated to be .4233. As the MTF requirement was .74, NanoSAM II failed to meet the SAM-II equivalent MTF requirement. Note that this does not take into account the degradation from being off focus which could be better explored by a future team via the use of Zemax. It was not done this year as the team found that the mirror MTF was much lower than that of the .74 requirement.

It is noted here that a larger OAP would produce lower wavefront error, and therefore a higher MTF. This is because a larger mirror would still contain the bolt deformations shown in Fig. 29, but there would be a larger low deformation area in the center. This would allow the area defined by the aperture to have a lower wavefront error, and thus a higher MTF. However, a larger OAP that still fits within the size requirements would need to be custom made, and the preliminary trade studies showed purchasing a larger mirror to be both time and cost prohibitive.

Another way to produce lower wavefront error is to minimize surface deformation by using a custom OAP that has external mounts, and the same size as the current mirror. A preliminary design was drafted for such a mirror. The preliminary design can be found in the optics final design section. It should be noted that a future team should look to perfect the mirror design.

Once the mirror surface had been measured, the pinhole was placed so that light could be seen coming through it. This was done by first placing the photodiode block in the back corner its space in the optical bench (flush with all three walls), and recording the micrometer measurements at this location. The photodiode block was then moved using the micrometers until light from the interferometer could be seen coming through the pinhole, and the micrometer displacements were recorded. These micrometers were later used to calculate the thickness of the shim stacks needed to attach the photodiode block to the optical bench in the correct location. It is noted here that while the pinhole does receive light through it, light received is not focused. Ideally, the pinhole placement would have been an iterative procedure that would have found the center of the beam of light reflected from the OAP, and placed the pinhole on the focus of the light beam. However, the team did not have time for this, and settled for getting light through the system instead. The interferometer return from the pinhole plate was used to calculate the defocus of the pinhole. These power fringes can be seen in Fig. 31.

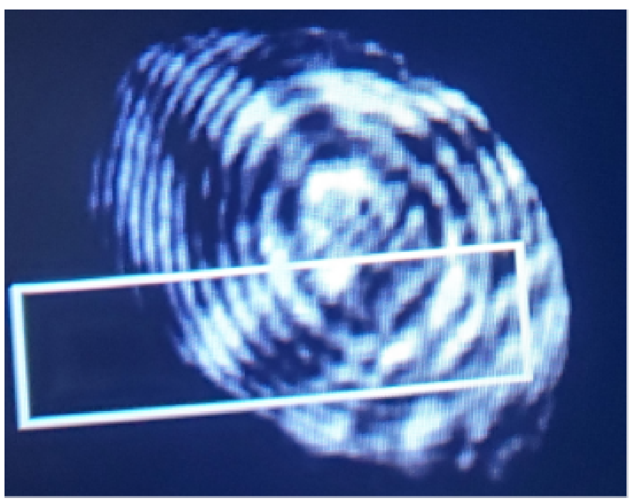

Fig. 31 Pinhole Plate Interferogram

Using the equation

$$\epsilon_z = 8 * (F/\#)^2 n/\lambda \tag{20}$$

where ϵ_z is the focus displacement, (F/) is the F-number of 2.2, n is the number of rings (12 can be counted in Fig. 31), and λ is the frequency of 633 nm, the focus displacement was calculated to be .2941 mm. The maximum possible radial displacement was then calculated using the same method used by NS1, shown in the equation

$$\epsilon_r = \frac{\epsilon_z}{(F/\#)^2} + d_{pin}(F/\#) \tag{21}$$

The maximum radial displacement was found to be .0676 mm. Referencing Fig. 28, the maximum allowable focus displacement is .045mm. Note that these values assume an ideal mirror MTF of .86 or greater otherwise the system would need to be better focused than a defocus of .045mm and radial displacement of .030mm. Due to this, the system is not focused, which will result in a blurry image of the sun.

The last thing done at Meadowlark was the alignment of the sighting tabs to the interferometer beam. The purpose of this is so later be able to use the sighting tabs to align NanoSAM to the sun, meaning that the OAP will be perpendicular to the rays from the sun. This was done by projecting the sighting tabs onto a piece of paper using the interferometer beam, and moving the tabs until their projections were lined up. Fig. 32 below shows the projection of the lined up sighting tabs.

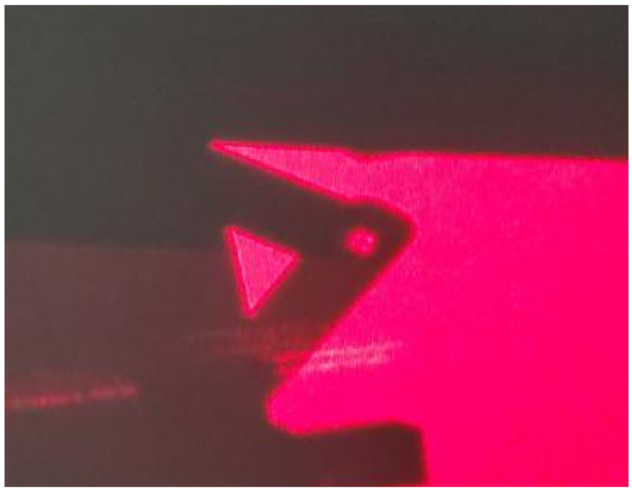

Fig. 32 Aligned Sighting Tabs

2. Software

Testing the software subsystem involves verifying correct module functions with changing parameters. When running the tests for a module, the software response will be compared to the desired response. This mainly consists of checking that information is communicated correctly between modules. The 5 subsystem tests are for commands, fault detection, sample rate,and loop simulation.
The testing setup for the software-only tests only involves a computer loaded with the software. setup consists only of a computer with the system software. Since specific modules need to be tested, the software will need testing modifications for the computer to control commands and module inputs.

Command Test The testing of commands requires the software to be set up so the computer can send the inputs and collect the outputs from each module. Using the computer, the different inputs of the modules should each be tested and their corresponding outputs compared with the expected outputs. Once the modules are tested, they can be integrated so that they reference each other as detailed in the module setups. The computer should still be the source of command inputs through the Command Handling module. Each command should be input through the computer and have the functionality verified. After this, many commands can be input at once to test if command oversaturation is an issue.

Fault Detection The fault detection test is a more specific module integration test. The computer should have control of the Fault Detection module inputs. Through the test, different errors are input to , make sure that the input faults are noted, move through the Fault Logging module, and transferred with the data through data transmission. This is not testing the system's fault mitigation ability (please see the electronics software section for that), but is instead focused on informing the user of a fault.

Sample Rate The sample rate test checks that the sample rate remains as the required 50 Hz under a maximum command load. This requires the computer to deploy thermal control, detect faults in the data, and receive all other possible commands at the same time.

Main Loop Simulation The software main loop simulation test is run purely on an external computer program, capable of performing the necessary software related actions NanoSAM must achieve. The simulation will be run with stubbed inputs, in the place of measurements, so that the outputs of each module can be verified. As with the flight routine, the software will start with the identification of the system's location with respect to the data collection window. During the standby phase, the memory scrubbing, housekeeping, and command handling modules' outputs must be verified. The data collection phase will allow verification of window timing, data processing, memory handling outputs. The team will ensure each module behaves as expected, with respect to the stubbed inputs, through the inspection of their processes. Fig. 33 illustrates the flow for this simulation test.

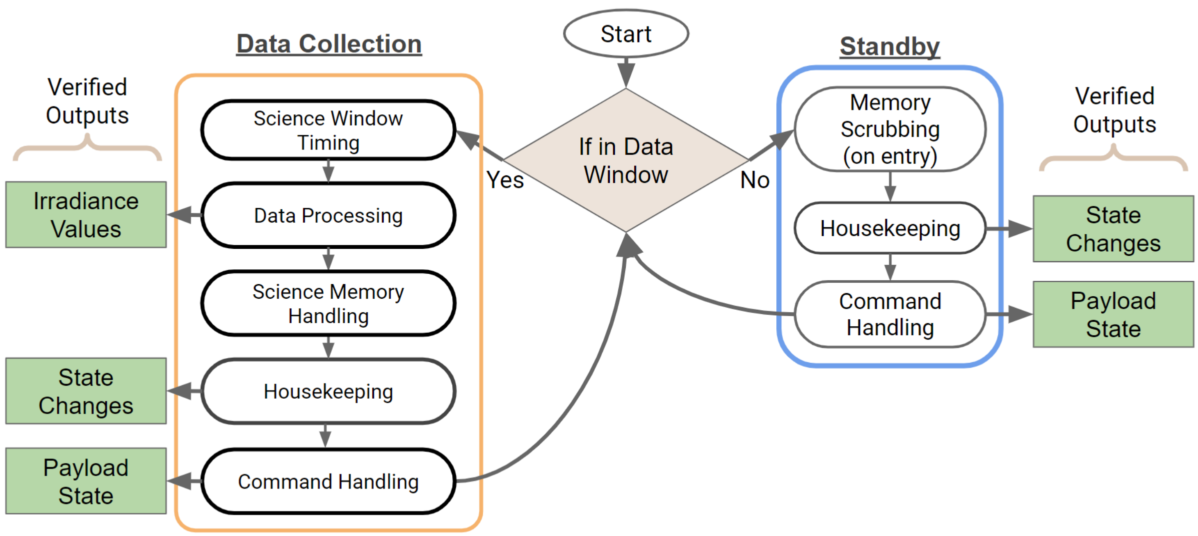

Fig. 33 Main Loop Sim flowchart

3. Electronics and Software

Baseline data collection The purpose behind this test is to ensure that the electronic subsystem captures and communicates conditioned data through the serial micro-controller connection. The Teensy micro-controller will be configured beforehand with the Arduino IDE software, including an add on made specifically for the Teensy. The team will be inspecting the resulting data and check for a sampling rate of 50Hz, a processing rate greater than 50Hz, 10 bit data resolution, storage capacity during an orbital period, and the collection of system state data (power, temperature, storage) for monitoring. These correspond, respectively, to the following requirements: 1.1.1, 1.1.1.1, 1.1.2, 1.1.3, 1.4.1, 1.4.2, 1.4.3. In order to conduct this test, the electronics subsystem will be connected to an external 12V power supply and the micro-controller serial port will be connected to any laptop program capable of data acquisition. Furthermore, the test must be conducted in an ESD-safe workspace. Flashlights can be used to create different photodiode inputs, yielding a data-set with a range of intensities, and allowing for a basic photodiode functionality check. Fig. 34 illustrates the setup of this test.

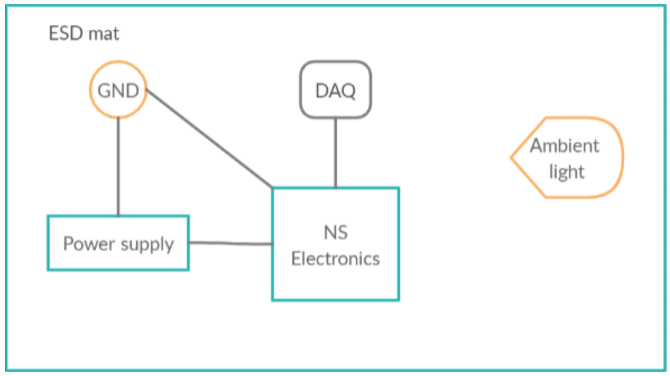

Fig. 34 Data collection test setup

Error Detection and Correction (EDAC) Test The EDAC test is a software subsystem test that will be run on a development computer emulating the Teensy. It will consist of the EDAC module and a testing function. The testing function will inject known errors into the flash memory, and then the EDAC module will be activated. The EDAC module will run as usual, carrying out the same processes that it would carry out during a full science run. The testing function will check the contents of the memory after the EDAC module runs. If the contents of the memory match the expected contents, then the test will be considered successful. If the contents do not match, the the EDAC module did not properly correct the error. Observing the contents of the memory will allow the development team to discover the source of the inaccuracy.

The types of errors injected into the memory are crucial to the success of this test. Hamming codes employed by the EDAC module can correct single bit errors and detect errors up to 2 bits in size. Therefore, the types of known errors should be both single and two-bit errors. These errors should also be crafted to cover outlier cases, such as neighboring errors and errors in the first and last bit of the dataset. Running this test for a wide array of initial conditions and injected errors will raise the confidence that the test accounted for scenarios that are representative of what we will see on orbit.

The method of injecting errors is built into C++ in the form of memory address indexing. The bits of each message can be accessed individually using the addressing operator, so injecting an error simply consists of changing the value of a bit at a known address within the dataset in the memory of the dev computer. Then, when the EDAC module scans all bits located within this dataset address range, it will (if functioning properly) realize that one or two of these bits do not align with the Hamming code at the end of the dataset. In the case of a single bit error, the EDAC module will then revert the value of the flipped bit back to what it was before the error was injected. This result can then be verified by the testing function when it re-scans the dataset address range after the EDAC module has completed its operation. In the case of a two-bit error, the test will be a success if the module flags the dataset as containing two errors. However, the Hamming codes are not capable of correcting these errors, so that will conclude the test in the two-bit case.

Upon passing the functionality test, the final step will just be to make sure the EDAC modules can run fast enough to satisfy all science timing requirements. This means that if EDAC is active during the science data window, the module must not delay the timing of science measurements to less than 50 Hz.

C. System Level Tests

1. Thermal test

The test setup for the thermal test is as shown in Fig. 35, in which the payload is placed in a thermal oven with electronics connected to an external laptop through the walls of the chamber. Equipment necessary for this test included the NanoSAM II payload, a laptop, a temperature resistant connector between the payload and laptop, a thermal test chamber, and port plugs which were provided by the testing facilities. Due to time constraints at the facility and room access setbacks, the test ran for only 2 hours. This allowed for one heat cycle between -45°C and 60°C. The test started at room temperature before driving the chamber down to -45°C first. This is past the thermal requirements of the system and tested heater functionality. After rising back up to -20 °C, the low end of the thermal requirement, the chamber stayed at that temperature to let the payload attempt to reach equilibrium. Then, the chamber rose in temperature to 60 °C and again paused for equilibrium. Finally, the chamber was returned to room temperature and the system was left to cool off. Overall, the goal of this test was to examine the effectiveness of the heater and associated thermal isolation on the optics bench and also verify that the electronics would function throughout the allowable temperature range of -20 °C to 60 °C. The heater was set to turn on when temperatures measured on the optics bench dropped below -10 °C and then turned off when the temperature of the optics bench rose to 20 °C. Data was collected from an optics temperature sensor located on the optics bench, and thermistors on the analog electronics board, and the digital electronics board throughout the test.

Fig. 35 Thermal Test Set Up

Fig. 36 shows the resulting temperature plots over the course of the thermal cycle performed. The shaded region shows where the heater resistor turned on in response to dropping below -10 °C as expected and turned off as the system rose above 20 °C also as expected. It's also important to note the separation and reduced slope of the optics bench temperature curve throughout the thermal cycle in comparison to the electronics boards and chamber temperature. This slope gives verification that the optics bench thermal isolation was functional even in an environment with convection. Finally, no electronics components failed during this test, which verified the electronics subsystem requirement of functionality between -20 °C and 50 °C. Although the electronics functioned throughout the test, whole system functionality could not be determined as the photodiode as the test design did not include the collection of photodiode data. The software was capable of collecting photodiode data at this point and it was a mistake on the part of test design to not collect that data. Therefore, while this test did not verify requirements 5.2.2 or the overall requirement of functionality in an vacuum temperature range of -120 to 120 °C, it did verify functionality of the heater as defined in requirement 5.2.1. Overall, poor test design that didn't call for photodiode data collection in the thermal chamber despite system capability combined with a lack of time caused the team to fail to verify thermal requirements and also prevented the team from verifying photodiode behaviour in an environment with rapid temperature change.]

Future testing would need to include 3 key things for system verification and validation beyond what was attempted by this years team. Firsty, more temperature sensors on the optics bench and particularly around the photodiode would be useful for testing a higher resoltion model preferably developed in Thermal Desktop. Secondly, the test should be run while collecting photodiode data, this way the thermal corrections being done by software would be able to be verified through the data and potential shortcoming in the correction system would be able to more easily be identified and fixed if needed. Lastly, the thermal test should be run to allow the NanoSAM payload to reach an equilibrium temperature to further verify thermal outputs from the electronics boards and resistor heater.

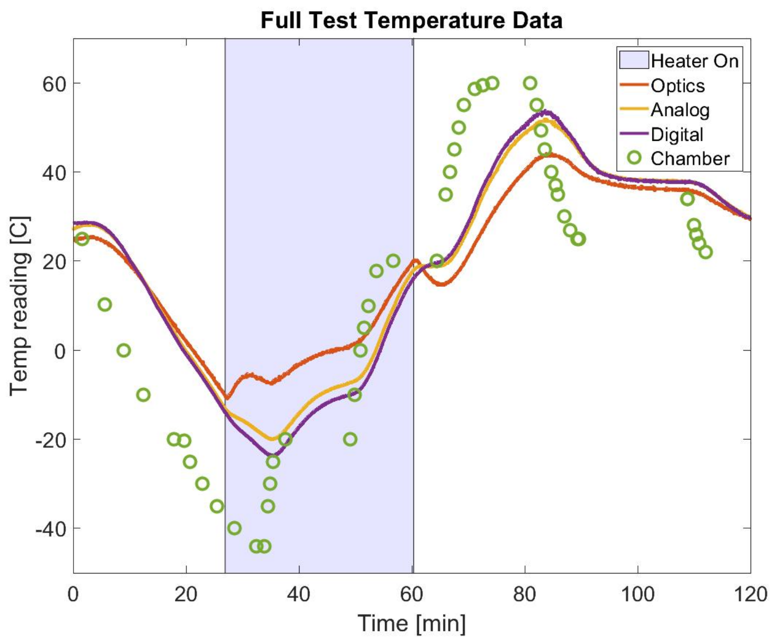

Fig. 36 Thermal Test Results

Thermal Model Verification The thermal model was not able to be directly verified from the thermal test because the system wasn't tested in a vacuum environment similar to the model or with similar solar and albedo heating conditions that result in certain parts of the satellite warming or cooling off quicker. Therefore, even if the model were to be changed to model air conditions like in the thermal test, useful verification of the original thermal model would be lost. However, using analysis methods involving transforming Newton's Law of Cooling into a form for transient temperature change (shown in Eq. 22 it was possible to get an approximation for the equilibrium temperatures of the electronics boards as well as the effective heat outputs of the resistor heater itself.

$$T(t) = T_{env} + (T(0) - T_{env})e^{-t/\tau} \tag{22}$$

In this equation τ represents the time constant of the system, T_{env} represents the environmental temperature, and T(t) is the temperature defined at a particular time. For this test, the heater is adding additional heat to the system so the system will actually trend toward being above T_{env} and as such instead of strictly using this equation, the general form is used to develop a line of best fit as shown in Eq. 23.

$$T(t) = a + be^{-ct} \tag{23}$$

Using the MatLab fit toolbox, the following fits were determined for the heater and electronics boards at an equilibrium temperature of -20 C and 60 C as shown in Fig. 37-39.

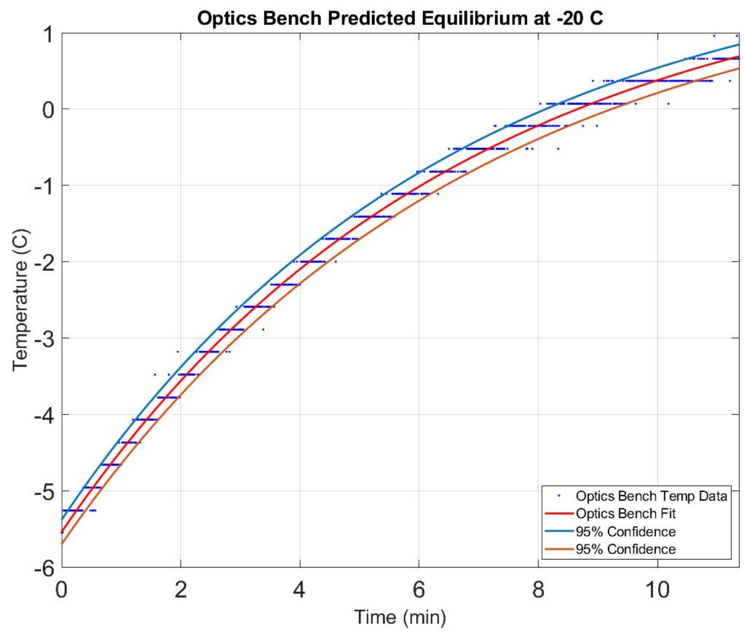

Fig. 37 Fitting Optics Bench Temperature Data

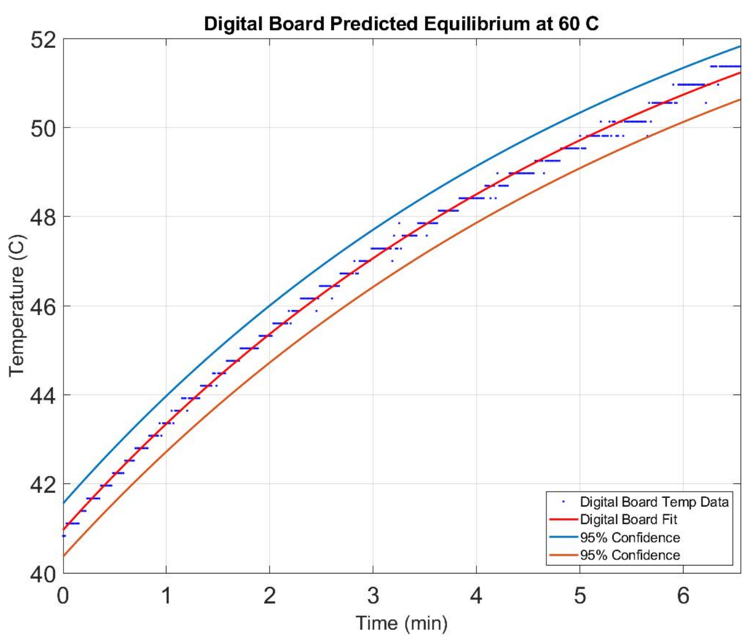

Fig. 38 Fitting Digital Board Temperature Data

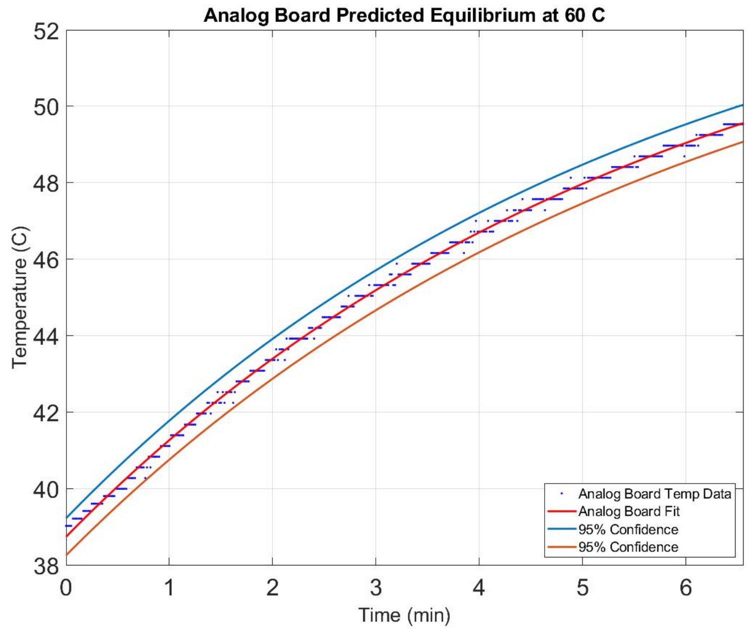

Fig. 39 Fitting Analog Board Temperature Data

The data shown in Fig. 37-39 shows 95% confidence error bounds that assume an inherent stability to the measurement. However, it is apparent this isn't the case due to the poor resolution observed in the experimental data shown (appears "step-like"). Linearizing Eq. 24 by taking the natural log of both sides allows for the ability to account for the error in measurements. The issue with this method is that there is no way to distinguish the coefficients 'a' and 'b' as they will appear combined as the intersect of the linear fit.

$$ln(T(t)) = ln(ab) + ct \tag{24}$$

Due to the fact that both the variables 'a' and 'b' are dependent on the equilibrium temperature of the system which is the primary unknown, further testing that allows the system to reach thermal equilibrium would be required to determine this value and associated error with more confidence. Additionally, the MatLab curve fitting toolbox does not include consideration for measurement errors, further suggesting that additional testing would be required to get a more exact estimation of the error associated with the calculated equilibrium temperatures shown directly in Tab. 16.

Due to the temperature equilibriums for the electronics boards being observed below the chamber temperature (shown in Tab.16) it was approximated that the electronics boards out negligible power (0 W). In order to determine the heater output on the optics bench, an additional thermal model was created using the chamber conditions and with a hole cut in the side wall to give an estimation of the actual structure used during the test. The model was iterated using the temperature bounds estimated by the lines of best fit shown in Fig. 37 to obtain an approximate heater output listed in Tab. 16.

Item	Chamber Temperature (°C)	Equilibrium Temp Calculated (°C)	Approximate Heat Output (W)
Optics Bench	-20	2.06 ± 0.09	2.4 ± 0.1
Digital Board	60	56.27 ± 0.07	0
Analog Board	60	54.24 ± 0.03	0

Table 16 Extrapolated results from Thermal Test Data

Applying these results by removing the heat output from the electronics boards and changing the heater output of the Solidworks/MatLab combined model gives the following thermal cycle under average orbital thermal conditions (defined more clearly in the Appendix C discussion of the solidworks model) in Fig. 40.

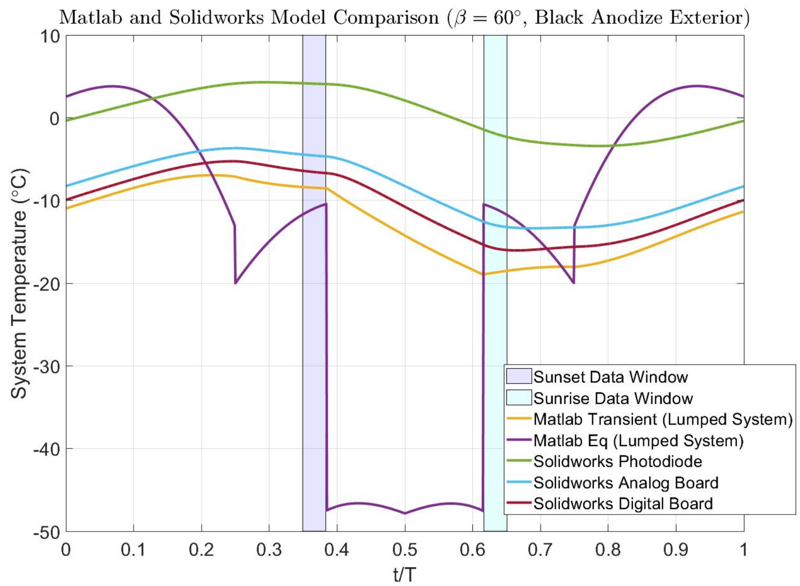

Fig. 40 Updated Model Output

As shown above, the electronics boards and optics bench stay above the minimum allowable temperature of -20 °C despite the electronics boards being estimated to have no heat output. It's also very important to note that it's already expected that the thermal model under-approximates the actual amount of heat entering the system due to the use of area factors. Area factors don't account for additional energy that may reach the satellite due to how close the CubeSat is to the Earth because the Earth is essentially treated as a point radiation source with this model. Overall, this suggests that if the heater were attached more rigorously using a thermally conductive adhesive as opposed to tape (which may have contributed to some power loss due to insufficient attachment to the bench) that the satellite would likely be able to meet it's temperature requirements in a space environment.

Furthermore, when examining the data windows as shown in Tab. 17, it can be seen that the power output from the heater has only not significantly increased or decreased the temperature ranges over the data window ($/pm$ 0.1 °C as compared to the previous iteration listed in Appendix C). Further suggesting that the current heater would be satisfactory for limiting the temperature change during the data windows.

Data Window	Max $\Delta T (K)$	**time (s)**
Sunset	0.10	192.6
Sunrise	0.88	192.6

Table 17 Temperature Change of the Photodiode over Sunset/Sunrise Data Windows Using Updated Data

In conclusion, it is highly recommended a future team perform further thermal testing in a vacuum environment in order to get a data set better suited for model verification of space environmental conditions. It is also highly recommended that future teams pursue using software such as 'Thermal Desktop' that the current team was not able to procure access to due to licensing limitations. To avoid issues with procurement, it is recommended the team get into contact with the Aerospace or other departments to attempt to obtain a license for use as early into the project continuation as possible. Thermal Desktop should be able to provide better insight into the expected thermal inputs from the Earth as well as provide a more rigorous program than SolidWorks to perform modeling.

2. Vibration Test

The vibration test was used to verify that there were no resonant frequencies below 100Hz to verify requirement 5.1.2 by a sine sweep survey along three orthogonal axis from 0-2000Hz. This test was performed with unpopulated electronics boards and a simulator optics bench, which included a photodiode block simulator and an aluminum cylinder instead of the OAP.

This test was performed at Altius Space Systems and vibe test hardware was designed with advice from Keith Drake at Altius. Models predicted regions of most displacement at the electronics boards and at the top of the system. To measure these displacements, two three axis accelerometers were attached to the payload at these locations, as seen in Fig. 41 below.

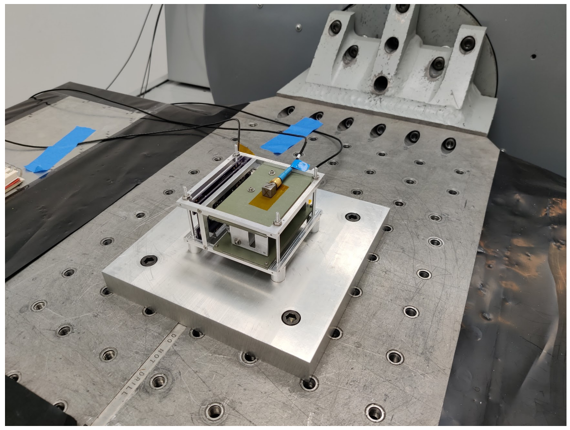

Fig. 41 Experimental Vibrational Test Setup

A third accelerometer was placed on the large baseplate for control feedback, and to generate the control data for the G/G plots, which measured the acceleration in the system relative to the baseplate. The G/G plots are generated by taking the acceleration measured at the other two sensors and dividing it by the acceleration measured at the control sensor. These plots show peaks where the sensors at either the electronics board or the top of the system are experiencing much larger acceleration than the input, and therefore likely corresponds to a resonant frequency. The main peaks from each axis are reported below in Tab. 18, synthesized from data in Appendix XV.A.

Axis	G/G Value	Frequency (Hz)
X	27.36 (at top of payload)	493.3
X	11.04 (at PCB)	901.1
Y	24.96 (at top of payload)	445.5
Y	9.64 (at top of payload)	621.4
Z	19.35 (at top of payload)	619.5

Table 18 Peaks from Vibrational Test

Here, the X axis is along the incoming light direction, Y ix normal to the electronics boards, and Z is orthogonal to X and Y (i.e. "up" as seen in Fig. 41). The results from Tab. 18 shows that there are no resonant frequencies below 100Hz, and so functional requirement 5.1.2 is met.

In comparison to predictive models generated in Solidworks and ANSYS, the experimental resonant frequencies are considerably lower. Before the vibration test was conducted, the following models were constructed in Solidworks and ANSYS, respectively.

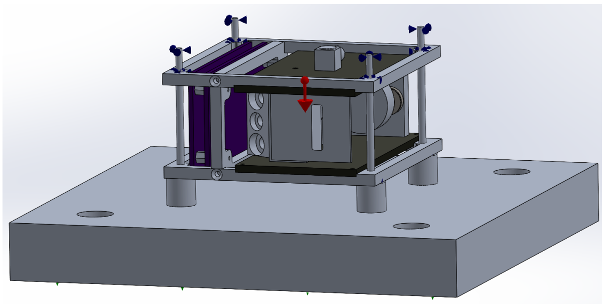

Fig. 42   Solidworks Vibration Test FEA Model

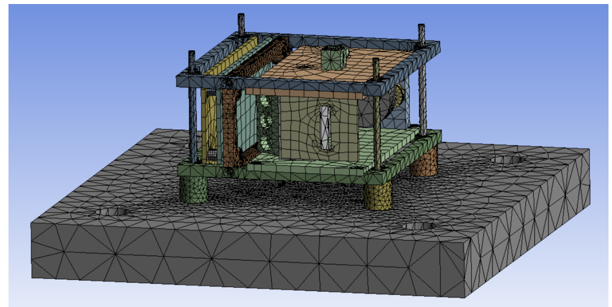

Fig. 43   ANSYS Vibration Test FEA Model

These models were constructed such that the bottom of the baseplate was fixed relative to the rest of the geometry, which corresponds to the baseplate being ridgidly fixed to the vibration test table. The first five predicted resonant frequencies are as follows:

Mode	Solidworks	ANSYS
1	1069 Hz	840 Hz
2	1233 Hz	1033 Hz
3	1306 Hz	1139 Hz
4	1328 Hz	1272 Hz
5	1871 Hz	1563 Hz

Table 19   Fixed Baseplate Mode Results

The first two modes predicted in both softwares are plate modes experienced by the electronics boards. The third mode is also predicted by both to be a whole body vibration, primarily in the Z direction. These two models are reasonable close together, and the discrepancies could be explained by slightly different material models in Soldiworks/ANSYS. After the vibration test was conducted, the significant discrepancies between the models and the results required additional analysis. The current hypothesis is that the Solidworks and ANSYS models above do not accurately represent some of the real world attachment methods. For instance, the place where the standoffs connect with the baseplate is modeled as completely fixed and rigid, whereas in reality, there may actually be some amount of room for displacement in these connections. Idealizations of this nature that assume rigid connections stiffen the model and raise the resulting modes. In an attempt to better match the experimental data, a model was constructed where three standoffs are elastically supported, and the fourth is fixed, shown in Fig. 44 below.

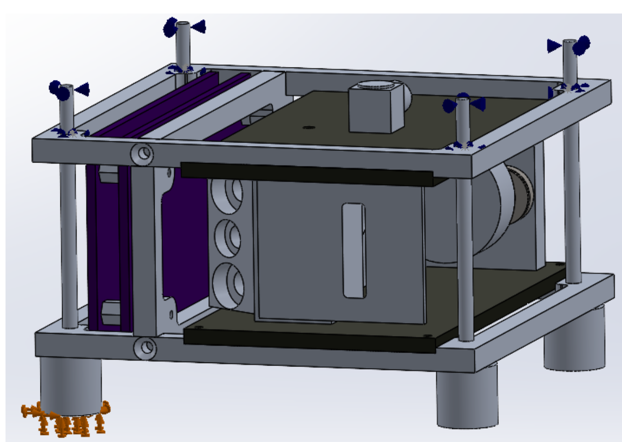

Fig. 44   Solidworks Elastic Fixture Vibration Test FEA Model

Adjusting the stiffness parameters on the model suggests that this might be a better way to match the experimental results, shown in the following table (Tab. 20). The parameters used to obtain this data was a normal stiffness of 10,000,000 N/m and a shear stiffness of 3,000,000 N/m across the three contacts. A more robust determination of these values might involve computing the actual stiffness of the screws used to hold the standoffs in place, and then removing some percentage due to allowable movement between the standoffs, the screws, and the baseplate.

Mode	**Solidworks**
1	487 Hz
2	655 Hz
3	852 Hz
4	1035 Hz
5	1111 Hz

Table 20 Elastic Fixture Mode Results

Overall, the vibration model is extremely complex and realistic interactions between the test article and the vibration table are difficult to model. Future teams may want to run several vibration tests, building up from smaller sections of the model, validating those, and then moving on and increasing complexity, rather than simply testing the entire system at once.

3. Regulated Light Source

The regulated light test incorporates the entire system to ensure correct system data collection when fully integrated. This functionality is dependent on accurate irradiance data being collected from a light source. Accurate data collection is dependent on multiple parameters. This includes irradiance values comparable to the known values of a light source, the correct wavelengths being collected, only relevant data being stored, and photodiode noise being at a manageable level. This test is not concerned with requirements such as sample rate, which are tested in the electronics subsystem tests. Comparing the collected irradiance to the expected irradiance from the light source will determine the accuracy and uncertainty of the system, as well as verify correct wavelength filtering. Relevant data storage means that data will only be stored once the irradiance dips below a certain level. Dark current noise is a predicted value, which can be compared to the measurements made with a covered photodiode.

To test these system attributes, the system is set up as seen in Fig. 45, with the payload being connected to an external computer and power supply and set up on a stable surface across from a light source. To measure the dark current, irradiance measurements should be collected after covering up the photodiode, aperture, and after making the room as dark as possible. Once this is done and the photodiode and aperture are uncovered, the regulated light source can be used. This will be set up directly across from the aperture and the distance between the two will be measured. The lightbulb should have a known temperature value. After setting up the system, irradiance measurements can be taken. Afterwards, a variable light source will be used to verify where the system starts and stops data collection.

The most essential measurements made are the system's measurements of irradiance. Problems with this may occur through different subsystems, but these subsystems are all tested individually before this test is conducted. Although provided through data sheets or production information, the light bulb operation temperature is also an important value. This will be used with Planck's Law to determine the expected irradiance measurement. If this is not accurate enough, a spectrometer may be needed for a more precise estimation.

This test failed when conducted on the completed system. While light could be channeled through the pinhole and into the photodiode when the system was seperated, integration of the two subsystems showed that the optics failed to channel light correctly into the photodiode. The alignment of the system was not sufficient to collect data and test the system's data accuracy. This proved to be the problem with the system as data also could not be collected when the light source was the sun instead of LEDs and a lightbulb.

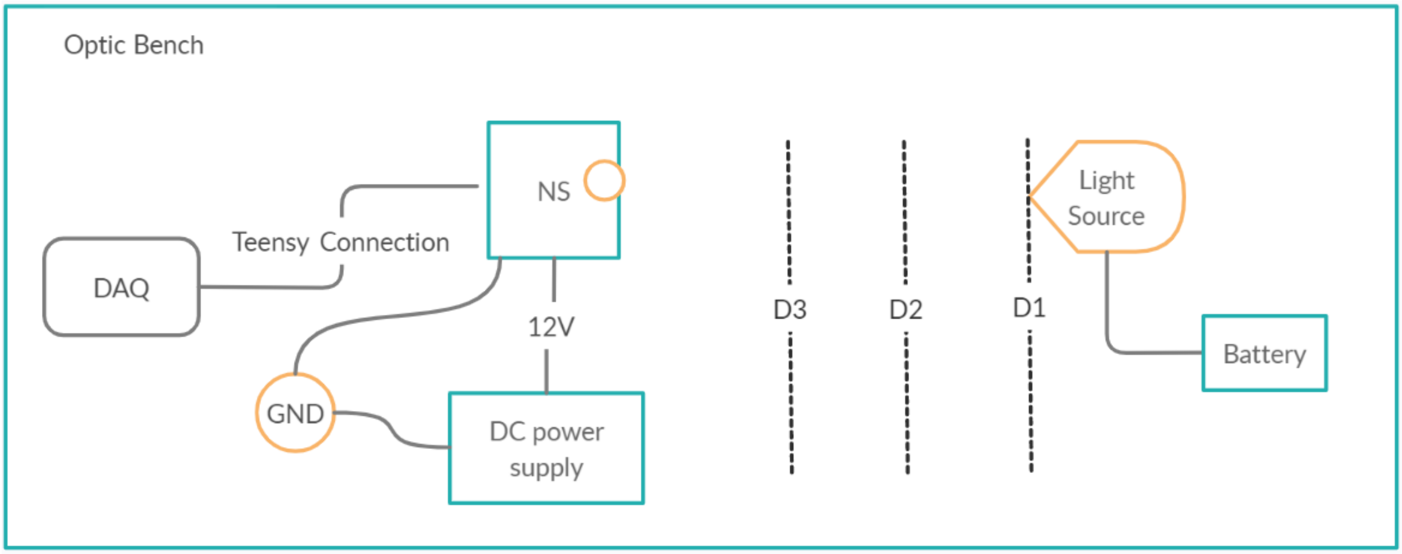

Fig. 45 Regulated light test setup

4. Solar Attenuation

The final comprehensive test to be performed is the solar attenuation, this is the method through which the NanoSAM system will collect mission data. This test will ensure that all of the subsystems interface properly together, and that the expected data is captured, transferred to a laptop, and stored for processing.

The physical components needed for this test consist of the fully integrated NanoSAM II hardware, a laptop, the micro-USB connector, the solar tracker and associated components (batteries and mount), and a power source (either portable or wired by extension). No test facility is needed for this test, because the test must be run outside. Like the solar tracking test, the test must be run on a sunny day.

The aligned optical subsystem must be interfacing with the electronics subsystem through the photodiode, and both need to be fully integrated within the structure subsystem. This is both to prove that NanoSAM II can meet data capture functional requirements within the .5U size requirement, and to keep the optical system clean from dust particles in the air. These three subsystems will transfer data from the electronics system to the laptop with a USB drive, and then accompanying software will process and store the data on the laptop.

Finally, the powered payload needs to be attached to the solar tracker. The solar tracker will then be turned on and aligned to the sun, so that it can be pointed at the sun for the duration of the test.

Once the systems have been integrated and connected to the power source, and the payload has been aligned to point at the sun, the test can be run. A diagram of the test can be seen below in Fig. 46.

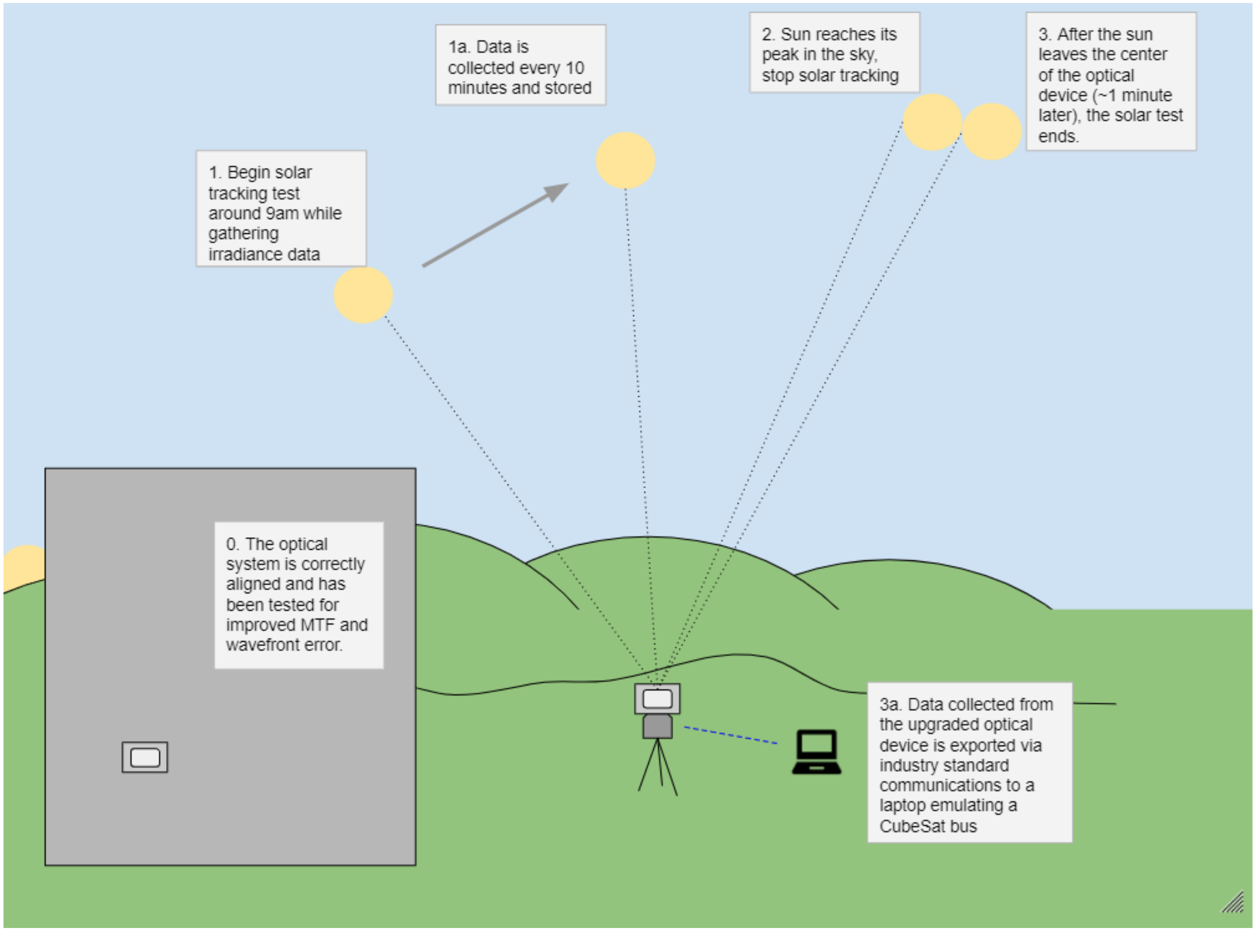

Fig. 46 Solar Attenuation Diagram

Shown in Fig. 46, the solar attenuation test will begin at about 9am. The exact time will be determined by the date of the test, as will be explained below. Once the test has started, the system will take solar irradiance data every 10 minutes for about 5 minutes until the sun reaches it's peak in the sky. The exact time that this happens will also be determined by the day that the test is run, but the time is approximated to be around 1am. Once the sun has reached its peak, the solar tracker will be turned off. This will allow the sun to leave the field of view of the payload. Once the sun has left the field of view, the test will be ended.

During the test, data is collected every 10 minutes for 5 minutes because this will lead to an amount of data that is similar to that collected over a day by NanoSAM in orbit, proving the memory capacity. Once solar irradiance data has been gathered, it will be used to make a Langley plot. A Langley plot is a graph of irradiance over a range of airmass values. An example plot, made with solar irradiance data taken from the sun photometer in CU Boulder's skywatch observatory on November 11th, 2020 is shown below in Fig. 47.

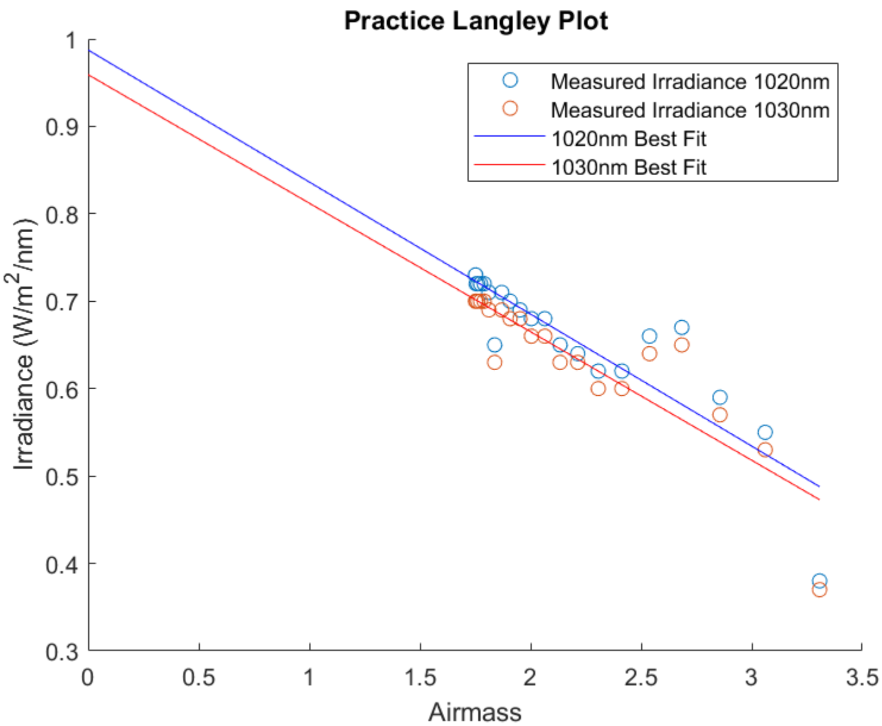

Fig. 47 Example Langley Plot

The airmass, shown on the x-axis of Fig. 47, represents the interference in the solar irradiance value due to Earth's atmosphere. Airmass is a dimensionless function of solar zenith angle, defined here as:

$$Airmass = sec(z) \tag{25}$$

In equation 25, z represents the solar zenith angle. The airmass value is scaled so that if the viewer is looking straight up at the sun through the atmosphere, there is a airmass value of 1. This occurs at a zenith angle of zero, and is the minimum possible airmass value from Earth's surface. As the viewer, or in this case NanoSAM, follows the sun through higher zenith values, the airmass gets higher.

The goal of the Langley plot is to extraploate the irradiance value at zero airmass, in order to model the irradiance value that will be received by NanoSAM when outside of Earth's atmosphere. To do this accurately, data needs to be taken at the maximum possible range of airmass values. The minimum irradiance value occurs at the sun's peak in the sky. The zenith angle at which this occurs will change over the course of the year as the Earth moves in relation to the sun, but the lowest value possible will likely be from about 1.4 to 1.7. Additionally, Eq. 25 is an approximation that does not take into account the curvature of the Earth. Error analysis done on this function revealed that the error of this equation starts at zero at a zenith angle of zero, and doesn't increase to 1% until a zenith angle of about 74° degrees is reached. At this point, the airmass is about 3.6. Therefore, in order to ensure that accurate data can be taken, the goal of the plot will be to have airmass values ranging from the minimum value possible up to an airmass of around 3. An airmass of 3 occurs at a zenith angle of 70.53°. The time of day at which this occurs will be determined based on the day of the test, and this is the time at which the test will start.

Once the Langley plot has been made with the experimental data, the extrapolated zero airmass value will be compared to the expected zero airmass value in order to determine the error of the overall system, and ensure that data is being collected at the correct wavelength. The expected zero airmass value is $.6977W/m^2/nm$. This value has been determined by running practice Langley plots with the CU sun photometer data, and will continue to be refined throughout second semester as more Langley plots are created.

VI. Risk Assessment and Mitigation

Authors: Jashan Chopra, Jackson Kistler, David Perkins, Daniel Wagner, Daniel Barth, Emma Tomlinson, Donavon Schroeder, Ryan Smithers, Abby Hause

Risk analyses have been carried out to reduce the likelihood and severity of various failures that the team may encounter while creating and testing NanoSAM II. The sections below walk through key risks and what steps the team is taking to mitigate these risks.

A. Structures

The structure has risks associated with it that would keep it from performing optimally. One of the more obvious risks is that the structure would not be able to be manufactured. The custom parts of the structure will be composed of 6061 aluminum and FRP (fiberglass-reinforced plastic). Therefore the main concerns were that the aluminum would not be able to be milled and the FRP would be too brittle to work with at its required thickness. The risk of not being able to mill the aluminum was mitigated by scheduling multiple meetings with Matt Rhode during the semester to go through each structural component individually. Any part that was deemed not fully manufacturable during these meetings was altered so that it would then satisfy the milling requirements. Most of the changes made were either eliminating or altering inner corners that would have to be cut. The problem with these cuts was that the milling tool would not be able to cut them at an angle that would allow for sharp corners. These cuts were removed by altering the rest of the design slightly. The other manufacturing concern was that the FRP would be difficult to work with. The original thickness of the FRP was 2mm. Ordering it at this thickness was explored but it proved difficult to find candidates with the required tolerances that would ship in a timely manner. This was mitigated by increasing the thickness of the FRP sheets in the design by decreasing the thickness of part of the structural rib. Doing this allows the FRP to be ordered from McMaster Carr. This way, the only cuts that will need to be done on the FRP can be done with the laser cutter and will be much less likely to shatter the FRP.

The next risk that was considered was that the structure would fail vibrational requirements. In order for the payload to withstand launch, QB50 requirements recommend that the structure have no resonant frequencies below 100 Hz. To verify that the system could withstand this vibrational requirement, Solidworks was first used to conduct a study on the vibrational modes of the payload. A vibrational test will also be conducted later once the structure has been constructed. To maximize accuracy, the Solidworks model was set up to mimic the actual vibrational test as closely as possible. Although this year's team will not be designing a bus interface for the payload, we have chosen the ISIS 3U cubeSAT structure to be used in our vibrational test models as a standard industry bus structure. Fig. 48 shows the set up of the model in Solidworks where the structure is connected to a fixed plate that represents the vibrational table used in actual testing. The structure is connected to this table in the same way that it would be connected to the bus, which is on rails that run through its four corners. Using finite element analysis with numerous boundary conditions, the Solidworks model yielded a lowest resonant frequency of 906 Hz, which is well above the 100 Hz requirement.

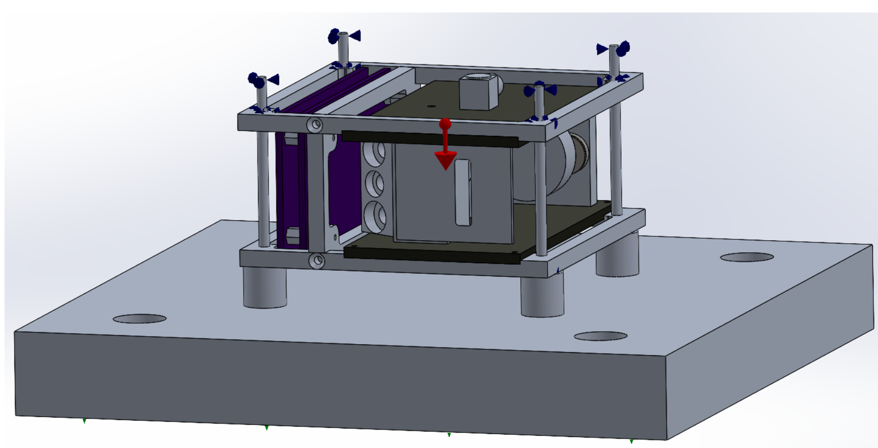

Fig. 48 Solidworks Vibrational Model Set Up

Another risk that must be considered is that the structure may fail thermal requirements. This requirement is important due to temperature sensitivity in the optics and photodiode. A few approaches were implemented to mitigate this. The first was choosing to construct the structure and optic out of 6061 aluminum whenever possible so that the components would expand and contract at the same rate in response to thermal changes. The next design choice that was made to mitigate thermal influence was thermally isolating the optic by adding FRP sheets on either side of it. Because of FRP's low thermal conductivity, it acts as a good isolator and makes any temperature changes less drastic around the optic. The final mitigation strategy that was employed is the inclusion of a 3 watt heater that will bring the temperature inside the structure up if it starts to drop. With these mitigation techniques in place the payload is in good condition to resist temperature changes that would affect the overall mission quality.

The final major structural risk is that the structure would not be able to be integrated with the separate optical and electronics designs. To ensure that this does not happen, the three technical design subteams are frequently in communication. Our customer is also very experienced with working with optics, so to ensure that the structure will fulfill optical requirements, frequent reviews with the customer are put in place. Reviews are also conducted with the electronics lead on the team to ensure that the electronics circuit boards will fit within the structure and the mounting system will not interfere with the electronics on the board. With these frequent checks in place, the team is confident that the each individual subsystem will be able to successful interface with the rest of the overall system.

B. Electronics

There are a number of risks associated with the electronics system that can prevent proper operation. The first are concerns with temperature effects on components over the expected operational range of $-30°C$-$30°C$. Across the board the temperature effects on components proves to be a negligible risk, except when it comes to the photodiode. For a comprehensive overview of temperature effects on the components, see Appendix D. Of particular concern is that the responsivity of the photodiode changes with temperature. At the expected 1020 nanometers we see a 0.6% error in the responsivity per kelvin. The error is linear, so we can correct this in software by associating a temperature measurement with the science measurement for each data point [57]. Due to the linearity, this will result in a 0.6% error in voltage per kelvin, or a 393 LSB error. We expect the minimum temperature change during the data collection to be around 0.28 kelvin. Although the accuracy of the LMT86LP is a maximum of 0.4°C, by using the same comparison to calibration technique for data we can directly look at the analog change in voltage output of the LMT86LP between science measurements. This analog signal will be sampled with the microcontroller ADC, which with 12 bits has a 0.8mV LSB resulting in a 0.043°C resolution, allowing us to correct this small temperature change and maintain our signal to noise ratio requirement. As the temperature of the photodiode decreases during both the sunrise and sunset events, the responsivity will decrease which will lower the current output and thus the measured voltage. Therfore, we add a correction factor corresponding to 0.6% of the difference in temperature measurements between the calibration point and the data measurement point, as shown below in Eq. 26. We also note in this equation the discussion point of a calibration measurement account for other sources of constant error. By subtracting the calibration measurement we are account for the voltage drop across the protective zener diode, the ADC offset error, and the mostly constant dark current. Although the dark current does increase with temperature, the increase is negligible for the space temperature change experienced during data collection [57].

$$V_{data} = V_{ADC} + 0.006(\mid V_{T\,meas} - V_{T\,cali} \mid) - V_{cali} \tag{26}$$

Overvoltaging pins, either from testing or data collection is another concern. The output of the AD8671 is capped by its voltage input, which is 5V. However, the analog to digital converter can accept no more than ±0.3V on the 3.3V supply it runs on. A 3.3V zener diode to ground is thus placed on the output of the AD8671 to clamp the input given more than 3.3V from any light source present. The zener diode does cause a voltage drop in the primary science data line, however, because this drop is constant over the short data measurement period, it is corrected for by the calibration measurement. Additionally, the optics bench resistor heater supplied by the bus voltage has a transient voltage suppression diode to prevent against unregulated bus supply. Thus, all inputs to the system are protected against overvoltaging, with particular attention provided to the ADC and Teensy 4.0 inputs [36]. Even with overvoltaging protection there are other possibilities that can lead to a failure to collect science data, which is the core requirement of the electronics system. The photodiode can over saturate and exceed the common mode input range of the AD8671, however it was discussed in the detailed design section that this is protected by the photodiode reverse biasing in photoconductive mode. The ADC itself does have an offset error of enough LSB to reduce our signal to noise ratio, however, this constant offset error is corrected through the comparison to the calibration measurements. Finally, a second backup trace runs from the AD8671 directly to the Teensy 4.0 onboard 12 bit ADC, which will still meet our signal to noise ratio requirements.

Due to the signal to noise ratio requirement, particular attention is placed on potential sources of noise in the system.

Although it is impossible to account for everything, using industry recommended practices in design, routing, and manufacturing can help us reduce any unexpected noise sources. The proper configuration for a master SPI device with three slaves is shown below in Fig. 49. We note here that standard 10 kohm pull up resistors are used on the chip select (CS) lines to keep them asserted high when not in use [56]. Because only one CS line can be pulled low at a time, any floating CS lines can result in noise, or a full blown error. We also use series 50 ohm resistors on the slave device master in slave out (MISO) lines and the master device clock line. These series resistors help to prevent any line reflections which can cause the slave devices to see a double clock edge and get out of sync, and also prevent cross talk between the SPI signals [55]. This is shown in Fig. 50. Noise can also come from high frequency signals, however, none of our key signals are high frequency. The internal operations of each voltage regulator does use high frequency switching signals, which is why care was taken to isolate the regulators on the left side of each board and also to use proper routing techniques as specified by the datasheets. The only other high frequency connection is the pulse width modulation signal that switches the resistor heater MOSFET. Noise will be prevented here by routing this signal on the ground plane away from any science signals. Additionally, the connection off board will be made using shielded wire to prevent creating any antenna like noise environments inside the CubeSat. We also use a signal-ground-signal routing strategy with the individual connector pins to isolate signals from noise. Additionally, there are two large decoupling capacitors on either side of the board connector to further reduce noise. With the low frequency DC signals we are passing through the board connector, we are not worried about signal noise in the form of crosstalk, propagation delay, return loss, insertion loss, or rise time degradation in the board to board connector [44]. Lastly, we expect overheating of the board not to be an issue. Similar CubeSat projects such as the miniature x-ray solar spectrometer 3U CubeSat have similar power requirements and also relied on conduction to dissipate heat into the CubeSat bus, which then radiates outwards into space [49]. No single component generates a large amount of heat, mainly because the voltage regulators are quite efficient, so we expect heat not to pool on the board. This concludes the discussion on electronics risk.

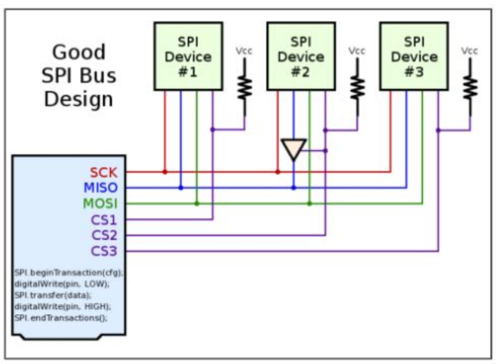

Fig. 49 SPI Pull Up Resistors & Configuration

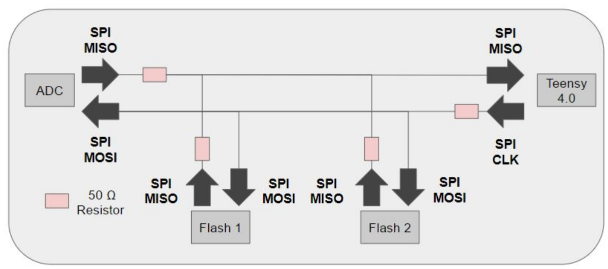

Fig. 50 SPI Series Resistors to Prevent Line Reflections

C. Optics

The risk of NanoSAM II not being aligned due to lack of facility access due to COVID-19 ended up being a legitimate problem. By the time the hardware had been manufactured, Meadowlark was only willing to allow the optics team to come in for two more alignment sessions. This left a total of four hours for the optics team to attempt to align the optical system. Additionally, due to COVID restrictions, only three people were allowed to attend each session, meaning that at least one person had to participate virtually, which reduced their capability to help. Two measures were implemented to allow the optics team to maximize the time at Meadowlark. The first was the thorough development of the alignment procedure ahead of time, so that the optics team could move quickly betwen predetermined steps. The second was the purchase of an optical breadboard, shown below in Fig. 51.

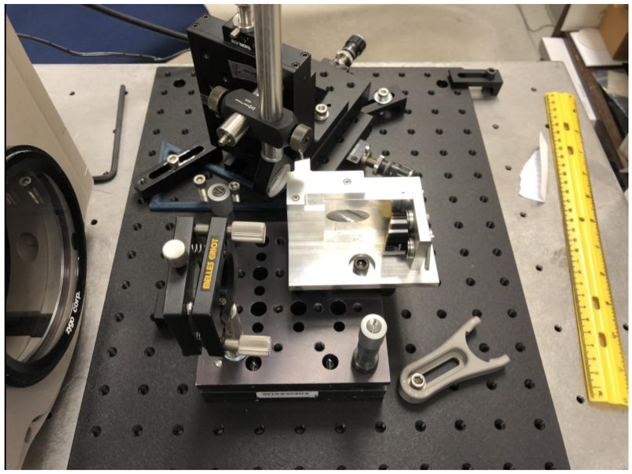

Fig. 51 Optical Breadboard

The optical breadboard allowed the optics team to set everything up ahead of time, so that upon arrival to Meadowlark the optical bench could be clamped to the table and ready to go. This greatly cut down on setup and clean up time, leaving more time to work. Additionally, the breadboard allowed progress to be carried over from the first session to the second, as the setup was not moved between sessions.

While the team did still run out of time to complete the alignment of the optical system, these time saving precautions did allow them to measure the OAP MTF, place the pinhole to receive light through the system, and align the sighting tabs.

D. Software

One of the chief software risks had to do with uncertainty in the maximum period between downlinks. The ADC can be configured to sample at either 833Hz or 208Hz, and at the maximum ADC sample rate of 833Hz the two external flash modules would be completely full after just 72 data collection windows, or 2.4 days. Once the flash memory is full, no more science data can be recorded or old science data must be overwritten. However, by downsampling to 50Hz the payload can go up to 38 days without downlinking before the flash memory is filled. The software is implemeted such that the sampling rate can be easily adjusted. If NanoSAM must wait several days between downlinks, the sample rate can be adjusted accordingly so that there will be ample space to collect data for each sunset and sunrise event. It preferable to adjust the resolution of the data as opposed to losing an entire window worth of data.

To maintain a consistent 50Hz sampling rate the flight software's main loop must take less than 20ms per iteration when under maximum load. An inconsistent sampling rate would undermine the reliability of all data, since accurate timing is assumed during data processing. To further complicate matters, housekeeping must be sampled at a frequency of 1Hz. To handle the timing of multiple processes on a single thread an event system was implemented that allows tasks to interrupt the software when needed without delaying execution of other tasks. Resource intensive tasks are staggered over multiple iterations of the main loop to reduce the time of each iteration.

The risk that radiation poses to science data is mitigated by encoding all science data with SEC-DED Hamming codes and periodically scrubbing the flash memory. Additionally, a robust fault mitigation subsystem monitors the hardware and software for abnormalities and takes corrective action when appropriate. Fault data is encoded on the EEPROM so that issues with the hardware or software can be diagnosed even after an unexpected hang-up or loss of power that clears the volatile memory. When the software is behaving unexpectedly it can be forced to run in safe mode. In safe mode only essential tasks are executed and memory usage is reduced to minimize the chance of encountering an error and thus facilitate troubleshooting.

VII. Project Planning

Authors: Jaret Anderson, Daniel Barth

Project management is a key function in uniting the technical work showcased in the previous sections. The management strategy, shown in Fig. 52 below, consisted of four looping stages: First the current deliverable was divided into small tasks which were scheduled out over the course of the design phase. Then, templates were created for team members to fill out their materials that were being presented in the next deliverable. Once these templates were in place, the management shifted their focus to removing blockers for the team as they arose on a case-by-case basis. Then, when the information was put into the template, a cohesion proofread was carried out to make sure the deliverable had a sensible flow and clear tone.

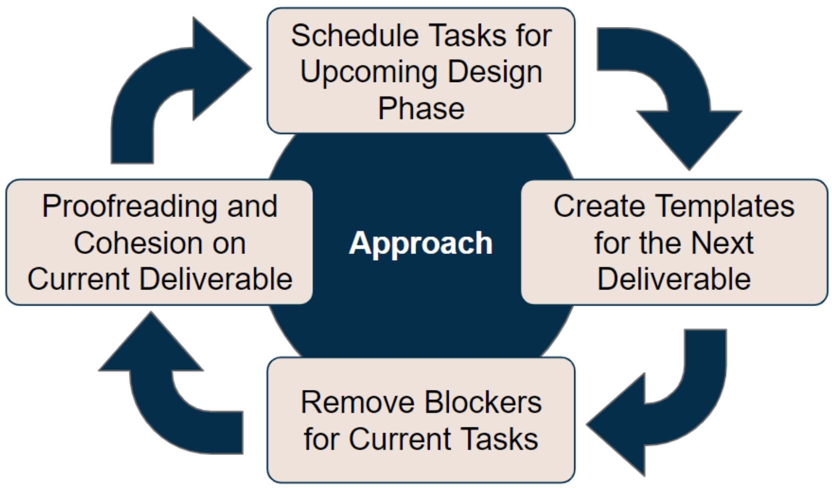

Fig. 52 Management process

The organization chart, work breakdown structure, work plan, and cost plan are included in this section to illustrate how the NanoSAM Management subteam plans to guide the future efforts of the team and turn a set of subsystem designs into an integrated payload.

A. Organizational Chart

It is a requirement of the senior design curriculum that each member of the team has a leadership role on the team. The organizational chart (Fig. 53) shows the leadership roles taken on by each member of the team. Each leadership role has the following responsibilities:

- Provide feedback to the management subteam on the feasibility of tasking
- Report blockers to the management subteam
- Coordinate work with members of your subteam
- Research technical details within your area of expertise
- Keep records of subteam discussions and the rationale behind choices
- Ensure the contents of reports and presentations accurately reflect the knowledge, goals, and actions of the subteam

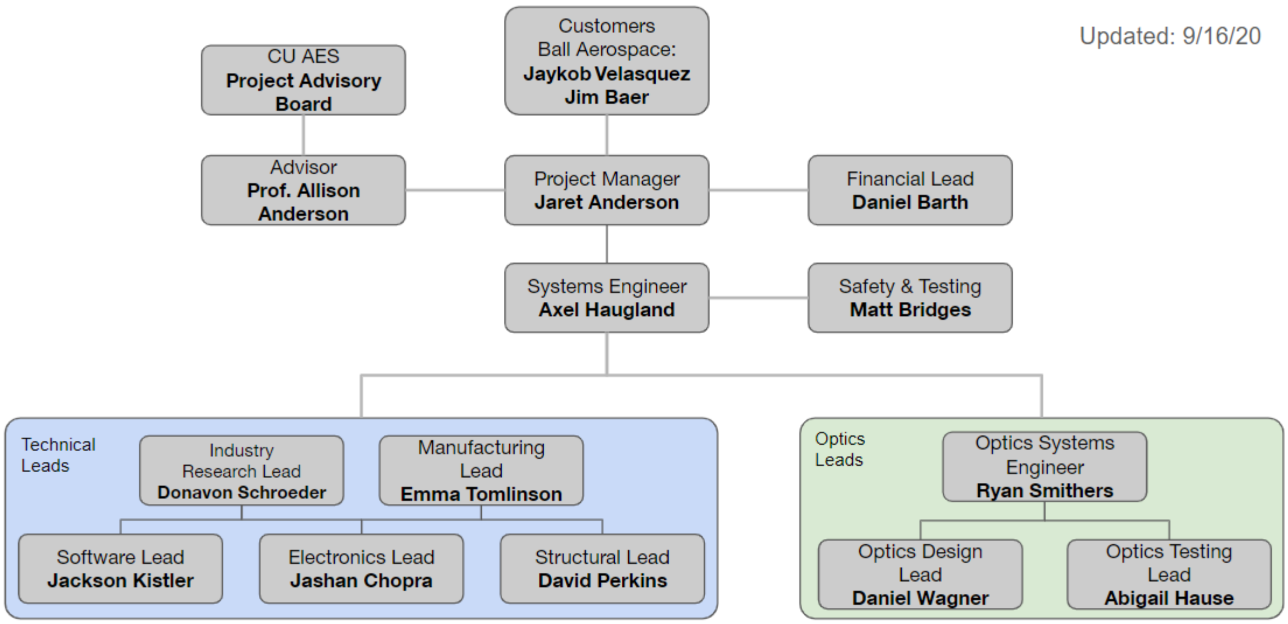

Fig. 53 Organizational Chart

Here is a detailed breakdown of the responsibilities of each of the positions listed in the organizational chart:

Project Manager (Jaret)
- Enable the team to complete their work as efficiently as possible (Remove blockers)
- Maintain a team schedule (WBS and WP)
- Quantify and mitigate risks associated with design, timeline, testing, and finances
- Create meeting agendas
- Assign action items to team leads
- Interface with the PAB and Customers, but not be an exclusive POC
- Proofread reports and presentations, edit for consistency in tone and style
- Communicate goals with leads and ensure that their efforts support the high-level objectives of the project

Systems Engineer (Axel)
- Write requirements
- Resolve inter-subteam design conflicts
- Technical understanding of all subsystems and how they interface
- Create test procedures on the system and subsystem levels
- Work with subteams to confirm subsystem test validity
- Create diagrams to support requirements and testing procedures (FBDs, CONOPS, etc)
- Have strong writing and proofreading skills

Safety & Testing Lead (Matt)
- Work with systems engineer to design tests
- Design and set up hardware required to execute each test
- Initially focus on existing NanoSAM I hardware, transition to NanoSAM II testing in the second semester
- Execute test procedures
- Oversee safety of project personnel
- Review experimental, manufacturing, and test plans to identify and mitigate safety risks
- Obtain safety approvals from project Advisor, or from Matt Rhode or Trudy Schwartz, as appropriate.

Financial Lead (Danny)
- Interface with ASEN department to handle budget given to the team
- Manage team finances spreadsheets
- Project Budget (PB)
- Expenditure Plan (EP)
- Evaluate necessary budget margins
- Evaluate financial risk associated with each purchase
- Approve each purchase before it is made, gather rationale from subteam requesting the purchase

Optics Design Lead (Dan)
- Determine feasibility of various optics implementations
- Carry out trade studies design alternatives and pick a path forward for the “Improve Optics” specific objective
- Read literature passed down from 2019-20 team
- Find new textbooks/research as necessary to support existing resources

Optics Testing Lead (Abby)
- Determine what testing is necessary for optics requirements verification
- Design optical test procedures (optics component of VV plan)
- Work with Optics Design Lead to verify that each test test returns useful measures in relation to the theory behind the system
- Coordinate optics testing with systems personnel

Optics Systems Engineer (Ryan)
- Evaluate optics integration with other subsystems
- Interface with the customer to ensure that the optics subsystem is meeting their expectations
- Flowdown feedback from customers into design and testing procedures

Electronics Lead (Jashan)
- Resolve issues with the ADC on last year’s board
- Potentially design and test a new board depending on the severity of previous issues
- Work closely with software subteam to ensure compatibility

Software Lead (Jackson)
- Scope new software based on what already exists from last year’s design and testing
- Research error detection and correction
- Write pseudocode
- Develop code
- Write unit tests for software
- Work closely with electronics subteam to ensure compatibility

Industry Research Lead (Donavon)
- Acquire ICDs for existing CubeSats
- Design an interface to maximize compatibility with a future CubeSat bus
- Work with Systems Engineer and subteam leads to apply this design to our instrument
- Research existing test procedures used to verify flight readiness
- Implement interoperable bus electronics and software protocols

Structural Lead (David)
- Design enclosure
- Trade studies for various materials
- Create and maintain CAD as design evolves
- Run simulations and/or physical tests to verify structure performance

Manufacturing Lead (Emma)

- Review designs for manufacturability
- Estimate associate manufacturing costs and time requirements
- Become certified with any necessary hardware
- Or submit manufacturing requests if students are not allowed in machine shop due to COVID restrictions
- Organize workflow of manufacturing activities to support the needs of the project

B. Work Breakdown Structure

The work breakdown structure (WBS) (Fig. 54) is a crucial precursor to a schedule, and provides a great overview of the progress made this year. These work products were determined using a three step process. First, the functional requirements were evaluated to determine high-level objectives for each subteam. From there, these high-level objectives were decomposed into tasks with tangible inputs and outputs. Finally, these tangible tasks were reviewed with the respective subteam leads to determine that there were not any crucial holes in the tasking coverage.

The Structures work products are the easiest to visualize. The structure needs to be designed in a 3D modeling software so that the team has a clear vision for what they are going to manufacture. This CAD must then be converted to dimensioned drawings for manufacturing so that the shop staff knows what parts to create for the team. The materials must be ordered to facilitate that manufacturing, and the structure must then be assembled from the manufactured parts. Following assembly, subsystem-level testing occurs, with vibration testing being a key test for the structures team. Once the subsystem is validated, it can be integrated with the other subsystems to form a complete payload.

Optics shares a lot of overlap with structures. The same design, manufacturing, assembly, testing, and integration series of tasks exists. However, the optics hardware from NanoSAM I was available to the team for additional testing and practice alignment on in the meantime. This means that along with the novel design, the optics team had testing to carry out with the NanoSAM I hardware. By doing the solar tracking testing with the NanoSAM I hardware in winter, the team was better prepared to carry out these tests on the NanoSAM II hardware in the spring. Another key task is aligning the NanoSAM II optic, which is crucial to gathering usable scientific data from the optic. This must be carried out using an interferometer, which is well outside the team's budget to acquire. Therefore, the team used the interferometer at Meadowlark Optics, who generously agreed to assist with the alignment process. However, Meadowlark Optics was only able to offer four hours of alignment on the NanoSAM II optic instead of the 20+ hours needed to properly align the system, which meant that the team was not able to complete the "NS2 Harware Alignment" task. As you will see, not completing this task had implications further down the line during testing.

Electronics does not contain much new information, it follows the same design, manufacturing, assembly, testing, and integration tasking cycle. The electronics components were tested individually before being assembled into the board using pick-and-place hardware for increased precision. The assembled boards were then be tested as a subsystem, before being integrated with the payload as a whole and used for system-level testing.

Software is the final subsystem to be discussed. The architecture was fleshed out in pseudocode so that the inputs, outputs, and module relationships were clearly defined as the team began development. This led to a efficient development cycle with concurrent unit testing, culminating in integration testing to ensure that the software functioned as expected with the EPS boards.

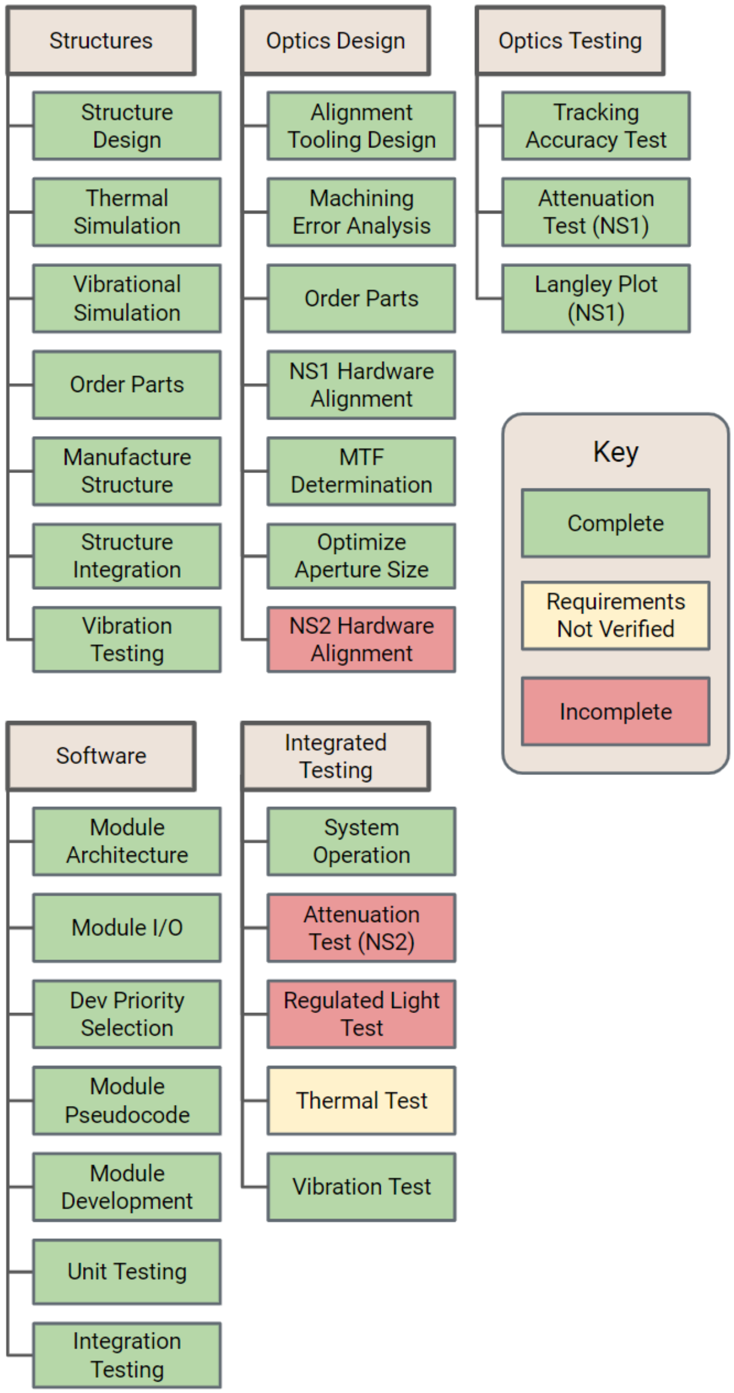

Fig. 54 Work Breakdown Structure

Once these subsystems tasks were completed and the payload is integrated, the final steps were to run system-level testing. The tests listed in the integrated testing section of the WBS are designed to verify high-level requirements contributing to project success. Many of these tests were successful, such as system operation and vibration testing. However, the failure to align the optic as discussed in the optics paragraph of this section meant that the attenuation test and regulated light tests could not be completed. Additionally, improper test design for the thermal test meant that photodiode data was not gathered during this test and consequentially the requirements associated with the thermal test could not be verified.

C. Work Plan

With the work breakdown structure established, these tasks can be organized into a work plan. For this project, we used a Gantt chart organization for the work plan, which allows dependencies, schedule, and task names to all be displayed conveniently. Fig. 55 shows the critical path for our project. This begins with ordering materials, and then flows through software development, and then finishes with environmental testing and other system-level testing to wrap up V&V for the project. Also shown on Fig. 55 are the class milestones for the spring. Many of the tasks on this chart had significant variability based on the availability of manufacturing or testing facilities, so there was multiple weeks of slack time built into the critical path going into the spring. All task times were estimated based on the procedure for the task, then a 25% time margin was applied to the end of the task. With this in mind, tasks also had their start and end dates chosen to overlap with team meeting days whenever possible to facilitate direct accountability for the tasks during the meeting status update. This Fig. does not include all tasks for the project, only the key tasks to the critical path. The team completed the majority of these tasks, with the main residual blocker being a lack of alignment time available to the team. We were unable to properly align the system in the limited amount of time available on the interferometer due to COVID-19 restrictions, which meant that the NanoSAM II Langley plot could not be generated. The thermal test also failed to verify its associated requirements as outlined in the Verification & Validation section of this report.

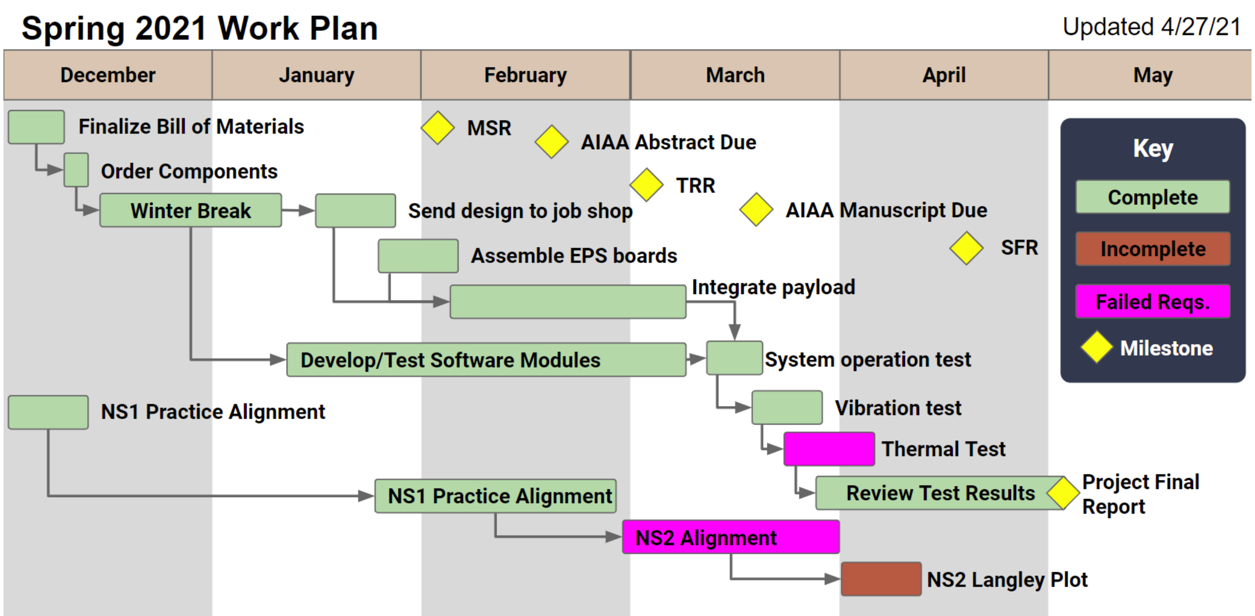

Fig. 55 Work Plan: Critical Path Results

Since the Fig. 55 only shows the critical path tasks, Appendix D contains the complete Gantt charts for each subteam's tasks. This detailed view includes the structures, electronics, and optics tasks as well as the software module development breakdown, illustrating the dependencies and order that dictated development in the spring.

The margin in the schedule proved quite useful as midway through the semester an issue was discovered with the electronics boards which required a new set of boards to be manufactured before testing could continue. This ended up moving the schedule back by approximately 3 weeks, eating into the majority of the margin for the months of February and March. While there still was enough time left for testing late in the semester, the Regulated Light test and Solar Attenuation test could not be completed because of issues with alignment as discussed in many sections previously. Additional margin could have enabled the team to run a repeat of the thermal test with a modified procedure, potentially allowing for the thermal requirements to be verified as well. However, successful structures, electronics, and software design and testing suggests that the overall schedule was highly effective.

D. Cost Plan

Shown in Fig. 56 is the overall breakdown of the designated $5000 budget designated to this project. Some primary notes include the fact that this cost plan originally included a 2x margin on all designated funds, without this margin its expected that the total cost of the system would total closer to $1965 which is less than 50% of the overall designated budget. Finally, its worth noting that the primary costs incurred from the optics system planned for initially were the purchase of an additional OAP mirror and the necessity for alignment tooling for the procedure to be performed in the spring.

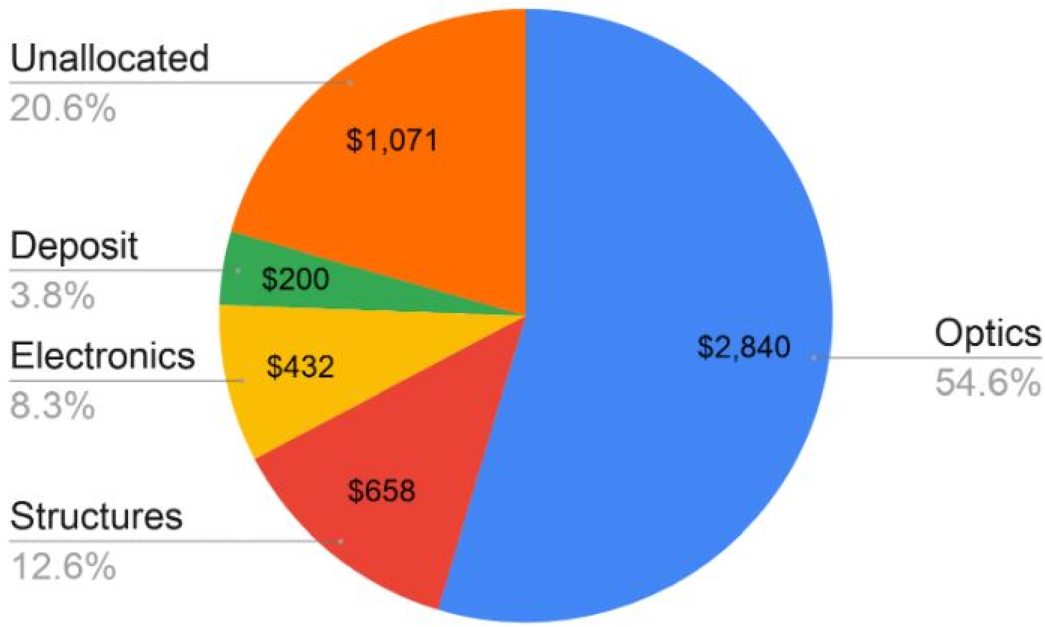

Fig. 56 Original Cost Plan for the NanoSAM II System

The finalized cost breakdown of the NanoSAM II project is shown in Fig. 57. The majority of the budget was designated to the optics subsystem as suspected but a large majority of the planned budget for the optics system went unspent due to the team opting out of buying an additional OAP mirror. Since the structural subsystem never required any additional or replacement parts the project also spent 60% of the designated budget to that system. The last major difference was the determination of the testing costs which did not significantly impact the overall system budget due to overestimation of costs done for the system budget. Based on this final budget, it is reasonable to say the a 2x margin was too large to adequately describe the actual funds necessary for the project and that a 1.5x margin would have been more than sufficient to properly plan for emergency expenditures (with the only exception being the electronics subsystem which used up its entire 2x margin and still went slightly over that margin).

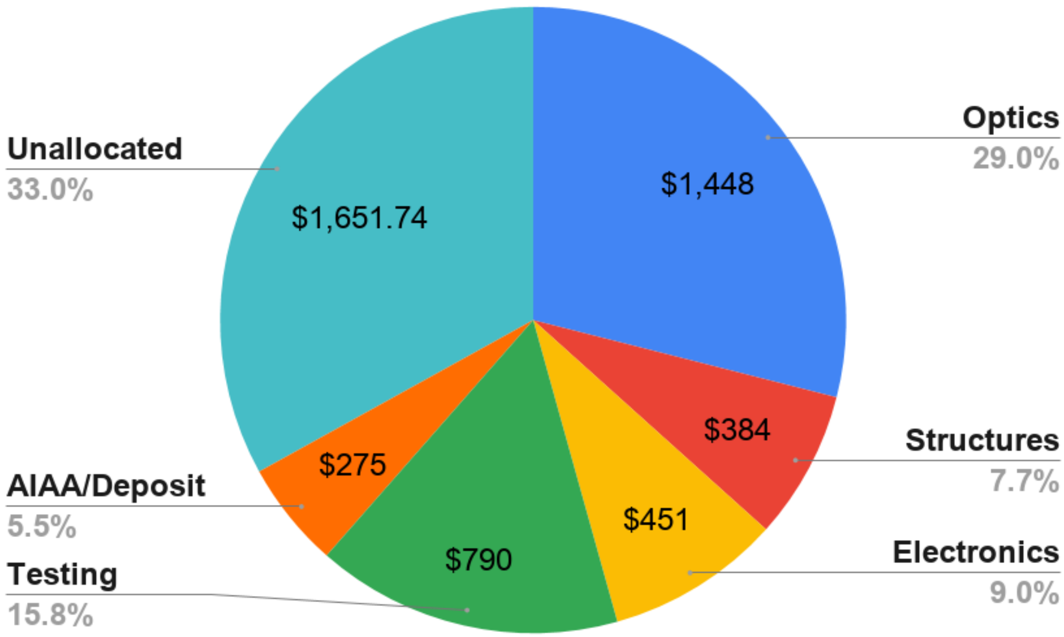

Fig. 57 Finalized Cost Breakdown of NanoSAM II

A breakdown of the total industry cost for NanoSAM II is shown in Tab. 21 which includes a 200% overhead. Since hours were not recorded for early in the semester, it was estimated that the average amount of hours per month was constant throughout the year and then extrapolated to the two missing months at the very beginning of the project. This resulted in 4025 hours total being spent on the project with the wage estimated as $31.25/hr. Also, it was estimated that testing facilities in industry for the thermal test would cost $680 based on information from the point of contact for the testing. Additionally, the Meadowlark optic alignment sessions would cost an additional $2000 in industry to perform and were also added to the expected cost.

Cost Component	Raw Cost	Cost w/ Overhead
Optics	$ 1,407	$ 2,814
Structures	$ 384	$ 768
Electronics	$ 451	$ 902
Testing	$ 1,440	$ 2,880
Alignment Sessions	$ 2,000	$ 4,000
Systems Deposit and AIAA	$ 275	$ 500
Labor	$ 125,781.25	$ 263,477
Total Industry Cost	**$ 131,738**	**$ 263,477**

Table 21 Total Industry Cost Breakdown

E. Test Plan

The test plan went very well in the months of February and March, as we successfully completed all subsystem testing in addition to completing the early phases of optics alignment. Early system testing such as the vibration test and data collection test were also successes, but in late March we discovered that Meadowlark was unable to provide enough time on their interferometer to complete optics alignment. This had a cascading effect, as an unaligned optic became an unresolvable blocker for the regulated light test and the solar attenuation test, leaving many key requirements unverified (as discussed in the Verification & Validation section). Also, since the thermal test did not have a light source and used a dummy optics bench, photodiode data was not available during that test, leading to a failure in functionality confirmation there as well. Some solutions for these issues are discussed in the Management Lessons Learned section below.

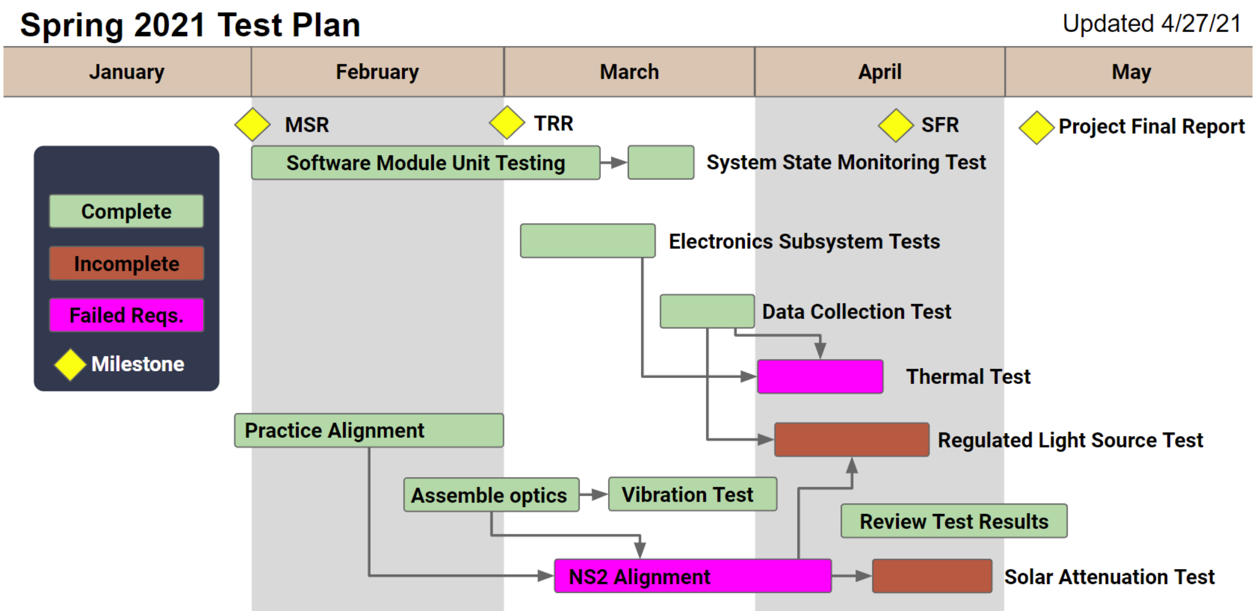

Fig. 58 Test Plan Results

Key facilities were used throughout the spring to enable testing. Alignment was made possible through Meadowlark Optics donating their time and allowing us to use their interferometer. Thermal testing ovens were provided by Prof. Nabity's lab at the CU Aerospace Building (Boulder, CO) with assistance from Matt Zola. Vibration testing was carried out at Altius Space Machines in Broomfield, CO. The time on this vibration table was paid for by the team. Electronics testing was done by the team using a multimeter and power supply provided by the CU Aerospace Engineering Electronics Lab.

VIII. Lessons Learned

A. Management

The overall management strategy was to divide large deliverables into smaller tasks that can be delegated to individuals or for subteam leads to further subdivide as they see fit. Fig. 52 in the Project Planning section shows this management process. This worked fairly well, but relied on the fact that the individuals doing the tasks were willing to spend enough time on them to get them done properly. This also meant that the workload was not evenly divided; the lowest number of hours contributed by a team member was 224 while the highest was 480 over the course of the year.

One strategy employed on the software team to even out hours and improve the overall product delivered was rigorous peer reviews. No commits could be pushed to the main branch before they were reviewed and signed-off by two team members besides the developer. This pull-request system is a standard process in the software industry, so it felt natural to implement it on the software team. Because of this, it is no coincidence that the software had very few issues during the integration phase of the project.

Given the chance to do the project over again, I would implement a similar peer-review system for requirements writing as well as test plan design. Unfortunately we found out very late in the project that many of our test plans were missing critical equipment or described processes that were impossible to carry out. One example of this is the thermal test, which was designed to verify requirements relating to fluctuations in the photodiode signal as temperature varied. However, the actual test was carried out without any photodiode signal being gathered as the team never found a solution to the problem of shining a light on the photodiode from inside the chamber and the test was too early to integrate an aligned optics bench. This was an issue that was discussed during weekly meetings, but ultimately left by the wayside as people had more pressing issues to deal with. This would have certainly been caught and remedied had there been a formal review process for test procedures.

B. Structures and Manufacturing

The structure houses and integrates all other subteams, and so one of the essential duties of the structure team is to create something that will allow all teams to integrate easily. Doing this requires clear communication with the other subteams. Future structures teams should receive design requirements for the structure from each of the subsystems to improve integration. For instance, communicate with the electronics team about what connections must go in/out of the payload, and where these are placed. Along these lines, model internal wire pathing in the CAD model to prevent interference issues. Discuss with the optics subteam to understand the alignment procedure and how the key measurements are taken to facilitate alignment. Lastly, communicate with the testing teams about what hardware is needed to attach the payload to thermal chambers/vacuum chambers/vibe tables, and ensure that there are suitable locations on the payload for test instruments.

On the topic of full system integration, one of the biggest issues was small tolerances required on a project of this size. Future teams should be aware of tolerances from both ordered and manufactured materials, and should take appropriate steps to mitigate interference issues, such as sanding parts by hand or designing parts with extra room. This issue became especially apparent during the alignment of the photodiode block relative to the optics bench. The pinhole itself has a target displacement of less than 0.05mm, or about 0.002". This tolerance is tighter than most machine shops, so additional steps must be taken to meet this requirement. Future teams may want to lap or sand/polish the photodiode block and optics bench surfaces that contact shims in order to ensure extremely close, even fits. Overall, the lead structures engineer needs to have specific knowledge of the electronics and optics subsystem interfaces, and should play a key role in supporting system and subsystem level test hardware design. Future teams should consider having full project integration meetings early in the process to ensure that all integration needs are met before manufacturing is completed.

C. Electronics

The first iteration of the boards had a major design flaw that required us to redesign on short notice and reorder the boards, eating up the majority of our manufacturing margin. The issue was that the layout of SamTec's board to board connector downloaded from their website had the copper annular rings of the successive pins within 6 mils, which is the minimum trace clearance for most manufacturers, including OSHPark. When uploading the free, online CAD schematic into Fusion360, it warned us that the spacing between the rings was too small but the warnings were ignored trusting that the schematic was correct. This resulted in a short between the copper pads for the board to board connectors and thus no communication between the analog and digital boards. The lesson to take away from this is to carefully monitor your layouts to ensure traces, solder points, and clearances match up. In general, when downloading layouts from the internet, perform due diligence and make sure they align with manufacturing drawings.

After the redesigned boards arrived and were manufactured, we initially had issues with both of the voltage regulators. The analog voltage regulator was converting the input into a positive and negative output, but it was not downconverting the input from 12V to 5V. This was due to an error in resistor values for the voltage divider circuit. For the digital voltage regulator, there were a few issues. First, the "Power Good" pin was supposed to output 3.3V to indicate that the digital voltage regulator was working. Unfortunately it does not output any voltage at all. We have not determined if this was due to a design error on our part or an error in the chip. Either way, even though the linear regulator outputs the right voltage, this pin should not be used as the only indicator of an operational power supply. Overall, it's important to verify resistor values when they are crucial to design. Sometimes, things are mislabeled or misidentified so to be safe take a multimeter, set it to measure resistance, and just check all the resistors on the board, because the part supplier is not always perfect. In the same vein, make sure you read the datasheets, know your design inside and out, and trust your reasoning. We spent a significant amount of time debugging the bipolar regulator even though we were almost certain the design was correct. It's also important to read the datasheet and check out the drawings for even small parts like the inductor, otherwise you may place them incorrectly or upside down. We burnt the first inductor with this mistake, so it's also a good idea to order multiple of all of your parts. Lastly, the voltage regulators are a crucial element of the design and they have no backups. Although the current design worked well for both of them, we would recommend designing backup voltage sources if possible.

In initial tests the analog to digital converter was not reading data. We recognized that the voltage output of the transimpedance amplifier was working because of our backup science data path to the Teensy on-board ADC. The issue boiled down to an incorrectly connected pin 6, the serial data output of the ADC, to the Teensy's MOSI pin (it should have been MISO). To fix the issue, we cut the trace from the board to board connector to the Teensy MOSI pin on the digital board, and then soldered a small wire from the board to board connector to the Teensy MISO pin. The design solution to this issue would be to simply rename the output net on pin 6 of the ADC and on pin 15 of the board to board connector to "SPI_MISO" in Fusion 360. The lesson learned here is that the electronics CAD software will warn you when you connect things wrong, but not when you simply name the output wrong! There are a number of smaller lessons learned and small steps that need to be taken in a further redesign, which are detailed heavily in the Electronics Master Summary in the Electronics folder.

D. Optics

The main lesson learned about the optics was the sheer amount of time needed to properly align the optic. Despite rigorous planning, the development of a thorough alignment procedure, and the time saving optical breadboard, the optics team simply did not have enough time to align the optic. This was due to lack of access to Ball's alignment facility, and Meadowlark understandably having limited time for NanoSAM to use their interferometer. The suggestion for any future teams is to get started on alignment as early as possible, and to schedule as much time as possible working with an interferometer.

The other lessons learned had to do with alignment of the optic. First, NanoSAM-II tried to take a shortcut to save time, and align the OAP using a concave lens and the return from the pinhole plate, instead of using a half-sphere. However, sufficient alignment was not achieved using this configuration, suggesting that in the future a half-sphere or return sphere should be used for OAP alignment. Either of these options would provide a better return than the concave lens or pinhole plate. NanoSAM-II did try to use a ball bearing in place of a return sphere (because a return sphere is to expensive to purchase or borrow) during a practice alignment session, and it provided a sufficient return but was very difficult to align, so it was not used moving forward.

Additionally, the measurement of the OAP showed that it does not meet the required MTF of .74 due to surface deformation from the mounting bolts. The best possible solution to this problem is to procure a larger (likely custom made) mirror. This would move the surface deformation farther from the center, leaving a center with sufficiently minimal wavefront error. Ideally, an OAP mounting procedure would be designed in order to minimize the torque on the mirror from the mounting bolts.

E. Software

The primary limiter when it came to software development was time. With only a small two-person team of software developers it was simply not possible to implement all of the features and fixes we would have liked to. Prior experience with manual memory management, serial communication interfaces, and large multi-file projects would have been helpful to streamline development, but becoming competent with these topics has been an excellent learning experience.

GitHub enabled the team to review changes to the codebase before merging them. Countless bugs and programming errors were caught during this peer review process, and so relatively few bugs remained when the final phase of bugfixes began. It would be beneficial to go even further, and have the other developers test new code on their own hardware before it is merged to the main branch. Several of the most persistent and baffling bugs could have been caught by testing the code with different inputs. Each developer had access to their own Teensy microcontroller, which enabled unit and system testing at any point during development, and this kind of rapid testing was an absolute necessity when it came to fixing bugs and inspiring confidence in the codebase.

A misunderstanding of the global namespace and the "static" keyword in C++ led to a major issue where crucial program variables existed in several instances instead of one unified instance. Some refactoring was necessary to convert all static global variables into external variables using the "extern" keyword, which exist as one instance shared across all files. Some other C++ concepts where the team's knowledge was fuzzy and misunderstanding occurred were class templates, pointers, single-bit operations, and volatile variables. Variables that may be changed between accesses by any outside factor, including external hardware such as flash memory or serial connections, must be declared with the "volatile" keyword. A single missing "volatile" keyword related to reading/writing to EEPROM caused the Teensy to overwrite its own program memory and become temporarily inoperable, this was perhaps the most distressing bug that occurred during development, and could have easily been mitigated with a greater understanding of memory management in C++

As software development progressed and the team's understanding of the software grew, previous work was constantly refactored to be more efficient, more elegant, and more generalized. Given more time, readability and safer namespace separation could have been achieved by encapsulating every software module into its own class — considered a best practice in object oriented languages like C++. After the software was functionally complete, it was too late to undertake this refactoring project, since doing so would have undoubtedly introduced several bugs into the code at a stage where most bugs had been fixed and the first system tests were imminent.

IX. Individual Report Contributions and References

Author	Contributions
Jaret Anderson	Project Purpose text, Project Objectives text, CONOPS diagrams and animation, FBD diagram and text, Org Chart/WBS/WP, section intro paragraphs, management lessons learned, whole-paper cohesion edits
Daniel Barth	V&V section for thermal testing. Cost plan diagrams and text. Appendix C thermal model details diagrams and text.
Matthew Bridges	General V&V section writing. Electronic systems test, software simulation loop, baseline data collection sections. Test setup diagrams
Jashan Chopra	Electronics Conceptual Design, Electronics Trade Studies, Electronics Baseline & Detailed Design, Electronics Risk Assessment, Electronics Verification and Validation, Electronics Manufacturing, Electronics Lessons Learned.
Axel Haugland	V&V Section Baseline Collection Test, Thermal Test, Regulated Light Test, Test Outlines, Testing Plan, Requirements Development
Abigail Hause	Optics Detailed Design, Optics Testing plans, Optics Risk Assessment and Mitigation, Optics lessons learned
Jackson Kistler	Software conceptual design, Software detailed design, Software risk assessment, Software lessons learned
David Perkins	Structures conceptual design, Structures detailed design, Structures trade studies, Structures baseline
Donavon Schroeder	Software Detailed Design EDAC research, Electronics Detailed Design proofread and adjustments
Ryan Smithers	Optics Conceptual Design Section, Optics Verification and Validation, Optics Final Design, Development of Alignment Procedure Subsection
Emma Tomlinson	Preliminary Manufacturing Plan section, Structures Risk Assessment and Mitigation section
Daniel Wagner	Optics Conceptual Design Section, Optics Verification and Validation, Development of Alignment Procedure Subsection

Table 22 Individual Report Contributions

References

[1] Allen, Bob. "Atmospheric Aerosols: What Are They, and Why Are They So Important?" NASA Langley, Web, 1 Aug 1996, Updated 7 Aug 2017, Accessed 20 Sep 2020. <https://www.nasa.gov/centers/langley/news/factsheets/Aerosols.html>

[2] Thomason, L.W. and J.-P. Vernier. "Improved SAGE II cloud/aerosol categorization and observations of the Asian tropopause aerosol layer: 1989-2005." Atmospheric Chemistry and Physics, 2013. <http://citeseerx.ist.psu.edu/viewdoc/download?doi=10.1.1.993.3341&rep=rep1&type=pdf>

[3] Powell, K. A. (1996). Stratospheric Aerosol Measurement II (SAM II) Langley DAAC Project Guide (pp. 1-5, Rep.). Hampton, Virginia: NASA Langley Research Center.

[4] "SAGE III on ISS", Wikipedia, Last Edited 10 September 2020. <https://en.wikipedia.org/wiki/SAGE_III_on_ISS#/media/File:SAGE_III_Instrument.jpg

[5] Chin, Jamie, et. al. *CubeSat 101: Basic Concepts and Processes for First-Time CubeSat Developers*. NASA CubeSat Launch Initiative, October 2017. <https://www.nasa.gov/sites/default/files/atoms/files/nasa_csli_cubesat_101_508.pdf>

[6] "Instrument: SAGE-III" Observing Systems Capability Analysis and Review Tool, updated 28 Aug 2019, accessed 20 Sep 2020, <https://www.wmo-sat.info/oscar/instruments/view/693>

[7] Ball Aerospace and Technologies Corp. (2020) NanoSAM: An Aerospace Senior Project [PowerPoint slides]

[8] Tang, Hui Min et. al. *Nano-Stratospheric Aerosol Measurement Project Final Report*, Ann and H.J. Smead Aersopace Engineering Sciences, University of Colorado Boulder, <https://www.colorado.edu/aerospace/current-students/undergraduates/senior-design-projects/past-senior-projects/2019-2020/nano>

[9] NASA - NSSDCA - Spacecraft - Telemetry Details. (n.d.). Nssdc.Gsfc.Nasa.Gov. Retrieved September 14, 2020, from https://nssdc.gsfc.nasa.gov/nmc/spacecraft/displayTrajectory.action?id=1978-098A

[10] QB50: System Requirements and Recommendations. Issue 7, Section 1.6 "Thermal Control" and Section 2.2 "Resonance Survey." Published 13 Feb 2015. <https://www.qb50.eu/index.php/tech-docs/category/QB50_Systems_Requirements_issue_76e8e.pdf?download=89:qb50-docs>

[11] Stafford, George. "Blue Canyon Technologies XB1: Enabling a New Realm of CubeSat Science", slide 6. Accessed Sep 10, 2020. <http://mstl.atl.calpoly.edu/simworkshop/archive/2012/Summer/Day%201/1200-Stafford-XB1.pdf>

[12] Anderson, J. Et. Al "NanoSAM II Preliminary Design Report". Published 13 October 2020. <https://www.colorado.edu/aerospace/sites/default/files/attached-files/nanosamii_pdr.pdf>

[13] Harris, C. M., Paez, T. L., Piersol, A. G. (2010). "Harris shock and vibration handbook". New York, NY: McGraw-Hill.

[14] "Cantilever Beam Natural Frequency." AmesWeb. Accessed 9 Dec 2020. <https://amesweb.info/Vibration/Cantilever-Beam-Natural-Frequency-Calculator.aspx>

[15] "304 Stainless Steel." MatWeb. Accessed 9 Dec 2020. <http://www.matweb.com/search/DataSheet.aspx?MatGUID=abc4415b0f8b490387e3c922237098da>

[16] "Polymer Resources PPX-FR4 Modified-PPO, V-1 Flame Retardant." MatWeb. Accessed 9 Dec 2020. <http://www.matweb.com/search/datasheet.aspx?MatGUID=fcbb32d6b39b4d59ae3f2b4a1bc1582f>

[17] "FR408HR Data Sheet." Isola Group (2016). Accessed 9 Dec 2020. <https://docs.oshpark.com/resources/four-layer-substrate-FR408HR.pdf>

[18] "PC/104 Specification", Version 2.6, PC/104 Embedded Consortium (2008). Accessed 9 Dec 2020. <https://pc104.org/wp-content/uploads/2015/02/PC104_Spec_v2_6.pdf>

[19] Garzón, A., amp; Villanueva, Y. (2018). Thermal Analysis of Satellite Libertad 2: A Guide to ... Retrieved November 30, 2020, from http://www.scielo.br/scielo.php?script=sci_arttext&pid=S2175-91462018000100342

[20] Anderson, B. Justus, C. Batts, G.. (2001). Guidelines for the Selection of Near-Earth Thermal Environment Parameters for Spacecraft Design.

[21] (n.d.). Retrieved December 02, 2020, from http://www.matweb.com/search/DataSheet.aspx?MatGUID=b8d536e0b9b54bd7b69e4124d8f1d20a

[22] "3-Unit CubeSat Structure." ISISPACE, inc. N.d. Accessed 2 Dec 2020. <https://www.isispace.nl/product/3-unit-cubesat-structure/>

[23] "Photodiode Characteristics and Applications." UDT Sensors, inc. N.d. Accessed 19 Sep 2020. <https://phas.ubc.ca/~beaudoin/PDS%20Papers/Position%20Detector%20Info/UDT_PhotodiodeCharacteristics.pdf>

[24] “Transimpedance amplifier circuit.” Texas Instruments. Jan 2019. Accessed 11 Nov. 2020. <https://www.ti.com/lit/an/sboa268a/sboa268a.pdf?ts=1605853737279&ref_url=https%253A%252F%252Fwww.google.com%252F>

[25] "Photodiodes" Sec. 4.7. University of Colorado Boulder Electrical Engineering. <https://ecee.colorado.edu/~bart/book/book/chapter4/pdf/ch4_7.pdf>

[26] "Photodiodes." Thor Labs. Updated 2020, Accessed 19 Sep 2020. <https://www.thorlabs.com/newgrouppage9.cfm?objectgroup_id=28>

[27] "Photodiodes." RP Photonics Encyclopedia. N.d. Accessed 19 Sep 2020. <https://www.rp-photonics.com/photodiodes.html>

[28] "Photodiode Detectors." Sohag University, Powerpoint Slides, N.d. Accessed 22 Sep 2020. <http://staffsites.sohag-univ.edu.eg/uploads/591/1536180611%20-%20Lect12-photodiode%20detectors.pdf>

[29] Mancini, Rob. *Op Amps for Everyone*, Texas Instruments, N.d. <https://web.mit.edu/6.101/www/reference/op_amps_everyone.pdf>

[30] Kester, Walt. "Which ADC Architecture is Right For Your Application?" Web, June 2005, Accessed 19 Sep 2020. <https://www.analog.com/en/analog-dialogue/articles/the-right-adc-architecture.html#>

[31] "Introduction to FPGAs" Imperial College London. 8 Oct 2019. <httphttp://www.ee.ic.ac.uk/pcheung/teaching/ee2_digital/Lecture%202%20-%20Introduction%20to%20FPGAs.pdf>

[32] "Types and Applications of Microcontrollers" Engineering Institute of Technology. N.d. Accessed 22 Sep 2020. https://www.eit.edu.au/cms/resources/technical-resourses/types-and-applications-of-microcontrollers

[33] Kovo, Yael. "Command and Data Handling" Updated 3 May 2020, Accessed 21 May 2020. <https://www.nasa.gov/smallsat-institute/sst-soa/command-and-data-handling>

[34] "An overview of on-board computer (OBC) systems available on the global space marketplace" satsearch, 11 March 2020. Accessed 21 Sep 2020. <https://blog.satsearch.co/2020-03-11-overview-of-on-board-computers-available-on-the-global-space-marketplace>

[35] Fuchs, Christian M. "Enabling Dependable Data Storage for Miniaturized Satellites" 29th Annual AIAA/USU Conference on Small Satellites. N.d. <https://digitalcommons.usu.edu/cgi/viewcontent.cgi?article=3223&context=smallsat>

[36] Scherz, Paul and Simon Monk. *Practical Electronics For Inventors*. Fourth Ed. ISBN: 978-1259587542

[37] "ROM, EPROM, and EEPROM Technology" University of Michigan Integrated Circuit Engineering Corporation. N.d. <http://web.eecs.umich.edu/~prabal/teaching/eecs373-f12/readings/rom-eprom-eeprom-technology.pdf>

[38] Mitchell, Robin. "DRAM, SRAM, FLASH, and a New Form of NVRAM: What’s the Difference?" 14 Feb 2020, Accessed 23 Sep 2020. <https://www.allaboutcircuits.com/news/dram-sram-flash-and-a-new-form-of-nvram-whats-the-difference/>

[39] "Product Search Page" Digi-Key Electronics. Accessed 25 Sep 2020 <https://www.digikey.com/products/en?keywords=>

[40] "AD8671 Datasheet" Analog Devices. N.d. <https://www.analog.com/en/products/ad8671.html>

[41] "LT2470 Datasheet" Analog Devices. N.d. <https://www.analog.com/media/en/technical-documentation/data-sheets/24702fb.pdf>

[42] "LT6654 Datasheet" Analog Devices. N.d. <https://www.google.com/search?q=lt6654&oq=lt6654&aqs=chrome..69i57j69i59l2j69i60.1021j0j7&sourceid=chrome&ie=UTF-8>

[43] "LTC3260 Datasheet" Analog Devices. N.d. <https://www.analog.com/en/products/ltc3260.html>

[44] "INTERCONNECT SIGNAL INTEGRITY HANDBOOK" SamTech Connectors. <http://suddendocs.samtec.com/literature/samtec_si_handbook.pdf>

[45] "Teensy 4.0 Datasheet" PJRC Store. N.d. <https://www.pjrc.com/store/teensy40.html>

[46] "TLV1704-SEP Single-Event Latch-Up (SEL) Radiation Report" Texas Instruments. N.d. <https://www.ti.com/lit/rr/slok014/slok014.pdf?ts=1606687997706&ref_url=https%253A%252F%252Fwww.google.com%252F>

[47] "MT25QL128ABA Datasheet" Micron Technologies. N.d. <https://datasheetspdf.com/datasheet/MT25QL128ABA.html>

[48] "LT8610A Datsheet" Analog Devices. N.d. <https://www.analog.com/media/en/technical-documentation/data-sheets/8610abfa.pdf>

[49] Mason, James., et. al. "Miniature X-Ray Solar Spectrometer (MinXSS) – A Science-Oriented, University 3U CubeSat" N.d. <https://arxiv.org/pdf/1508.05354.pdf>

[50] "LT6105 Datasheet" Analog Devices. N.d. <https://www.analog.com/media/en/technical-documentation/data-sheets/6105fa.pdf>

[51] C. Briscoe., & W. Dufee, University of Minnesota, "Using LabVIEW to Measure Temperature with a Thermistor" N.d. <https://zeus.phys.uconn.edu/wiki/images/LabViewThermistor.pdf>

[52] Whitlock, Bill., et. all, Massachusetts Institute of Tech, "UNDERSTANDING, FINDING, ELIMINATING GROUND LOOPS", N.d. <https://web.mit.edu/jhawk/tmp/p/EST016_Ground_Loops_handout.pdf

[53] "FD11A Photodiode Datasheet" ThorLabs. N.d. <https://www.thorlabs.com/thorproduct.cfm?partnumber=FD11A>

[54] "Understanding Data Converters" Texas Instruments. N.d. <https://www.ti.com/lit/an/slaa013/slaa013.pdf?ts=1606648902588&ref_url=https%253A%252F%252Fwww.google.com%252F>

[55] "Introduction to SPI devices" Analog Dialouge. N.d. <https://www.analog.com/en/analog-dialogue/articles/introduction-to-spi-interface.html>

[56] "Better SPI Bus Design in 3 Steps" PJRC Store. N.d. <https://www.pjrc.com/better-spi-bus-design-in-3-steps/>

[57] Wang, W. National Tsing Hua University. "Optical Detectors". N.d. <https://depts.washington.edu/mictech/optics/me557/detector.pdf>

[58] Wells, G. James. University of Toronto Institute For Aerospace Studies. "Canada's Smallest Satellite: The Canadian Advanced Nanospace eXperiment (CanX-1)". <https://digitalcommons.usu.edu/cgi/viewcontent.cgi?article=1925&context=smallsat>

[59] Ødegaard, Kjell Arne. International Conference on Computer Safety, Reliability and Security. "Simple Methods for Error Detection and Correction for Low-Cost Nano Satellites". <https://hal.archives-ouvertes.fr/hal-00848615/document>

[60] "General Environmental Verification Standard: GSFC-STD-7000", Office of the NASA Chief Engineer, NTSS Version 7.0, 30 Sep 2015, updated 29 March 2019 <https://standards.nasa.gov/standard/gsfc/gsfc-std-7000>

[61] Kim, Sung-Hwa Hwangbo, Chang-Kwon. "Temperature Dependence of Transmission Center Wavelength of Narrow Bandpass Filters Prepared by Plasma Ion-Assisted Deposition." Journal of the Korean Physical Society. Vol. 45, No. 1, July 2004. https://inis.iaea.org/search/search.aspx?orig_q=RN:41100734

[62] McCormick, M. P. Et. Al. "Satellite Studies of the Stratospheric Aerosol." Bulletin American Meteorological Society. Vol. 60, No. 9, September 1979.

[63] "2000 ASTM Standard Extraterrestrial Spectrum Reference E-490-00." National Renewable Energy Laboratory. https://www.nrel.gov/grid/solar-resource/spectra-astm-e490.html

[64] Ødegaard, Kjell Arne & Amund Skavhaug. Simple Methods for Error Detection and Correction for Low-Cost Nano Satellites. SAFECOMP 2013 - Workshop DECS (ERCIM/EWICS Workshop on Dependable Embedded and Cyber-physical Systems) of the 32nd International Conference on Computer Safety, Reliability and Security, Sep 2013, Toulouse, France. pp.NA. ffhal-00848615f

[65] Hillier, Caleb & Balyan, Vipin, "Error Detection and Correction On-Board Nanosatellites Using Hamming Codes", Journal of Electrical and Computer Engineering, vol. 2019, Article ID 3905094, 15 pages, 2019. https://doi.org/10.1155/2019/3905094

[66] Crail, Clayton B. "Ranking CubeSat Communication Systems Using a Value-centric Framework." Massachusetts Institute of Technology, 2013.

[67] Iii, L. E., Zaun, N. H., Mccormick, J. M., Guy, J. H., amp; Vaughn, W. R. (1985). Stratospheric Aerosol And Gas Experiment II Instrument: A Functional Description. Optical Engineering, 24(2), 242307. doi:10.1117/12.7973473

[68] Nieto-Peroy, C., amp; Emami, M. R. (2019). CubeSat Mission: From Design to Operation. Applied Sciences, 9(15), 3110. doi:10.3390/app9153110

[69] Wang, Pi-Huan Mccormick, M. Minnis, Patrick Kent, G.S. Yue, G.K. Skeens, K.M.. (1995). *A method for estimating vertical distibution of the SAGE II opaque cloud frequency*. Geophysical Research Letters. 22. 10.1029/94GL02992.

[70] Ball Aerospace and Technologies Corp. (2020) NanoSAM: An Aerospace Senior Project [PowerPoint slides]

[71] Finckenor, Miria M., de Groh, Kim K. "Space Environmental Effects." NASA, 2013, https://www.nasa.gov/sites/default/files/files/NP-2015-03-015-JSC_Space_Environment-ISS-Mini-Book-2015-508.pdf

[72] Jeon, Seungjune & Kumar, Vijaya Hwang, Euiseok & Cheng, Michael, "Evaluation of Error-Correcting Codes for Radiation-Tolerant Memory", NASA IPN Progress Report, vol. 42-181, May 15, 2010.

[73] Masoomi, Ashkan & Hamzehiyan, Roozbeh, "A New Approach for Detecting and Correcting Errors in the Satellite Communications Based on Hamming Error Correcting Code", International Journal of Computer Theory and Engineering, Vol. 5, No. 2, April 2013.

[74] Tang, Hui Min et. al. *Nano-Stratospheric Aerosol Measurement Conceptual Design Document*, Ann and H.J. Smead Aersopace Engineering Sciences, University of Colorado Boulder, <https://www.colorado.edu/aerospace/current-students/undergraduates/senior-design-projects/past-senior-projects/2019-2020/nano>

[75] "TriRail Carriers." Ealing Catalog. Updated 2014, Accessed 19 Sep 2020. <https://www.ealingcatalog.com/opto-mechanics/optical-rails/trirail-carriers.html>

[76] "SM1Z - Z-Axis Translation Mount, 30 mm Cage Compatible." Thor Labs. Updated 2020. Accessed 19 Sep 2020. <://www.thorlabs.com/thorproduct.cfm?partnumber=SM1Zad-image-0>

[77] "Optical Mirrors." Edmund Optics. Updated 2020. Accessed 21 Sep 2020. <https://www.edmundoptics.com/c/optical-mirrors/609/>

[78] University of Central Florida. Metrology of Optical Systems. OP-TEC, 2015.

[79] Hawks, Chuck. "Simple Formulas for the Telescope Owner." Sky amp; Telescope, 20 Nov. 2017, skyandtelescope.org/observing/stargazers-corner/simple-formulas-for-the-telescope-owne.

[80] "Precision Pinholes." Edmund Optics. Updated 2020. Accessed 21 Sep 2020. <https://www.edmundoptics.com/f/precision-pinholes/12073/>

[81] "Precision Air Slits." Edmund Optics. Updated 2020. Accessed 21 Sep 2020. <https://www.edmundoptics.com/f/precision-air-slits/12136/>

[82] "Kinematic Bases." Newport Corporation. Updated 2020. Accessed 21 Sep 2020. <https://www.newport.com/f/kinematic-bases>

[83] "Z-Axis Translation Mounts." Thor Labs. Updated 2020, Accessed 19 Sep 2020. <https://www.thorlabs.com/newgrouppage9.cfm?objectgroup_id=188>

X. Appendix A: Conceptual Design - Design Alternatives

Structures Conceptual Design

Options for Structural Mounting of Electronics Board

The electronics mount options boil down to essentially three main choices: a direct metal contact, a slotted friction fit, or a thermally and/or vibrationally isolating mount. These options all present tradeoffs which are quantified in the Structures Trade Studies section below.

The direct metal contact provides a few advantages. One, it makes it easy to provide a chassis ground to the electronics board. Two, it is mechanically simple to model and to manufacture. Three, it is easily implemented. This is the design shown in Fig. 97.

Another electronics mount option considered was a slotted friction fit. This design takes the two electronics boards, fixes them together, and then has a tight slot in the structural ribs that the assembly slides between, unlike the direct metal contact shown in Fig. 97, this option would not have any solid fixtures to any of the ribs. This option was considered due to the advantages it would provide during the testing stages of the instrument, as it would facilitate testing on the electronics subsystem. This design was quickly abandoned after a manufacturability review due to concerns over tolerances required to fit the board assembly tightly, as well as concerns over a chassis ground.

The thermally and/or vibrationally isolating mount described was an elastomer nut from Parker LORD, which is shown below in Fig. 59:

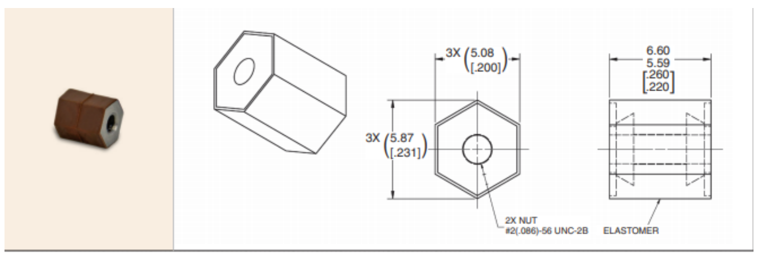

Fig. 59 Parker LORD Micro Mount Elastomer

This component was originally considered due to its ability to thermally isolate the optics bench as well as its ability to provide high-frequency vibration isolation to protect electronics during launch. This component can be seen in Fig. 96 as the connecting piece between the two electronics boards and the central rib. Manufacturer provided lead times were extremely long and so other solutions were preferred and later implemented, especially considering the relatively minimal impact on design requirements this component provided.

A. Electronics Design Alternatives

Photodiode Options

In the broadest terms a photodiode is an analog semiconductor device that converts absorbed photons and high energy particles into an electrical current as the particles strike the semiconductor surface. In Fig. 60 we see an example of the typical P-N photodiode, noting that the silicon construction is essentially that of a typical diode. The depletion region in the diagram is sometimes called the impurity region, and can be made of different materials with different electrical properties. Striking light on the silicon surface creates electron-hole pairs in the material, which generates an electric signal to be measured. [25].

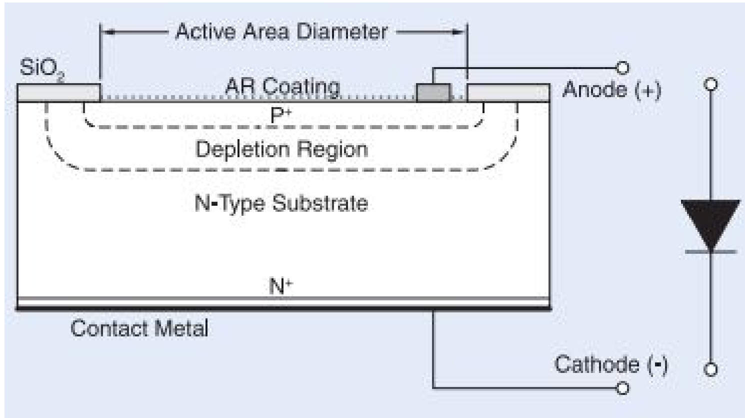

Fig. 60 A planar diffused silicon photodiode [23]

Converting the incoming photons into current allows the irradiance information to be read by the ADC, which can then be converted back from an electrical signal into usable data. Photodiodes have a number of properties of concern to the project, most of which are dictated by the material used. In particular, the noise of the selected photodiode is of primary concern to meet the SNR requirement. Shot noise arises due to statistical fluctuations in the actual generated current, as well as the dark current. The dark current is, as the name describes, the current that flows from the photodiode when there is no light - essentially pure noise to the measurement. Temperature changes affect the dark current drastically, doubling it for every 10 degree change in Celsius [23]. The responsivity of the photodiode will be important for attaining sampling frequency requirements. The responsivity is given by equation 27. A higher responsivity allows the incident power to be more easily converted to a raw current value from the photodiode. Also noted is the operating mode of the photodiode (photovoltaic or photoconductive). Both of these options are inspected when designing the interaction of the photodiode with the larger electrical system, and do not warrant a standalone trade study.

$$R_\lambda = \frac{I_p}{P} \tag{27}$$

Material The right material needs to be chosen by the team to meet our functional requirement for wavelength, whilst keeping the noise and overall cost of the printed circuitry down. Fig. 61 presents common material types of photodiodes sold by Thorlabs, a photodiode manufacturer [26].

Material	Dark Current	Speed	Spectral Range	Cost
Silicon (Si)	Low	High Speed	Visible to NIR	Low
Germanium (Ge)	High	Low Speed	NIR	Low
Gallium Phosphide (GaP)	Low	High Speed	UV to Visible	Moderate
Indium Gallium Arsenide (InGaAs)	Low	High Speed	NIR	Moderate
Indium Arsenide Antimonide (InAsSb)	High	Low Speed	NIR to MIR	High
Extended Range Indium Gallium Arsenide (InGaAs)	High	High Speed	NIR	High
Mercury Cadmium Telluride (MCT, HgCdTe)	High	Low Speed	NIR to MIR	High

Fig. 61 Photodiode Material Characteristics [26]

The most common material type used in photodiodes is silicon. Silicon photodiodes are used for wavelengths between 190-1100 nanometers and produce lower dark current than most materials, resulting in less inherent noise. Considering these desirable qualities and the relatively low cost on the market, silicon is one of the most common materials for photodiodes in industry. This means we can get a larger active area for the same price as higher-end materials, resulting in overall better measurements. Silicon photodiodes also have flight heritage to our specific project, being used in the SAGE II instrument. InGaAs photodiodes use a combination of indium, gallium, and arsenic to achieve measurement abilities at higher wavelengths than silicon photodiodes, particularly from 800-1700 nanometers [27]. Lastly, germanium photodiodes typically work in the 900-1600nm range. They have the largest active area resulting in stellar sensitivity in this described region, but this comes at an increased price and larger dark current than other variants.

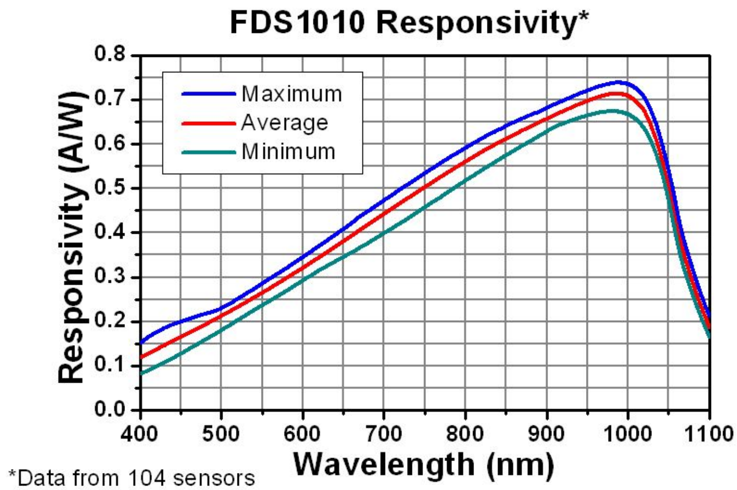

Fig. 62 Silicon Responsivity Curve [26]

Ideally, the bandgap energy of the chosen photodiode material should be similar to the photon energy corresponding to the longest wavelength we expect to encounter. This ensures strong response and low dark current [28]. Thus, the design choice will heavily rely on this quality, but will be affected by inherent dark current generated noise, as well as the material cost. Since all materials cover the 1020-1030 nanometer range, the trade study will primarily look at responsivity curves for photodiodes. We see a sample responsivity curve below in Fig. 62.

Analog to Digital Converter Options

The analog to digital converter is the heart of NanoSAM II's circuitry. It takes the current output from the photodiode and converts it to a digital signal that can be read by the chosen computer system. The choice of ADC will heavily determine the final circuit layout, as each variant of ADC has a different configuration to suit its needs. Our ADC choice ultimately depends on the resolution, conversion speed, power requirements, physical size, compatibility with our computer choice, and the photodiode interfaces [29]. ADCs often require some signal conditioning of the analog signal, which will be accomplished by some form of amplifier and low pass filter depending on the chosen ADC.

Successive Approximation (SAR) A successive approximation ADC works by taking a sample of the electric signal and holding it (sample and hold, or SHA). An internal comparator determines if this SHA output is greater than an internal digital/analog converter (DAC) output, and stores the result in the successive-approximation register. The scale on the internal DAC is then either raised or lowered depending on the SHA return, and the process repeats. This type of ADC is the most popular in most data-acquisition uses, and is often used for multiplexing of varying channels [30]. We see a diagram of the basic internal workings of a typical SAR ADC in Fig. 64. These ADCs consume low power, and are often smaller in board space. Resolutions typically range from 8-16 bits, but it has lower sampling rates for higher resolution applications. Additionally, the size of the SAR ADC will increase rapidly as resolution increases.

Sigma-Delta The sigma-delta ADC works similarly through a 1-bit comparator and switch, providing strong linearity in the differential digitized signal. The ADC encodes the analog signal using a technique known as delta modulation, where the change in the signal is recorded, as performed by an analog integrator inside the circuity. The results are then sent to a digital filter to perform noise shaping (essentially a low pass and high pass filter combined). The number of internal integrators determines the order of the delta modulating component of the ADC. We see a diagram of the basic internal workings of a typical first order sigma delta ADC in Fig. 63. The benefit of this ADC is high resolution and low noise results, due to the inherent oversampling and noise-shaping discussed previously. Similar to the SAR ADC, sigma-delta ADCs have increased in popularity and exist in low cost and low power consumption models.

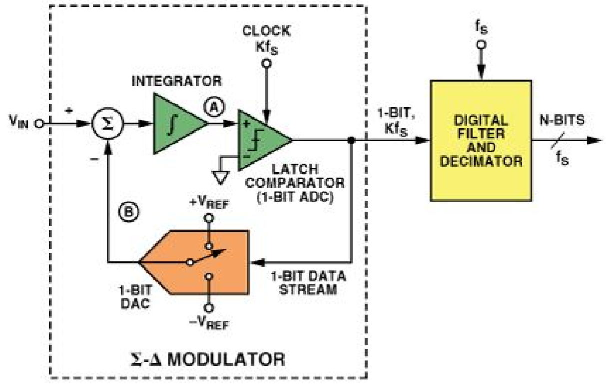

Fig. 63 **Basic Sigma Delta ADC [30]**

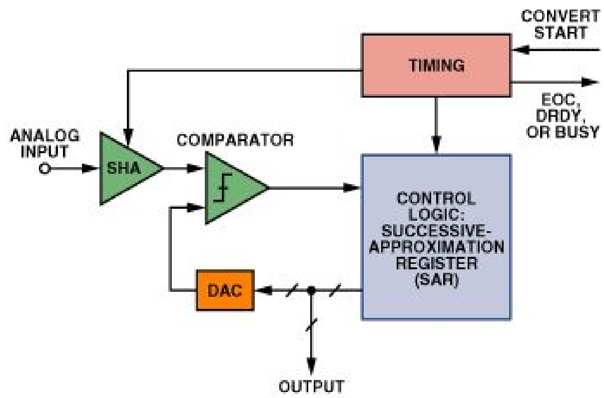

Fig. 64 **Basic SAR ADC [30]**

Pipelined The pipelined ADC, sometimes referred to as flash ADC, has the simplest internal workings. They use a simple chain of resistors to divide the voltage level of the arriving signal, which is then sent through a comparator to return a binary output. We see a diagram of the basic internal workings of a typical 6-bit pipelined ADC in Fig. 65. The benefit of this simple model is speed, as it performs much faster than the SAR and sigma delta ADC variants. However, increasing the resolution beyond 8-bits requires a large number of resistors in the chain, and is highly susceptible to temperature changes. Overall, this results in less accuracy and resolution for this ADC type, and higher noise produced. Due to the number of internal components, although simple, the ADC utilizes higher power consumption than other variants. There is also a subtle disadvantage when working in short bursts of data collection because low sampling rates extend the hold times on the internal track and cause conversion errors [30].

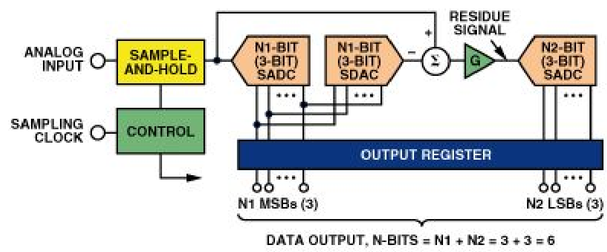

Fig. 65 **Basic Pipelined ADC [30]**

On Board Computer Options

If the ADC was the heart of our printed circuitry, then the on board computer will be the brain. After light is measured by the photodiode and transformed into a digital signal by the ADC, we need a computer system to packetize data, perform any required calculations, and then save the data. The on board computer must also communicate with the specified bus communications system, to transfer data for eventual downlink back to ground systems on Earth. There are three traditional types of computers used on board CubeSats. All of these options are susceptible to radiation damage and single event upsets (SEUs). Choosing an OBC that has multiple connection varieties will simplify transfer of data on the board, as well as simplify testing by allowing for easy access to data. Ideally, we would like to use USB for real time testing, and a straightforward option like a serial bus interface (SBI) between individual board components.

Field Programmable Gate Array (FPGA) The field programmable gate array is essentially a large collection of small logic gates that can be configured to the needs of the user. The FPGA is divided into groups of logic blocks that are connected through simple routing channels, and have input/output pads that surround them to take in data and run it through the complex logic. The logic gates within a modern FPGA are typically controlled by high level programming through Verilog or VHDL. The major benefit of using an FPGA is specificity and versatility. They can be programmed for almost any usage, and to an extremely precise level [32]. Thus, they have strong flight heritage for interaction with multiple parts of the electronic block, including data collection, storage, communication, ADCS, etc. The downside to the FPGA is that they are difficult to program, and may be overkill depending on the inherent challenge of the mission.

Microcontroller Moving up the chain of abstracted complexity, we have the microcontroller. The microcontroller is a chip that contains a small CPU, memory, I/O ports, timers, and other accoutrements. Essentially, it is a small computer. Microcontrollers lower the complexity associated with performing data handling, often at the cost of versatility. However, they are good at doing straightforward and repetitive tasks, and can still be used in a variety of applications, often through a higher level programming language like C. The small size makes them good for size limited applications like CubeSats, but comes at the cost of limited computational power. Most microcontrollers with significant flight heritage use ARM processors [33]. Most hobbyist microcontrollers typially use USB I/O, which is good for ground testing applications, but can communicate via a serial programming interface with other active electronics, such as traditional op-amp ADCs. An example of a microcontroller is the Teensy 4.0, employed by the NanoSAM I electronics design, and shown in Fig. 66.

PCB Computers Finally, we arrive at the top level of printed circuit board computers. These are also sometimes referred to as single board computers. Following the same logic as before, these devices abstract out more complexity associated with programming the computers applications. These devices are larger than microcontrollers, and have greatly increased processing power. They often come with additional features, such as multiple ADCs, different I/O options, and specialized attachments. The issue with these additional features is that often they must be selected ahead of time and increase the cost of the computer [34]. The most popular example of the on board computer is the Raspberry Pi, often used by hobbyists for a variety of simple projects, and sometimes for student projects in space. One model of the Raspberry Pi is shown below, in Fig. 67. Although the Raspberry Pi is a cheap option, most PBC computers with flight heritage are radiation hardened and cost thousands of dollars.

Fig. 66 Teensy 4.0 Microcontroller

Fig. 67 Raspberry Pi On Board Computer

Storage Options

With all satellites on orbit, data can only be downlinked back to Earth in very specific windows. Thus, most satellites must have a form of on-board storage to hold collected data before it can be downlinked. The selection of an on-board computer has a large part in determining the type of storage, since the two must communicate with each other. Although some microcontrollers and OBCs contain their own internal storage, it is strong redundancy to have a backup form of external storage, as the OBC internal storage can be used for housekeeping data not related to the mission crucial data [35]. The previous team's storage trade study focused on the differences between SSD, microSD, USB, and flash storage. Although USB and the SSD/microSD storage options are useful for testing with a computer, the electronic design for NanoSAM II will require external storage that exists within integrated components (IC's) for placement on the PCB. IC's providing external storage fall within four categories: flash, SRAM, DRAM, and EEPROM [39].

Flash Flash storage is made of memory cells that use MOSFET transistors to operate as either NAND or NOR gates [36]. The differences between NAND and NOR flash are irrelevant at this stage, and will be determined by exact electrical characteristics required during the design phase. Flash memory is non-volatile, which means that if the power to the external storage is lost, the data will not be lost. However, the network topology of flash memory is such that individual bits cannot be erased, and require erasure of a block of memory. Furthermore, removing data is physically destructive due to the voltage required to remove trapped electrons from the MOSFETS [38]. Flash memory is cheap, small, fast, and provides some inherent radiation resistance to single event upsets. Flash memory also has increasing usage in OBCs, giving it flight heritage.

SRAM and DRAM Random access memory (RAM) is a volatile storage type, meaning that if the IC chip loses power, data is lost. Thus, RAM is typically used for temporary storage, and could be used to store collected data before being downlinked, depending on difference between downlink times. DRAM stands for dynamic RAM, and it consists of a transistor and a capacitor. DRAM in particular is destructive during the read operation, and will require another write operation to save data that is read. SRAM consists of six transistors in a flip-flop latch as opposed to the single transistor and capacitor. This latch removes the DRAM flaw of destructive reads, making it faster. However, the increased number of transistors makes it more expensive than DRAM [38]. Some modern day variants of DRAM include synchronous DRAM, which allows the memory to be synced with the clock speed of a microprocessor, but this is more complex in an external storage configuration.

EEPROM Electrically Erasable Programmable ROM (EEPROM) is a type of read only memory (ROM), and one of the older types of external memory out of the options here. Although not often used with modern electronics, it is included in the potential design options to show depth of research. EEPROM utilizes two transistors that activate based on their threshold voltage, applied during the read operation. The driven current goes through a sense amplifier to return a 1 or 0 during the read [37]. EEPROMs are programmed by the IC manufacturer to specifications as determined by the part listing. Although EEPROM is a viable form of read only memory, one of the requirements of our external storage is that it provides write capabilities to store the data that is collected on orbit. Thus EEPROM is not included in the trade study because it does not meet our requirements.

B. Software Design Alternatives

Data Capture Timing

NanoSAM II will collect optical data sets twice each orbit: once during sunrise and once during sunset. The software must be able to capture data in both scenarios by defining an accurate data collection window of consistent duration. See the CONOPS section for more information on these optical data collection windows.

Continuous Data Collection In this configuration, data will be continuously recorded and temporarily stored, but only data of interest will be marked for transmission. In the case of a sunrise the photodiode will detect some threshold value at the beginning of the collection window, and data collected over the following period will be marked for storage and transmission. In the case of a sunset the photodiode signal will drop below the threshold value at the end of the collection window, and data collected over the preceding period will be marked for storage and transmission.

Triggered via Integrated Clock with Calibration via Photodiode In this configuration, data will only be collected and stored during predefined windows measured by the hardware-integrated clock. The timing of the data collection windows will be periodically adjusted by measuring the time of sunset and sunrise via the photodiode signal.

Calibration

To ensure the accuracy of data, NanoSAM II will measure a reference value when the photodiode's line of sight to the sun is outside the atmosphere. This reference measurement will be at the maximum solar intensity, and gives a baseline against which the data will be compared. Its magnitude will determine the precision of all following data. For ground testing the calibration value shall be measured at solar noon and the actual extra-atmosphere value will be extrapolated.

In Situ Calibration With this method NanoSAM II will re-calibrate at each data capture window. The calibration data will be stored internally and all incoming data will be modified relative to the calibration value before it is stored and transmitted.

On Ground Processing An alternative method is to store and transmit the raw, unmodified photodiode data as well as the calibration value. The data will then be analyzed relative to the calibration data once it has been transmitted to ground systems.

Error Detection

To identify and potentially correct data corrupted by interference, an error detection method will be implemented in all transmission packets. Additionally, an error detection method will be implemented within NanoSAM II's internal data storage to mitigate the effects of single event errors caused by charged particles.

Longitudinal Redundancy Check (LRC) With this method, also known as two dimensional parity, data units are grouped into blocks. Each data unit is appended with a single parity bit, and additionally each column of bits is assigned a parity bit. The column parity bits are then appended to the data stream as a redundant unit. LRCs are capable of detecting burst errors and single bit errors, but can easily miss two bit errors in any column [72].

Cyclic Redundancy Check (CRC) With a Cyclic Redundancy Check, data blocks are subjected to polynomial division and the remainder is appended to the block as a check value. The receiving hardware performs the same polynomial division accepts the data only if the check values match. CRCs are capable of detecting burst errors [72].

Hamming Code A Hamming code consists of parity bits placed within the data unit at all positions that are powers of two. Each parity bit considers only a portion of the total data unit according to its position, thus allowing the receiver to both detect and correct a single bit error. By appending a single parity bit to each data block a two bit error may also be detected, but not corrected. Hamming codes can detect errors up to two bits with certainty, and are capable of correcting single bit errors [65].

Repetition Code A simple-to-implement method of error detection in which data units are redundantly transmitted a fixed number of times. An error is detected whenever repeat data units are not identical, and by taking the majority of the units to be the correct data, errors can be ignored. Repetition codes can correct errors of any size, but cannot handle simultaneous errors in more than one identical data set [64].

C. Optics Design Alternatives

Telescope Selection NanoSAM I considered four different types of telescopes: Schmidt-Cassegrain, Newtonian, Herschelian, and Prime Focus. These four telescopes were compared through a trade study that evaluated each on the basis of cost, manufacturing complexity, optical aberrations, effective focal length, and obstruction. Based on these metrics, the Herschelian telescope was determined to be the optimal design choice. The trade studies and analysis performed by NanoSAM I are shown in Tab. 23,54-56, and Section 6.2.3 of NanoSAM I's Conceptual Design Document [74], and are summarized below.

The Herschelian telescope has a relatively simple design when compared to the other design options considered (shown in Fig. 12 of source [74]). The main reason for this is that the Herschelian telescope only uses one mirror, while some of the other design options considered use pairs of mirrors. Shown in Fig. 105, the main component of the design is the OAP mirror, which reflects the incoming incident light and focuses it to a focal point off the optical axis. Due to the presence of a single, off-axis mirror, there are no obstructions. Therefore, the Herschelian telescope accepts the most light for a given aperture size. The simplicity of the design also vastly reduces the amount of manufacturing complexity, because there is only one mirror that needs to be aligned. Even with the simplicity of a single mirror, NanoSAM I proved that alignment is still very difficult, to the point where NanoSAM I failed to reach mission-critical alignment. Due to the complexity that would be added by the addition of a second mirror, NanoSAM II has decided to remain with a telescope design that utilizes a single mirror. Additionally, the Herschelian telescope designed by NanoSAM I has a focal length of 54.45 mm, which fits within the NanoSAM II payload size requirement of 0.5U without introducing additional complexity. Finally, the major components for the Herschelian telescope designed by NanoSAM I (mainly the OAP mirror) have already been purchased by NanoSAM I, lowering the cost and logistic risk of the optical system for NanoSAM II if this design is used. Because of the low cost, relatively low manufacturing and alignment complexity, sufficiently short effective focal length, and lack of obstructions, NanoSAM II has chosen to remain with the telescope design selected by NanoSAM I. The Herschelian telescope does have the possibility of optical aberrations which is true of all telescopes, but the aberrations of this type of telescope are manageable and the other selection parameters favor the use of a Herschelian telescope.

Filter Selection Originally, NanoSAM I intended to isolate a pass region at a central wavelength (CWL) of 1.02 µm, the wavelength of light measured by the SAM II instrument, but the team could not find COTS filters to accomplish this. Aerosols are not specifically correlated with absorption of 1.02 µm light. Aerosols absorb light with a large range of frequencies in the low IR spectrum. When measuring aerosol density by solar occultation, a quiet portion of the spectrum is all that is necessary. NanoSAM I found COTS filters to isolate 1.03 µm light. In this wavelength, aerosol absorption is the dominant change in signal wavelength, and scattering due to other sources is negligible. Additionally, there are minimal amounts of chemical reaction in this region [78]. Finally, NanoSAM II's photodiode is sufficiently sensitive to 1.03 µm light to detect aerosol absorption with an SNR of at least 3500 [8].

NanoSAM I purchased a bandpass and lowpass filter that together isolate a CWL of 1.03 µm light with a bandwidth of 0.0239 µm. The light outside of the passband is excluded by stacking a ThorLabs FLH1030-10 Bandpass filter and a ThorLabs FELH1000 Longpass (Lowpass) filter. The 1030 nm wavelength is optimal to measure aerosols because at this wavelength the aerosol concentration is higher than that of other atmospheric molecules (such as $N0_2, O_2$, and H_2O) by approximately an order of magnitude [78]. As is explained in Tab. 66-68 in NanoSAM I's Conceptual Design Document [74], these filters are hard-coated, and so they offer the best transmission when compared to the other filters. This increased transmission leads to more light entering the measurement instrument, and therefore a higher sensitivity for solar occultation. Additionally, these filters produce high optical density compared to other filter choices, which will also improve the instrument's sensitivity by reducing the amount of light received outside of the desired wavelengths [74]. Because these filters accomplish their purpose and are available to NanoSAM II at no cost, they will be used in NanoSAM II's design.

Thermal Effects on Filter CWL An experiment that was conducted by Sung-Hwa Kim and Chang-Kwon Hwangbo [61] found that for filters with a CWL of 1550 nm, the CWL changed as a function of temperature as shown in Fig. 68.

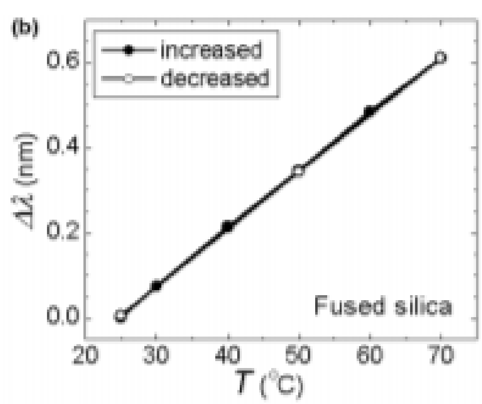

Fig. 68 Experimental Data Showing Changes of CWL with Temperature at 1550 nm [61]

The change in filter CWL at 1020 nm, as verified by optical engineer and project costumer Jim Baer, can be found using the following equation.

$$\Delta\lambda_{1020nm} = \frac{1020}{1550}\Delta\lambda_{1550nm}$$

Using this equation yields the equation for change in CWL as a function of filter temperature:

$$\Delta\lambda = 0.0089T_{filter} - 0.2174nm$$

This equation is graphed for a variety of filter temperatures in Fig. 69.

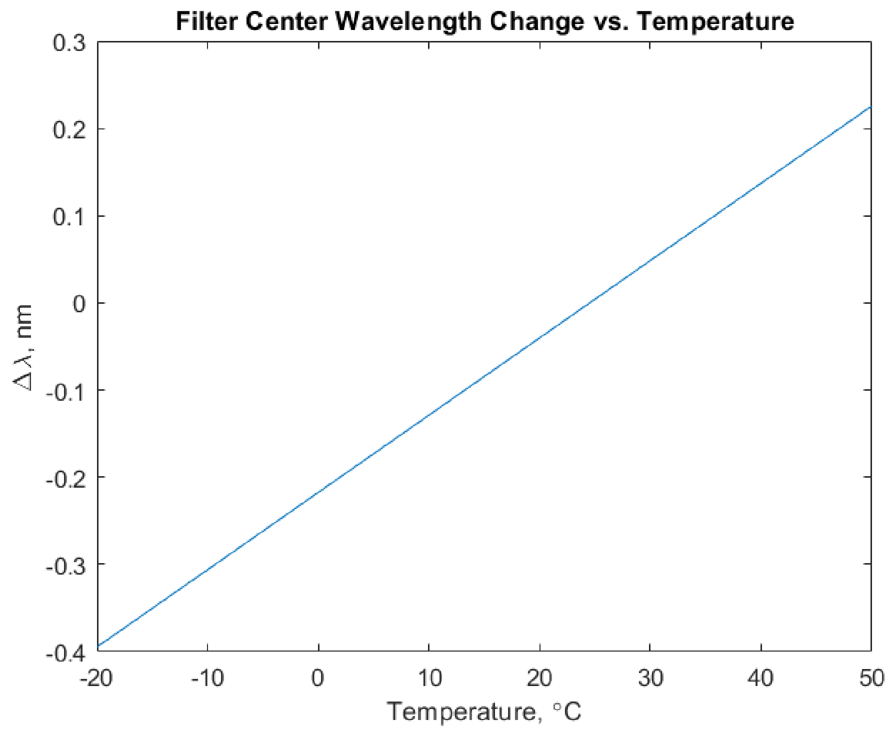

Fig. 69 Change in Filter CWL with Temperature at 1020 nm

The change in CWL affects the photodiode incident power and responsivity which in turn affect the photodiode current and the shot noise of the photodiode. The maximum incident power and responsivity were estimated in detail and will be discussed later in this section whereas the shot noise was discussed previously. The change in these parameters relative to filter temperature is highlighted below. Starting with how the incident power changes with filter temperature, the two parameters which are affected by changes in filter temperature are the solar spectral irradiance value, Φ, and the reflectivity of the mirror, as described by the following equations:

$$\Phi = -0.0013T_{filter} + 2.0128W/nm/m^2$$

and

$$R_{OAP} = 1.0679 * 10^{-5}T_{filter} + 0.8783$$

Combining these two parameters and plugging all values into equation 28 yields the equation for maximum incident power shown below.

$$P_i = -9.059 * 10^{-8}T_{filter} + 0.00658W$$

Note that the partial derivative of incident power with respect to filter temperature is on the order of 10^{-8} and as such the change in incident power due to filter temperature is negligible.

When looking at the responsivity at 1020 nm, using the equation 29, the partial derivative with respect to filter temperature can be found using the following equation which yields a value of -3.5126*10^{-6} A/W/K at the maximum photodiode temperature predicted by the thermal model. Note that the constant C = 0.0092 %/nm/K as explained later in this section.

$$\frac{\partial R}{\partial T_{filter}} = 0.01R_{1020nm,25°C}C(T_{photodiode} - 25°C)\frac{\partial \lambda}{\partial T_{filter}}$$

Similarly the partial derivative of the shot noise with respect to filter temperature was found by using the following equation where the parameters are the same as explained in the electronics detailed design section:

$$\frac{\partial I_{shot}}{\partial T_{filter}} = \frac{2qf(P_i \frac{\partial R}{\partial T_{filter}} + R \frac{\partial P_i}{\partial T_{filter}})}{\sqrt{2qf(P_i R + I_{dark})}}$$

Plugging in maximum values for incident power, responsivity, and dark current yields a value for this parameter of -7.567*10^{-15} A/K, and this change is negligible as the shot noise is on the order of 10^{-10} A.

Similarly the partial derivative of the total current with respect to filter temperature was found using the equation. Note that the Johnson and dark noises are independent of filter temperature, but not photodiode temperature.

$$\frac{\partial I}{\partial T_{filter}} = \frac{\partial I_{shot}}{\partial T_{filter}} + R \frac{\partial P_i}{\partial T_{filter}} + P_i \frac{\partial R}{\partial T_{filter}}$$

Plugging in maximum values yields a maximum value of -5.634*10^{-8} A/K. Multiplying this value by the expected maximum filter temperature of 30.8491 ° C gives an estimate for the maximum change in current due to filter temperature which is significant at -1.738 μA as the photodiode current is on the order of a few mA.

Due to this factor being not negligible, the bandpass filter should be included within the bounds of the thermal isolation of the optical bench, but due to the difficulty of manufacturing parts to do this, this task will be one that is deemed out of scope and will be done by a future team.

Mirror Substrate and Coating Selection Because NanoSAM II has elected to use NanoSAM I's legacy components, the substrate and coating of the OAP Mirror has been decided; Aluminum will be used for both. Use of the same material throughout the optics system is optimal because it ensures that all components will have the same CTE, which will eliminate thermal stresses. NanoSAM I chose protected aluminum as the optimal mirror coating due to the cost, reflectivity at 1.03 µm, and durability. As is outlined in the trade study analysis performed in section 6.2.3 of NanoSAM I's Conceptual Design Document [74], protected aluminum is a popular mirror coating for devices measuring wavelengths in the required spectrum. Additionally, protected aluminum is relatively durable (when compared to other possible coatings such as protected silver or gold). Because smoothness of the mirror surface is critical to taking successful measurements, using a material that is resistant to scratches can increase the likelihood of proper measurements being taken. While protected aluminum is not as reflective as other possible mirror coatings, this is outweighed by the optimization of protected aluminum for the desired wavelength. Finally, protected aluminum was also the least expensive of the options considered. Once protected aluminum was chosen as the mirror coating, the mirror substrate material was chosen to be Aluminum 6061-T6 in order to have a continuous CTE across the mirror [74].

Photodiode Saturation Calculations The calculations for these parameters are gone through in depth in the following.

The maximum incident power can estimated using the assumption of a uniform solar disk by equation 28.

$$P_i = \frac{FOV}{\theta_{sd}} \Phi BW A_{ap} F_{corr} F_{trans} \tag{28}$$

The values used for the field of view and uniform solar disk diameter were 1.3 arcminutes and 31.99 arcminutes respectively. The value for the bandwidth was estimated to be the same size as the bandwidth of the NanoSAM I filter system of 24 nm and the area of the aperture is calculated from the dimensions of the aperture to be 1*10^{-4} m^2. Note that F_{corr} is a correction factor for the use of the uniform solar disk assumption. This value was found by estimating the average value of a SAM-II signal (radiance) obtained from the paper by McCormick Et. Al. [62] by estimating the integral over the time period that corresponds to a data capture period and dividing it by that time interval. This process is illustrated in Fig. 70.

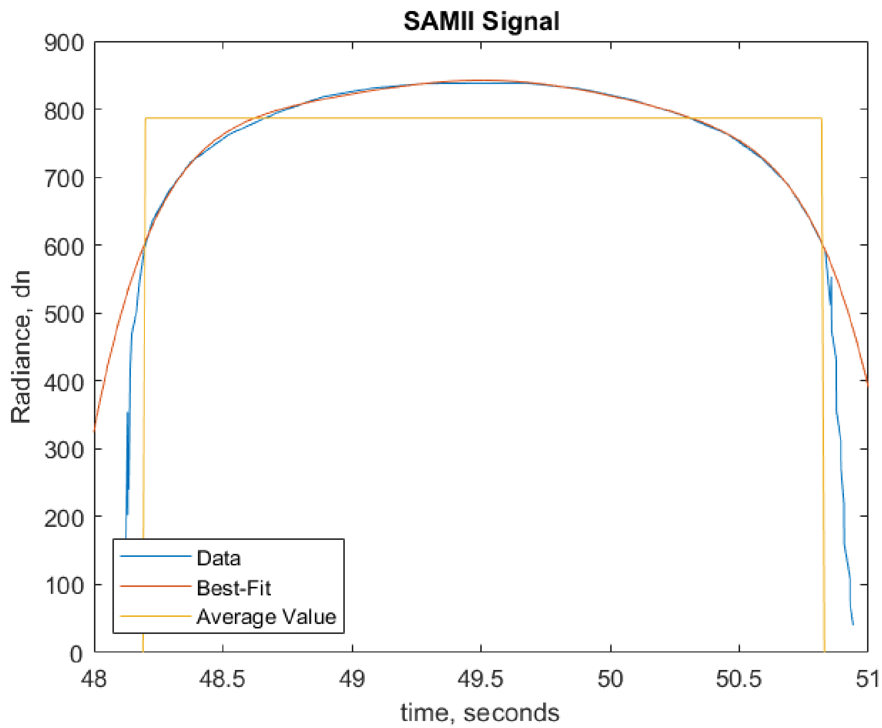

Fig. 70 Average value of SAM-II signal versus SAM-II signal

The correction value was found using the following equation where r is the radiance value recorded by SAM-II.

$$F_{corr} = r_{max}/r_{avg} = P_{i,max}/P_{i,avg}$$

Doing this calculation yields a value for F_{corr} of 1.0702.

The values for the solar spectral irradiance, Φ, were obtained from the National Renewable Energy Laboratory [63] and were taken at wavelengths around 1020 nm. Using this data, an estimate for the solar spectral irradiance as a function of filter temperature was found as discussed in the filter section above. This yields this equation:

$$\Phi = -0.0013T_{filter} + 2.0128W/nm/m^2$$

The transmission factor F_{trans} can be found by multiplying the transmission factors of part in the path of the light before the light reaches the photodiode as shown in this equation:

$$F_{trans} = F_{bandpass}F_{longpass}R_{OAP}$$

The average values for the transmission factors within a small band around the CWL of the bandpass filter and past the cutoff frequency of the longwavepass filter were used for the calculation of incident power. The average transmission factor of the FLH1030 was used as a substitute for the transmission factor of the 1020 nm CWL filter that will be ordered by a future team as it was assumed that both filters will have similar transmission profiles. The transmission value of the filter system was estimated to be 0.9443.

The reflectivity of the mirror is shown below in Fig. 71, obtained from the manufacturer of the OAP, Edmund Optics.

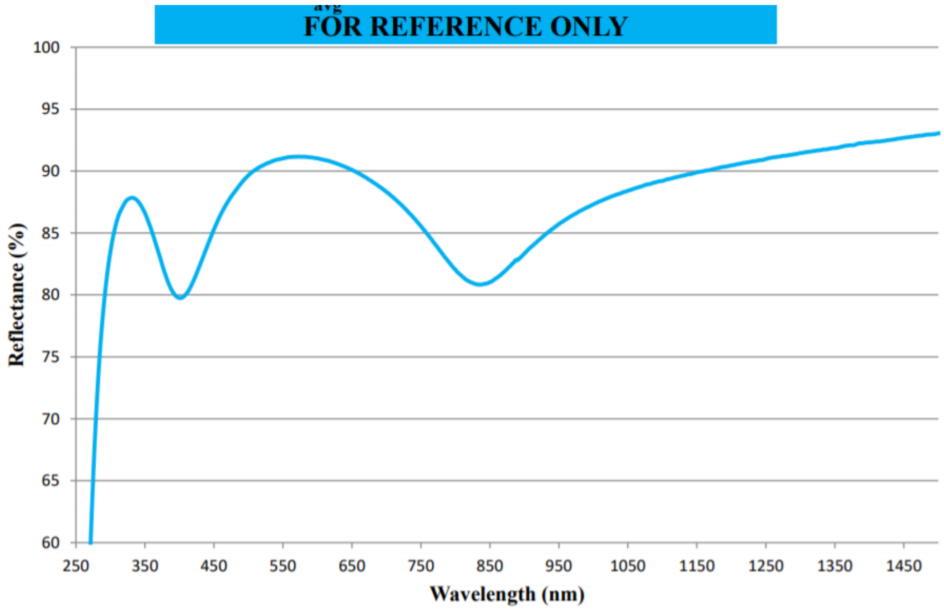

Fig. 71 Reflectivity of OAP as a Function of Wavelength from Edmund Optics

The value at 1020 nm was estimated using the following curve fit shown in Fig. 72 and the equation below the Fig. where $\Delta\lambda$ is the CWL shift of the filter system with filter temperature.

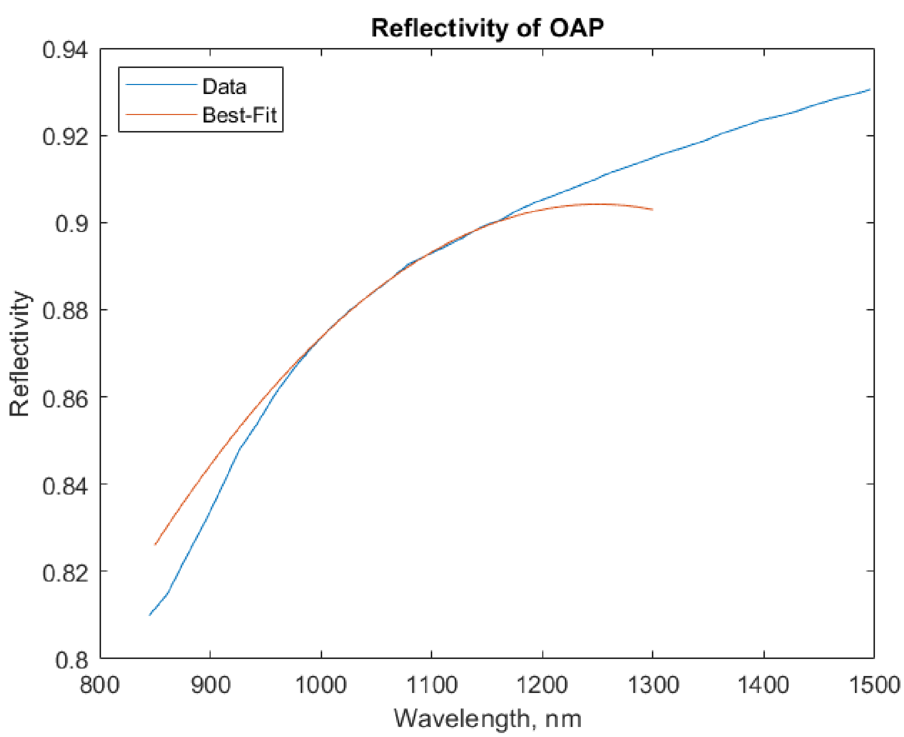

Fig. 72 Best Fit Curve for Reflectivity

$$R_{OAP} = -4.8878 * 10^{-7}(\lambda + \Delta\lambda)^2 + 0.0012(\lambda + \Delta\lambda) + 0.1405$$

With all of this information, an equation for the incident power as a function of filter temperature was found to be the following equation:

$$P_i = -9.059 * 10^{-8} T_{filter} + 0.00658W$$

From this equation, an estimate for the maximum incident power was found to be 0.0066 W.

Next, an estimate for the responsivity of the photodiode was found at various photodiode temperatures. This was done by first finding a base value at 1020 nm 25°C as a baseline. This was done by using the plot obtained from the manufacturer of the photodiode, ThorLabs, which is shown in Fig. 73.

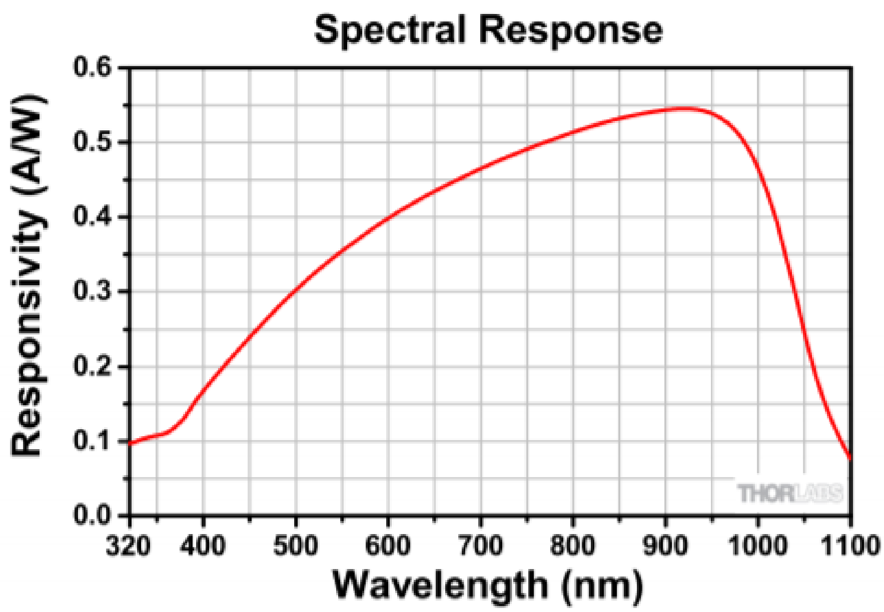

Fig. 73 Responsivity of the Photodiode as a Function of Wavelength at 25°C [26]

Next the figure shown in Fig. 74 was used to find how the responsivity changes with photodiode temperature and an equation was found for the responsivity as a function of photodiode temperature and CWL shift in the neighborhood of 1020 nm. This was done using each curve at different temperatures to find an average rate of change of responsivity with wavelength and generalizing it for different temperatures. This equation can be seen in equation 29 where the constants C = 0.0092 %/nm/K and λ_0 = 952.85 nm.

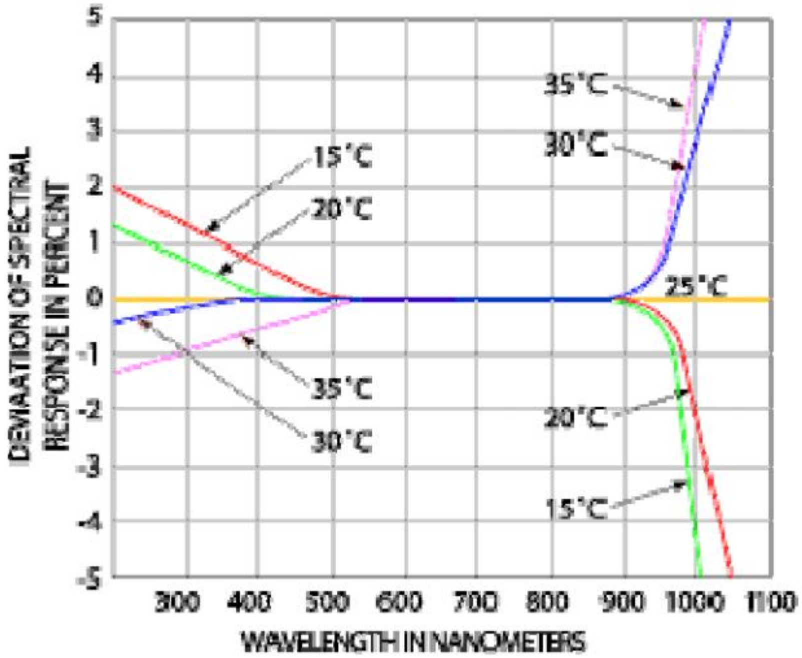

Fig. 74 Deviation in Responsivity with Temperature

$$R = R_{25^{\circ}C}(1 + 0.01C(T_{photodiode} - 25^{\circ}C)(\lambda + \Delta\lambda - \lambda_0)) \quad (29)$$

Plugging in the temperature values obtained by the thermal model, for both photodiode and filter temperatures, yields a maximum responsivity during a sunrise and sunset event respectively to be 0.3456 A/W and 0.3660 A/W. To ensure a large factor of safety, the value at a photodiode temperature of 30°C of 0.4046 was selected to be the absolute maximum the system could handle, before photodiode saturation could occur.

Optical Axis - Interferometer Beam Alignment Method NanoSAM I used two tilt micrometers, controlling yaw and pitch, to precisely dial in the alignment of the OAP mirror's optical axis to the interferometer's beam. NanoSAM II will continue to use tilt micrometers to control pitch and yaw and add a kinematic base [82] which will allow the radiometer to be removed and replaced throughout the alignment process without disturbing its orientation relative to the interferometer's beam.

Photodiode Block Translation Tunability Options

NanoSAM II's alignment procedure will follow the same concept as NanoSAM I's procedure, identically if shims are the selected option, similarly if rails or translational mounts are the selection. A brief overview of each alignment process is given below.

Alignment Procedure using Shims The interferometer's beam will be aligned along the OAP mirror's optical axis, Z-axis (See Fig. 75), using tilt micrometers and reflected along the Z'-axis. Next, the photodiode block, the structure which holds the pinhole field stop and photodiode, is mounted to a 3-axis stage. A chrome half sphere is centered on top of the pinhole so that interferometric measurements can be made to move the pinhole closer to the focus of the OAP. The 3-axis stage is used to position the chrome half sphere at the focus point using the interferometric measurements minimize the aberrations. During each step, the required offsets along each axis are calculated, and the equivalent shims are placed. These steps are repeated until the radiometer is aligned and aberrations are below the acceptable maximum.

Alignment Procedure using Rails or Translational Mounts The interferometer's beam will be aligned along the OAP mirror's optical axis in the same manner as the case for shims. Divergently, the rails and/or mounts are attached to the optical bench. The photodiode block is attached to the rails and/or mounts. A chrome half sphere is centered on top of the pinhole for interferometric measurements. The rails and/or mounts are used to position the chrome half sphere at the focus point using the interferometric measurements. These half sphere steps are repeated until the radiometer is aligned.

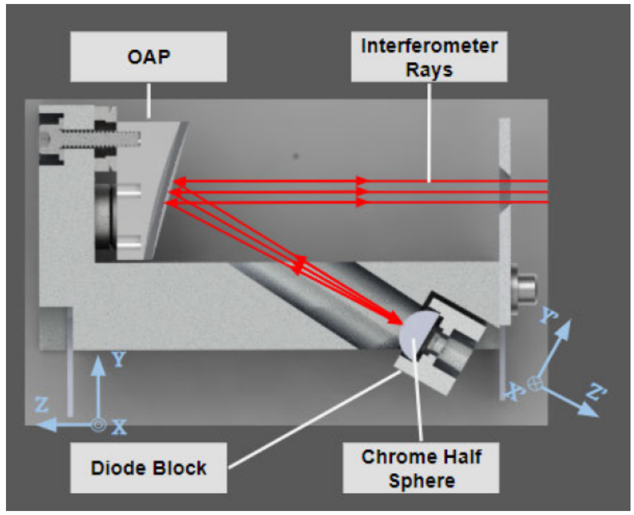

Fig. 75 Alignment Diagram [8]

As seen in the overview of the alignment process, the pinhole assembly must be adjusted to be directly centered on the focus produced by the OAP of the interferometer beam. Because the pinhole is rigidly mounted to the photodiode block, the photodiode block's mounting points on the optical bench must be adjustable relative to the OAP mirror. Descriptions of each option to adjustably mount the photodiode block are listed below.

Shims Shimming is the most simple, industry practice for offsetting components precisely in optical engineering. By placing shims of well-characterized thickness in gaps between rigidly mounted components, off-sets can be achieved with relative ease with tens of micrometers of precision. NanoSAM I's shim sizes ranged from 25.4μm to 254μm.

Rails By placing the photodiode block on COTS optical rails, adjusting offsets would be as simple as sliding components to the desired location and securing position via set screws during testing. Prior to flight, adhesive is applied to reinforce the orientation. Rails would reduce the amount of time adjustments take during the alignment process. [83]

Translational Mounts The photodiode block could be translated along the axes using a COTS translational optics mount. These mounts use high-thread count bolts to precisely dial translational displacement with single micrometer precision. The orientation is held by set screws during testing. Prior to flight, adhesive is applied to reinforce the orientation.

The three possible options are shown in Fig. 76 below.

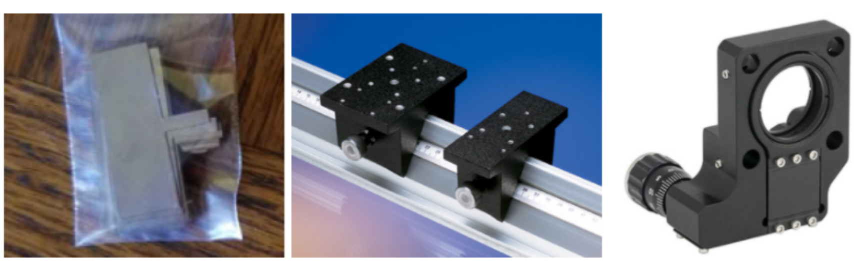

Fig. 76 From left to right: NanoSAM I Shims [8], Ealing Optical Rails [75], Thorlabs Z-axis Translational Mount[76]

Reducing Diameter of OAP Mirror

Due to the anchor points deforming the mirror, NanoSAM I's OAP mirror introduces tilt aberrations, which causes the wavefront to displace (WFE), which decreases the MTF value of the radiometer. Minimizing these aberrations yields a more acceptable MTF value. This can be done by increasing the diameter of the OAP, since the deformation at the center of the mirror due to the anchor points is smaller as the anchors are farther away.

Current COTS OAP Mirror By keeping NanoSAM I's OAP mirror, significant financial costs and technical bottlenecks are avoided. The current OAP mirror is a well-characterized COTS component supplied by Edmund Optics. This is the largest, COTS, OAP mirror within the team's budget. Keeping the current OAP mirror will not decrease the amount of WFE.

Custom OAP Mirror Replacement By custom ordering a new OAP mirror with a larger diameter, the tilt aberrations can be reduced. Ordering a custom part may have significant financial cost/lead time, which may cause budget issues and project delays.

Photodiode Shield Geometry

A light blocker must be placed directly in front of the photodiode to select the desired field of view of the radiometer. The geometry of this blocker determines the shape and dimensions of the field of view. A pinhole will result in a circular FOV. A slit will result in a rectangular FOV.

Pinhole NanoSAM I selected a pinhole as their field stop. The pinhole selected was a circular opening 15 μm in diameter, which resulted in a circular field of view with a diameter of .95 arcminutes. According to the NanoSAM I calculations, the pinhole should have allowed in the necessary amount of power to achieve the required signal-to-noise ratio [8].

The field of view of the field stop is calculated using the equation

$$FOV = \frac{Ocular\ Field\ Stop\ Diameter}{Telescope\ Focal\ Length} * 57.3 \tag{30}$$

Slit Alternatively, a slit could be used instead of a pinhole. Because NanoSAM is only interested in vertical resolution, a slit geometry would allow for a greater amount of light to be collected. The slit would be a rectangular opening, with a maximum height of 20 μm, as this is the diameter needed to achieve the desired 1.3 arcminutes field of view using Eq. 30. The length of the rectangular opening would be 3 mm [81].

XI. Appendix B: Trade Study Metrics, Weighting, and Values

Structures Trade Studies

Material Options

Metric	Weight	Driving Requirements	Description and Rationale
Cost	0.3	6.0	Cost of the material is a driving factor since the structure is one of the main places to incur costs, especially due to manufacturing hours.
Density	0.3	4.2	The density of the material is directly related to the total mass of the system. In order to reduce the mass of the system, density must therefore be minimized. This assumes that all structures will have approximately the same volume.
Shear Modulus	0.2	5.1	The shear modulus of the material is directly related to its ability to resist deformation, and is critical in damping vibrations encountered during launch.
Coefficient of Thermal Expansion	0.1	5.2	The coefficient of thermal expansion (CTE) is related to requirement 5.2, which indicates that the entire payload shall remain operable over -120 to 120 C. Minimizing the CTE will reduce the effects of thermal swings and provide a more consistent structure for the payload.
Availability	0.1	5.0	The availability of materials is a driving metric separate from cost. The reason for this is that a material should be readily available in order to facilitate the completion of the project on time.

Table 23 Material Metrics and Weighting

Metric	1	2	3	4	5
Cost	>3.52$\$/in^3$	3.52-2.82$\$/in^3$	2.82-2.11$\$/in^3$	2.11-1.40$\$/in^3$	<1.40$\$/in^3$
Density	>2.78g/cc	2.78-2.75g/cc	2.75-2.73g/cc	2.73-2.70g/cc	<2.70g/cc
Shear Modulus	<26.0 GPa	26.0-26.2GPa	26.2-26.4GPa	26.4-26.6GPa	>26.6GPa
CTE	>23.02 $\mu m/mK$	23.02-22.68 $\mu m/mK$	22.68-22.34 $\mu m/mK$	22.34-22.00 $\mu m/mK$	<22.00 $\mu m/mK$
Availability	Not Widely Available and/or not in form factor needed	N/A	Widely Available, but not in form factor needed	N/A	Widely Available and in form factor needed

Table 24 Structural Material Metric Values

Optical Bench Integration Options

Metric	Weight	Driving Requirements	Description and Rationale
Thermal Isolation	0.35	5.2	A mounting method that thermally isolates the key components from the rest of the structure will help to meet requirement 5.2, as it will facilitate the use of resistive heaters or other elements to reduce the temperature variation due to conduction on orbit.
Vibration Isolation	0.25	5.1	A mounting method that reduces vibrations that reach the optics helps to meet requirement 5.1.1 in particular; reducing these vibrations will help to prevent misalignment in the optics.
Availability	0.25	6.0	Using widely available components that have been demonstrated to be useful for the desired application reduces risk in the project and increases overall confidence.
Space Cost	0.15	5.0	A mounting method that takes up a minimal amount of space is preferred, as it will make it easier to make later changes and be more adaptable if the geometry of the structure is less constrained.

Table 25 Optical Bench Integration Metrics and Weighting

Tab. 25 above has the driving weights and metrics for the optical bench integration method. In the CDD [74], the thermal isolation was weighted at only 0.25, and the availability was weighted at 0.2. With an improved understanding of how the temperature of the photodiode block affects the signal to noise ratio, the relative importance of thermal isolation was increased. Additionally, all of the methods considered can be modeled and are likely to succeed, so those metrics from the CDD were removed. In their place, a space cost metric was added that allows for the footprint of the part to be considered.

Metric	1	3	5
Thermal Isolation	Provides no thermal isolation	Provides minimal thermal isolation	Provides a significant amount of thermal isolation
Vibration Isolation	No vibration isolation	Isolation in less than three degrees of freedom	Isolation in three degrees of freedom
Availability	Needs to be designed in-house	Demonstrated, but needs additional work to implement	Commercially available off the shelf
Space cost	Part takes up a significant volume or requires a specialized mount	Mount requires minimal changes to other parts to fit	Mount requires no changes to any other structural parts to fit

Table 26 Optical Bench Internal Integration Metric Values

The above table for the optical bench mounting method has a few qualitative metrics, which is necessary since some of the mounting methods are speculative and would need to be designed by the structural team. As such, many of the metrics are presumptive and chosen with the intent to determine if the potential cost of designing a mounting method would be acceptable. Cost was not a differentiating factor, as the team expects all methods to have about the same cost. Instead, the primary cost consideration is included in the availability metric.

Electronics Integration Options

Metric	Weight	Driving Requirements	Description and Rationale
Electronics Input	0.40	5.0	The input of the electronics team was taken into account, including the ability to connect the board to the chassis ground and the impact the mount has on the available surface for parts.
Vibration Isolation	0.25	5.1	A mounting method that reduces vibrations ensures that the electronics will remain functional in orbit.
Availability	0.25	6.0	Using widely available components that have been demonstrated to be useful for the desired application reduces risk in the project and increases overall confidence.
Space Cost	0.10	5.0	A mounting method that takes up a minimal amount of space is preferred, as it will make it easier to make later changes and be more adaptable if the geometry of the structure is less constrained.

Table 27 Electronics Integration Metrics and Weighting

Metric	1	3	5
Electronics Input	Electronics team has to make a significant amount of compromises	Electronics team can make a minimal amount of compromises	Electronics team preferred design, based on electrical and board considerations
Vibration Isolation	No vibration isolation	Isolation in less than three degrees of freedom	Isolation in three degrees of freedom
Availability	Needs to be designed in-house	Demonstrated, but needs additional work to implement	Commercially available off the shelf
Space cost	Part takes up a significant volume or requires a specialized mount	Mount requires minimal changes to other parts to fit	Mount requires no changes to any other structural parts to fit

Table 28 Electronics Internal Integration Metric Values

The above table for the electronics mounting method has a few qualitative metrics, which is necessary since some of the mounting methods are conceptual and not explicitly defined. Moreover, all of the options considered are considered to have roughly the same availability.

Electronics Trade Studies

1. Photodiode Options

Metric	Weight	Driving Requirements	Description and Rationale
Dark Current	0.4	2.1, 5.2	The leading cause of noise for photodiodes is the dark current. Reducing dark current sources is vital to collecting accurate data and maintain a high signal to noise ratio. Dark current is proportional to temperature and active area.
Responsivity	0.4	1.1	Responsivity is a measure of the effectiveness of converting light into current. It is important to select a photodiode material that exhibits high responsivity in the bandwidth region closest to 1030 nm. Different photodiodes work best in different wavelength ranges, so picking a material that expresses high responsivity in a wavelength range closest to 1030 nm is crucial.
Active Area	0.1	5.1.1	A larger active area provides more surface for light to hit the semiconductor material and be converted into current, which allows for redundancy in optical system alignment, giving room for error introduced in vibrational scenarios.
Cost	0.1	6.0	In NanoSAM I, the optical system took a significant portion of the budget. Any replacement of optical parts will consume a large portion of the budget, and thus, keeping electronics pieces cheap and simple is crucial to maintaining the 5000 dollar budget. Photodiode cost can range heavily, and can be quite expensive.

Table 29 Photodiode Metrics and Weighting

Metric	1	3	5
Dark Current	1-5	1-5 nA	1-5 pA
Responsivity	0-0.5 A/W	0.5-1.0 A/W	>1.0 A/W
Active Area	0-1 mm^2	1-5 mm^2	>5 mm^2
Cost	>$100	$50 - $100	$5 - $15

Table 30 Photodiode Metric Values

2. Analog to Digital Converter Options

Metric	Weight	Driving Requirements	Description and Rationale
Resolution	0.4	1.1.2, 2.1	The ADC must digitize the continuous photodiode current into data with discrete measurements. The bit resolution of the ADC must be enough to resolve aerosol concentrations from the irradiance measurements, meeting the customer set requirement.
Power Consumption	0.2	1.4.5	Active circuits on the PCB will contribute to a large sink of total power budget, which is defined by the batteries aboard the selected bus design.
Conversion Speed	0.1	1.1.1, 2.1	The speed of conversion will consequently determine the data sampling rate, meeting the 50 hertz requirement. Low weight is assigned here however, because almost all modern ADCs can reach this requirement.
Size	0.1	4.0	The optical bench will take up a majority of 0.5U space for our payload. The ADC will be one of the larger elements on the PCB, and reducing size of the overall PCB to fit along the optical bench is crucial to the 0.5U requirement.
Computer Compatibility	0.1	1.0	It will be necessary for the ADC to communicate digitzed data with an on board computer system for data operations, transfer to storage, and downlink. This joint necessity is shared by the trade study for OBCs, and communication capability is typically versatile, so weight here is reduced.
Cost	0.1	6.0	ADCs are more expensive than photodiodes, but also relatively small compared to the on board computer, and thus weighted lower. Overall rationale for keeping costs low is described in the photodiode trade study, and is not repeated here.

Table 31 Analog to Digital Converter Metrics and Weighting

Metric	1	3	5
Resolution	< 8 bits	< 16 bits	< 24 bits
Power Consumption	> 0.01 W	0.001-0.01 W	< 0.001 W
Conversion Speed	< 1 kHz	1-10 kHz	> 10 kHz
Size	> 10 mm^2	3-10 mm^2	< 3 mm^2
Computer Compatibility	Parallel	SPI	SPI and DSP
Cost	> $100	$10-$100	< $10

Table 32 Analog to Digital Converter Metric Values

3. On-Board Computer Options

Metric	Weight	Driving Requirements	Description and Rationale
Versatility	0.3	1.0	The selected option must be able to communicate with the ADC, storage, and with the selected bus design. Since each of these items are dictated by trade studies, it will be important to select an option that has multiple I/O types and has strong redundancy with other PCB components.
Size	0.2	4.0	The size of the on board computer will be the largest element of the final PCB design, and thus it is vital that we choose options that allow our PCB to fit in the 0.5U requirement.
Cost	0.2	6.0	The OBC contributes to the largest individual element cost on the PCB. Overall rationale for keeping costs low is described in the photodiode trade study, and is not repeated here.
Complexity	0.1	1.0	With any time constrained project such as this, we seek a solution that meets requirements with minimum complexity. The OBC can be difficult to program in the FPGA case, or could come with existing open source software solutions in the case of some microcontrollers.
Processing Power	0.1	1.0, 1.1.1.1, 1.1.2	The selected OBC must be able to handle the data from the ADC, and store the data at a rate below the sampling rate to ensure no lost information. It also must be able to simultaneously handle bus interfacing, and any payload handling programs that are put on it. The weight here is lower however, because most OBCs should easily be able to handle our needs.
Power Consumption	0.1	1.4.5	OBCs are actually typically quite power efficient, but the power consumption, which is defined by the batteries aboard the selected bus design, must still be considered.

Table 33 On-Board Computer Metrics and Weighting

Metric	1	3	5
Versatility	1-3 I/O	3-5 I/O	> 5 I/O
Size	PCB Sized	-	IC Sized
Cost	> $1000	$100-$1000	$10-$100
Complexity	Custom/Proprietary Software	Standard Hardware (RS232)	Open Source (C++)
Processing Power	0-100 MHz	100-1000 MHz	> 1 GHz
Power Consumption	> 1 W	0.1-1 W	< 0.1 W

Table 34 On-board Computer Metric Values

4. External Storage Options

Metric	Weight	Driving Requirements	Description and Rationale
Computer Compatibility	0.4	1.0	Similar to the ADC, the memory must be compatible with the on board computer system for reading and writing of data. This joint necessity is shared by the trade study for OBCs. Modern storage requirements should handle our capacity and speed needs readily, so compatibility with the down selected ADC and OBC is most important here.
Storage Capacity	0.2	1.1.3	The memory storage capacity must be able to hold all the gathered data in the time difference between downlink periods.
Read/Write Speed	0.2	1.1.1.1	The memory internal read/write speed must be able to keep up with the ADC's sampling rate requirements, as well as the OBC's transfer requirements.
Size	0.1	4.0	On board storage sizes will be smaller than the OBC, but still not negligible on a PCB where every millimeter will count. Size in the presented storage design options varies significantly.
Cost	0.1	6.0	Memory costs will be lower than the PCB active components, so the weight is lower here. Overall rationale for keeping costs low is described in the photodiode trade study, and is not repeated here.

Table 35 Storage Metrics and Weighting

Metric	1	3	5
Computer Compatibility	Parallel	SPI	SPI & DSP
Storage Capacity	< 64 mB	64-128 mB	> 128 mB
Read/Write Speed	< 100 MHz	100-200 Mhz	> 200 MHz
Size	> 10 mm^2	5-10 mm^2	0-5 mm^2
Cost	> \$5	\$3-\$5	\$1-\$3

Table 36 Storage Metric Values

Software Trade Studies

5. Data Capture Timing

Metric	Weight	Driving Requirements	Description and Rationale
Timing Accuracy	0.8	1.1.4, 1.2.1	The ability to maintain an accurate data collection window over several hundred orbits will assure that data is reliably captured, while maintining a consistent data capture window duration will simplify the storage and transmisson processes. Reliable data capture is at the core of NanoSAM II's mission and is thus accurate timing is weighted highly.
System Resource Use	0.2	1.1.1.1	The usage of onboard memory and computation time must be optimized such that data can be processed at a minimum sample rate of 50Hz given by Requirement 1.1.1.1. Excess memory usage may unnecessarily increase the frequency of single event errors, potentially compromising data quality.

Table 37 Data Capture Timing Metrics and Weighting

Metric	1	3	5
Timing Accuracy	Collection window is prone to drift over time, potentially resulting in a total loss of science data	Data collection process may be susceptible to partial data loss over time	Data collection process is not susceptible to data loss.
System Resource Use	Resource load could necessitate a reduction in data processing speed	Resource load is nontrivial but unlikely to affect data processing speed. Additional storage space may be required	Resource use is trivial

Table 38 Data Capture Timing Metric Values

6. Error Detection Method

Metric	Weight	Driving Requirements	Description and Rationale
Maximum Correctable Error	0.35	1.3, 2.0	Uncorrected single event upsets in programming variables could cause software systems to malfunction and fail, thus it is essential that the error detection method includes some degree of error correction.
Maximum Detectable Error	0.3	1.3, 2.0	Error detection is required both for data transmission and memory to catch and ignore corrupted data packets which could compromise data quality and software operations.
System Resource Use	0.2	1.1.1.1	The usage of onboard memory and computation time must be optimized such that data can be processed at a minimum sample rate of 50Hz given by Requirement 1.1.1.1. Excess memory usage may unnecessarily increase the frequency of single event errors.
Downlink Data Rate	0.1	2.3	The ratio of total transmitted data that is not redundant. A low data rate may unnecessarily increase the size of each downlink.

Table 39 Error Detection Method Metrics and Weighting

Metric	1	3	5
Maximum Correctable Error	None	1 bit	> 1 bit
Maximum Detectable Error	1 bit	2 bits	> 2 bits, potentially burst errors
System Resource Use	Resource load could necessitate a reduction in data processing speed	Resource load is nontrivial but unlikely to affect data processing speed. Additional storage space may be required	Resource use is trivial
Downlink Data Rate	<50%	50% - 95%	>95%

Table 40 Error Detection Method Metric Values

Optics Trade Studies

7. Photodiode Block Translation Tunability

Metric	Weight	Driving Requirements	Description and Rationale
Material Complexity	0.3	5.2.2	The effects of thermal stresses on complex components are more difficult to control for than on simple components. Components with varying material type are more apt to have mechanical or structural relationship changes when subject to temperature changes than single material components. These changes adversely affect the optical alignment.
Friction Interactions	0.3	5.1.1	Mechanical and structural assemblies held in orientation by friction (e.g. set screws) are prone to change when subjected to vibrational stress. These potential changes in orientation would adversely affect the optical alignment.
Alignment Precision	0.2	3.2.2	NanoSAM I determined acceptable alignment errors last year which informs the metric of Alignment precision. These acceptable alignment errors were found by backsolving MTF estimates to ensure a particular error resulted in a minimum MTF of 0.74. As NanoSAM II's optical design progresses, the acceptable alignment errors may shift, but NanoSAM I's calculations offer a reasonable estimate.
Cost	0.1	6.0	The successful translation tuning of the photodiode block to the OAP mirror image is mission critical. However, the least expensive of equal options should be pursued.

Table 41 Photodiode Tuning Metrics and Weighting

Metric	1	3	5
Material Complexity	>3 unique materials	2-3 unique materials	1 unique material
Friction Interactions	Orientation fully dependent on Friction	Orientation dependent on Friction but reinforced with glue	Orientation independent of Friction
Alignment Precision	>25 µm	10 - 25 µm	<10 µm
Cost	>$300	$150-250	<$150

Table 42 Photodiode Tuning Metric Values

Metric	Weight	Shims	Rails	Translation Mounts
Material Complexity	0.3	5	3	3
Friction Interactions	0.3	5	3	3
Alignment Precision	0.2	3	1	5
Cost	0.2	3	1	1
Total	1.0	**4.2**	2.2	3.0

Table 43 Photodiode Tuning Trade Study Results

Information for this trade study came from the specifications provided by the manufacturers, and NanoSAM I's Project Final Report, shown in Sources [75],[76], and [8]. The price of shims are based on NanoSAM I's expense breakdown [8] while the price of rails and translation mounts are based on the estimated number of each component needed multiplied by the unit cost of that component, [75] and [76]. Alignment precision was sourced from [8] for shims, [75] for rails, and [76] for translation mounts.

8. OAP Mirror Selection

Metric	Weight	Driving Requirements	Description and Rationale
Diameter	0.2	3.2.2	A large source of wavefront error (WFE) is due to the anchor points that are used to mount the reflector. The anchors cause the surface of the reflector to deform which contributes WFE as the wavefront is also deformed. A reflector with a larger diameter has the anchor points farther away from the center of the mirror, which is where the light hits it, which means that the center is less deformed. Keeping WFE as low as possible will allow for it to be easier to meet requirement 3.2.2. In order to get a part with the same focal length (FL) and a larger diameter, a custom part would have to be ordered and created as there are not suitable COTS parts that would meet these requirements.
Cost	0.4	6.0	The cost of part is also important as a custom part will cost a significant portion of the budget whereas continuing to use the current OAP mirror will not have any cost associated with it. This will likely be the most prohibitive of the metrics as losing a large chunk of the budget could cause major issues down the line if the team does not have sufficient funding left to complete the project.
Production Time	0.4	1.0, 3.0	A custom part also will take a while to be made, which may cause project delays and will increase the project risk overall as not having the reflector will impact many aspects of the project.

Table 44 OAP Diameter Increase Metrics and Weighting

Metric	1	3	5
Diameter	<20 mm	20-25.4 mm	>25.4 mm
Cost	>$1000	$501 - 1000	$0 - 500
Production Time	61-120 days	30-60 days	0-30 days

Table 45 OAP Diameter Metric Values

A diameter of less than 20 mm is less than nominal as the aperture dimensions are 20mm by 5mm. In essence, this wastes light that is entering the system as some of the light entering the aperture would travel past the OAP. The current OAP has a diameter of 25.4 mm, an FL of 54.45 mm, and an incident-to-reflection angle of 30° and an Aluminum coating [8]. The proposed custom OAP would have a diameter of 38.1 mm, to keep the mirror around the same size, and maintain a FL of 54.45 mm and incident-to-reflection angle of 30° and the Aluminum coating [77],[78],[79]. The cost of using the current OAP is $0 since it was made available from the previous team's inventory. The rough cost estimate received for a custom OAP from Edmund Optics was found to be around $1000-$1200, which is a significant chunk of the team's budget and the production time was estimated to be a 12-17 week lead time. Using this information, the following table was compiled to complete the trade study giving each option values for each metric and computing the weighted average to determine the optimal strategy.

Metric	Weight	Custom OAP	COTS OAP
Diameter	0.2	5	3
Cost	0.4	1	5
Production Time	0.4	1	5
Total	1.0	1.8	**4.6**

Table 46 OAP Diameter Trade Study Results

9. Field Stop Geometry

Metric	Weight	Driving Requirements	Description and Rationale
Field of View	0.4	3.2.1	To meet requirement 3.2.1, the field of view must be 1.3 arcminutes in order to achieve a resolution of 1km. If the field stop is too small to achieve this requirement, the data taken will not meet the minimum accuracy to be useful.
SNR	0.4	2.1	The field stop must let in enough light to allow for a SNR of 3500 or greater in order to satisfy requirement 2.1
Cost	0.1	6	While cost is important, the cost of the field stop is relatively low compared to other optical systems. Therefore, cost is a consideration but is not weighted as heavily as the previous metrics.
Design Complexity	0.1	3	The system designed by NanoSAM I used a pinhole field stop, and so the design is already built for a pinhold field stop. If a pinhole is used by NanoSAM II the design will not need to be changed. If a slit is used the design will need to be modified to account for the change in field stop.

Table 47 Field Stop Metrics and Weighting

Metric	1	3	5
SNR	<3150	3150-3500	>3500
Field of View	<1.3 arcminutes	N/A	>1.3 arcminutes
Cost	> $100	<$100	$0
Design Complexity	Field Stop Redesign	Field Stop Modification	Use previous Field Stop

Table 48 Field Stop Metric Values

NanoSAM I used a 15 μm pinhole, and calculated that this was a sufficient diameter to meet the SNR requirement [8]. The field of view of a pinhole was calculated using the information found in source [80], assuming the same 15 μm diameter pinhole. The pinhole used by NanoSAM I does not meet the 1.3 arcminute field of view requirement. Instead, a 20.6 μm pinhole would need to be used, as was calculated using Eq. 30. Because a slit will let in more light that a pinhole, a slit will also meet the minimum field of view and SNR requirements that the pinhole does. Additionally, costs for the pinhole and slit field stops can be found in sources [81] and [80].

Metric	Weight	Pinhole	Slit
Field of View	0.4	5	5
SNR	0.4	5	5
Design Complexity	0.1	4	1
Cost	0.1	4	1
Total	1.0	**4.8**	4.2

Table 49 Field Stop Trade Study Results

XII. Appendix C: Detailed Thermal Model Derivation and Iteration

This appendix section will be used to go over a comprehensive and detailed view of the thermal model used to verify the electronics and structural designs used on NanoSAM II. To cover the important assumptions made by the primary MATLAB model, one of the first assumptions made is that there are parallel rays from the sun. This assumption is good particularly for a low Earth orbit satellite since the effects of the cone shadow behind the Earth are the least significant the closer the satellite is to the Earth and can almost always be ignored. Another important assumption is that all albedo/longwave radiation from the Earth travels directly along the radial line from the center of the Earth to the satellite. This assumption allows for the use of area factors which work to determine the fraction of the area of a particular surface that is directly exposed to incident radiation. However, comparing to other models, this area factor analysis may be a source of extreme error since it doesn't account for the diffusion of radiation from all points on the Earth and the effects of this additional radiation could be on the order of 1 W of additional incident heat on the satellite as per the Libertad 2 CubeSat analysis [19]. As such, the area factor analysis is of primary concern for the validity of the model. Another assumption used is that bodies other than the Earth/Sun don't produce significant incident radiation, which is expected particularly for a satellite in low Earth orbit. Kirchoff's law was also applied to simplify the equations describing the absorbtivity of the satellite for longwave radiation and since the Earth and satellite are at similar temperatures (with the satellite operating in an expected range of 250-320 K) this assumption is also appropriate. The satellite was assumed to be radiating to deep space as is done with most thermodynamic models used to gauge the temperature ranges of satellites as seen in the analyisis on Libertad 2 [19]. A final important assumption that the initial MATLAB model used is that the system was modeled to be a lumped entirely aluminum system in which no temperature gradients were present. The later developed Solidworks model eventually eliminated the lumped system analysis to get a better determination of the temperature of the photodiode block in particular.

Thermal Model Analysis Done Prior to Testing

Thermal modeling was started early on in the project due to the importance of temperature on the functionality of electronic components particularly relating to requirements 2.1 and 5.2 with the optics photodiode temperature change being of particular concern relating to the SNR requirement as shown in Fig. **??**.

The initial thermal model was developed to ensure that requirement 5.2 was completely satisfied such that the CubeSat would remain in the desired temperature range of -20 °C and 50 °C and functioned as a proof of concept for the structural design. A detailed description of all equations and procedures used in the development and iteration on the thermal model from MATLAB to Solidworks can be found in Appendix C. It is worth noting that the MATLAB model was initially used to analyze an extreme cold and hot case for a LEO 0.5 U CubeSat to determine the size of the heater required for the system. Following the MATLAB model, a more detailed Solidworks model was developed to analyze an intermediate case to examine the changes in temperature on the photodiode specifically. Descriptions of the parameters used in these models can also be found in Appendix C in Fig. 80 as well as the detailed discussion on the Solidworks model iteration. This discussion will focus on the important results of the thermal model and how they were used in the electronics and structural design.

Firstly, in order to make use of the transient model, the maximum power necessary for the heater was determined from the amount of energy necessary to shift the cold case transient temperature curve such that the minimum temperature is -20 °C. Iteration was performed to find the required heater power, with the results shown in Fig. 77.

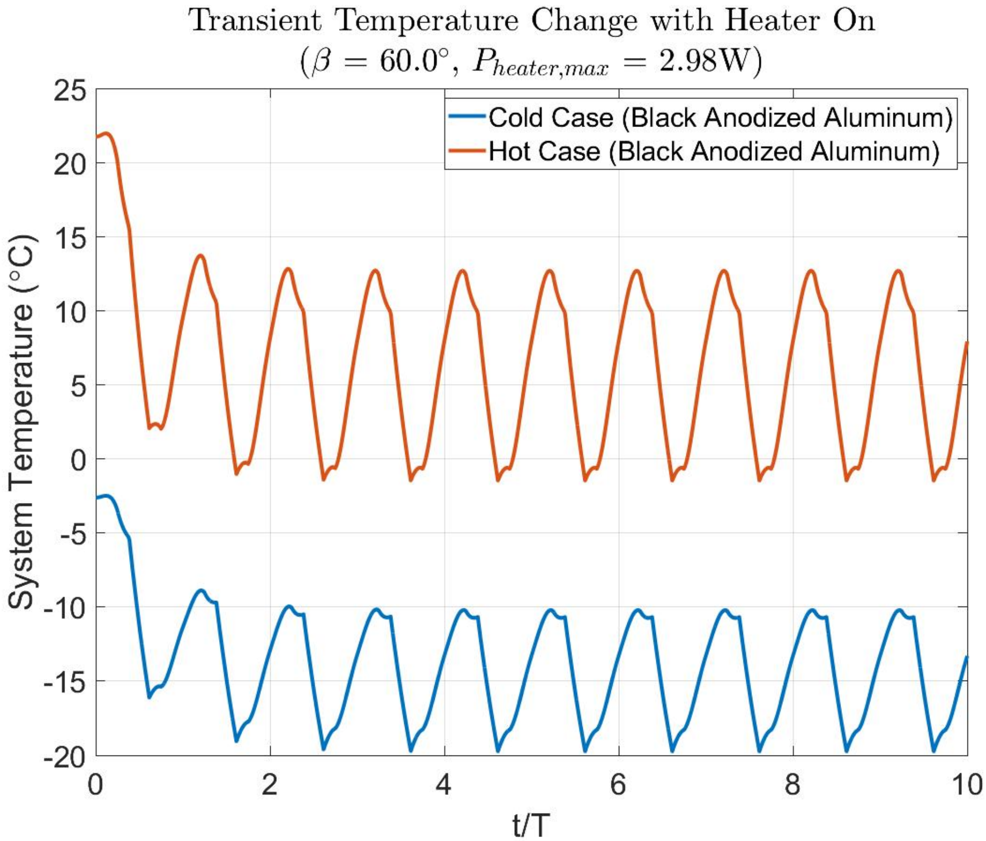

Fig. 77 Transient Temperature Model w/ Heater (Matlab)

With the maximum required power for the heater determined, it was possible to size the necessary resistor for placement on the NanoSAM II optic bench. It can also be verified from Fig. 77 that the heater does not cause the satellite to exceed its maximum temperature of 50 °C, further verifying the feasibility of this heater for use on the NanoSAM II. Finally it is worth noting that this power draw for the heater also keeps NanoSAM II within its power budget of 7.3 W, which will be further explored in the electronics section of the report.

Later in the design process, it was deemed necessary to know the more detailed temperature change on the photodiode specifically. This lead into the development of a more detailed MATLAB based Solidworks model in which the sunset and sunrise deta windows were specifically analyzed for an orbit with a beta angle of 60°. Using the processes described in Appendix C, it can be observed that the temperature is decreasing during both of these windows as shown in Fig. 78 & 79.

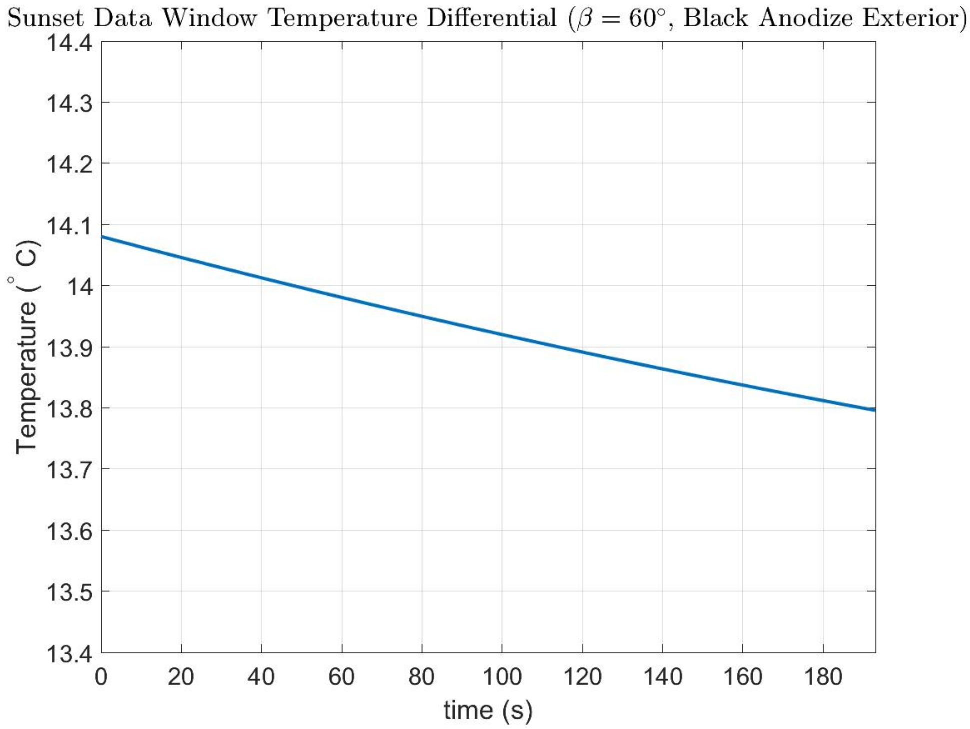

Fig. 78 Photodiode Temperature Change during Sunset

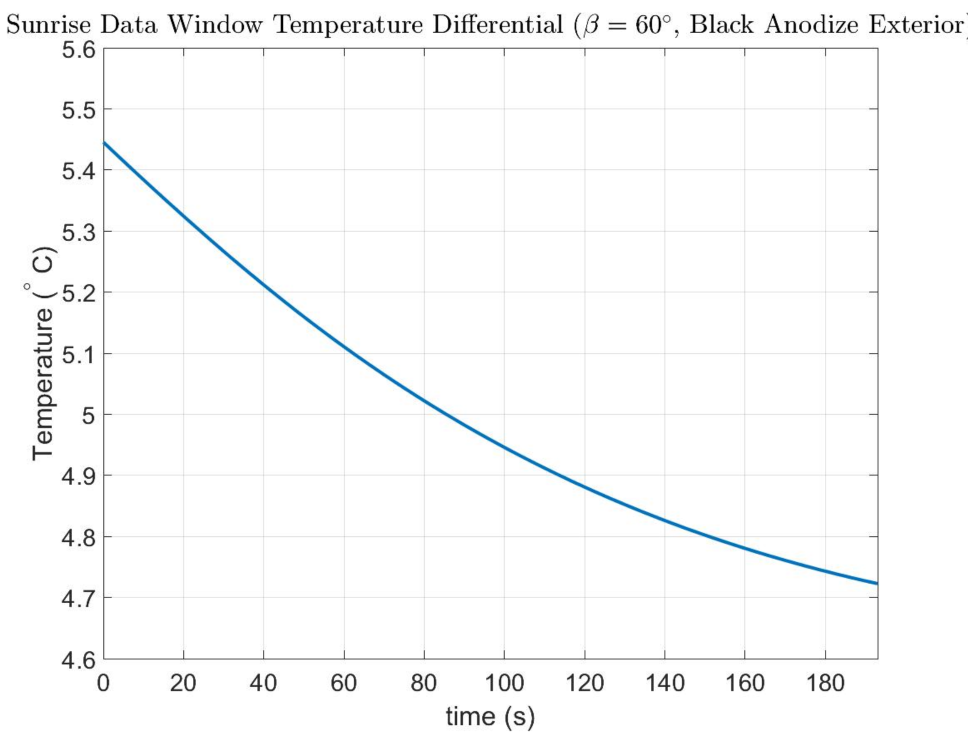

Fig. 79 Photodiode Temperature Change during Sunrise

It is important to note that the reason that the temperature is decreasing during the sunset window is due to the decrease in incident energy due to loss of albedo as the satellite passes behind the dark side of the Earth (observed in Fig. 88, located in Appendix C). The reason the temperature is decreasing during sunrise is due to thermal isolation causing a time delayed response by stopping the solar radiation from immediately increasing the temperature of the system.

The overall temperature change over the data windows is shown in Tab. 50. While these temperature changes are significant, they are expected to be small enough such that they can be mitigated by software using the linear relationship described in the electronics section by Fig. **??**.

Data Window	Max $\Delta T(K)$	**time (s)**
Sunset	0.28	192.6
Sunrise	0.72	192.6

Table 50 Temperature Change of the Photodiode over Sunset/Sunrise Data Windows

Finally, a summary of some points of note for future teams looking to iterate on the thermal model and get more precise estimates of the temperature change on key components. The most important change that should be made is the implementation of view factor analysis. Based on results from the Libertad 2 model, the incident heat not accounted for by area factors could be significant, particularly for a LEO satellite [19]. View factor analysis introduction could be as seamless as simply replacing the area factor function in the Matlab package provided. Although this analysis is not trivial, it should be possible given enough time and effort. Another option is to simply find software capable of or designed for analysing satellites and view factors for systems involving the Earth. Secondly, the team should find a way to account for a more specific external CubeSat bus chosen which would involve likely changes to external surface thermal properties. Actual CubeSats typically have varying thermal properties from face to face depending on the location of the solar arrays.

All Matlab materials will be provided in the NanoSAM team folder, along with a detailed procedure on how the Solidworks model was created and run such that a future team can adjust and iterate on the model as needed.

A. MATLAB Model

In order to determine project feasibility and determine the necessity of the presence of a heater within the CubeSat, two engineering extreme cases were explored within the lumped system MATLAB model. These cases were determined through NASA data documents on albedo and longwave radiation from the Earth for high inclination orbits which usually correspond to higher beta angle (ideal for NanoSAM since higher beta angles correspond to longer data windows) [20]. The duration of our 500 km orbit was approximated to be 90 minutes for this data sheet, with the satellite spending approximately 60 minutes on the sunlit side of the Earth (to get average values for albedo) the values found corresponding to the coldest and hottest scenario were found to be as shown in Fig. 80. Black anodized aluminum was assumed to be the surface coating on each face, and internally dissipated power from the electronics board was assumed to be 0 W for the minimum case and 1.16 W for the maximum case (this comes from 70% of the maximum power the board could dissipate). The p-h-s axes shown Fig. 80 is the reference axis used to determine which face is recieving incident power at any point in time, with the p axis pointed in the direction of the Earth's velocity vector, the s axis pointed toward the sun, and the h-axis pointed to satisfy the right hand rule. The box to the left of the axes represents the CubeSat to show that the h-axis corresponds to a face with a larger area than the p and s axes faces.

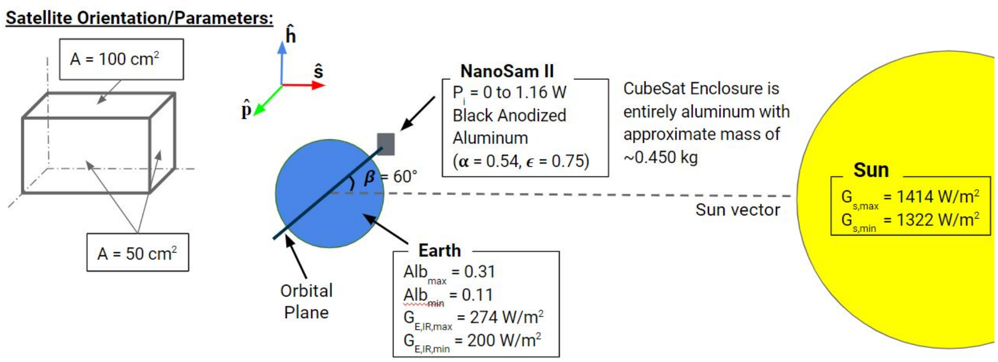

Fig. 80 Overall Thermal Model Overview

Using these initial parameters and orbit setup, area factors could be calculated for the orbit by defining two separate angles. The first angle (θ) simply characterizes the position on orbit in the same way the true anomoly does for an elliptical orbit, or the argument of latitude for a circular orbit. For the conveniences of the model, $\theta = 0$ °when the satellite is located directly between the Earth and Sun as shown in Fig. 80. The second angle (θ_h) is defined to describe the movement of the satellite above and below the ecliptic plane which is related to the orbital inclination and specifically beta angle in this simplified case. (θ_h) was defined as shown in Eq. 31, 32 & 33:

$$\omega_\beta = \frac{4\beta}{T} \tag{31}$$

$$\theta_h = \beta - \omega_\beta t \tag{32}$$

$$\theta_h = -\beta + \omega_\beta t \tag{33}$$

Firstly, Eq. 31 shows the angular rate of change of θ_h as it sweeps through 4 times the beta angle every orbit, twice as it descends from the "top" of the orbit, and twice as it ascends from the "bottom" of the orbit. Eq. 32 shows how θ_h changes for the portion of the orbit where the satellite is travelling from the "top" of its orbit down toward the descending node and to the "bottom" of its orbit. Then, Eq. 33 describes the equation when the satellite is traveling from the "bottom" of the orbit toward the ascending node and to the top of of its orbit. The area factor for each face can be calculated using process exemplified in Fig. 81:

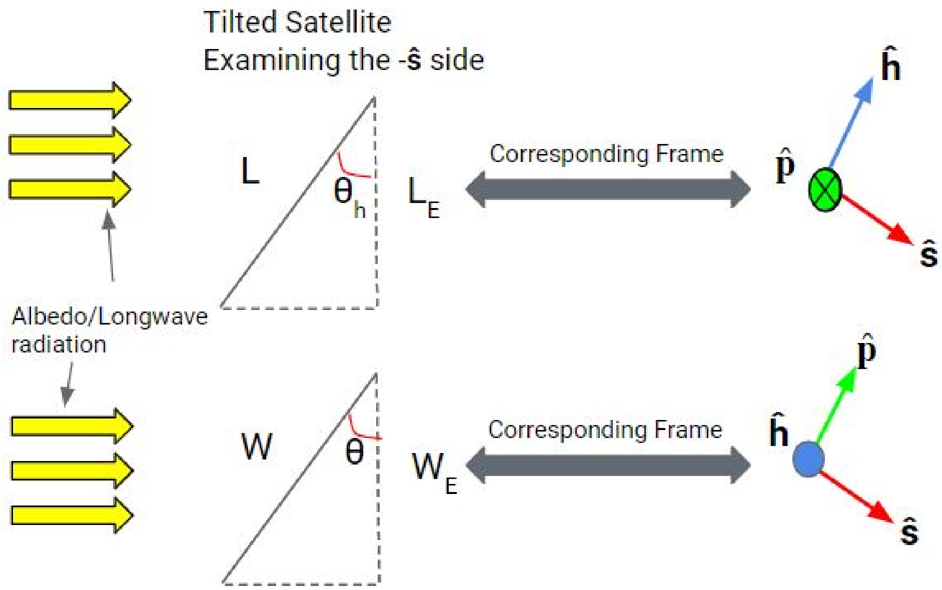

Fig. 81 Area Factor Analysis

For the -$\hat{s}$ face, area factor can be derived by the following equations:

$$W_E = cos(\theta)W \tag{34}$$

$$L_E = cos(\theta_h)L \tag{35}$$

$$AF_{-s,Earth} = \frac{W_E L_E}{WL} = cos(\theta)cos(\theta_h) \tag{36}$$

Since θ does not always have a reference at zero degrees as in Fig. 81, equations for the remaining $\hat{s}$ and $\hat{p}$ faces will be shifted 90 degrees out of phase. The $\hat{h}$ faces are only dependent on θ_h due to the assumed orientation of the satellite. All of the equations for the remaining area factors can be found as shown below:

$$AF_{s,Earth} = -cos(\theta)cos(\theta_h) \tag{37}$$

$$AF_{-p,Earth} = sin(\theta)cos(\theta_h) \tag{38}$$

$$AF_{p,Earth} = -sin(\theta)cos(\theta_h) \tag{39}$$

$$AF_{-h,Earth} = sin(\theta_h) \tag{40}$$

$$AF_{h,Earth} = -sin(\theta_h) \tag{41}$$

Further constraints on these functions are placed such that they are only valid while a face is exposed to the Earth and are otherwise zero. In the case of albedo specifically, all of these functions become zero when θ is greater than $\pi/2$ and less than $3\pi/2$ since that is the range of angles for which the satellite is no longer exposed to the sunlit portion of the Earth. The results of this analysis can be seen in Fig. 82 & 83 for the area factors relating to radiation from the Earth.

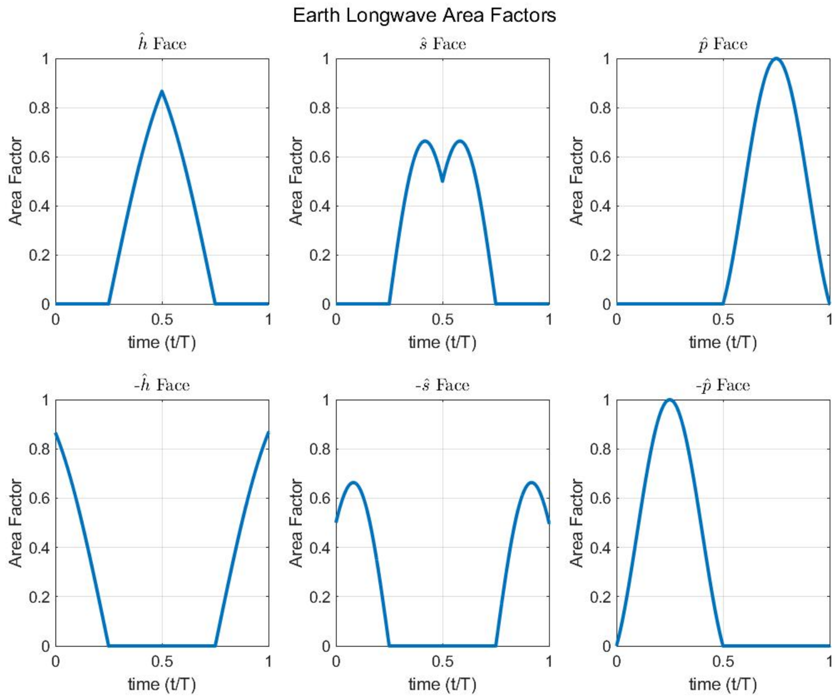

Fig. 82 Longwave Radiation Area Factors

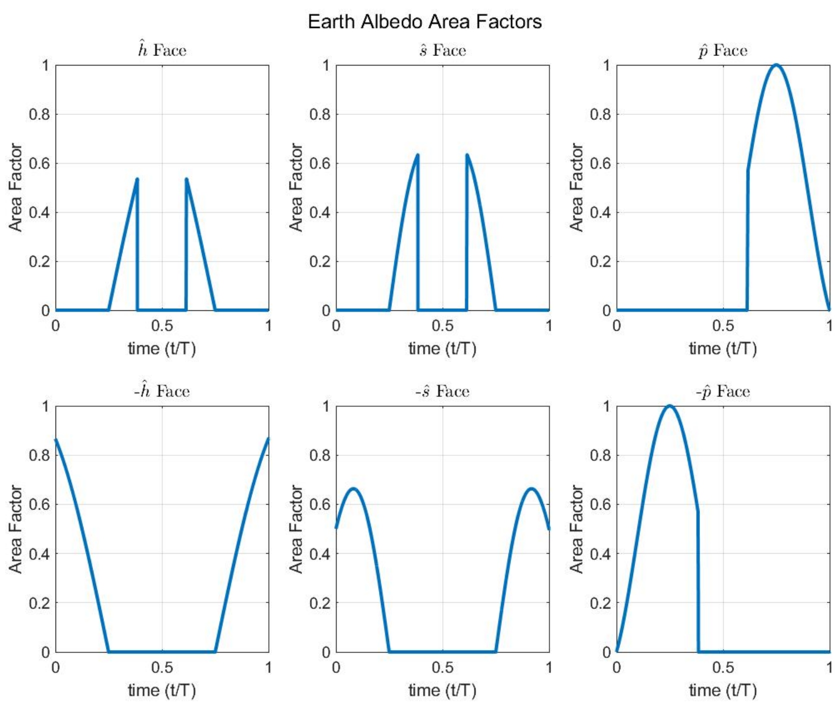

Fig. 83 Albedo Radiation Area Factors

The area factor from the sun was zero for all faces except for the face always pointed toward the sun in the $\hat{s}$ direction. For the $\hat{s}$ face, the area factor relating to solar flux was one at all times except as the satellite disappears behind the Earth. In order to determine the θ's at which this occurs, simple geometry with ellipses were used along with the knowledge of a given beta angle. By viewing the simplified orbit from the perspective of the solar vector pointed toward the center of the Earth, the following diagram can be created as shown in Fig. 84:

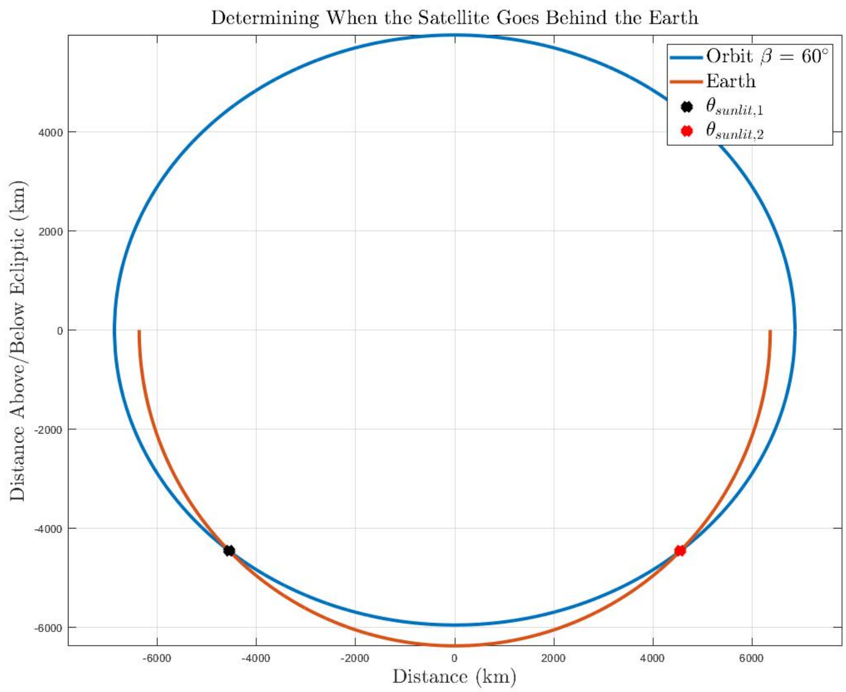

Fig. 84 Eclipse Duration Determination

The position of $\theta_{sunlit,1}$ and $\theta_{sunlit,2}$ can be determined first by finding the x and y positions on the plot through the following equations for the intersection of an ellipse and circle:

$$x = \pm r_{orbit}\sqrt{\frac{R_E^2 - (r_{orbit}sin(\beta))^2}{r_{orbit}^2 - (r_{orbit}sin(\beta))^2}} \tag{42}$$

$$y = -r_{orbit}sin(\beta)\sqrt{\frac{R_E^2 - (r_{orbit}sin(\beta))^2}{r_{orbit}^2 - (r_{orbit}sin(\beta))^2}} \tag{43}$$

The actual angular position relative to $\theta = 0°$can then be determined by the process shown in Fig. **??**

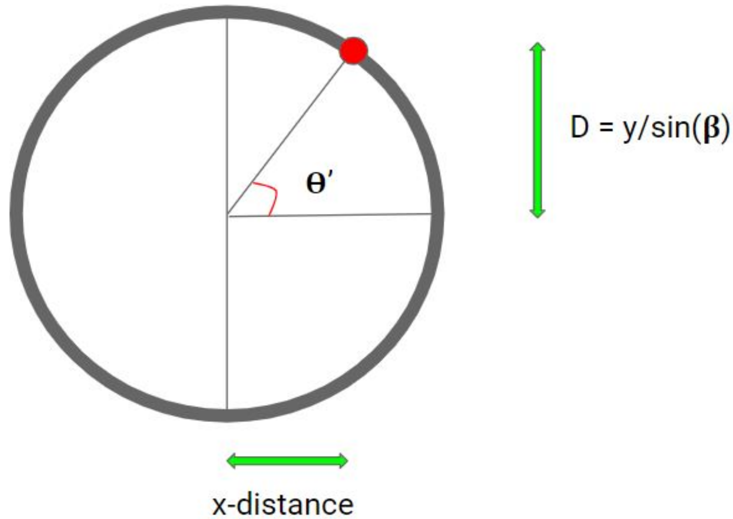

Fig. 85 Eclipse Duration Determination (Geometric Calculation)

Substituting and calculating both angles results in the following values for the eclipse θ's shown in Eq. 44 & 45. $\theta_{sunlit,1}$ is the point at which the satellite goes behind the Earth in a "sunset", and $\theta_{sunlit,2}$ is the point at which the satellite is returning into the sun in a "sunrise".

$$\theta_{sunlit,1} = 2.42rad \tag{44}$$

$$\theta_{sunlit,2} = 3.87rad \tag{45}$$

The area factor from the sun can then be defined to be 1 outside of that range for the $\hat{s}$ face, and 0 for every other face/position on orbit. Length of the data window was determined using the same process, using larger radii circles for a 200 km altitude where the window starts and an 8 km altitude where the window ends. This model does not account for refraction, the data window would be slightly longer in this case however the extra analysis was not deemed necessary in determining the temperature change on the photodiode.

Since mission operations will be performed in a vacuum, the energy balance only needs to include equations for radiation heat transfer for a lumped system analysis. With this knowledge and assuming emission to deep space at 0 K results in Eq. 46.

$$\dot{Q}_{out} = 2\sigma_B \epsilon T_{sys}^4 (A_s + A_p + A_h) \tag{46}$$

Where ϵ is the emmisivity as defined in Fig. 80 and the subscripts on the area correspond to the face of interest (since $A_s = A_{-s}$ are equivalent, only one is used as with the other two areas listed). The longwave radiation into the system is defined by Eq. 47 (NOTE: ϵ is used in this equation as the absorption for longwave radiation from Kirchoff's Law).

$$\dot{Q}_{LW,in} = \epsilon G_{IR} \left[A_h (AF_{s,Earth} + AF_{-s,Earth}) + A_p (AF_{p,Earth} + AF_{-p,Earth}) + A_h (AF_{h,Earth} + AF_{-h,Earth}) \right] \tag{47}$$

With corrections to area factor accounting for only when the satellite is in the sunlight, the equation for the power into the system from albedo is defined by Eq. 48 (NOTE: α is used in this equation because albedo is reflected SOLAR radiation).

$$\dot{Q}_{albedo,in} = \alpha AlbG_s \left[A_h(AF_{s,albedo} + AF_{-s,albdeo}) + A_p(AF_{p,albedo} + AF_{-p,albedo}) + A_h(AF_{h,albedo} + AF_{-h,albedo})\right] \tag{48}$$

The final external energy source is the sun, which has the simplest equation described by Eq. 49.

$$\dot{Q}_{solar,in} = \alpha AF_{s,solar} A_s G_s \tag{49}$$

Rearranging Eqs. 46-49 to solve for the system equilibrium temperature results in the following equation:

$$T_{sys} = \left(\frac{\dot{Q}_{solar,in} + \dot{Q}_{LW,in} + \dot{Q}_{albedo,in} + \dot{P}_i}{2\sigma_B(A_s + A_p + A_h)}\right)^{(1/4)} \tag{50}$$

Since an equilibrium model isn't very useful in determining the actual temperature range the satellite will experience on orbit (as seen in Fig. 86), a numerical model was developed to determine the transient temperature at each point in time on orbit using Eq. 51.

$$\dot{Q}_{net}(t) = \frac{mc_p\Delta T}{\Delta t} = \dot{Q}_{solar,in} + \dot{Q}_{LW,in} + \dot{Q}_{albedo,in} + \dot{P}_i - \dot{Q}_{out} \tag{51}$$

Where m is the mass of the system as estimated in Fig. 80, c_p = 896 J/kg-K for aluminum 6061-T6 [21], Δt defines the timestep of the model and $\dot{Q}_{net}$ describes the net heat transfer in/out of the system as a function of the area factors which are directly related to time (t = 0 seconds when θ = 0 °). Rearranging Eq. 51 results in Eq. 52 which defines the transient model for the lumped system analysis.

$$T(t) = \frac{\dot{Q}_{net}(t)\Delta t}{mc_p} + T(t - \Delta t) \tag{52}$$

Iterating on Eq. 52 eventually allows the system to reach a steady state as shown in Fig. 87. The transient model can be verified by the equilibrium model as in the case of both the hot and cold cases, the transient model is always trending toward the equilibrium temperature and never reaches the extremes that are observed in the equilibrium model.

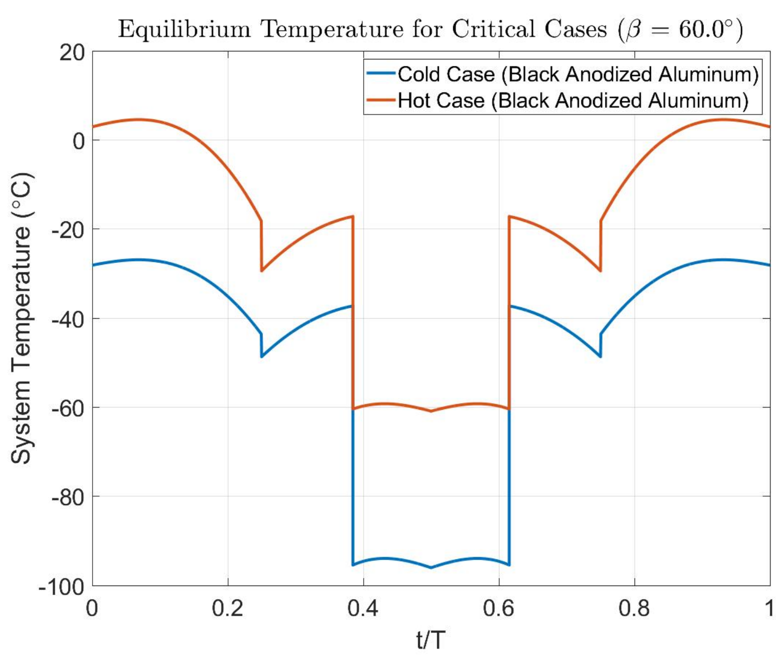

Fig. 86 Equilibrium Temperature Model (Matlab)

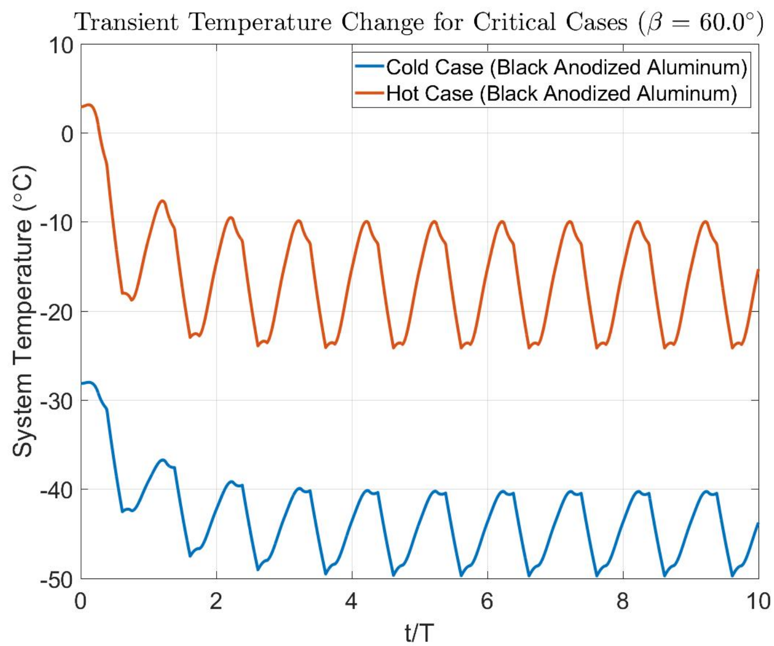

Fig. 87 Transient Temperature Model (Matlab)

In order to determine the heater power required to shift the transient curve from Fig. 87, an additional heater term was added to Eq. 51 and the power dissipated by the heater was increased through iteration until the transient curve had a minimum at -20 °C.

B. Solidworks Model

The purpose of the more detailed Solidworks model was to more closely examine the effects of the introduced thermal isolation on the temperature of the photodiode block during the sunrise and sunset data windows. This model was developed in the "Flow Simulation" module using only the radiation heat transfer mechanisms and surface sources. Since the Earth is not able to be modeled within Solidworks to produce viewfactors, the MATLAB model was used to determine the power on each face as a function of time as shown in Fig. 88. Analysis for the power onto each face was done using area factors.

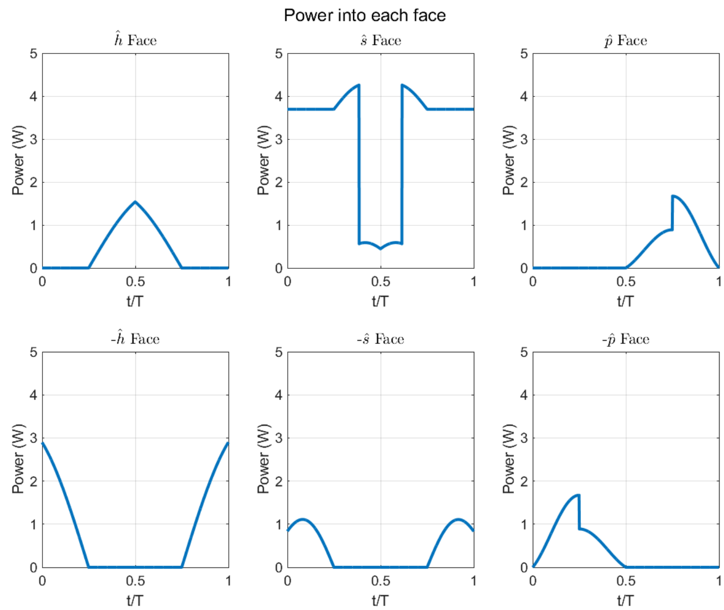

Fig. 88 Matlab Results to Inform Solidworks Model

Each face is set to be a surface source with properties over time as defined by Fig. 88. The external surfaces are thin aluminum walls to enclose the structure to fill the 0.5 U space, and have emission and absorptive properties as defined in Fig. 80. Solar irradiation, albedo, and longwave radiation are set to be average values of those displayed in Fig. 80. Internal power dissipation is taken to be 70% of the maximum power that could be dissipated (the same is displayed in the model overview) and the heater power is set to 3 W. The functions that define the incident power on each face are computed by summing all of the incident external power sources on each face as a function of time individually.

Within the satellite, two surface sources are placed on top of each electronics board, each source radiating half of the assumed internal power dissipation (not including the heater). Finally, the last surface source is placed on the bottom of the optics bench with a constant power dissipation of 3 W to model the heater. The model can then be run to specifically measure the temperature change of the photodiode block as seen in Fig. 89.

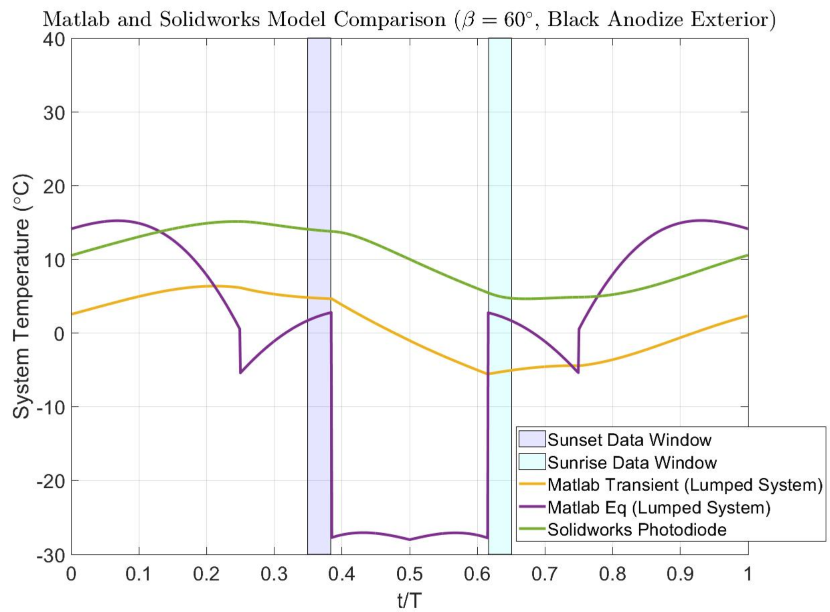

Fig. 89 Thermal Model Comparison

As expected, the Solidworks model follows the same trend as predicted by Matlab due to the inputs into the model being derived from Matlab, the main differences being smoother inflection and critical points as well as being at a higher overall temperature. This higher temperature is expected because the thermal isolation keeps some of the heat from the heater and electronics board trapped within the system. Overall, the results from Fig. 89 give confidence that the Solidworks model is accurate enough to be useful due to the similar trends in temperature to the Matlab model and a reasonable temperature increase due to thermal isolation.

XIII. Appendix D: Detailed Gantt Charts

These detailed Gantt charts are taken from the cloud-based software that the team uses for scheduling, ClickUp. This allows for clear dependencies, time tracking on a per-task basis, and a variety of schedule views customized with the tasks most relevant to the user. Fig. 90 shows the exhaustive work plan for the Optics subteam, while Fig. 91 shows an example of what the Gantt chart looks like zoomed in, showing day-by-day deadlines and clear dependencies. This detailed view is what is used during status meetings to keep the team updated on what tasks are open, upcoming, and completed to ensure that nothing slips through the cracks. To round out the work plan, Figs. 92, 93, and 94 show the tasks for Structures, Electronics, and Software respectively.

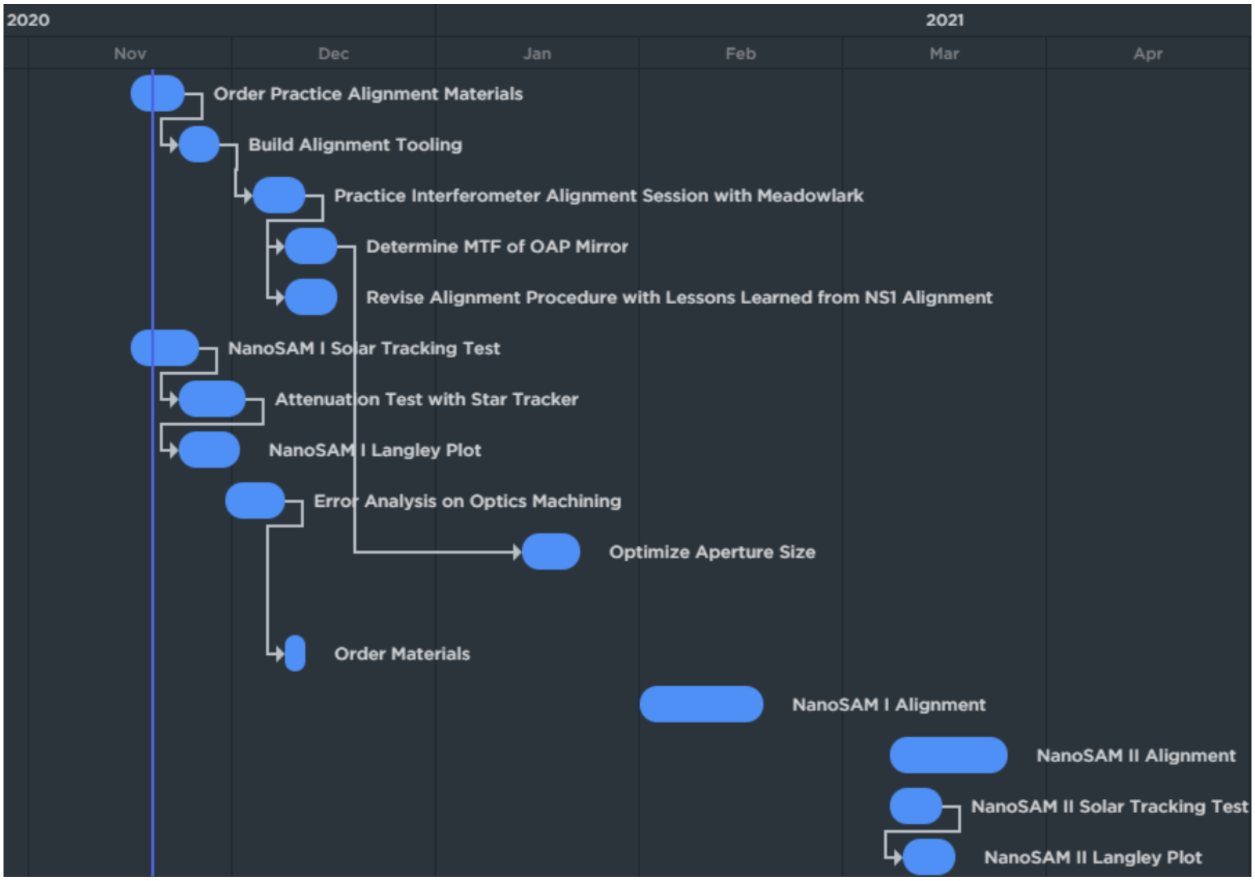

Fig. 90 Work Plan: Optics

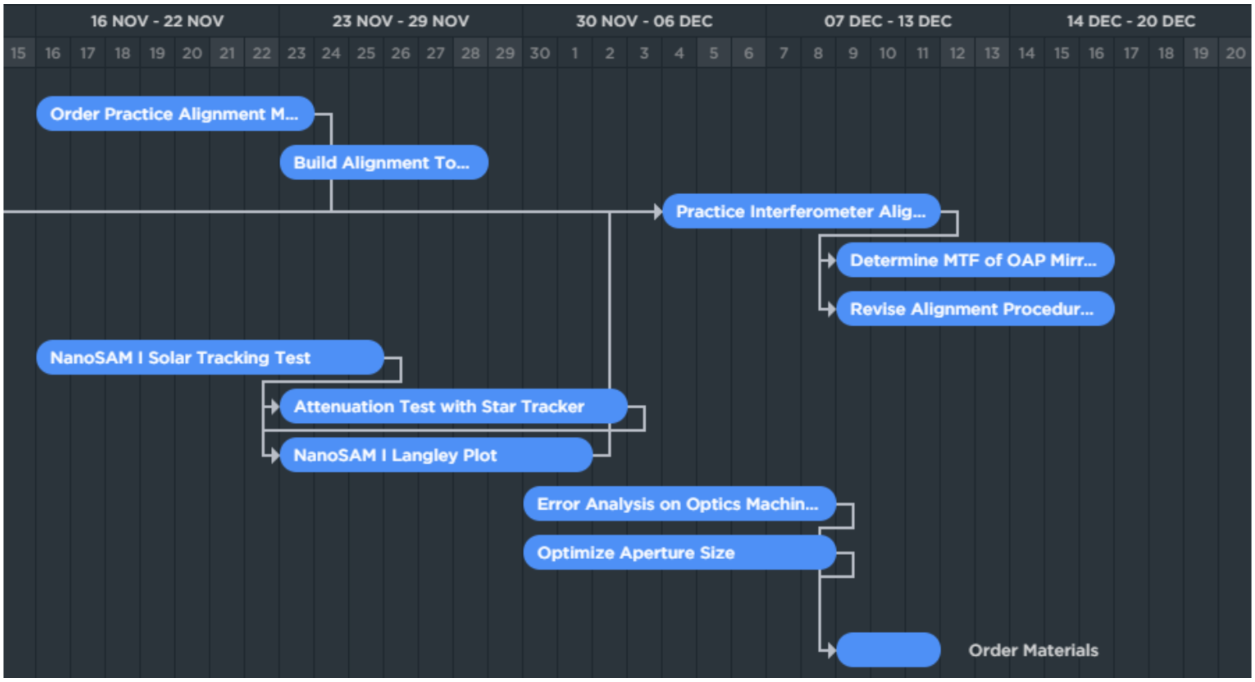

Fig. 91 Work Plan: Optics (Detailed View)

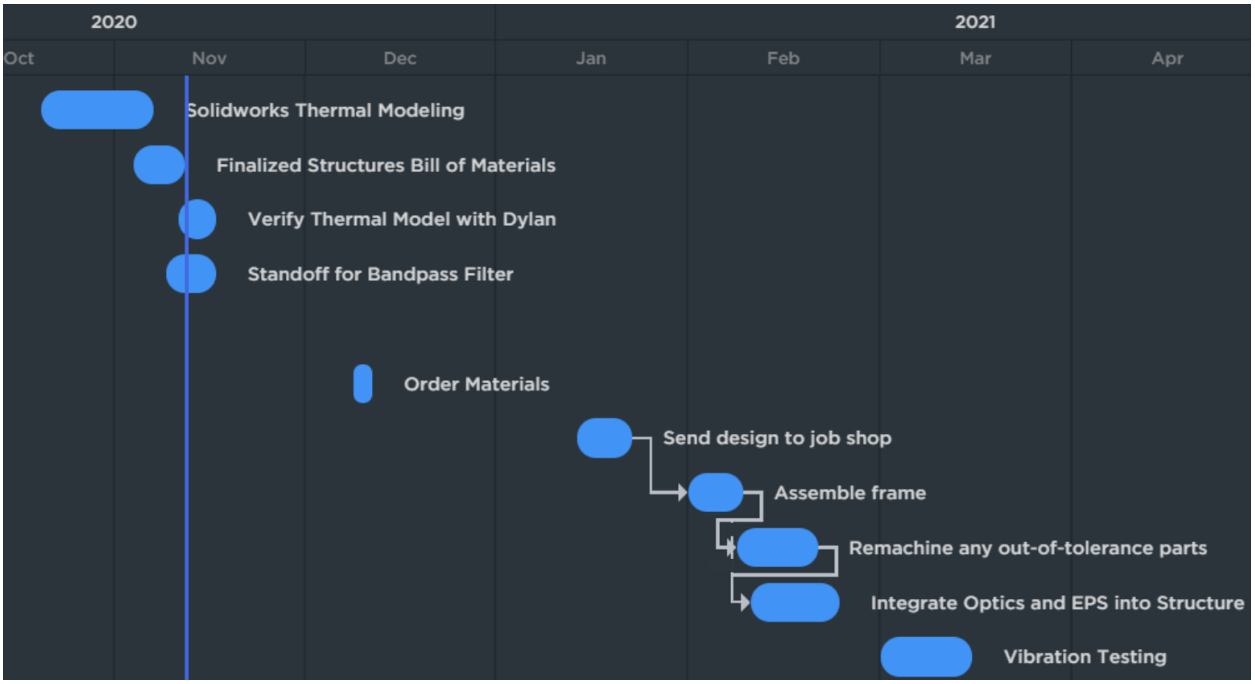

Fig. 92 Work Plan: Structures

Fig. 93 Work Plan: Electronics

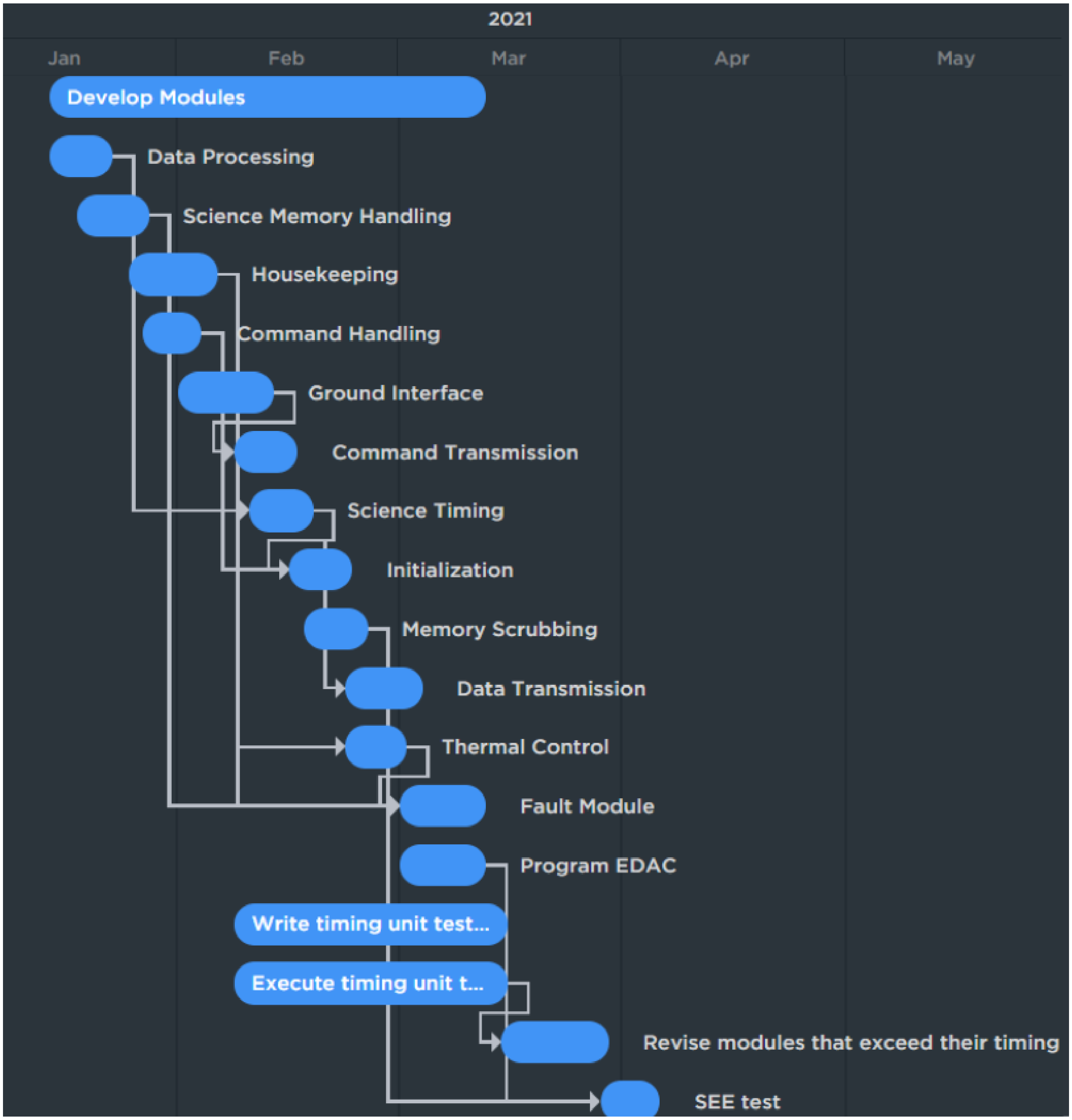

Fig. 94 Work Plan: Software

The module development priority shown in Fig. 94 was decided based on the order that the modules would be needed to support testing. For example, the data processing, housekeeping, and memory handling modules are essential to any test using the electronics boards or optics bench, so they will be developed and tested first. Other modules, such as thermal control, fault handling, and error detection and correction, are not crucial to early tests, so their priority was low and they will be developed near the end of the development cycle. There will be two full-capacity developers during the spring, which is why there is significant overlap between the tasks on this chart. Additionally, two more team members are available to support with unit testing, so those tests can be written while the developers are working on new modules.

XIV. Appendix E: Conceptual Design Alternatives

A. Structures Conceptual Design

Structures Design Alternatives

The primary motivation for the structure for NanoSAM II is to produce an enclosure for the other subsystems that meets functional requirements 4.0 and 5.0. These requirements are centered around producing a structure that is small and marketable to future CubeSat programs. Requirement 4.0 drives three subrequirements: Payload Size (4.1), Payload Mass (4.2), and Payload interface (4.3). Based on these subrequirements, the structure is designed to fit within 0.5U, weigh less than 0.615kg, and have a defined interface for integrating with a future CubeSat bus. These requirements help to define the design space for the structure, and the specifics for how the other subsystems interface with the structure are motivated by functional requirement 5.0.

Key design considerations were future compatibility and internal flexibility within the design. In particular, this means that a structure that can be easily modified as needed in the future so that it can fit with a wider variety of CubeSat designs. Another key design consideration was ease of testing of the physical hardware, both in subsystem level tests and in system level tests. These considerations played a role in designing additional hardware that might not necessarily be present on an actual flight-ready unit.

Optical Bench Mount Options

One of the key functions of the structure is to mount the optics bench and provide a system that reduces temperature fluctuations across the bench during the measurement window. Throughout the semester, the optical bench mount was iterated on, with special consideration as to how the optical bench would fit in conjunction with the electronics boards. From this, two basic optical bench mount options were considered. Since the optical bench is the single largest component in the structure, its position influences the majority of the other design choices.

The first concept was based off of initial recommendations from the customer, with the central design philosophy to utilize the electronics boards as the mounting points for the optical bench, shown in Fig. 95 below.

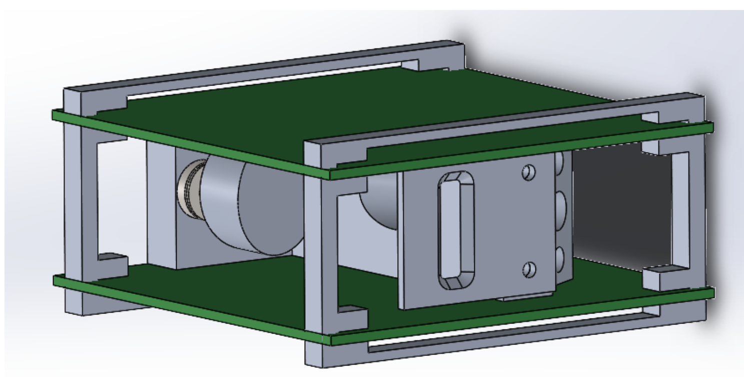

Fig. 95 Stacked PCB Concept

The stacked PCB design has a few advantages. Firstly, the total footprint of the instrument is reduced by incorporating the electronics boards and the optical bench thermal isolation together. Secondly, it reduces the overall mass of the instrument by minimizing the number of structural ribs needed to fully support the system. The main concerns with this design are manufacturing concerns with the ribs, electronics constraints imposed by the design, and integration issues with future CubeSat buses. Ultimately, it was determined that this design introduced additional risks and additional design constraints that were ultimately unnecessary to meet requirements. These design constraints primarily affects the electronics team, as the ribbon cable needed to connect the two electronics boards would greatly increase the noise risk of the overall system. This was a known issue with this design, and was a primary factor for considering a separate optics and electronics mount.

The alternative design considered was one that separated the electronics boards from the electronics. This design initially featured a cantilevered mount for the optics bench, as shown in Fig. 96 below. This design is representative of the NanoSAM II structural design at the end of the preliminary design review (PDR) [12].

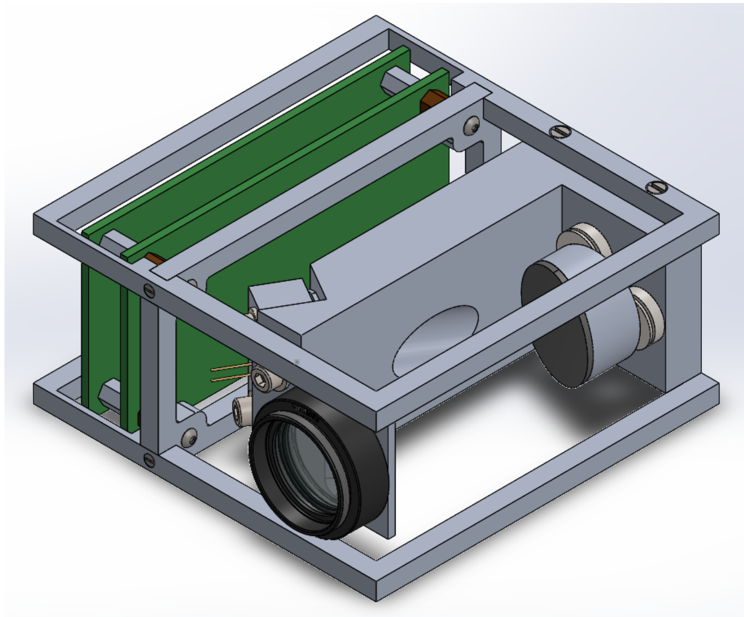

Fig. 96 Separated PCB Concept

The optical mount pictured above was selected for PDR based on the benefits it provided to the electronics subteam. The main benefit to the electronics subteam is that this optics mount allows for a direct board to board connector between the electronics boards. Furthermore, the design was demonstrated to meet size and vibrational requirements, while also being straightforward to manufacture and test.

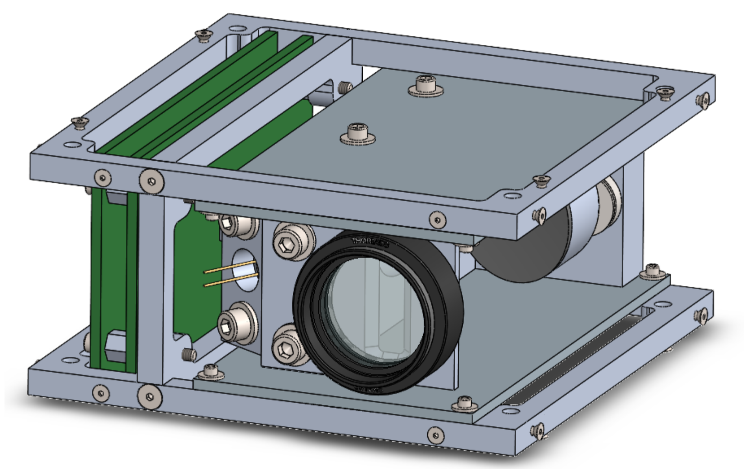

Fig. 97 Thermally Isolating Boards Concept

This optical mount retains all of the previous benefits to the electronics team, but also greatly improves the thermal performance of the optical bench. With the cantilever mount in Fig. 96, the optical bench is in direct thermal contact with the structural ribs, which causes the optical bench's temperature to fluctuate more quickly. The use of the thermally isolating fiberglass boards reduces the metal-to-metal contact paths, which slows the rate at which temperatures on the photodiode block change, thereby reducing the error in optical measurements.

One final optical mount that was considered was a micro shock mount. This part would be similar in concept to an aluminum shock absorber used in model RC cars, seen in Fig. 98 below. The technical challenge to this part is that this would almost certainly need to be designed in house. Additionally, the size constraints imposed on the structure make this component difficult to manufacture.

Fig. 98 Micro-shock mount concept

The team also considered various options for mounting the electronics bench. These considerations ended up being very similar to the metrics used to trade-off between different optics mounting methods. The team ended up settling on screws and standoffs for simplicity, reliability, and cost. This process is described in more detail in Appendix A.

Structures Trade Studies

Several trade studies were performed as part of the structural design process. Key trade studies are: the material selection for the majority of the structure, optical bench thermal isolation methods, and the electronics mount methods. These three sections are fundamental to the final form of the payload, and so they are the main driving factors for design.

With these trade studies, the metrics for evaluating these options are primarily focused around the space cost of the option as well as the financial/time cost. This is because the structure needs to maximize internal volume for the optical bench and electronics, so options that impede on these other subsystems are preferred. The secondary metric for evaluation is generally how it impacts functional requirement 5.0, which pertains to vibrational/thermal properties.

For each trade study, the detailed description, rationale, and metric values are given in Appendix B.

Material Consideration

The primary metrics for the material consideration are cost and material properties. Cost is a key factor for selecting the material, as minimizing the budget impact is desired. Cost was estimated based on the cost of the material per cubic inch, provided from McMaster-Carr. The metrics for availability were based on previous experience with ordering parts. Material properties, such as density and shear modulus, directly impact how the structure meets the functional requirements. Specifically, density of the material directly influences the final weight of the payload, and this must be minimized. Additionally, properties such as shear modulus are important since they describe how the material performs under load and vibration.

Metric	**Weight**	**Al 7075**	**Al 6061**	**Al 5005**	**Al 5052**
Cost	0.3	1	5	3	2
Density	0.3	1	4	4	5
Shear Modulus	0.2	5	2	1	1
CTE	0.1	1	1	5	4
Availability	0.1	5	5	3	4
Total	1.0	2.2	**3.7**	3.1	3.1

Table 51 Material Trade Study Results

Fortunately, NanoSAM II came to the same conclusion as NanoSAM I to use 6061 Aluminum. This is advantageous because the work that has been done previously on the optical bench thermal expansion can be reconfirmed by this year's team. Additionally, 6061 Aluminium is commonly used in the commercially available CubeSat buses, which builds confidence in the selection of this material for NanoSAM II.

Optical Bench Thermal Isolation Methods

The primary metrics for evaluating the optical bench thermal isolation method was driven by the option's ability to provide thermal isolation and vibrational isolation, with secondary consideration to availability. In general, the metric that determined the best option, as presented in Tab. 52, was the availability. Since the isolating boards option was readily available and proven to work, it was preferred.

Metric	**Weight**	**Stacked PCB**	**Isolating Boards**	**Shock Mounts**
Thermal Isolation	0.35	5	5	3
Vibration Isolation	0.25	3	5	5
Availability	0.25	3	5	1
Space Cost	0.15	3	3	1
Total	1.0	3.7	**4.7**	2.7

Table 52 Optical Bench Integration Trade Study Results

The thermally isolating boards was chosen due to its ease of implementation, ability to thermally isolate the optical bench, and its ability to resist vibration. The implementation can be seen in Fig. 97.

Electronics Mount Methods

In general, the metrics for the electronics mount methods are essentially the same as the metrics for the optics bench mount method. The primary difference is that the vibration concerns for the electronics mount are reduced, so this metric is weighted less. Additionally, the manufacturability of the mount is a greater concern, so the weight of the availability is increased to account for this. Finally, the concepts were passed along to the electronics leads, and their input was included as an additional metric. The bulk of the electronic lead feedback was based around how much the design impacted available board space and the design's ability to electrically ground the boards to the chassis.

Metric	**Weight**	**Direct Contact**	**Friction Slot**	**Elastomer Mount**
Electronics Input	0.40	4	5	3
Vibration Isolation	0.25	3	3	5
Availability	0.25	5	3	3
Space Cost	0.10	5	3	1
Total	1.0	**4.1**	3.8	3.3

Table 53 Electronics Board Integration Trade Study Results

From this, the direct contact mount was selected. The primary reason for its selection is its electrical chassis ground connection, the minimal impact on the electronics board surface, and the simplicity of the design. This design is can be seen in Fig. 101 in the following section.

Structures Baseline Design

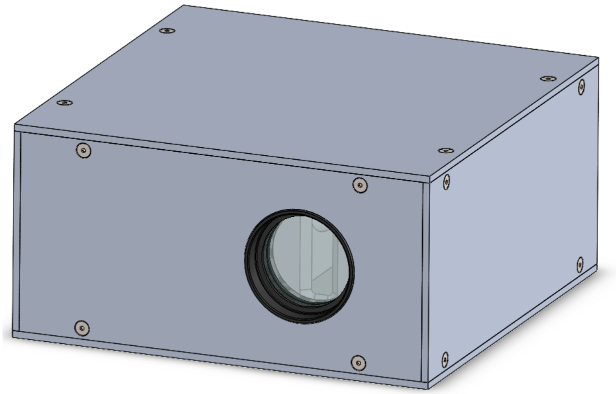

Fig. 99 Baseline - Walls On

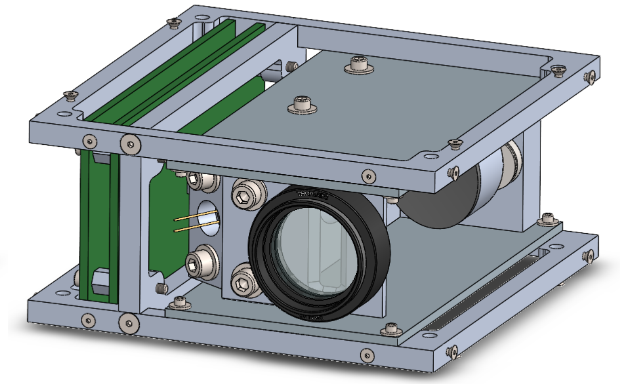

Fig. 100 Baseline - Walls Off

Optical Bench Integration

The optical bench integration can be seen in Fig. 100 above. As mentioned previously, the thermally isolating boards are used based on their ability to reduce temperature swings on the photodiode block during orbit. For the actual hardware used for this method, two sets of four #0-80 socket head cap screws with washers are used to secure the isolating boards to the structural ribs. To prevent a direct thermal path through metal from the outer structure to the optical bench, there are a separate set of #2-56 socket head cap screws with washers to secure the optical bench directly to the fiberglass boards. Washers are used in conjunction with the socket head cap screws to spread the screw load out across a larger surface of the fiberglass boards.

Electronics Integration

A representative corner of the electronics mount is shown below in Fig. 101.

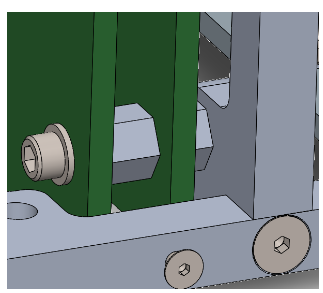

Fig. 101 Representative corner of electronics mount

This mount features two smaller metal standoffs to facilitate a direct mount to the central rib. The height of the mount between the boards is equal to the height of the board to board connector used in the electronics. The two metal standoffs are a close fit to the central #2-56 socket head cap screw, and are secured from spinning or translating since the central rib is threaded, and the socket head cap screw is then tightened. A small washer is used with this socket head cap screw to distribute the load across a slightly larger surface area of the electronics board. Additionally, the screw is electrically connected to the ground plane on the PCB, which then grounds the whole electronics system to the chassis.

Future CubeSat Integration

In general, there are a few considerations not mentioned above that are present in the structures baseline design. Firstly, the top and bottom ribs include PC104 standard mounting holes. These holes are commonly used on commercially available CubeSats to mount internal hardware. Additionally, the structure features additional hardware to put walls on, which is necessary to protect the internal components during physical testing.

A representative way that the NanoSAM II payload might fit within a commercially available CubeSat structure (Fig. 102) [22] is shown in Fig. 103, which is a single 1U bay. The external walls are removed for clarity.

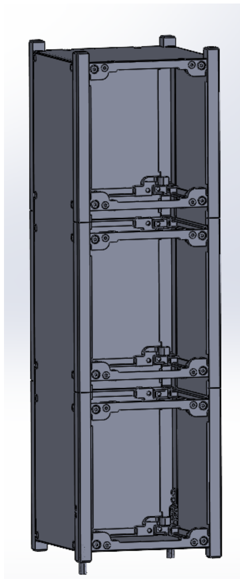

Fig. 102 ISIS 3U CubeSat structure

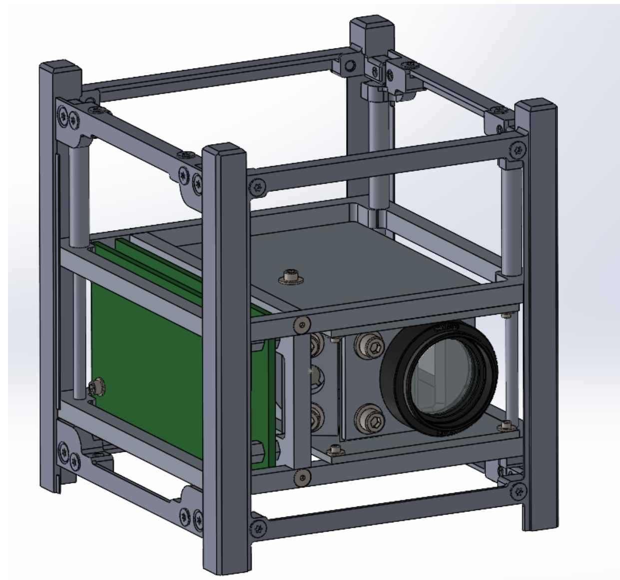

Fig. 103 NanoSAM II mount in ISIS 3U CubeSat

B. Electronics Conceptual Design

Electronics Design Alternatives

At its core, the electronics system must complete functional requirement 1.0, digitizing and packetizing the information collected by the optical system. Thus, the electronics system requires a photodiode that interfaces with the optical bench to convert gathered light into a current. Following the photodiode is an amplifier and low pass filter combination to improve and condition the signal. An analog to digital converter (ADC) is then required to convert the current into usable data, which is then packetized in an on board processing unit. Finally, the system will require on board storage to temporarily hold data until it can be downlinked from orbit and as a form of redundancy for microcontroller storage. All components will require voltage, likely to be regulated to fit the preferences of the ADC and on board computer, as well as noise constraints in analog components.

Thus, the key design options considered for the electronics board are variations of component types that will exist in the manufactured board. We will explore design options on the photodiode, analog to digital converter, on board processing unit, and storage modules. We note that radiation hardening on components that need it the most is often prohibitively expensive for a student project, so other radiation mitigation strategies will be explored in software. A fundamental design consideration when it comes to electronics is simplicity. Complicated components often require advanced designs, increased cost, and more board space. Sticking with well defined basics makes debugging easier along the way, and will support a future team in designing a bus or integrating with an industry bus. Since these options and the chosen alternatives have not changed, the full array of detailed options considered is shown in Appendix A.

Electronics Trade Studies

It is often difficult to determine exact quantitative values for certain metrics without conducting the full electronics design. Often parts are specifically chosen out of hundreds of manufacturer options for extremely specific characteristics. Thus, the quantitative numbers used in the following metric categories are not exact specifications of any one part, but are averages created from browsing the Digikey part website [39]. Although these averages do not reflect the exact part specifications, they provide a quantitative means to compare broad part categories. For each trade study, the detailed description, rationale, and metric values are given in Appendix B.

1. Photodiode Options

For the photodiode, we consider the dark current, the responsivity, the active area, and the cost of the average photodiode in each material category. Dark current is proportional to active area, and any material can be made with feasibly any active area. To differ between materials here, we discuss general trends in available parts. Particularly, the dark current value is compared between photodiodes with the same area. Responsivity values are taken at the designed wavelength for the part reported from manufacturer data sheets. Still, the overall responsivity curve for multiple photodiodes in the material classification were analyzed to make sure that the responsivity at 1030 nanometers was similar to the responsivity at the designed wavelength.

Metric	**Weight**	**Si**	**InGaAs**	**Ge**
Dark Current	0.4	5	3	1
Responsivity	0.4	3	3	1
Active Area	0.1	1	1	5
Cost	0.1	5	3	1
Total	1.0	**3.8**	2.8	1.4

Table 54 Photodiode Trade Study Results

2. Analog to Digital Converter Options

For the ADC, we consider the resolution, power consumption, conversion speed, size, computer compatibility, and cost. Similar to the photodiode section, with the thousands of options you can typically find an ADC in each of the three categories that will fit the needs of the project. To differentiate, ADC qualities are compared in relatively similar price ranges. To determine cost metrics, the average individual digikey part costs are estimated per category. Power consumption here was calculated based on maximum input voltage and current, using equation 53. For computer compatibility, parallel connections were deemed the lowest level as they are less common. SPI interfaces are the most common, so they were deemed middle, and additional points were given if the ADC also had DSP interfaces.

$$P = V_{dd} * I_{dd} \tag{53}$$

Metric	**Weight**	**Successive Approx.**	**Sigma-Delta**	**Pipelined**
Resolution	0.4	3	5	1
Power Consumption	0.2	3	3	1
Conversion Speed	0.1	3	3	5
Size	0.1	3	3	1
Computer Compatibility	0.1	5	3	1
Cost	0.1	3	5	1
Total	1.0	3.2	**4.0**	1.4

Table 55 Analog to Digital Converter Trade Study Results

3. On-Board Computer Options

For the OBC, we analyze versatility, size, cost, complexity, processing power, and power consumption. Versatility, the most important metric here, is often driven by cost as much as it is by category. The ADC section was ranked in compatibility by having SPI interfaces, so ideally, we look here for SPI interfaces in the OBC. Since almost every OBC here has an SPI interface, we rank versatility by total number of I/O streams. Complexity is dictated by the typical software used for programming. Power consumption is dictated by Eq. 53. Processing power is determined by internal clock speed. Cost is determined by the average cost between commonly used parts. For size, we only differentiate between items roughly the size of a typical printed circuit board (PCB), or the size of a typical integrated circuit (IC), like an op-amp.

Metric	**Weight**	**FPGA**	**Microcontroller**	**PCB Computer**
Versatility	0.3	5	5	3
Size	0.2	1	5	1
Cost	0.2	3	5	1
Complexity	0.1	1	5	3
Processing Power	0.1	3	3	5
Power Consumption	0.1	5	3	1
Total	1.0	3.2	**4.6**	2.2

Table 56 On-Board Computer Trade Study Results

4. External Storage Options

For the external storage considerations, we analyze computer compatibility, storage capacity, read/write speed, size, and cost between the three storage options considered. There are no additional notes for these options.

Metric	**Weight**	**Flash**	**SRAM**	**DRAM**
Computer Compatibility	0.4	3	1	1
Storage Capacity	0.2	3	1	5
Read/Write Speed	0.2	3	1	5
Size	0.1	5	1	3
Cost	0.1	5	3	1
Total	1.0	**3.4**	1.2	2.8

Table 57 Storage Trade Study Results

Electronics Baseline Design

Trade studies were performed on four essential elements of the electronics system: the photodiode, the analog to digital converter, the on board computer, and the external storage. Trade studies were taken to help validate maintaining current design elements, but additionally, these trade studies allow a redesign from previous hardware to focus on individual part selection and sizing. Redesign efforts this year included different individual part selections based on the need to reduce the board size in the new multi-board configuration.

Photodiode Selection

The selected trade study option for the photodiode will be a silicon photodiode running on a photoconductive system. Silicon's low dark current, high responsivity, and low cost make it ideal to collect strong data within the program budget. The differences between the photoconductive and photovoltaic system are small, but the photoconductive system will provide better responsivity and result in a more straightforward circuity design. The downside to silicon is that the wavelength range is typically more suited for smaller wavelengths than 1030 nm, so depending on the signal to noise ratio achieved in other parts of the circuit and the available budget, the team should not be opposed to exploring the InGaAs photodiode. The photodiode selected for design was the ThorLabs FD11A.

ADC Selection

The selected trade study option for the analog to digital converter will be the sigma-delta type. Sigma-delta ADCs typically offer most resolution at similar price ranges over the other ADCS, at a relatively low power consumption and size. They offer good compatibility with a serial programmable interface, and have more than enough conversion speed to meet design requirements. Although they do cost more on average than the other variants, they are not expensive compared to the electronics system at large, and the increase in quality and signal to noise ratio from the larger resolution is worth the cost. The team selected the LTC2470 ADC based on the trade studies.

On Board Computer Selection

The selected trade study option for the on board computer will be the microcontroller. This is the expected outcome for a student project, and matches a variety of other CubeSat projects that members of the team have had experience in. Both FPGA's and full single board computer systems are too costly, especially since the ones with good flight heritage are often thousands of dollars. The complexity of coding the FPGA's puts them outside of the design scope with the number of other elements to work on between the electronic and software designs. Microcontrollers providing great versatility, working with the ADC and external memory selections, easily interfacing with a laptop for ground testing, and provide solutions to standard bus interfacing for future teams. They are also small, cheap, and require low power, making them perfect for small CubeSats that seek to perform in constellations. The team selected a Teensy 4.0 microcontroller for its small size.

External Storage Selection

The selected trade study option for the on board computer will be flash memory. Flash is reliable, cheap, provides large storage, and easily meets our speed requirements. Flash memory has flight heritage both in external storage, as well as on most radiation hardened on board computers. It can easily interface via SPI, making it perfect for redundancy and communication with the microcontroller. The team selected two MT25QL128ABA flash modules.

Although the general system layout is nearly identical, we've seen that care was taken to review each component and it's interactions with new components and the new multi-board construction. The decision to transition to a multi-board design came down to the 0.5U sizing requirement, and was a logical derivation from the separation of grounds for analog and digital devices for noise concerns. Additionally, the split board design came with some side benefits. Namely, it is actually slightly cheaper to order, allows for isolated testing of the analog and digital elements, and had the backing of Professors Schwartz and Hodgkinson, whom I trusted to validate the design at each step in the process. The top board must contain the photodiode connection point due to the photodiode being attached physically to the optical block, which is above the electronics board stack in the structural design. Thus, the top board was made the analog board, and the bottom board was made to be the digital board. This has the added benefit of allowing for the bus connections to be placed on the digital board, which is closed to the back face of the CubeSat. A functional block diagram of the system is given in Fig. 104. In section five, the team will dive into the details of each component in this two board stack.

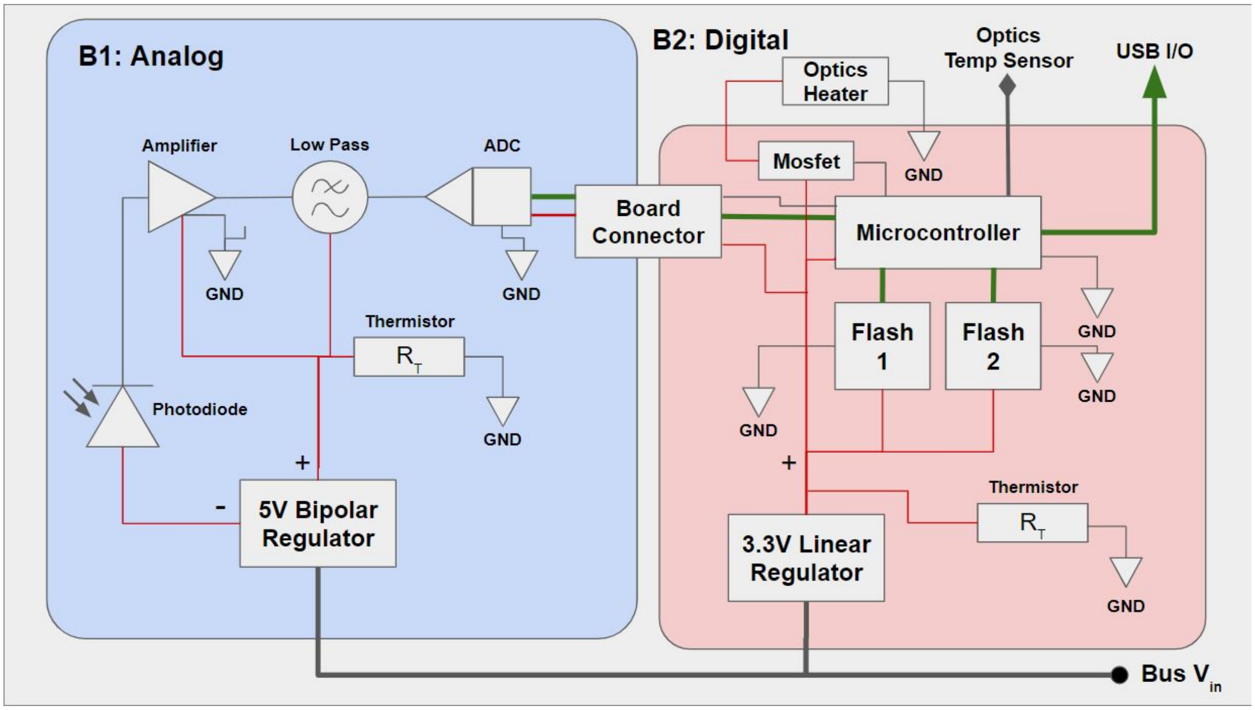

Fig. 104 Electronics System Functional Block Diagram

C. Software Conceptual Design

Software Design Alternatives

Software design choices will be coupled with the electronics system to handle data processing, storage, and transmission. Many of the low level and high level software design choices are largely driven by the design of the electronics system, but there still remain many choices to be made in the design of software. Trade studies were performed for two critical project elements: the method of data capture timing, and the choice of EDAC code to protect against radiation induced errors.

The first timing implementation considered is a method in which science data is continually captured and stored in a buffer. The buffer is then saved to long term memory when a sunset is detected by the photodiode, or after a sunrise is detected. The main advantage of this method is that it is coupled to the rising and setting of the sun, and thus it is not susceptible to drift as NanoSAM's orbit changes, however, storing data in a temporary data buffer comes at the cost of memory. An alternative timing method is one in which the collection window is triggered by the micro controller clock. This method is more prone to drift, but its accuracy can be improved by periodically re-calibrating the expected sunset and sunrise times by examining the photodiode data.

In the absence of radiation shielded components error Detection and correction will play a prominent role in NanoSAM's software system. Several potential EDAC codes were examined.

The first EDAC code evaluated was the longitudinal redundancy check, or LRC, which is similar to a simple single parity check with the key difference that parity bits are assigned to both rows and columns of a data word. An LRC is suitable for detecting single bit errors and burst errors that flip many bits, but fails to detect any even number of errors in a single row or column of a data word. The cyclic redundancy check, or CRC, was also considered, which excels at detecting burst errors and can be configured to correct an error of any size, however, CRCs are computationally expensive. Another EDAC code with a significantly lower overhead cost is the Hamming code. Hamming codes are capable of single bit error correction, and With the addition of a single extra parity bit a Hamming code can be designed to detect double bit errors. Finally, the last and simplest method we considered was the repetition code, which can theoretically correct any size of error by copying all data at least three times and voting on the majority. A repetition code has the obvious disadvantage of drastically increased memory usage. [72]

Software Trade Studies

Software is unique among NanoSAM's subsystems in that its implementation is not constrained by size, weight, or financial cost, but instead by the feasibility of its implementation and the robustness of its design. These metrics are often difficult to quantify, and so our trade studies consider both qualitative and quantitative factors.

Data Capture Timing

The data capture timing methods were evaluated based primarily on their accuracy and to a lesser extent their use of system resources. Accuracy is the driving metric for the selection of the timing method, because the timing of the data collection window dictates which data is collected, and even minor drift or inconsistency in this window can compromise the integrity of the science data, which would threaten NanoSAM's primary mission.

Metric	Weight	Continuous Data Collection	Integrated clock with calibration via photodiode
Timing Accuracy	0.8	5	3
System Resource Use	0.2	5	5
Total	1	**5**	4.6

Table 58 Data Capture Timing Trade Study Results

1. Error Detection Method

Each error detection method was evaluated based on the maximum size of the error it can practically correct as well as the maximum size of error it can reliably detect. If an error occurs in program memory that is larger than the EDAC code can correct for, the software could stop functioning. It will be necessary to scrub all system memory frequently, so each method was also evaluated based on its system resource use, which includes the computational cost of decoding and the required memory volume. Lastly, the data rate of each EDAC code was assessed, which is the ratio of original data to redundant data. A low data rate will cost more memory and require extended downlink times.

Metric	Weight	Longitudinal Redundancy Check	Cyclic Redundancy Check	Hamming Code	Repetition Code
Maximum Correctable Error	0.35	3	3	3	5
Maximum Detectable Error	0.3	5	5	3	5
System Resource Use	0.25	3	1	5	1
Downlink Data Rate	0.1	3	5	5	1
Total	1	2.9	3.1	**3.7**	3.6

Table 59 Error Detection Method Trade Study Results

Software Baseline Design

NanoSAM II will feature a much expanded software system compared to that of NanoSAM I, adding data capture capability for both sunrise and sunset, as well as a more robust error detection system for onboard data storage and transmission. The primary functions of the software system include data capture, data storage, and data transmission. From these functions, two critical design choices were extracted.

Data Capture Timing

Continuous data collection was chosen primarily for its robustness when faced with variations in the time of sunset and sunrise. Timing the data capture window via the integrated clock may provide a similar level of timing precision, but the accuracy of the timing may become compromised if the software must pause for any reason, affecting subsequent data capture windows.

Error Detection Method

Hamming codes will be used as the primary method of error detection and correction in both the external science memory and internal program memory. While Hamming codes do not always detect burst errors, they are capable of detecting and correcting single bit errors, which account for approximately 98% of single event errors [65]. Hamming codes are thus suitable for use in both data transmission and data storage.

Calibration Method

A preliminary trade study concluded that calibration would be performed on-board the instrument prior to data transmission. This method was selected to minimize the the number of data types that must be stored and transmitted. However, further discussion with the customer concluded that the calibration window and science window are not separate events, but one continuous event. Based on this new understanding it was determined that the instrument will feature no self-calibration capabilities and instead all data will transmitted and calibration will be performed on the ground.

D. Optics Conceptual Design

Overview of NanoSAM I Design

Last year, the NanoSAM I senior project team designed and manufactured an optical sensor, a radiometer, to measure the intensity of 1.03 µm light. A radiometer has three distinct stages: Filtering, Focusing, and Sensing. In order to accomplish each stage, NanoSAM I designed and manufactured an Off-axis Parabolic (OAP) Telescope which uses an OAP Mirror to focus filtered 1.03 µm light onto the photodiode.

Due to time constraints, NanoSAM I was never able to fully align the radiometer and the performance of this instrument and the system as a whole was never verified nor tested. Despite this, the process of designing, manufacturing, and aligning yielded a wealth of lessons and analysis which will be applied this year to create an improved radiometer specifically with regards to alignment tooling. Additionally, this radiometer will be aligned, tested, and validated, a process which NanoSAM I was unable to complete due to circumstance.

Below is a simplified diagram of the Radiometer design.

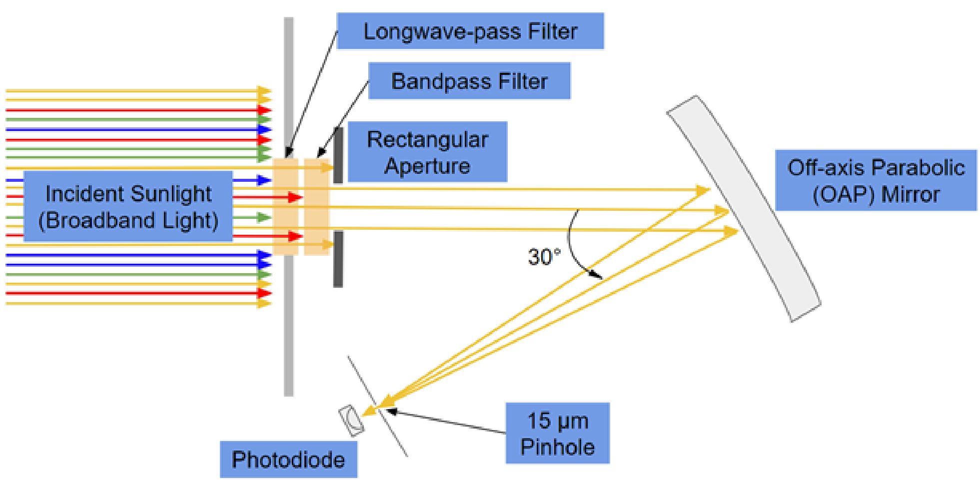

Fig. 105 NanoSAM I Radiometer Diagram

Maintained and Reviewed Design Decisions

The baseline design of the Herschelian telescope designed by NanoSAM I will be used by NanoSAM II. A complete redesign of the optical system was considered, but it was decided to be out of the scope of the NanoSAM II project. Instead, NanoSAM II will improve the alignment and alignment tooling of the existing optical system. Several optical components were purchased by NanoSAM I, and are now available to NanoSAM II for no cost. Due to the low cost, reduced logistical risk, and reduced design complexity of using already provided components, NanoSAM II will be reusing several components from NanoSAM I.

NanoSAM II will use the same OAP mirror and filters, the core optical components of the radiometer, as NanoSAM I. It was determined by NanoSAM I and reaffirmed by NanoSAM II that the selected filters satisfied Requirement 3.1 - Wavelength. Replacement of the OAP mirror was considered, but after a short investigation that a larger COTS mirror which still satisfied the 0.5U CubeSat requirement was not available and a custom mirror was cost-prohibitive. The trade studies conducted on each design decision are available in Appendix B.

The primary updates to the optics design are in the alignment tooling and procedure. NanoSAM I failed to precisley align their radiometer. NanoSAM II has the benefit of taking the previous team's advice to improve the alignment process. For instance, a kinematic base will be added to the alignment setup which will allow for the easy removal, shimming, and replacement of the optics bench during alignment. Unrelated to NanoSAM I's work, the COVID-19 pandemic has limited NanoSAM II's access to Ball Aerospace's Optical Alignment facilities. NanoSAM II updated its alignment procedure and tooling accordingly. The primary difference in the alignment procedure is that NanoSAM II will use a convex return sphere (reflective steel ball) instead of a concave return sphere. Late in the fall semester, the NanoSAM II optics team conducted its first practice alignment session using the steel ball method. The resulting alignment was poor, likely a result of the team's inexperience with interferometers. However, to mitigate the risk of a fundamental flaw in the steel ball method, the NanoSAM II optics team has developed an alternative method, placing a reflective coating on the curved surface of a spherical lens which could be used as a custom concave sphere similar to NanoSAM I's alignment design. Finally, some optics design updates were caused by the new, 0.5U CubeSat requirement. The 5cm width constraint forced a partial redesign of the optics bench to fit within the new boundaries.

Optics Baseline Design

NanoSAM II will build off of the system designed and built by NanoSAM I. In order to reduce cost and logistical risk, NanoSAM II will reuse several parts ordered by NanoSAM I. New components will be added in order to improve the alignment and the alignment process.

Photodiode Block Translation Tunability In order to tune the Photodiode Block Translation, the trade study demonstrated shims to be the optimal design choice. Shims can be made of a single material which reduces thermal deformation uncertainty. Additionally, shims do not rely on friction interactions, which could be disrupted when subjected to vibrational stress. Shims are not quite as precise as translational mounts, but the disadvantage here is outweighed by the low material complexity and lack of friction interactions. Shims are a less expensive tuning method than rails or translational mounts which further reinforces the results of the trade study.

OAP Mirror Selection There were two options for the OAP mirror diameter: to continue using the OAP mirror ordered by NanoSAM I or to replace it with a custom OAP mirror with a slightly larger diameter in order to reduce wave front error resulting from the slight deformation due to the mirror's mounting points. The NanoSAM I OAP mirror is available immediately at no cost, while a custom mirror was estimated to be around $1200 (more than a fifth of NanoSAM II's budget), and to have a 12-17 week lead time. Even though a custom OAP mirror could improve the quality of optical measurements, the cost and lead time of attaining one prohibits this option. Therefore, NanoSAM II will be using the OAP mirror purchased by NanoSAM I.

Field Stop Geometry Two field stop geometries were considered, that of a pinhole and that of a slit. NanoSAM I used a 15 μm pinhole, that was calculated to meet a satisfactory intensity for the functional requirement of SNR. However, a 120 μm pinhole will be needed to meet the required field of view of 1.3 arc minutes. Because a slit will let in more light than a pinhole, a slit will also meet the requirements for SNR and field of view. Therefore, the decision came down to design complexity and cost. The system designed by NanoSAM I is already designed for a pinhole field stop requiring no major changes to the overall design. A new pinhole of the appropriate size (20 μm) will need to be purchased, but will be less expensive that purchasing a slit field stop. In contrast, NanoSAM II would have to buy a slit, which is about twice the cost of a pinhole, and adjust the optical system to account for a slit instead of a pinhole. These factors make a pinhole the optimal design choice, because it meets the necessary optical requirements with minimal additional cost and design complexity.

XV. Test Data

A. Vibrational Test Data from Altius Space Machines

The following figures are the raw test data provided to us by Altius Space Machines. The full report from Altius is available on the google drive under /Structures/2021$_{0}$3$_{2}$4$_{N}$$anoSAM_{R}eport_{V}ibe.pdf$

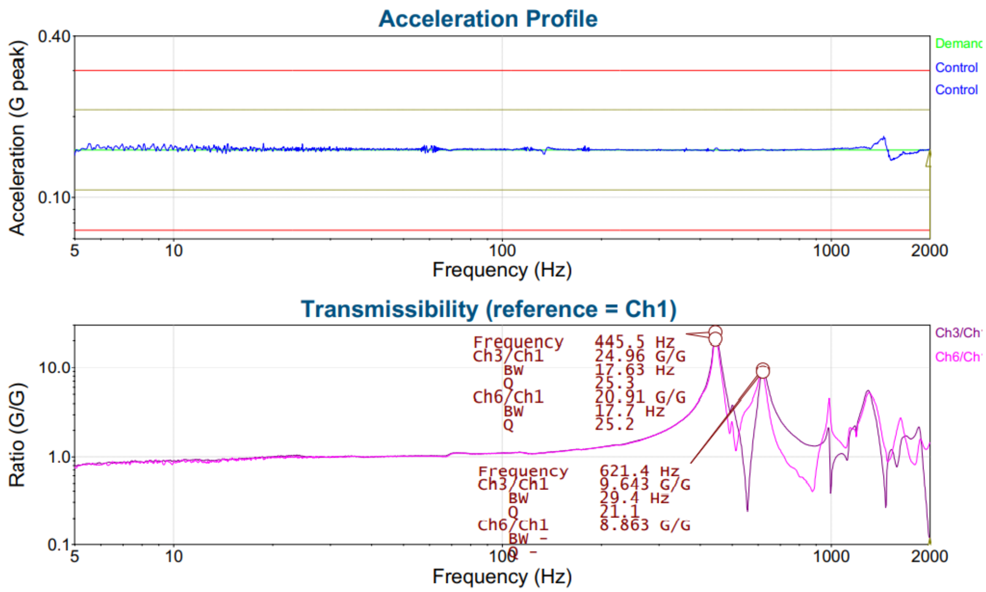

Fig. 107 Y Sine Sweep Results

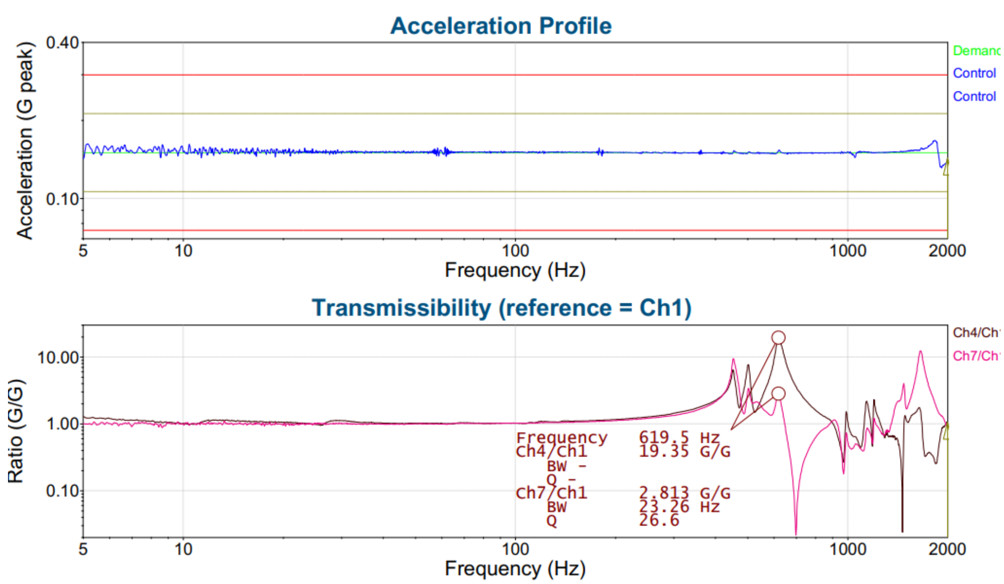

Fig. 108 Z Sine Sweep Results